

UNCLASSIFIED

AD NUMBER

AD856711

LIMITATION CHANGES

TO:

Approved for public release; distribution is unlimited.

FROM:

Distribution authorized to U.S. Gov't. agencies and their contractors; Critical Technology; MAY 1969. Other requests shall be referred to Air Force Rome Air Development Center, EMASS, Griffiss AFB, NY 13440. This document contains export-controlled technical data.

AUTHORITY

radc, usaf ltr, 17 sep 1971

THIS PAGE IS UNCLASSIFIED

AD856711

RADC-TR-68-340, Vol I
Final Technical Report
May 1969

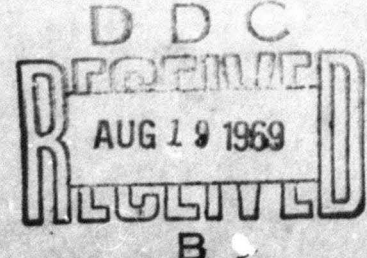


INVESTIGATION OF SCATTERING PRINCIPLES

Dr. George W. Gruver
General Dynamics
Fort Worth Division

This document is subject to special export controls and each transmittal to foreign governments, foreign nationals or representatives thereto may be made only with prior approval of RADC (EMASS), GAFB, NY 13440

Rome Air Development Center
Air Force Systems Command
Griffiss Air Force Base, New York



253

When US Government drawings, specifications, or other data are used for any purpose other than a definitely related government procurement operation, the government thereby incurs no responsibility nor any obligation whatsoever; and the fact that the government may have formulated, furnished, or in any way supplied the said drawings, specifications, or other data is not to be regarded, by implication or otherwise, as in any manner licensing the holder or any other person or corporation, or conveying any rights or permission to manufacture, use, or sell any patented invention that may in any way be related thereto.

ADMISSION for	
OFB#	WHITE SECTION <input type="checkbox"/>
DS%	BUFF SECTION <input checked="" type="checkbox"/>
UNANNOUNCED	<input type="checkbox"/>
JUSTIFICATION	
BT	
BUREAU SECTION/AVAILABILITY COPIES	
INST.	AVAIL. AND/ OR SPECIAL
2	

Do not return this copy. Retain or destroy.

ABSTRACT

The results of a comprehensive investigation of the principles of long- and short-pulse radar scattering are presented. Analytical expressions are derived for use in computing the radar cross section and scattering phase of a variety of generic and composite shapes. Measurements obtained by use of a coherent radar are utilized to validate these expressions. Procedures necessary for obtaining high-quality, coherent, long- and short-pulse scattering matrix measurements are presented along with the derivation of a method of processing phase data in order to determine, as a function of aspect angle, the absolute position of the target phase center in space. Consideration is given to the results of an extensive investigation of the use of linear superposition as a means of computing the scattering matrix of a vehicle which is composed of a number of generic surfaces. The salient points of an investigation of the use of radar signatures in four computerized inverse scattering techniques are included. These techniques are based on the use of (1) cross section and phase, (2) polarization, (3) phase, and (4) short-pulse signatures.

INVESTIGATION OF SCATTERING PRINCIPLES

**Dr. George W. Gruver
General Dynamics
Fort Worth Division**

This document is subject to special export controls and each transmittal to foreign governments, foreign nationals or representatives thereto may be made only with prior approval of RADC (EMASS), GAFB, NY 13440

FOREWORD

This report is a documentation of a program designed to enhance the state of knowledge of the principles of radar scattering. During this program, particular attention has been given to the development of computerized techniques based on the application of radar signatures for use in inverse scattering analyses.

This work was sponsored by the Space Surveillance and Instrumentation Branch of Rome Air Development Center under the auspices of Mr. John Cleary. The investigation was conducted by the Fort Worth Division of General Dynamics, Fort Worth, TX 76101, under Contract F30602-67-C-0074. This report was prepared by Dr. G. W. Gruver of the Fort Worth division. Major contributions to this program were made by Dr. C. C. Freeny, Mr. W. P. Cahill, and Mr. R. G. Hajovsky of the Fort Worth division. Mr. R. A. Ross of Cornell Aeronautical Laboratories conducted an extensive analytical investigation under subcontract to the Fort Worth division.

This report is General Dynamics Report No. FZE-791; its contents and the abstract are unclassified. The RADC project number is 6512, task 651207. Distribution is limited by the Mutual Security Acts of 1949.

This technical report has been reviewed and is approved.

Approved: *John C. Cleary*
JOHN C. CLEARY
Contract Engineer

Approved: *WILLIAM T. POPE*
WILLIAM T. POPE
Acting Chief
Surveillance & Control Division

FOR THE COMMANDER: *Irving J. Gabelman*
IRVING J. GABELMAN
Chief, Advanced Studies Group

T A B L E O F C O N T E N T S

<u>Section</u>	<u>Title</u>	<u>Page</u>
1	Introduction and Summary	
	1.1 Introduction	1
	1.2 Summary	4
2	Experimental Investigation	
	2.1 General	11
	2.2 Long Pulse Measurements	12
	2.2.1 Electronics System	13
	2.2.2 Radar Range Setup Procedures	15
	2.2.3 Absolute Phase Calibration	19
	2.2.4 Bistatic Measurement Procedures	25
	2.2.5 Vehicle Model Specification	26
	2.2.6 Measurements Data Recording and Processing	28
	2.3 Short Pulse Measurements	33
	2.3.1 Electronic System	35
	2.3.2 Radar Range Setup Procedures	44
	2.3.3 Amplitude and Phase Calibration	48

<u>Section</u>	<u>Title</u>	<u>Page</u>
	2.3.4 Measurements Data Recording and Processing	55
	2.4 Results and Conclusions	65
3	Analytical Investigation	
	3.1 General	67
	3.2 Results	70
	3.3 Conclusions	76
4	Superposition Investigation	
	4.1 General	79
	4.2 Technical Approach	82
	4.3 Superposition Example (Model F5CY5)	91
	4.4 Superposition Results	128
	4.4.1 Model AC4	128
	4.4.2 Model AC1	145
	4.4.3 Model A2	151
	4.4.4 Model A3	161
	4.4.5 Model X2	174
	4.4.6 Model X1	185
	4.5 Conclusions	192
5	Synthesis Investigation	
	5.1 General	197
	5.2 Technical Approach	197
	5.3 Results and Conclusions	199

<u>Section</u>	<u>Title</u>	<u>Page</u>
6	Inverse Scattering Investigation	
	6.1 General	201
	6.2 Matched Filter Technique	202
	6.2.1 Analytical Approach	202
	6.2.2 Application of MFT to Synthesized Signatures	205
	6.2.3 Application of MFT to Measured Signatures	212
	6.3 Polarization Technique	213
	6.3.1 Analytical Approach	213
	6.3.2 Computation Technique	216
	6.4 Phase Signature Technique	218
	6.4.1 Analytical Approach	218
	6.4.2 Computation Technique	219
	6.5 Results and Conclusions	219
7	Short Pulse Equivalence Class Technique	
	7.1 General	221
	7.2 Technical Approach	225
	7.3 Technical Investigation	227
	7.4 Results and Conclusions	228
	7.4.1 Results	228
	7.4.2 Conclusions	231
8	Recommendations	232
	References	233

LIST OF FIGURES

Number	Title	Page
2-1	Radar Scattering Range	14
2-2	Absolute Phase Location Geometry for Cylinder	21
2-3	Phase Reference Points for Composite Targets	24
2-4	Typical Vehicle Models	29
2-5	Construction of Composite Vehicles	30
2-6	Flow Diagram for Processing Radar Signature Data	31
2-7	Block Diagram of Short-Pulse Radar	36
2-8	System Timing Diagram	38
2-9	C-band Short-Pulse Data	41
2-10	Short-Pulse System Stability	42
2-11	Block Diagram of Recording System	43
2-12	Magnetic Tape Format for Short-Pulse Data	45
2-13	Ground Plane Range Geometry	46
2-14	Interpretation of Amplitude Calibration	52
2-15	Interpretation of Phase Data	53
2-16	Comparison of System Phase Response with a Circular Function	56
2-17	Short-Pulse Library Tape Processing Sequence	59
2-18	Short-Pulse Data Frames	62

Number	Title	Page
3-1	Radar Cross Section for Model F5CY5, VV Polarization	72
3-2	Scattering Phase for Model F5CY5, VV Polarization	73
3-3	Radar Cross Section for Model F5CY5, HH Polarization	74
3-4	Scattering Phase for Model F5CY5, HH Polarization	75
4-1	Surface Discontinuity Between Cone and Cylinder	82
4-2	Geometrical Model for Alignment Error Analysis	84
4-3	Amplitude Error Resulting from Location Error	87
4-4	Example of Target Translation Using Superposition Parameters	89
4-5	Phase Signature for Model F5 - VV Polarization	92
4-6	Cumulative Phase for Model F5 - VV Polarization	93
4-7	Bistatic - Monostatic Relationship	95
4-8	Phase Center Coordinate System	97
4-9	Position Errors for Model F5	98
4-10	Measured and Corrected Phase for Model F5 - VV Polarization	101
4-11	Geometrical Relationship Between Location Vectors	103
4-12	Phase for Model CY5 - VV Polarization	105

Number	Title	Page
4-13	Position Errors for Model CY5	106
4-14	Illustration of Vehicle Rotation	107
4-15	Illustration of Shadow Regions for Model F5CY5	109
4-16	Flow Diagram of Superposition Process	111
4-17	Logic Diagram of Superposition Program	112
4-18	Measured Cross Section for Model F5CY5 - VV Polarization	113
4-19	Computed Cross Section for Model F5CY5 - VV Polarization	114
4-20	Measured Phase for Model F5CY5 - VV Polarization	115
4-21	Computed Phase for Model F5CY5 - VV Polarization	116
4-22	Measured Cross Section for Model F5CY5 - HH Polarization	117
4-23	Computed Cross Section for Model F5CY5 - HH Polarization	118
4-24	Measured Phase for Model F5CY5 - HH Polarization	119
4-25	Computed Phase for Model F5CY5 - HH Polarization	120
4-26	Illustration of Coupling at Interface of Two Vehicles	122
4-27	Measured and Computed Cumulative Phase for Model F5CY5	124
4-28	Measured and Computed Phase Center Location for Model F5CY5 - VV Polarization - Polar Plot	126

Number	Title	Page
4-29	Measured Cross Section for Model AC-4 - VV Polarization	132
4-30	Computed Cross Section for Model AC-4 - VV Polarization	133
4-31	Measured Phase for Model AC-4 - VV Polarization	134
4-32	Computed Phase for Model AC-4 - VV Polarization	135
4-33	Cumulative Phase for Model AC-4 - VV Polarization	136
4-34	Measured Position of Phase Center for Model AC-4 - VV Polarization - Polar Plot	137
4-35	Measured Position of Phase Center for Model F1 - Polar Plot	138
4-36	Measured Cross Section for Model AC-4 - HH Polarization	139
4-37	Computed Cross Section for Model AC-4 - HH Polarization	140
4-38	Measured Phase for Model AC-4 - HH Polarization	141
4-39	Computed Phase for Model AC-4 - HH Polarization	142
4-40	Measured Cross Section for Model AC-1 - VV Polarization	147
4-41	Computed Cross Section for Model AC-1 - VV Polarization	148
4-42	Measured Phase for Model AC-1 - VV Polarization	149
4-43	Computed Phase for Model AC-1 - VV Polarization	150

Number	Title	Page
4-44	Measured Cross Section for Model A2 - VV Polarization	153
4-45	Computed Cross Section for Model A2 - VV Polarization	154
4-46	Computed Cross Section for Model A2-3 - VV Polarization	155
4-47	Measured Phase for Model A2 - VV Polarization	156
4-48	Computed Phase for Model A2 - VV Polarization	157
4-49	Illustration of Shadow Region for Model A2	162
4-50	Illustration of Shadow Region for Model A3	164
4-51	Measured Cross Section for Model A3 - VV Polarization	165
4-52	Computed Cross Section for Model A3 - VV Polarization	166
4-53	Measured Cross Section for Model A3 - HH Polarization	167
4-54	Computed Cross Section for Model A3 - HH Polarization	168
4-55	Measured Phase for Model A3 - VV Polarization	169
4-56	Computed Phase for Model A3 - VV Polarization	170
4-57	Measured Phase for Model A3 - HH Polarization	171
4-58	Computed Phase for Model A3 - HH Polarization	172

Number	Title	Page
4-59	Illustration of Shadow Regions for Model X2	175
4-60	Measured Cross Section for Model X2 - VV Polarization	177
4-61	Computed Cross Section for Model X2 - VV Polarization	178
4-62	Measured Phase for Model X2 - VV Polarization	179
4-63	Computed Phase for Model X2 - VV Polarization	180
4-64	Measured Cross Section for Model X2 - HH Polarization	181
4-65	Computed Cross Section for Model X2 - HH Polarization	182
4-66	Measured Phase for Model X2 - HH Polarization	183
4-67	Computed Phase for Model X2 - HH Polarization	184
4-68	Illustration of Shadow Regions for Model X1	185
4-69	Measured Cross Section for Model X1 - VV Polarization	188
4-70	Computed Cross Section for Model X1 - VV Polarization	189
4-71	Measured Phase for Model X1 - VV Polarization	190
4-72	Computed Phase for Model X1 - VV Polarization	191

Number	Title	Page
5-1	Generic Surface Discontinuities Exhibited by Synthesis Vehicles	200
6-1	Geometry Used with Program MFTGE 265	208
6-2	Geometry of Problem Illustrated in Figure 6-3	208
6-3	Correlation Coefficients Computed By Use of MFTGE 265	210
6-4	Target Symmetry Envelope	215
6-5	Flow Diagram of Polarization Program - AG3	217
6-6	Flow Diagram of Phase Subroutine - AG3	220
7-1	SOI/BMD Data Processing	223
7-2	Flow Diagram of Generalized ECT	226
7-3	Short-Pulse Library Tape Processing Sequence	229
7-4	Computer Program SPECT Processing Sequence	230

LIST OF TABLES

Number	Title	Page
2-1	Vehicle Measurement Data	27
2-2	Magnetic Tape Format for Long Pulse Data	34
2-3	Short-Pulse Radar Characteristics	39
2-4	Short-Pulse System Calibration	49
3-1	Measurement and Computation Parameters	71
4-1	Superposition Targets	129
4-2	Model AC-4 Superposition Parameters	130
4-3	Model AC-1 Superposition Parameters	146
4-4	Model A2 Superposition Parameters	152
4-5	Model A2 Superposition Parameters	160
4-6	Model A3 Superposition Parameters	163
4-7	Model X2 Superposition Parameters	176
4-8	Model X1 Superposition Parameters	187
6-1	Listing of Program MFTGE 265	206
6-2	Input and Output Parameters for MFTGE 265	207

EVALUATION

The objectives of contract F30602-67-C-0074 were to establish and apply the mechanics of radar scattering from complex objects in terms of actual measurement data and the resulting empirically derived mathematical relationships. Scattering matrix data was obtained for 54 different model configurations. A number of different conditions of frequency and bistatic angle were used to obtain 72 complete sets of scattering matrix data.

Geometric diffraction theory was used to predict radar scattering cones, frustra, cylinders, hemispheres and combinations of these generic surfaces. Comparisons of theory and measurement were generally very good. However the form of geometrical diffraction theory used was only valid at and near nose-on and tail-on axial aspects. Additional effort is needed to improve prediction techniques for the cone at other aspects. Moderate success was obtained in using linear superposition of radar range signature data to construct radar signatures of composite targets.



JOHN C. CLEARY
Contract Engineer

SECTION 1

INTRODUCTION AND SUMMARY

1.1 Introduction

This document is Volume I of a set of four volumes (References 1, 2, 3) which comprise the Technical Documentary Report on the Investigation of Scattering Principles, Contract F30(602)-67-C-0074. This investigation was performed during 1967 and 1968 by the Fort Worth division of General Dynamics under contract to Rome Air Development Center. The overall investigation was divided into the following elements:

1. An experimental investigation of the scattering matrices of a broad spectrum of target configurations and frequencies
2. An analytical investigation of the use of the geometrical theory of diffraction (GDT) to compute the monochromatic scattering matrix of selected targets
3. An investigation of the applicability (and limitations) of using linear superposition of target signature data to construct radar signatures of composite targets
4. An investigation of the possibility of synthesizing the signatures of complex targets by the use of

targets exhibiting various degrees of physical similitude to the target of interest

5. An investigation of the use of long- and short-pulse radar signatures in inverse scattering analyses as a means of estimating target physical characteristics.

Comprehensive coverage of the spectrum of scattering mechanisms and geometries was needed to fulfill the requirements for the various investigations conducted under this contract. Consequently, the scope of the measurement program was quite large, and a wide range of different surface and body configurations had to be constructed and measured. In fact, the scope of these measurements was so extensive that the resulting data may represent a significant contribution in the field of radar signature measurements. For this reason, the results of the long-pulse measurement program are being published in a separate volume (Volume II).

Volume II contains measured scattering matrix data obtained by the use of 54 different model configurations. A number of different conditions of frequency and bistatic angle were used in order to obtain 72 complete sets of scattering matrix data in which the scattering matrix was recorded for a full 360 degrees of target aspect in steps of 0.1 degree. In order to obtain the scattering matrix,

it was necessary to obtain cross section and phase measurements under at least two polarization conditions; three polarizations were required in the case of asymmetrical targets. Consequently, the measurement program involved the accomplishment of 154 measurement runs in which targets were used. A total of well over 300 measurements were required for the measurement runs necessary (1) to calibrate the system, (2) to ascertain the field gradients across the target volume, (3) to ascertain and reduce the background levels, and (4) to establish an absolute phase reference for each target.

Short-pulse measurements were utilized in two areas of this investigation. The C-band short-pulse signatures of a sphere-tipped cone were used in connection with the analytical investigation of the scattering from a cone. These data are contained in Volume III of this report. Both C- and X-band data were obtained from a short-pulse measurement program conducted by the Fort Worth division under Contract AF30(602)-67-C-0185 with Rome Air Development Center. The cooperation of Mr. Dan Tauroney of Rome Air Development Center is gratefully acknowledged with regard to the use of these data which were used to provide for the initial checkout of the short-pulse equivalence class technique.

An analytical investigation conducted by Cornell Aeronautical Laboratory under subcontract to the Fort Worth Division of General Dynamics is presented in Volume III. The objectives of this investigation were the derivation of analytical techniques for predicting the radar cross section and scattering phase of a set of surface configurations, including cones, frusta, cylinders, hemispheres, and combinations of these generic surfaces. The derivation of these formulae, the predictions obtained by their use, and a detailed comparison of these predictions with the measurements obtained by use of physical models are contained in Volume III.

The results of the synthesis investigation and the inverse scattering investigation are contained in Volume IV of this report. Volume IV has been assigned a SECRET classification by virtue of (1) the potential military applications of the inverse scattering techniques contained therein and (2) the use of models which represent, to varying degrees of synthesis, targets that are presently of military interest.

1.2 Summary

The overall objective of the scattering principles investigation was an attempt to advance the state of knowledge of scattering phenomena, particularly from the viewpoint

of practical utilization of radar scattering information.

The investigation comprised five basic tasks:

1. Experimental Investigation
2. Analytical Investigation
3. Superposition Investigation
4. Synthesis Investigation
5. Inverse Scattering Investigation.

The results obtained from each of these tasks are published in a Technical Documentary Report comprised of four volumes.

This volume, Volume I, contains a summary of each task as well as detailed documentation on the experimental and superposition investigations. Volume III contains the results of the analytical investigation conducted by CAL under subcontract to the Fort Worth division of General Dynamics. An extensive set of analytical expressions for computing the scattering matrices of a set of rotationally symmetric surfaces were derived in this effort.

Volume II contains the results of the experimental investigation. In this effort, the scattering matrices of 66 separate vehicles were measured by use of coherent radars on the Radar Range at the Fort Worth Division. These measurements included the measurement of the position, in space, of the absolute phase center of each measurement vehicle. The 66 vehicles included a set of 12 generic surfaces (cones,

frusta, and cylinders) and composite vehicles obtained by interconnecting these surfaces. Section 2 of this document contains a complete description of this investigation, although the bulk of measurement data is contained in Volume II. These measurements provided a broad spectrum of signature data for use in the other tasks conducted during this program. These included data for use in validating the analytical expressions derived by CAL and for use in the superposition, synthesis, and inverse scattering investigations.

Section 4 contains the documentation of the analysis and results of the superposition investigation in which the feasibility of superimposing vehicle signatures to produce the signature of a composite body was investigated. The results of this effort indicate that the superposition process is highly feasible within certain limitations. These limitations are related to the confidence level associated with the use of superposition at aspect angles where one surface may be directly behind another surface, such as aspects near the axis of a target and at intermediate aspects in the case of vehicles which exhibit a large number of scattering centers. Within these constraints, superposition appears to be a powerful tool for use in

obtaining a quick look at the detailed radar signature of composite targets.

In the practical use of superposition it should be noted that scattering matrix signatures must be available for a set of surfaces from which a large number of vehicles can be constructed and for a set of radar frequencies of interest. The number of frequencies utilized by both operational and developmental radars which are designed for use against exo-atmospheric and reentry type targets is actually quite small. Consequently, it appears feasible to develop a bank of generic signatures at a frequency utilized by a particular radar of interest. These generic signatures could then be used, in conjunction with the superposition process, to provide initial signature information on any vehicle whose physical characteristics become available.

The vehicle designer and the weapon system designer alike would derive a great deal of information from the utilization of such a bank of signatures. The development of such a bank would be of moderate cost; however, its maintenance and operation would be insignificant since (1) any general-purpose computer could be used, (2) signature data could be stored very efficiently on tape or discs, and (3) the computer would be available for other uses at all

times when signature data were not being processed. The real keys to the establishment of such a bank are (1) the demonstrated capability of obtaining accurate amplitude and absolute phase measurements on generic surfaces and (2) the definition of a set of surfaces into which the majority of the composite vehicles of interest can be decomposed.

Section 5 contains a brief description of an investigation of the feasibility of synthesizing signatures of one vehicle by use of measurements on a different vehicle which displays a given degree of similitude to the original vehicle. A set of computerized techniques for comparing signatures was developed for use in deriving objective measures of the similitude of signatures obtained by use of vehicles. These techniques can be used to synthesize the physical characteristics of a basic vehicle to varying degrees. The results of this investigation are reported in detail in Volume IV. However, in general, the results obtained with reference to physical synthesis complement those obtained by use of superposition (e.g., the severest errors occur near axial aspects and at intermediate angles where a number of scattering centers combine to produce the total scattered return).

Section 6 contains the derivation and definition of a set of three inverse scattering techniques based on the

use of (1) polarization, (2) phase, and (3) amplitude and phase signatures. Each of these techniques provide information for use in comparative signature analyses, as well as in the estimation of the actual physical characteristics of targets. The results obtained by use of these techniques to measured signatures for a number of vehicles, including the synthesis vehicles, are described in Volume IV. The reader who is interested in SOI will be particularly interested in some of the remarkable results obtained by use of these rather simple processing techniques. Moreover, techniques, such as the Matched Filter Technique, are shown to produce good results when used with signatures that represent only a very small variation in target aspect.

The investigation described in Section 7 is related to the definition of an equivalence class technique based on the use of short-pulse signatures. As in the case of signature synthesis and inverse scattering, the results of this investigation are described in Volume IV. However, Section 7 does contain a basic description of the rationale of the equivalence class technique, as well as a general discussion of the various discriminants which may be efficiently extracted from the equivalence classes and the information which these discriminants display in terms of

vehicle physical characteristics. The application of this technique in real time, in conjunction with operational radars, is described in Volume IV.

SECTION 2

EXPERIMENTAL INVESTIGATION

2.1 General

The objective set for the experimental investigation was to provide comprehensive scattering data on a selected set of scattering surfaces and bodies in order to fulfill the needs of the varied investigations conducted under this contract. Consequently, the scope of the measurement program was quite large, and a wide range of different surface and body configurations had to be constructed and measured.

Measurements data obtained on this program consists of long- and short-pulse radar cross section and phase measurements obtained by use of the Radar Range at the Fort Worth division of General Dynamics. These measurements were obtained for a variety of conditions of the parameters of the radar system including pulse width, frequency, polarization, and bistatic angle. These measurements were such that the monostatic and/or bistatic scattering matrix was obtained for each vehicle model at at least one frequency by use of the long-pulse system. Sub-sections 2.2 and 2.3, respectively, contain a description of the measurement systems and detailed descriptions of the specific techniques which were used to ensure the quality of long- and short-pulse measurements.

Paragraph 2.2.5 contains data related to the physical characteristics of the vehicle models which were measured. Paragraphs 2.2.6 and 2.3.4 contain descriptions of the methods used to edit the long- and short-pulse data in order to provide these data in calibrated form on magnetic tapes for use as library data in a variety of computer programs.

Selected data is shown in this section in order to demonstrate the various measurement techniques used. However, due to the scope of the experimental investigation an effort has been made to present the experimental data to as large an audience as possible by presenting all of the analog plots of cross section and phase for the 54 different target vehicles in a separate volume of this documentary report, Reference 1.

Paragraph 2.2.5 contains a summary of the long-pulse measurements obtained under this program. This summary provides a readily accessible index to the radar parameters used to obtain each measurement.

2.2 Long Pulse Measurements

The long-pulse radar cross section and phase measurements utilized in this program were obtained through use of the Radar Range at the Fort Worth facilities of General Dynamics. A detailed description of this range is contained in Reference 4, however, a brief description is presented in the following paragraphs.

Figure 2-1 shows an illustration of the Radar Range configuration during a typical measurement run. The important components of the measurement system are discussed under separate paragraphs.

2.2.1 Electronics System

The radar used to obtain long-pulse measurements consists of a coherent pulsed radar which incorporates a range gate to provide target environment isolation. A dual antenna system is used in order to allow bi-static operation, denoted by β , the bi-static angle. Both amplitude and absolute phase measurements are obtained with the same system.

The radar transmitter consists of a coherent oscillator which drives a pair of traveling wave tubes in series to provide approximately one kilowatt of output power. The receiving system is a typical superheterodyne receiver which incorporates a variable range gate that is manually controlled to gate a 60-megahertz IF amplifier on during the time interval of the range gate. This variable range gate is controlled by the operator so that the location in space of the scattered signal can be varied between the target rotation and the secondary standard in order to calibrate the system.

Within the receiver system, a fixed range gate is utilized to turn on the receiver at a range at which no target is present in order to inject a reference signal from the

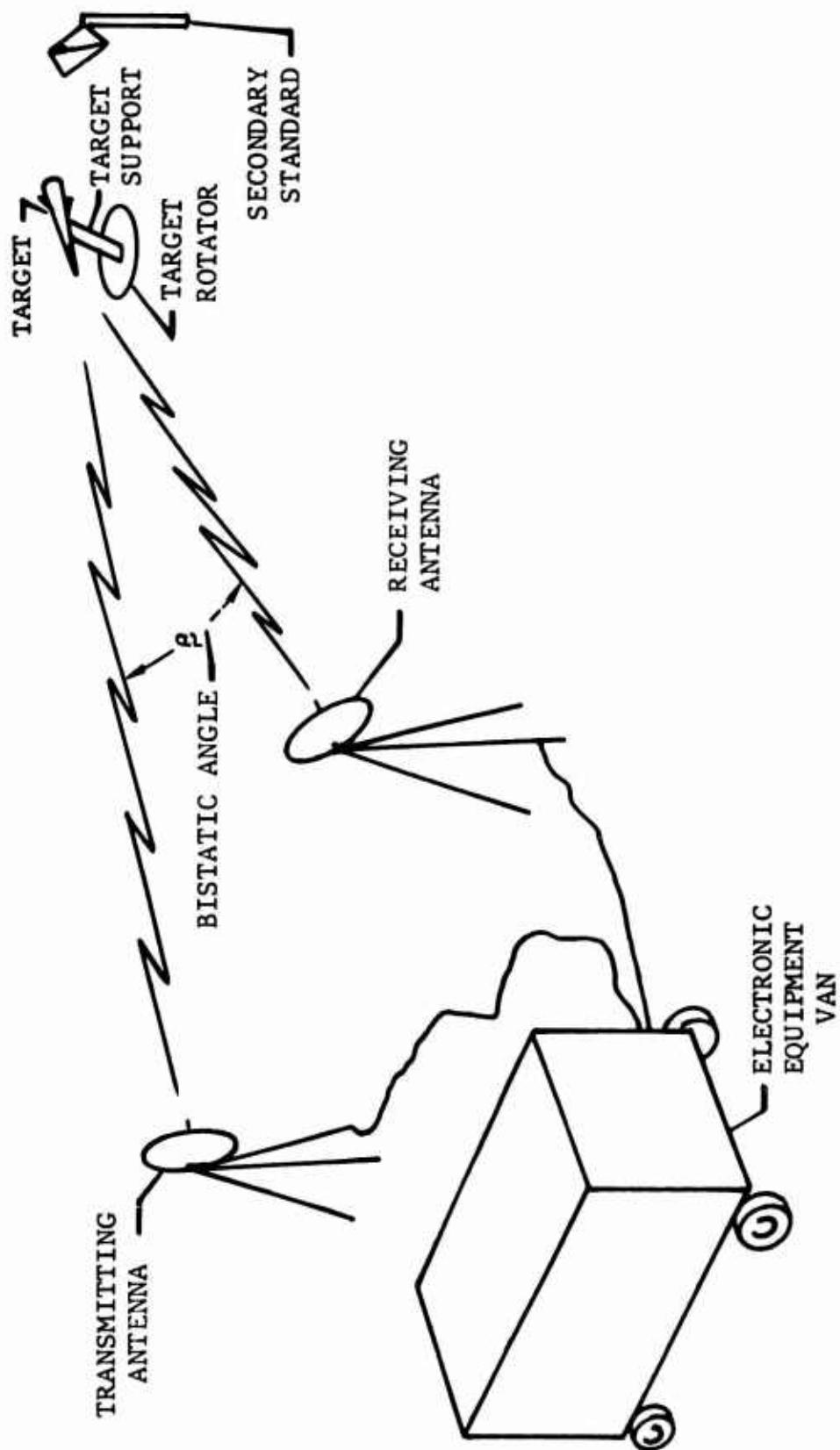


Fig. 2-1 Radar Scattering Range

transmitter. This reference signal is a 60-megahertz pulse which is injected from a pulsed coherent oscillator through a linear attenuator and a variable phase shifter. The difference between the target signal and the injected reference signal is applied to an amplitude servo and a phase servo which, if differences exist, are used to drive the calibrated attenuator and the variable phase shifter to force the two signals to correspond in both amplitude and phase. The resulting changes in the attenuator and the phase shifter are used to drive a pair of analog recorders and are also encoded to provide a digital output which is recorded on punch paper tape. During the calibration process, the outputs of the attenuator and the phase shifter are calibrated by use of a target of known cross section and location to provide radar cross section in decibels above a square meter (dBsm) and absolute phase.

The recording system records cross section to the nearest 0.1 dB, phase to the nearest degree (modulo 360 degrees), and aspect angle to the nearest 0.1 degree. The dynamic range of the cross section measurement system is 50 dB.

2.2.2 Radar Range Setup Procedures

In order to achieve accurate scattering measurements, a number of detailed setup procedures are necessary. These include:

1. Adjustment of the antenna heights and pointing directions to obtain maximum sensitivity and a uniform field amplitude and phase across the volume of space to be occupied by the target.
2. Adjustment of the target rotator so that the target rotates in the plane of the radar beam.
3. Utilization of all means possible to reduce the cross section of the target support, the target rotator, and other back-scattering mechanisms which might be located in the target range gate.
4. Calibration of the radar by use of a primary standard and calibration of a secondary standard.

The antenna heights are adjusted so that the target is located in the first lobe of the radar interference pattern.

The relationship

$$H_A = \frac{\lambda r}{4 H_T}$$

was used to provide an initial height, where

H_A = antenna

H_T = target height

λ = wavelength

r = radar range

Final adjustment is achieved by maximizing the return from a calibrated target.

In the subject effort, the uniformity of the field in the target area was determined by raising a calibration probe (in this case a corner reflector) through the target region and recording the signal return as a function of the height of the probe. If necessary, the radar range was then increased so that the amplitude gradient across the target volume was less than 0.5 dB/foot.

The tilt angle of the target rotator was adjusted so that the target would rotate in the plane of the radar beam, which generally is not parallel to the ground as a result of the ground plane action. This procedure was accomplished by adjusting the target rotator so that the radar cross section of each side of a flat plate was identical.

In order to determine the radar cross section and phase of a target accurately, the return from the rotator and other background objects must be minimized. Reduction in the cross section of the column was accomplished by physically changing the column size and making small adjustments in frequency. The combined effects of these two actions were used to time the column so that the reflections from the front and back of the column tended to cancel. In some cases, it was necessary to tilt the column away from the perpendicular in order to reduce the background level over a large angular region. Use of this tilting process essentially positioned the column so

that the radar illuminated a null in the column's back-scatter pattern; however, this result could not be achieved at all aspect angles. In such cases, the column was positioned so that the high value of background coincided with a high value of target cross section in order to introduce as insignificant an error as possible.

The background levels achieved during the measurements presented in this report averaged less than -40 dBsm, well below the value of cross section for a typical target.

In order to accurately measure the target scattering matrix, the antenna system must be capable of rejecting energy produced by undesirable polarizations. Such capability is usually expressed in terms of the dB rejection obtained when an antenna is required to receive a signal whose polarization is orthogonal to that of the antenna. The total field received by a vertically polarized antenna can be expressed as the phasor sum of a vertically polarized signal, \bar{E}_V , and a horizontally polarized signal, \bar{E}_H , as expressed in the following relationship.

$$\bar{E} = \bar{E}_V + \alpha_{VH} \bar{E}_H$$

α_{VH} represents the rejection of the antenna to horizontally polarized signals. The rejection achieved with the radar used to obtain the subject measurements was measured by use of a spherical target to be approximately 29.0 dB.

Amplitude calibration of the measured cross section was achieved by using a precision sphere for a primary standard and a corner reflector which was located outside of the target range gate for a secondary standard. The radar system was initially calibrated by placing a sphere of known cross section on the support column and measuring its cross section. The range gate was then moved to the vicinity of the corner reflector and its cross section was calibrated in terms of the cross section of the sphere. The secondary standard was subsequently measured before and after each measurement run so that system changes would be detected and corrected before the target was removed from the rotator.

2.2.3 Absolute Phase Calibration

A unique technique was used in order to determine the precise position in space of the instantaneous target phase center. Phase calibration was achieved by placing a cylinder with its axis vertical directly over the center of rotation of the target support column. When the rotator was rotated, the analog phase recording produced a periodic plot of phase similar to a sine function of aspect angle. The amplitude of this sine function is related to the deviation of the center of the cylinder from the true axis of rotation of the rotator. Although knowledge of this function allows the deviation to be post-calibrated for any deviation, the reference point on

the top of the rotator was generally moved so that the measured deviation was less than 360 degrees; this deviation corresponded to a maximum off-center distance of 1.0 inch. The actual equation which should be used to correctly locate the center of rotation along the radar line of sight (RLOS) is given by

$$R_e = \frac{1}{4k} \psi_e$$

where k = wave number

ψ_e = maximum measured phase deviation in degrees

R_e = distance the cylinder axis should be moved to be colinear with the center of rotation.

The value of 4 is necessary to account for the two-way radar path as well as the fact that the radius R_e is half of the measured geometrical difference. The aspect angle where ψ_e is maximum, is easily determined from the analog phase plot.

This same technique can be applied directly to a target if it possesses vertical planes of symmetry. For example, the actual center of rotation of a cylinder with its axis horizontal can be determined by determining the measured phase deviation between the opposite ends of the cylinders and that between the opposite sides of the cylinder. An illustration of how a cylinder might be erroneously placed on the rotator is shown in Figure 2-2.

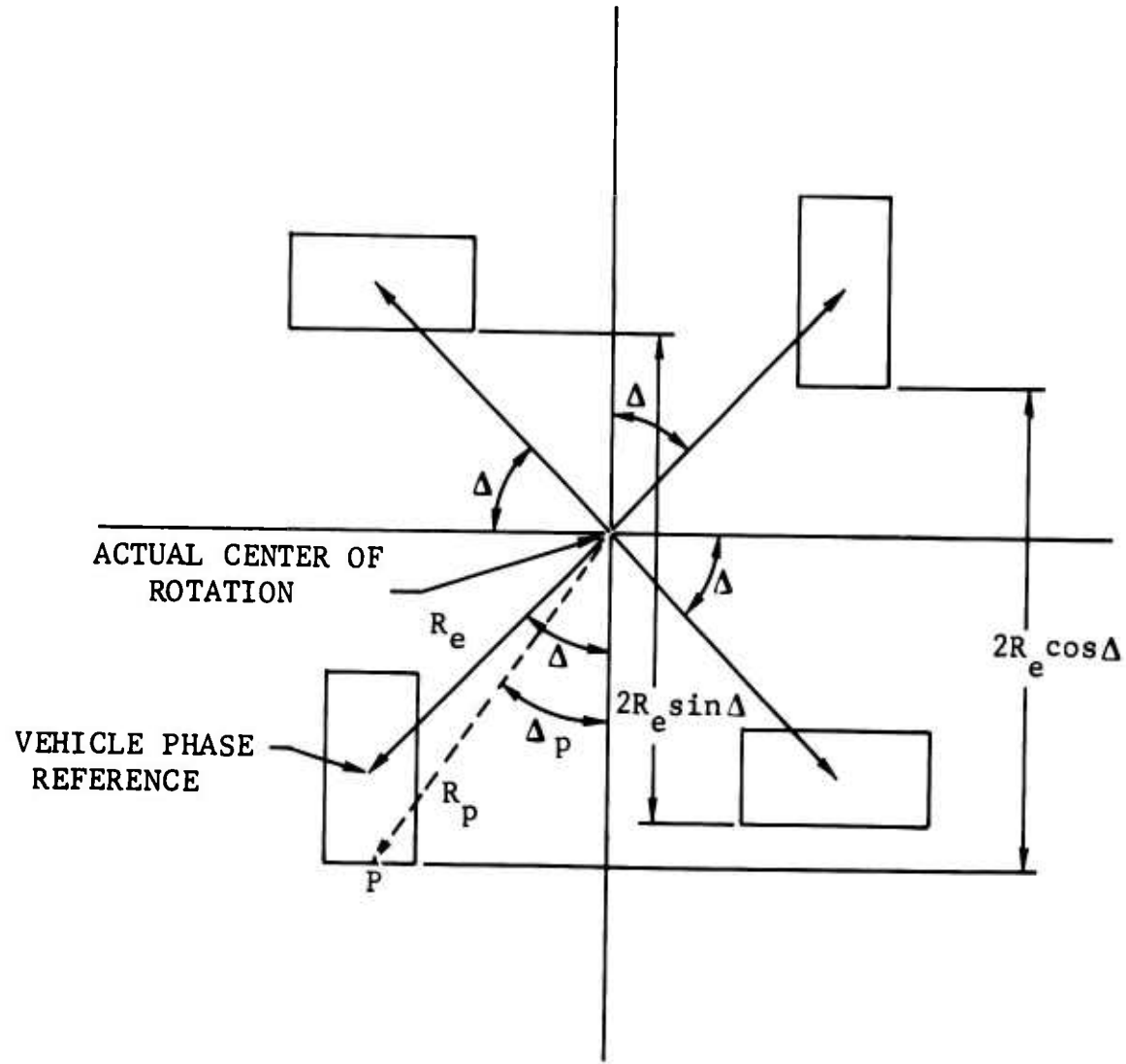


Fig. 2-2 ABSOLUTE PHASE LOCATION GEOMETRY FOR CYLINDER

The object of these measurements is to determine exactly where the target is located in relation to the center of rotation of the rotator. Consequently, the absolute position of the target phase center was determined so that its behavior could be traced as a function of target rotation.

The position of the center of the cylinder illustrated in Figure 2-2 can be determined from the plot of measured phase obtained when the rotator is rotated through 360 degrees in azimuth. The difference in measured phase obtained when the target presents its two end-on aspects to the radar is given by

$$\begin{aligned}\Delta\psi_{eo} &= 2k(2R_e \cos \Delta) \\ &= 4kR_e \cos \Delta\end{aligned}\quad (2-1)$$

Similarly, the difference in measured phase obtained when the target presents its two broadside views to the RLOS (broadside is here used to indicate that the cylinder axis is perpendicular to the RLOW) is given by

$$\begin{aligned}\Delta\psi_{BS} &= 2k(2R_e \sin \Delta) \\ &= 4kR_e \sin \Delta\end{aligned}\quad (2-2)$$

Equations 2-1 and 2-2 may be solved simultaneously to give the radius arm, R_e , and its position angle, Δ , which is measured relative to an end on view. The solution of these equations gives

$$R_e = \frac{1}{4k} \sqrt{(\Delta\psi_{eo})^2 + (\Delta\psi_{BS})^2}$$

$$\Delta = \tan^{-1} \left[\frac{\Delta\psi_{BS}}{\Delta\psi_{EO}} \right]$$

The location of points on the target other than its geometrical center may also be referenced in a similar manner by simple vector manipulations. Point P on the cylinder could be used as a reference, for example, by noting that

$$P = \sqrt{R_e^2 \sin^2 \Delta + (R_e \cos \Delta + L/2)^2}$$

and $\Delta_p = \tan^{-1} \left[\frac{R_e \sin \Delta}{R_e \cos \Delta + L/2} \right]$

where L is the length of the cylinder.

This type of transformation is necessary when the location of a target is to be synthesized by operations on its measured phase data. The use of these transformations is discussed in detail in Section 4 with regard to the superposition of targets.

This technique was used to locate the position of the center of rotation on the top of the target support column. Reference marks were then used to locate each target model with respect to the center of rotation. Figure 2-3 illustrates the method in which different target types were referenced to the center of rotation.

During each measurement sequence, the following items were continuously monitored to assure the accuracy of all

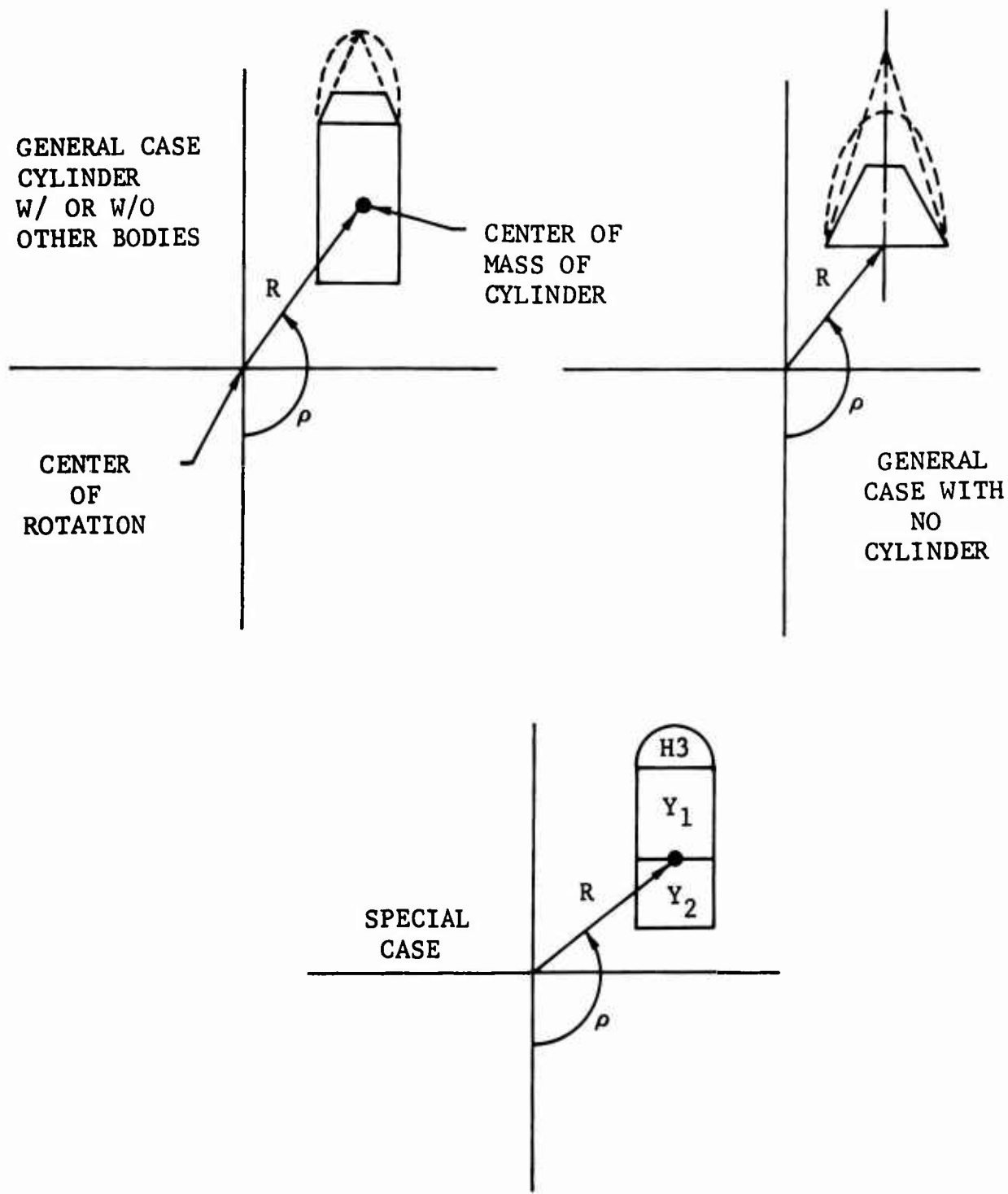


Fig. 2-3 PHASE REFERENCE POINTS FOR COMPOSITE TARGETS

measurements:

1. Repeatability of all measurements were assured by rotating the target and recording all signatures over at least 380 degrees of aspect.
2. Phase closure within ± 8 degrees was achieved during all measurements.
3. The position of the phase center for both the VV and HH polarizations was checked at a specular point on each target to measure accurate phase calibration.
 $\psi_{VV} = \psi_{HH} \pm 8$ degrees was necessary for acceptance.
4. The accuracies of the digital encoding equipment was checked before and after each measurement run by noting the limiting values on the digital display.
5. The absolute accuracy of cross section measurements was checked against computed values of the cross section of the generic shapes on the basis of the physical optics approximation. These values checked within ± 2 dB.

2.2.4 Bistatic Measurement Procedures

The calibration procedures used in the bistatic measurements were identical to those used in the monostatic measurements. This approach was made possible by noting that the bistatic radar cross section of the calibration sphere was essentially the same at the bistatic angle of interest,

namely 0, 10, and 30 degrees. Computed bistatic sphere data was available at the Fort Worth division for a range of ka from 0.01 to 20 and for bi static angles between 0 and 180 degrees.

2.2.5 Vehicle Model Specifications

The target models which were used to provide scattering measurements during this program were designed so that the following objectives might be accomplished:

1. To provide data on the coupling between tightly connected continuous surfaces.
2. To provide generic type surfaces from which an analysis of various scattering phenomena can be made.
3. To provide a set of generic models which can be interconnected in order to fabricate a large number of different composite shapes.

Table 2-1 contains target model data for each model and type of measurement obtained during the measurement program. This table contains a description of each model and the frequency and bistatic angle of the measurements obtained using each model. Also, the value of the residual radius arm R and position angle ρ that remains in the processed data is presented. The target models are grouped into a set of five surface classifications as follows:

Table 2-1 VEHICLE MEASUREMENT DATA

TARGET	DESIGNATION	MAX DIA (Inches)	MIN DIA (Inches)	MAX LENGTH (Inches)	MEASUREMENT FREQUENCY (GHz)	BISTATIC ANGLE (Degrees)	ρ (Degrees)	R (Inches)
CYLINDER 1	CV1	6.320	-	6.344	6.0	0	223.9	0.688
CYLINDER 2	CY2	6.320	-	8.313	5.975	0	0.0	0.000
CYLINDER 3	CY3	6.320	-	10.5.3	5.975	0	138.5	0.206
CYLINDER 5	CY5	7.500	-	17.260	6.0 5.885 6.050	0 10 30	234.3 97.8 245.3	0.678 0.226 0.020
CYLINDER 6	CY6	15.736	-	44.320	6.0 5.885 6.050	0 10 30	339.4 162.5 76.9	0.661 0.226 0.371
CONE 1	C1	6.320	0	11.783	6.0	0	214.6	0.806
CONE 2	C2	6.320	0	15.814	6.0	0	2.4	1.620
CONE 4	C4	7.500	0	13.983	5.975	0	177.4	2.302
FRUSTRUM 1	F1	6.316	2.000	4.030	5.975	0	183.4	0.365
FRUSTRUM 2	F2	7.500	6.320	2.200	6.0	0	0.0	1.150
FRUSTRUM 3	F3	7.500	6.320	3.358	6.0	0	116.3	0.505
FRUSTRUM 4	F4	6.312	4.892	4.063	6.0 5.885 6.050	0 10 30	31.4 37.0 65.0	0.902 0.187 0.179
FRUSTRUM 5	F5	7.500	4.892	7.421	6.0 5.885 6.050	0 10 30	4.5 163.9 216.4	4.313 0.487 0.049
HEMISPHERE 2	H2	4.892	-	2.446	5.975	0	90.0	0.004
HEMISPHERE 3	H3	6.320	-	3.160	5.975	0	239.6	0.027
CONNECTING ROD 1	CR1	1.500	-	6.000	5.975	0	0.0	0.494
CONNECTING ROD 2	CR2	1.500	-	12.000	5.975	0	180.0	0.077
CONNECTING ROD 3	CR3	1.500	-	24.000	5.975	0	180.0	0.016
APT RACK 1	AR1	6.320	5.500	8.000	5.975	0	0.0	0.00
APT RACK 2	AR2	6.320	5.500	8.000	5.975	0	0.0	0.00
APT RACK 3	AR3	6.320	5.500	8.000	5.975	0	0.0	0.00
PARABOLOID OF REVOLUTION	P1	4.892	-	3.50	5.975	0	0.0	0.000
DIPLANE 1	D1	10.000	-	10.000	5.975	0	135.6	8.486
FRUSTRUM 2 CYLINDER 5	F2Y5	7.500	6.320	19.460	5.975	0	180.0	0.530
FRUSTRUM 4 CYLINDER 3	F4Y3	6.320	4.892	14.576	5.975	0	97.3	0.228
FRUSTRUM 5 CYLINDER 3	F5Y3	7.500	4.892	24.680	5.975 5.885 6.050	0 10 30	00.0 232.9 230.6	0.000 0.114 0.317
CYLINDER 4 FRUSTRUM 4	Y4F4	6.312	4.892	12.063	5.975 5.885 6.050	0 10 30	204.3 0.0 180.0	0.047 1.373 0.019
FRUSTRUM 2 CYLINDER 5 FRUSTRUM 3	F2Y5F3	7.500	6.320	22.818	5.975	0	180.0	0.012
CONE 1 CYLINDER 3	C1Y3	6.320	0.000	22.246	5.975	0	0.0	0.000
CONE 2 CYLINDER 3	C2Y3	6.320	0.000	26.327	5.975	0	37.8	0.343
CONE 3 CYLINDER 3	C3Y3	6.320	0.000	12.543	5.975	0	215.8	0.019
CONE 4 CYLINDER 5	C4Y5	7.500	0.000	31.243	6.0	0	225.8	0.571
CONE 2 FRUSTRUM 2	C2F2	7.500	0.000	18.014	6.0	0	24.5	0.525
CONE 1 CYLINDER 1 FRUSTRUM 3	C1Y1F3	7.500	0.000	21.485	6.0	0	279.0	2.554
CONE 2 CYLINDER 3 FRUSTRUM 3	C1Y3F3	7.500	0.000	25.654	5.975	0	193.9	1.202
CONE 4 CYLINDER 5 FRUSTRUM 3	C1Y5F3	7.500	0.000	34.601	5.975	0	18.4	0.096
HEMISPHERE 2 CYLINDER 4	H2Y4	4.892	-	10.446	5.975	0	239.6	0.027
HEMISPHERE 3 CYLINDER 1	H3Y1Y2	6.320	-	17.817	5.975	0	173.8	0.963
CYLINDER 2	H3Y3	6.320	-	13.673	5.975	0	107.8	0.259
PARABOLOID 1 FRUSTRUM 4	P1F4	6.314	-	7.563	5.975	0	182.8	0.329
PARABOLOID 1 FRUSTRUM 4 CYLINDER 3	P1F4Y3	6.320	-	18.076	5.975	0	180.0	0.134
SMOOTH AEROSPACE VEHICLE A0	P1F4Y3F2Y5F3Y2F1	7.500	-	53.237	3.0	0		
SMOOTH AEROSPACE VEHICLE A1	P1F4Y2F2Y5F3Y3F1	7.500	-	53.239	3.0	0		
SMOOTH AEROSPACE VEHICLE A2	C1Y3F3Y5F2Y1F1	7.500	0.000	55.488	3.0	0		
SMOOTH AEROSPACE VEHICLE A3	H3Y1Y2Y5Y3C3	7.500	-	47.620	6.0	0		
6.0					6.0	0		
6.0					6.0	0		
COMPLEX AEROSPACE VEHICLE A0	ACTUAL AEROSPACE MODEL				5.975	0		
COMPLEX AEROSPACE VEHICLE A1	P1F4Y3F2Y5F3AR3F1	7.500	-	52.924	5.975	0		
COMPLEX AEROSPACE VEHICLE A2	P1F4Y3F2Y5F3AR2F1	7.500	-	52.924	5.975	0		
COMPLEX AEROSPACE VEHICLE A3	P1F4Y3F2Y5F3AR1F1	7.500	-	52.924	5.975	0		
COMPLEX AEROSPACE VEHICLE A4	P1F4Y3F2Y5F3Y2F1	7.500	-	53.237	5.975	0		
COMPLEX AEROSPACE VEHICLE A5	P1F4Y2F2Y5F3Y3F1	7.500	-	53.237	5.975	0		
SCIENTIFIC SATELLITE X1	H3F1C1H2	6.320	1.500	15.636	3.0	0		
SCIENTIFIC SATELLITE X2	C3F1C1AR2CR2H3	6.320	1.500	20.660	5.95	0		
					5.95	0		

1. Generic Surfaces
2. Composite Generic Surfaces
3. Smooth Aerospace
4. Complex Aerospace
5. Scientific Satellites

Figure 2-4 contains a photograph of some typical generic and composite generic models measured during this program.

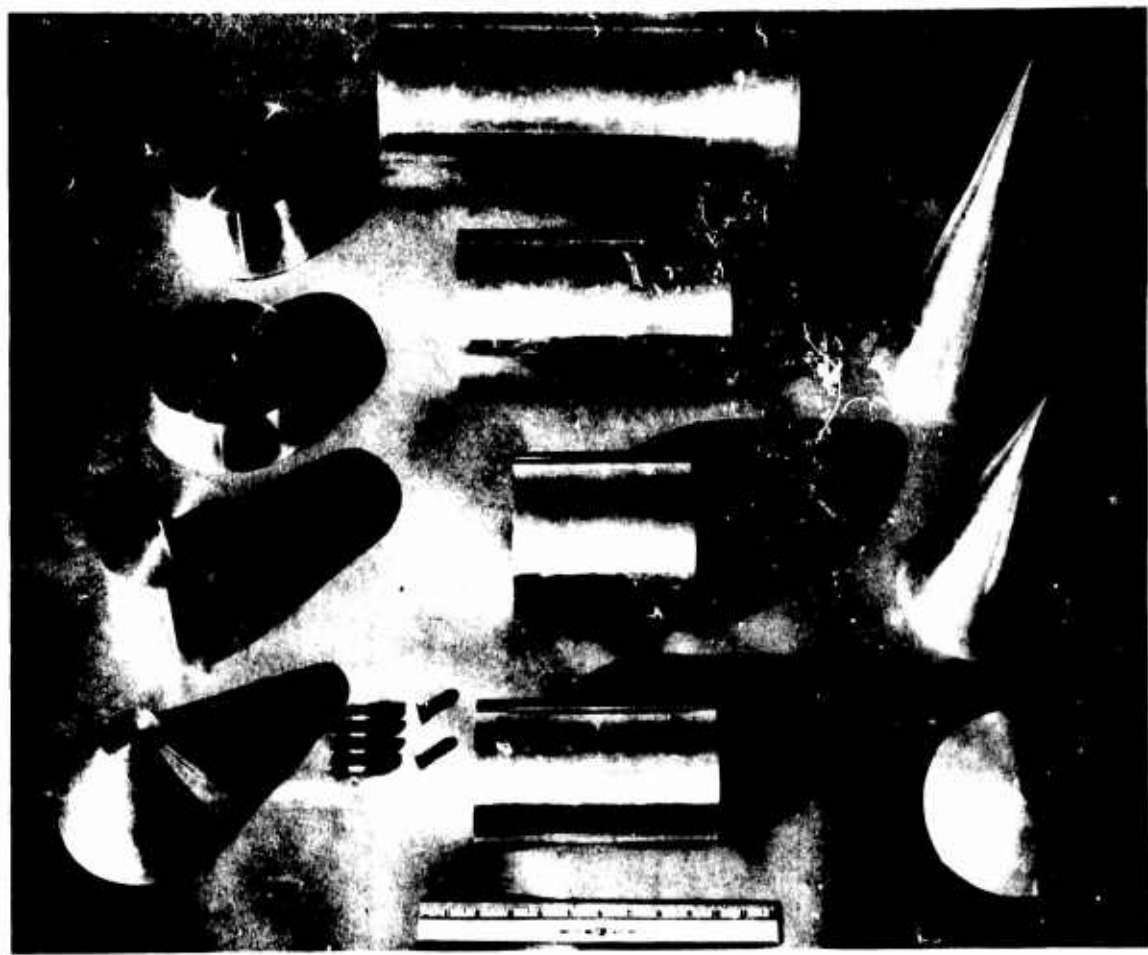
Figure 2-5 contains an illustration of the method of construction used to form composite models from generic models. Additional photographs of other models are contained in Reference 2 along with the analog plots of measured data.

2.2.6 Measurements Data Recording and Processing

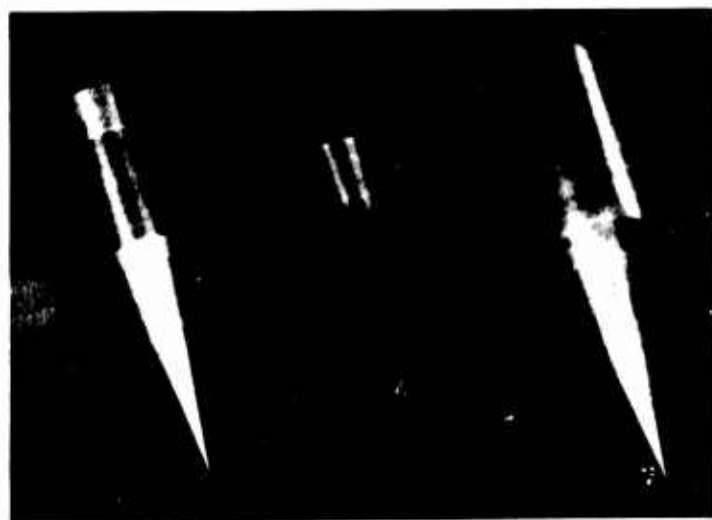
In order to prepare scattering measurement data for use as library data for the various processing techniques developed during this program, it was necessary that these data must be edited, calibrated, and recorded on magnetic library tapes. Figure 2-6, contains a flow diagram showing the evolution of scattering data between the radar range and the completed library tape.

In its final form, the cross section, phase, and aspect data for each measurement run have the following characteristics.

1. Data on magnetic tape is recorded for exactly 3600 discrete aspect angles beginning with $\theta = -180.0$



Typical Generic Vehicles



Typical Composite Vehicle

Fig. 2-4 TYPICAL VEHICLE MODELS

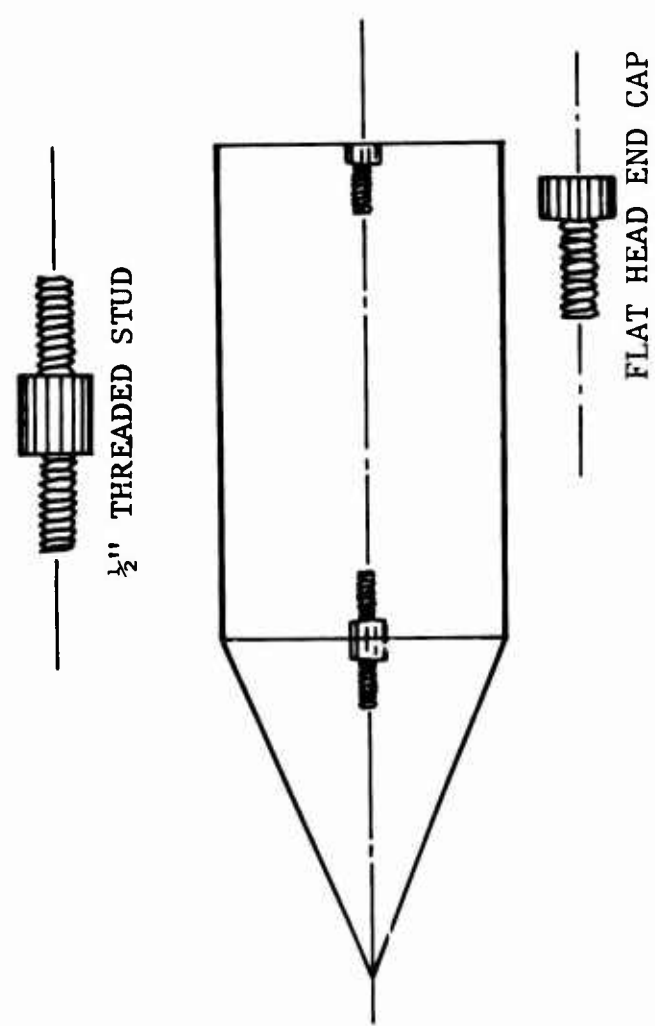


Fig. 2-5 CONSTRUCTION OF COMPOSITE VEHICLES

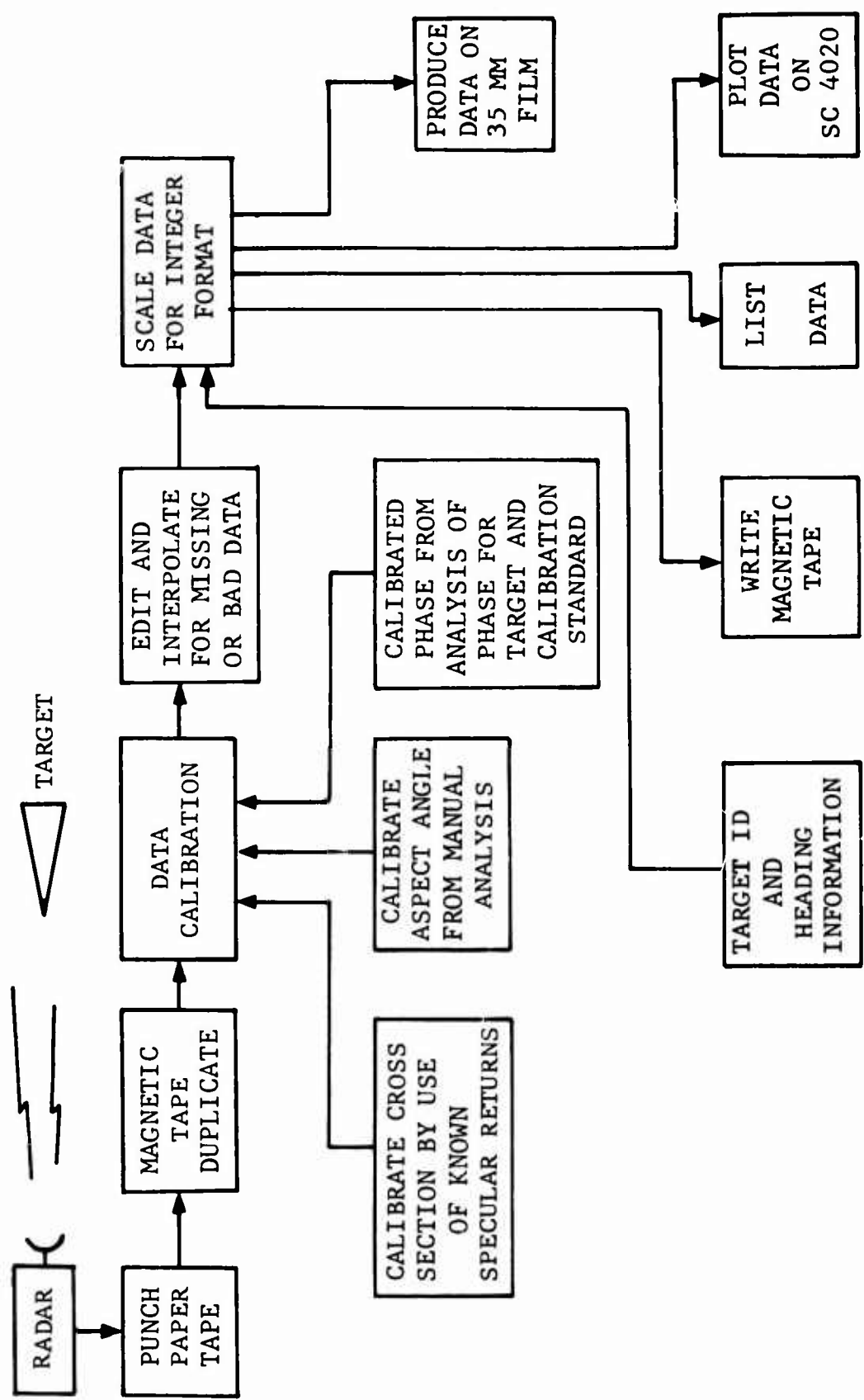


Fig. 2-6 FLOW DIAGRAM FOR PROCESSING RADAR SIGNATURE DATA

degrees, increasing to $\theta = 0.0$ degrees and then increasing to $\theta = 179.9$ degrees in increments of 0.1 degree. Aspect angle data is recorded on tape in an integer mode for $\theta = -180.0$ through 0 degrees to $\theta = 179.9$ degrees.

2. Aspect angle data is calibrated from knowledge of the orientation of specular returns. This calibration assures, for example, that the specular returns from the end-on aspects of a cylinder will occur at $\theta = 0.0$ degrees and $\theta = 180.0$ degrees.
3. In some instances, cross section data was post-calibrated (1) in accordance with post-calibration radar range data or (2) by use of computed cross section values obtained by use of the physical optics expressions for cross section at specular points for cones, frusta and cylinders.
4. If a phase bias error was detected, a fixed bias value was added to the measured phase as a correction.

The target model data contained in Table 2-1 indicates the value of the residual radius arm R and position angle ρ which remains in the final library data after it is formatted on magnetic tape. The position vector determined by R and ρ indicates the position of the target phase reference with respect to the actual center of rotation of the turntable.

Scattering measurements data was recorded on magnetic tape as BCD information in the following manner. Each file on a tape consists of 903 records or card images and an end-of-file mark. Each record consists of 14 words and represents one 80 column card. The first two records contain alphanumeric information identifying the target and the parameters of the radar range for that sequence of measurements. These two records are followed by 900 records containing measured data. Each of these records contains a set of four values of aspect angle, cross section, and phase. The last record of each file consists of an end-of-file mark. Table 2-2 illustrates, in detail, the format of a typical data file.

2.3 Short Pulse Measurements

The short pulse measurements utilized during this program were also obtained on the Radar Range at the Fort Worth Division. C-band measurements on a sphere-tipped cone were obtained for use in the analytical investigation of the geometrical theory of diffraction. These data are discussed in Appendix C of Volume III of this Technical Report (Reference 2). Short-pulse data were also used in the inverse scattering investigation reported in Volume IV (Reference 3). The important components of the short-pulse radar and the procedures utilized to ensure the quality of short-pulse measurements are discussed in the following paragraphs.

Table 2-2
MAGNETIC TAPE FORMAT FOR LONG PULSE DATA

Card #1	Alphanumeric Heading Information
Card #2	Alphanumeric Heading Information
Card #3	-1800, $\sigma(-1800)$, $\emptyset(-1800)$; -1799, $\sigma(-1799)$, $\emptyset(-1799)$; -1798, $\sigma(-1798)$, $\emptyset(-1798)$; -1797, $\sigma(-1797)$, $\emptyset(-1797)$
	...
Card #453	-0, $\sigma(-0)$, $\emptyset(-0)$; 1, $\sigma(1)$, $\emptyset(1)$; 2, $\sigma(2)$, $\emptyset(2)$; 3, $\sigma(3)$, $\emptyset(3)$
	...
Card #902	1796, $\sigma(1796)$, $\emptyset(1796)$; 1797, $\sigma(1797)$, $\emptyset(1797)$; 1798, $\sigma(1798)$, $\emptyset(1798)$;
	1799, $\sigma(1799)$, $\emptyset(1799)$
Card #903	End of File

2.3.1 Electronic System

The measurement systems used in this program to obtain short-pulse signature data were phase coherent C- and X-band radars which exhibit range resolution of 6 and 3 inches, respectively. Figure 2-7 contains a simplified block diagram of the radar system and the tie-in between the radar system and the recording system.

In operation, a dc pulse from an impulse generator is transmitted to the waveguide modulator at a rate of 20,000 pulses per second. When the waveguide modulator is triggered by these dc pulses, it produces a short RF pulse from the continuous wave input. This pulse is amplified through a 3-stage TWT and amplifier chain and is passed through the system attenuator to the transmitting antenna. The system attenuator is accurately calibrated in db for use as a calibration reference. The received signals are amplified in a low-noise TWT and applied to one channel of a sampling oscilloscope. The output of this channel is used as an analog of the target response and is applied to the recording system and the phase comparator network. The input from the continuous wave reference oscillator is applied to the other channel of the sampling oscilloscope through a phase shift reference. The phase shifter is also used as a calibration device.

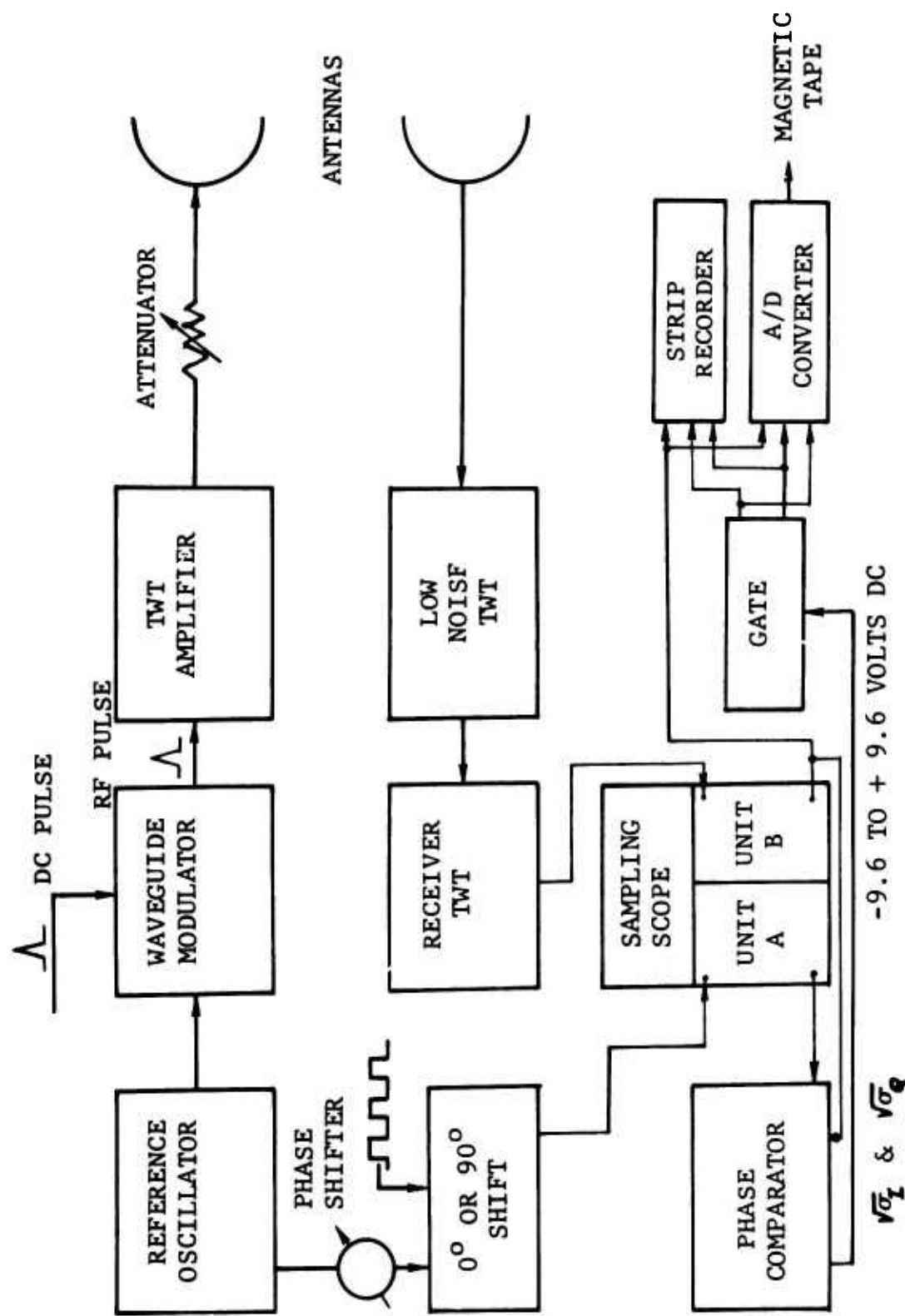


Fig. 2-7 BLOCK DIAGRAM OF SHORT PULSE RADAR

The phase of the reference signal at the oscilloscope is shifted 90 degrees intrapulse in order to provide a phase reference for both the quadrature and in-phase channels of the phase comparator. Representative system timing relationships used in the operation of the radar and recording system are presented in Figure 2-8. The timing relationships shown in this figure include the real time and the processing time required for operation of the radar and the recording components.

Details of the characteristics of the radar systems are presented in Table 2-3. The primary items of interest in this table are the pulse characteristics and the radar sensitivity and stability. Pulse data is obtained by recording the signal from a large sphere in the vicinity of the target during a calibration process. A 3-dB pulse width of less than 0.5 nanosecond can be obtained at C-band (.3 nanosecond) at X-band. However, optimum C-band system performance is usually established by observing both the 3-dB and 25-dB levels and adjusting the optimum until a 0.6-nanosecond pulse width is obtained at the 3-dB point and a 1.8-nanosecond signal at the 25-dB point. The time sidelobe level is initially set approximately 30 dB down from the peak signal amplitude. The time sidelobe remains at a level greater than 25 dB down during the course of a measurement series.

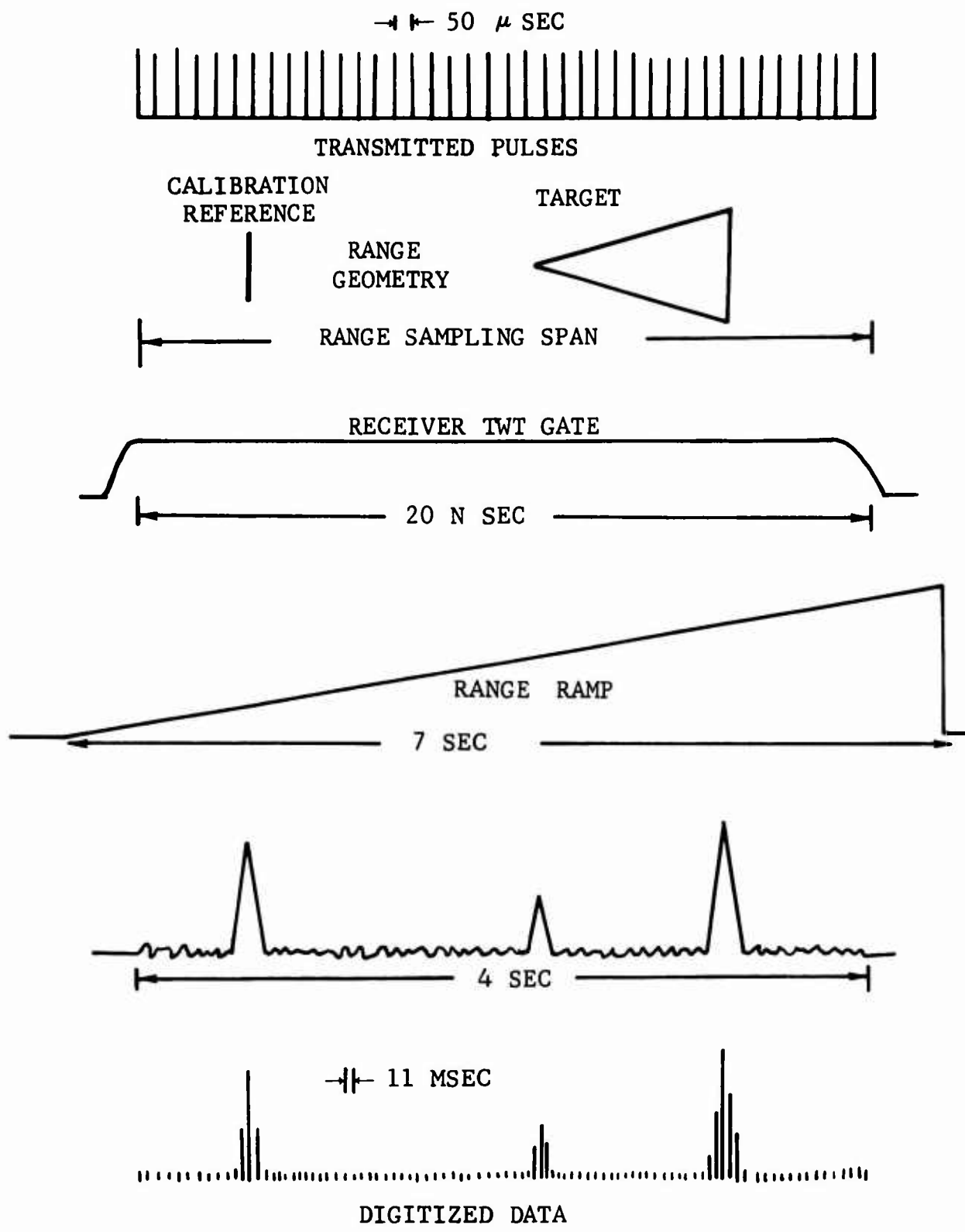


Fig. 2-8 SYSTEM TIMING DIAGRAM

Table 2-3 SHORT PULSE RADAR CHARACTERISTICS

Band	Approx. Freq. (GHz)	PW 3 dB (ns)	PW -25 dB (ns)	Time Side Lobe Max. (dB)	Noise Fig. (dB)	Power Output (Watts)	Dynamic Range (dB)	Max. Antenna Size (Feet)	Range (feet)
C*	6.0	.7	2	-27	10	400	26	4	300
X*	9.2	.6	1.8	-27	10	500	26	4	300

* Coherent with phase measurement

Typical C-band data obtained by using these parameters are shown in Figure 2-9. These data were recorded at two attenuation levels in order to display the pulse width at the 25 dB points and define the sidelobe levels.

The use of an accurately calibrated reference attenuator and phase shifter, in conjunction with exceptional system stability, provides the basis for accurately determining the amplitude and phase response of target scattering centers.

A measure of the system stability is presented in Figure 2-10. These data represent the analysis of a large number of data runs which were obtained over a time period longer than typical data runs. These results indicate that system stability in phase and amplitude are represented by a standard deviation of less than 2.5 degrees and 0.45 dB, resp.

The recording system used to produce target and aspect angle information is designed to provide an easily manageable form of analog and digital data. The functional tie-in between the radar and the recorder was previously shown in Figure 2-7. A more detailed diagram of the digital recorder is shown in Figure 2-11. The output of the sampling oscilloscope, the envelope of the target response, appears at the input to the recorder amplifier and is subsequently recorded on 4 channels of a strip chart recorder. The aspect angle data, target amplitude data, and the in-phase and quadrature components

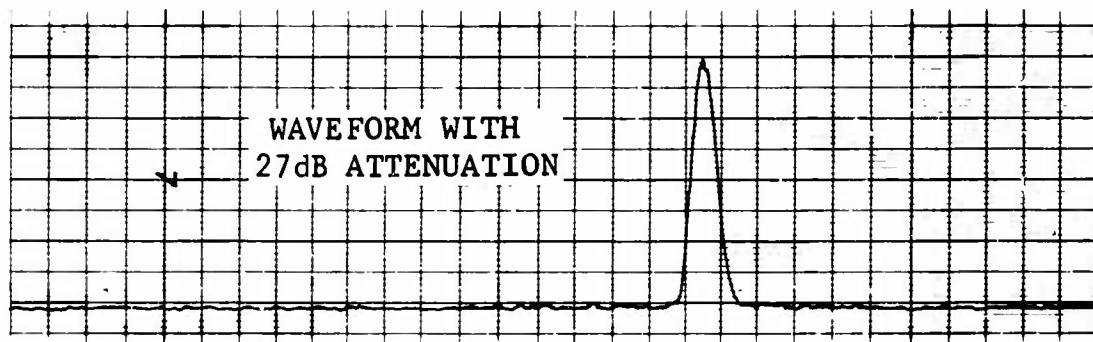
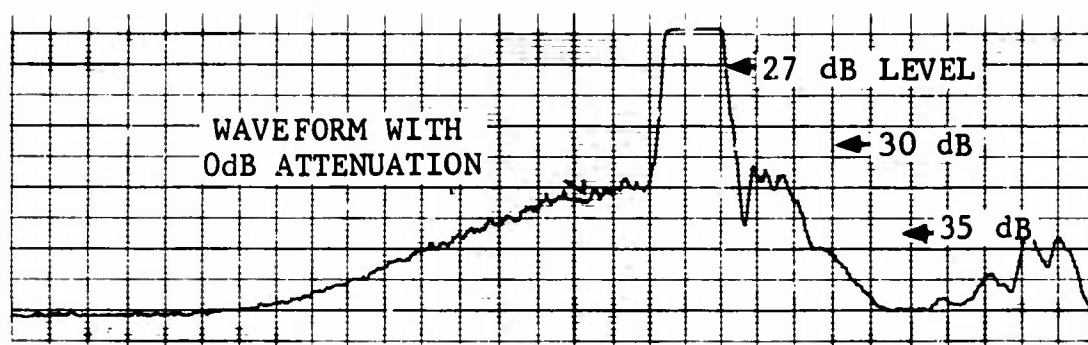
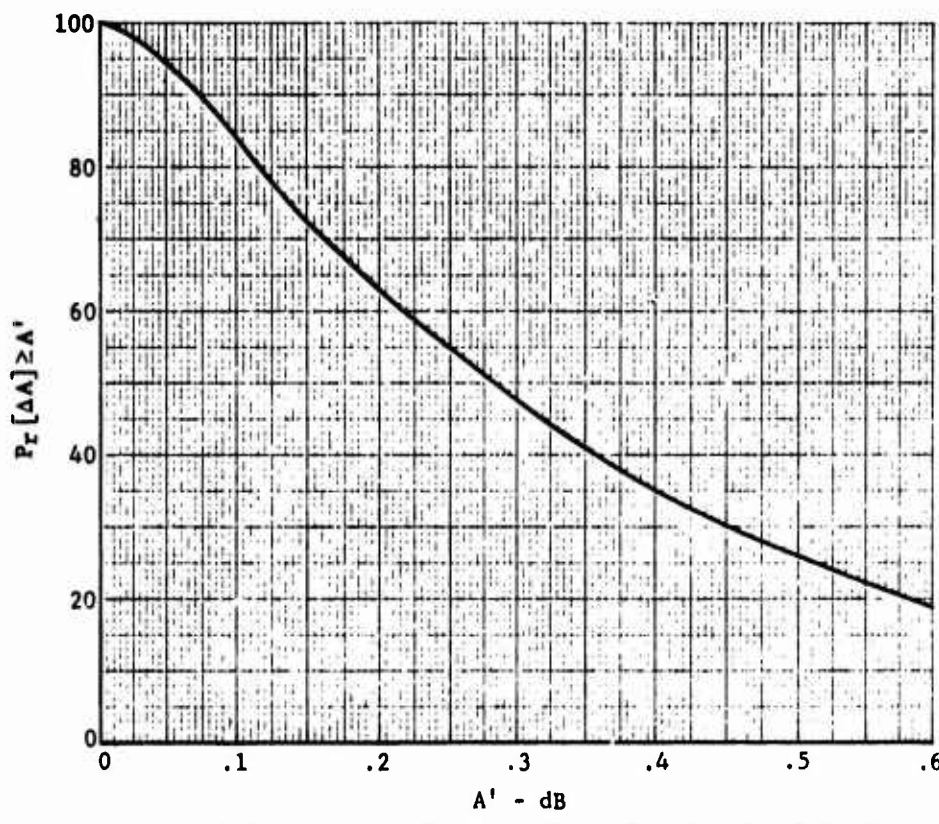
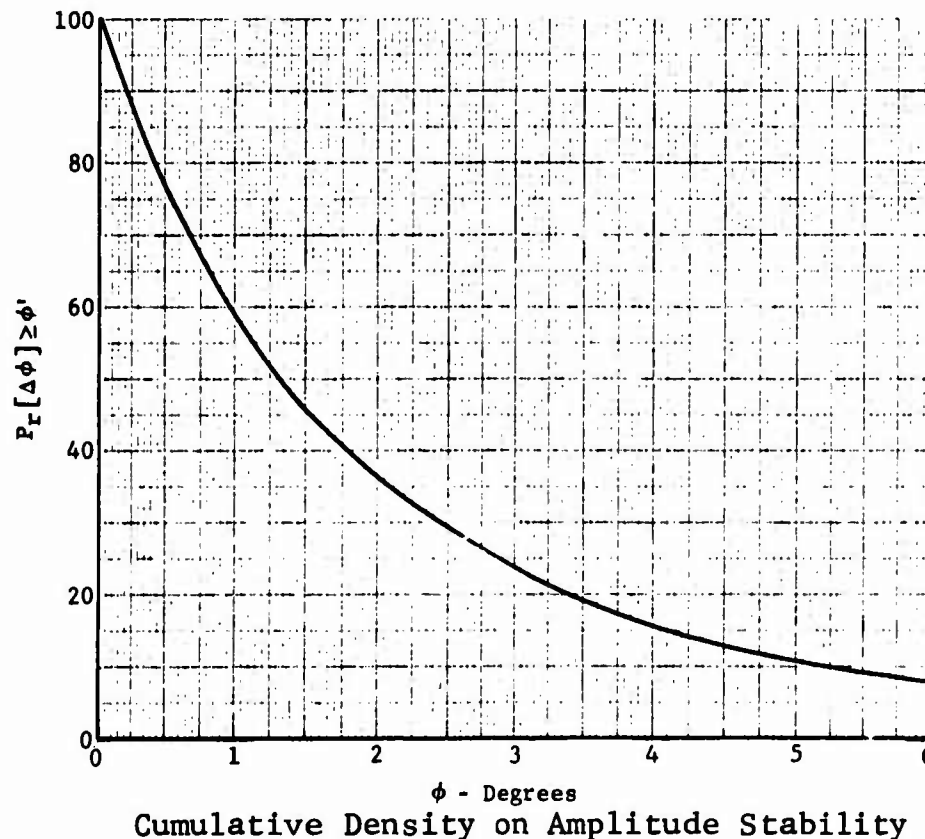


Fig. 2-9 C-BAND SHORT PULSE DATA



Cumulative Density on Amplitude Stability



Cumulative Density on Amplitude Stability

Fig. 2-10 SHORT-PULSE SYSTEM STABILITY

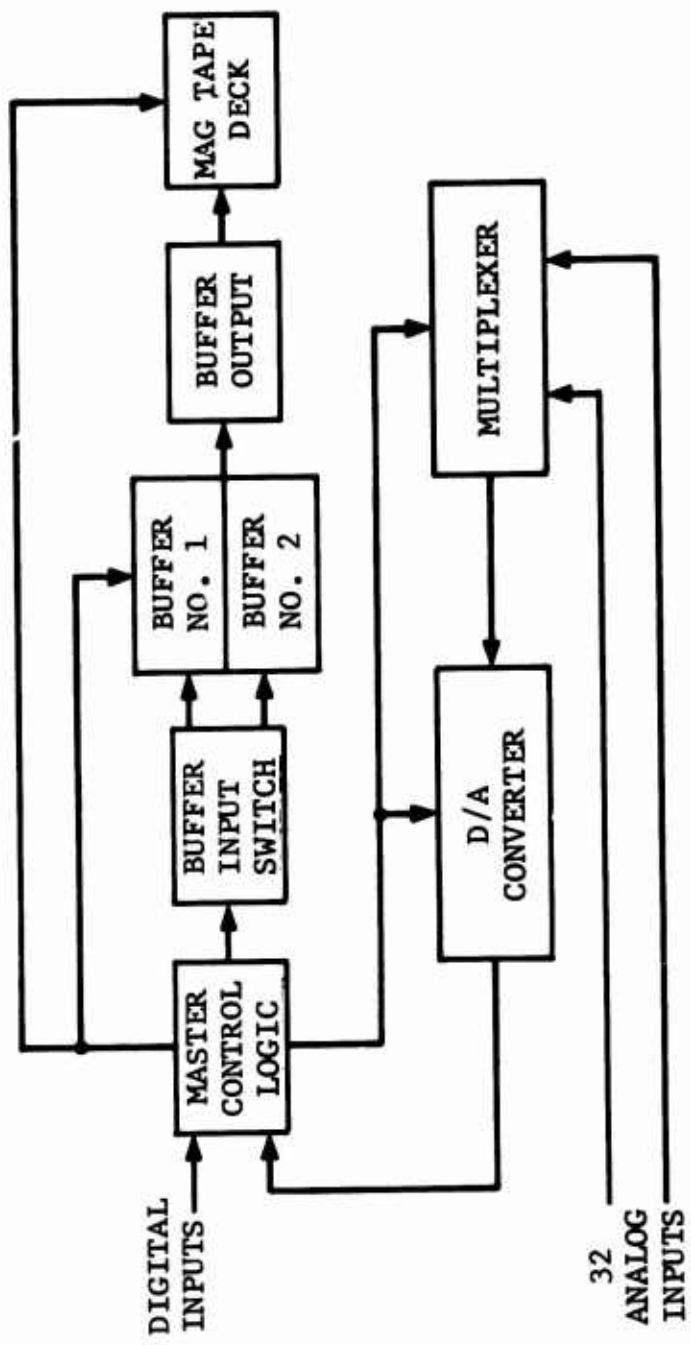


Fig. 2-11 BLOCK DIAGRAM OF RECORDING SYSTEM

of the phase data are recorded. Analog voltages are used in the digital system to produce the digital data through analog-to-digital (A/D) conversion of the analog signals. The digital recorder is programmed to accept the output of various A/D converters, the aspect angle information from the angle encoders, and other input data required as designators, and to produce a 7-track magnetic tape. The IBM-compatible format used to produce the 7-track binary coded decimal (BCD) magnetic tape is shown in Figure 2-12.

2.3.2 Radar Range Setup Procedures

The range geometry used in a typical short pulse measurement program is illustrated in Figure 2-13, where the offset-fed antennas are only applicable to C-band measurements. With this exception, the geometry can be applied equally well to X-band measurements, where, lunberg lens antennas are utilized at present.

The ground plane mode is utilized with this range configuration in order to reduce the background by virtue of the null near the ground. This null is an inherent property of the configuration, and advantage is taken of the constructive interference between the direct and indirect waves in the target vicinity to obtain additional sensitivity. Test results obtained by using this range geometry have indicated two salient facts. First, theoretically possible gain is realized.

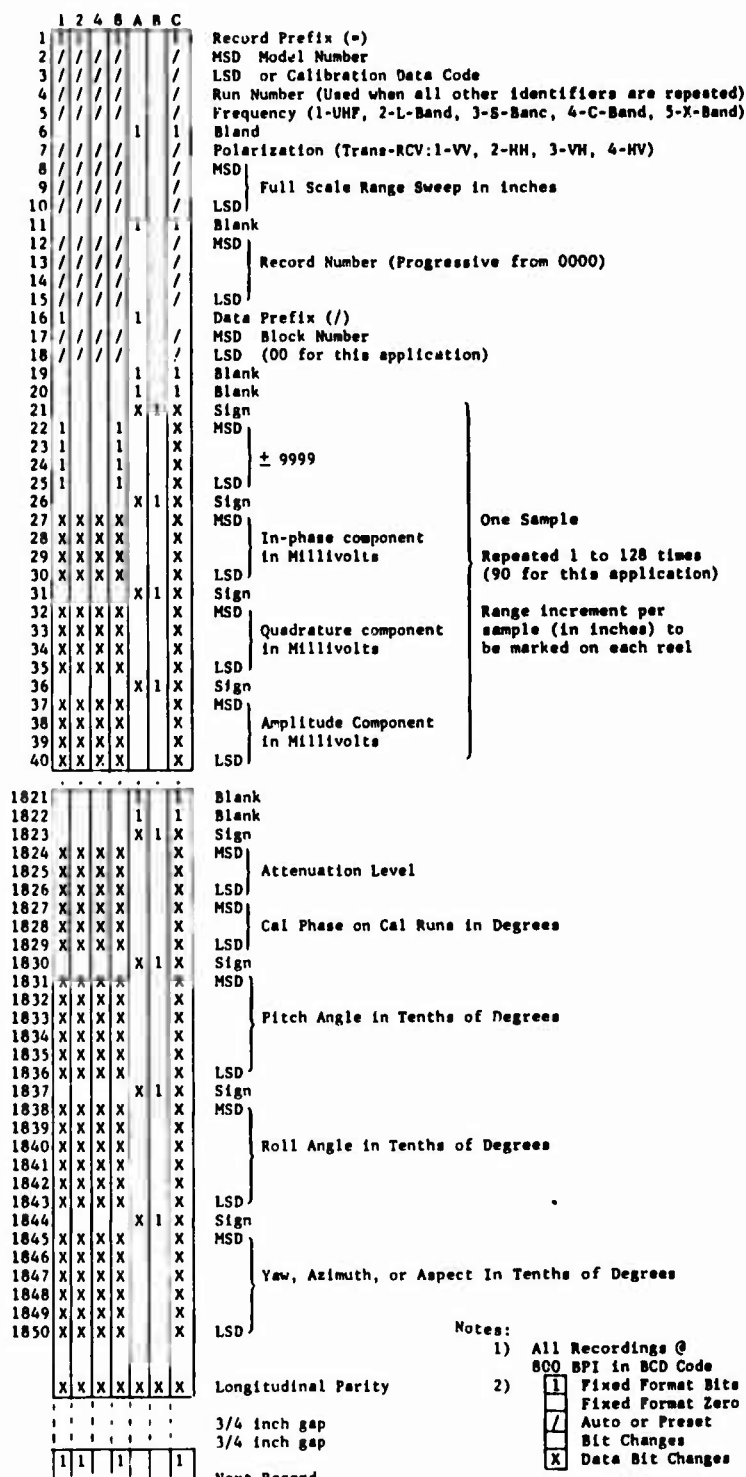


Fig. 2-12 MAGNETIC TAPE FORMAT FOR SHORT PULSE DATA

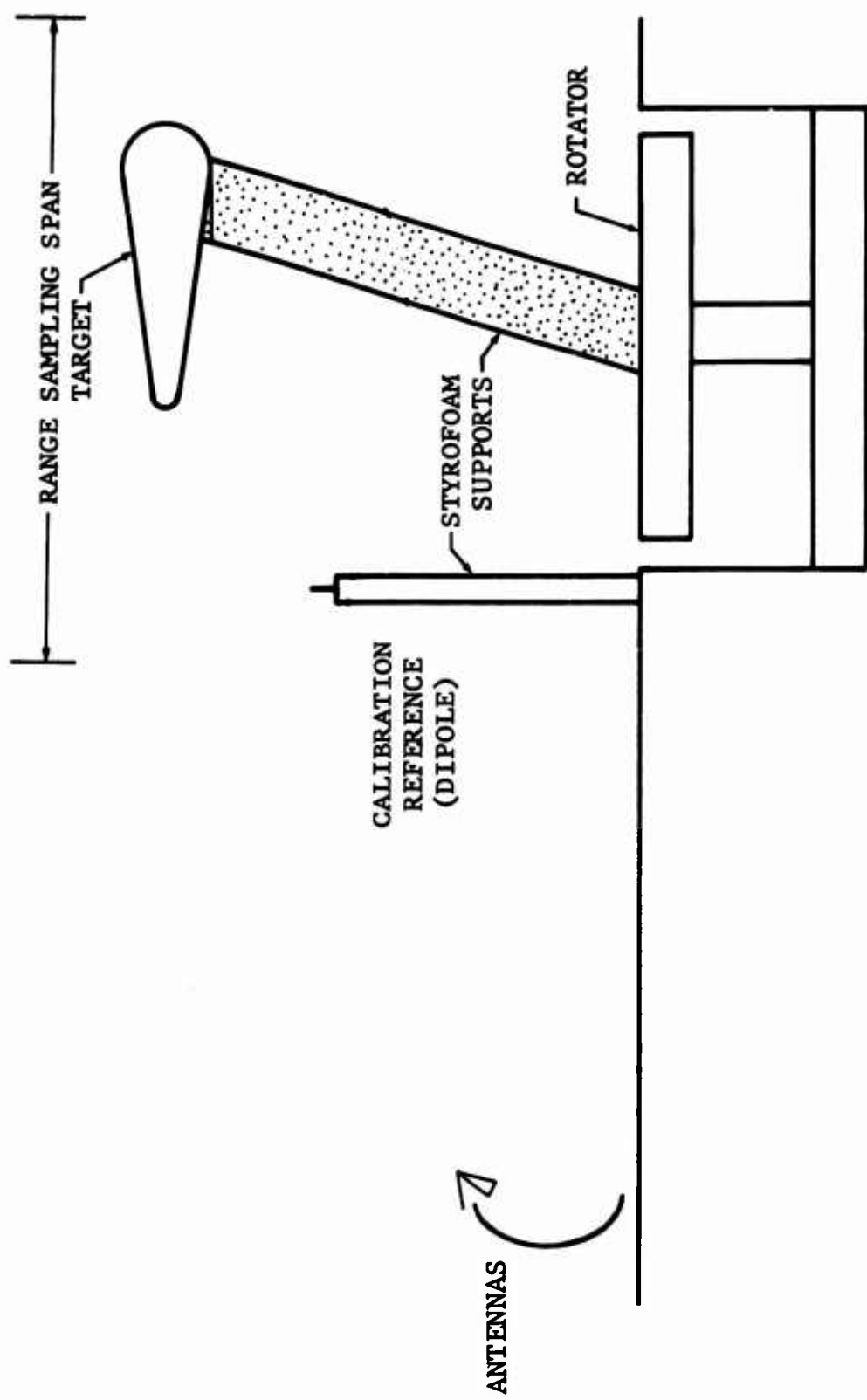


Fig. 2-13 GROUND PLANE RANGE GEOMETRY

Second, pulse dispersion effects resulting from differences in the time of arrival of the direct and ground reflected waves produce no significant impact on the system pulse width characteristics or the time sidelobe levels. The offset fed dishes used for C-band measurements have provided additional sensitivity concurrent with a high degree of antenna rejection. This sensitivity has been obtained without introducing undesirable reflection levels, and it is a result of the fact that the focal length is much longer than a pulse width and aperture blocking effects are minimized.

As illustrated in Figure 2-13, the range sampling span must encompass the calibration reference and the entire volume occupied by target. It is desirable to minimize the length of the range span in order to reduce the amount of data recorded. However, this action is practical to a limited extent since the radial range difference between the calibration reference and the target must be great enough to eliminate interaction between the time sidelobes of the reference and the low-level components of the target signature.

Calibration of the measurement system involves (1) establishing an accurate time (range) reference on the recording system, (2) recording system noise levels, (3) establishing a system response curve for both phase and amplitude, and (4) determining system amplitude and phase

stability via post-calibration after a series of target measurements. Calibration of the C-band system is accomplished by completing the 12 steps delineated in Table 2-4. Prior to calibrating the system, the reference scatterer is positioned to produce a signal level about 2 dB below full scale at full sensitivity and system performance is extensively examined. In Step 1, the appropriate system parameters are commonly adjusted to provide a 2-nanosecond time interval (1 foot) per centimeter on the analog data strip chart. In steps 2 and 3, system noise levels are recorded. Steps 4 and 5 are used to establish the basic phase and amplitude calibration of the reference scatterer.

Steps 6 through 8 of the procedure are used to calibrate the reference scatterer in VH polarization. Calibration in amplitude and phase is accomplished by using the relationship

$$\sigma_{VV} = \sigma_{HH} = \sigma_{VH} = \sigma_{HV}.$$

In Step 9, the background level is measured for all polarizations of interest and target measurements are obtained in Steps 10 and 11. In order to validate the target data, a post-calibration procedure (Step 12) is included. In this step, selected initial calibration steps are repeated.

2.3.3 Amplitude and Phase Calibration

Data obtained in the system calibration procedure is used to calibrate a reference scatterer which, in turn,

Table 2-4 SHORT-PULSE SYSTEM CALIBRATION

1. Record 1-GHz signal.
2. Record detector zero and sampling noise.
3. Record receiver noise.
4. Place calibration sphere on support.
5. Record scattering from calibration sphere and reference scatterer in all polarizations to establish phase and amplitude calibration of the reference.
6. Remove sphere and place 45-degree dipole on support.
7. Determine cross section of 45-degree dipole in VV relative to the reference.
8. Determine reference cross section relative to 45-degree dipole.
9. Remove 45-degree dipole and record background.
10. Place target on support and mechanically align aspect angles.
11. Record target data in all polarizations.
12. Perform post-calibration.

provides a calibration signal on each recorded frame in a target data run. Amplitude calibration is accomplished by monitoring a constant signal (the scatter from a sphere) and recording the response as a function of the setting of a calibrated attenuator. Calibration data are then recorded in conjunction with changes in the attenuator. The results of this procedure are used to construct an amplitude response curve in dB. Absolute amplitude calibration of the reference scatterer in dBsm is then deduced by noting the difference in the response of the reference and the sphere whose cross section is known. For other than VV and HH polarizations, a dipole oriented at 45 degrees is used for calibration.

The system phase response is determined by recording data in conjunction with 10-degree changes in the system phase shifter. This data is then used to construct a phase response curve from which any corrections necessary for system nonlinearity can be obtained. No absolute calibration is provided for phase since all phase data is to be interpreted relative to the phase of the reference, Modulo 2π . However, a phase correction factor for the i^{th} polarization, relative to VV polarization, is established through the relationship

$$\phi_i = (\phi_R^V - \phi_S^V) - (\phi_R^i - \phi_S^i)$$

where ϕ_R = Phase of the reference scatterer

ϕ_S = Phase of the calibration sphere

The method of calibrating typical target data in amplitude is shown in Figure 2-14. The basic curve (a) represents the system amplitude response derived from the calibration measurements. Curve (b) illustrates the procedure used to calibrate the reference scatterer by comparing the reference signal with that of the sphere. In this example, a 9-inch sphere whose radar cross section is -14 dBsm is found to produce a response of 5.3 dB above the level of the reference. Thus, it is evident that the radar cross section of the reference scatterer is -19.3 dBsm. An actual target response, with an additional 4 dB of attenuation, is shown in curve (c). At this attenuator level, the effective cross section of the reference is still -19.3 dBsm; however, a scale change on the record has been introduced so that the larger target signals can also be observed. The target response is conveniently converted to dBsm by using the response curve and noting the difference in amplitude levels (7.3 dBsm) between the returns from the reference and the target.

Target phase calibration is illustrated in Figure 2-15. Since the phase detectors are bipolar, there is no offset in the presentation as in the case of the amplitude record. The primary consideration in obtaining accurate phase data is that of correcting all target data to produce a numerical

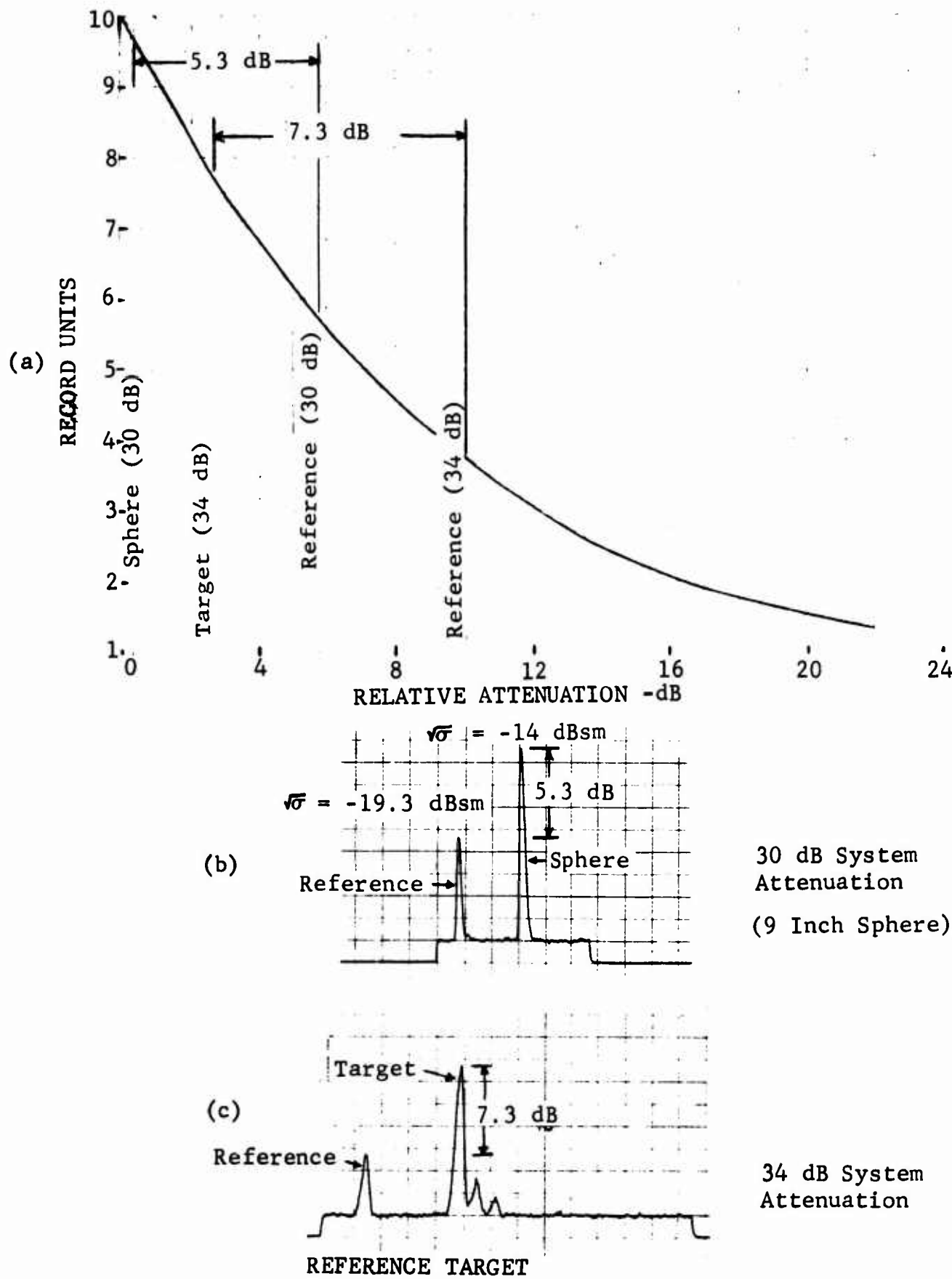
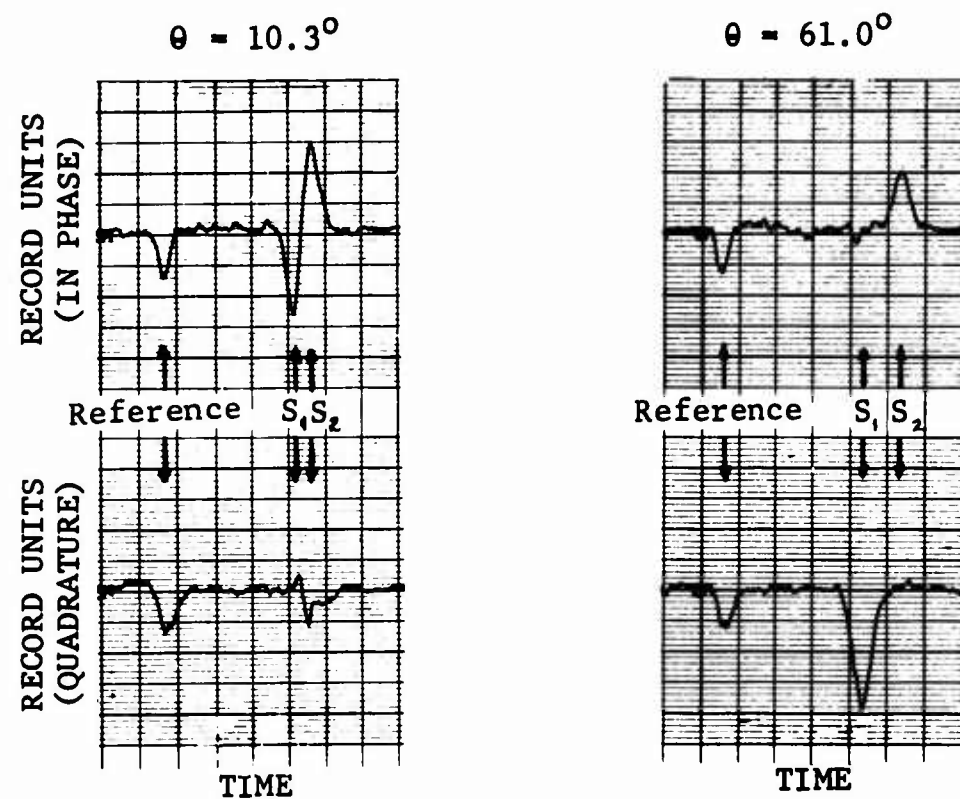


Fig. 2-14 INTERPRETATION OF AMPLITUDE CALIBRATION



	ASPECT ANGLE	REFERENCE*	TARGET	
			SCATTERER 1	SCATTERER 2
MEASURED	10.3°	225.3°	169.1°	352.2°
CORRECTED	10.3°	45.0°	348.8°	172.9°
MEASURED	61.0°	225.0°	271.5°	8.5°
CORRECTED	61.0°	45.0°	91.5°	188.5°

* ORIGINAL REFERENCE SETTING --- 45°

Fig. 2-15 INTERPRETATION OF PHASE DATA

result which is a measure of the phase of the target response relative to the phase of the reference scatterer.

The phase of the signal from a scattering center can be written as

$$\phi_t = \phi_o(t) + 2k(t)R_o + \phi_s(f, \theta) = 2kR \cos(\theta + \psi)$$

where t denotes time, f denotes frequency, θ denotes aspect angle, k denotes wave number, and ψ denotes a position angle associated with the geometry of the scattering center. The ϕ_o term corresponds to the actual phase of the transmitted signal. This term, which is dependent on the stability of the system, can be a sensitive function of time. The $2k R_o$ term, where $k = 2\pi f/c$ and R_o is the range from the radar system reference to the center of rotation of the target, is a sensitive function of time if (1) R_o is large and (2) significant frequency changes occur. The function $\phi_s(f, \theta)$, which is a phase term arising from the characteristics of the scattering center, is one of the elements of interest. This term is commonly insensitive to frequency. The $2kR \cos(\theta + \psi)$ term is a result of rotation of the target about some axis where R is the distance from the axis of rotation to the scattering center; since R is small, the time dependence of this term is insignificant. Thus, it can be seen that provisions of only nominal frequency stability and a reference scatterer in the target vicinity allow the phase term

to be reduced to the expression

$$\theta_t = \theta_1 + \theta_s(\theta) + 2kR \cos(\theta + \psi)$$

where θ_t is measured relative to the reference and θ_1 accounts for the effective distance between the reference and the center of rotation of the target. Thus, the measured parameter is the desired parameter except for an additive constant which is of no consequence.

By using the notation of Figure 2-14,

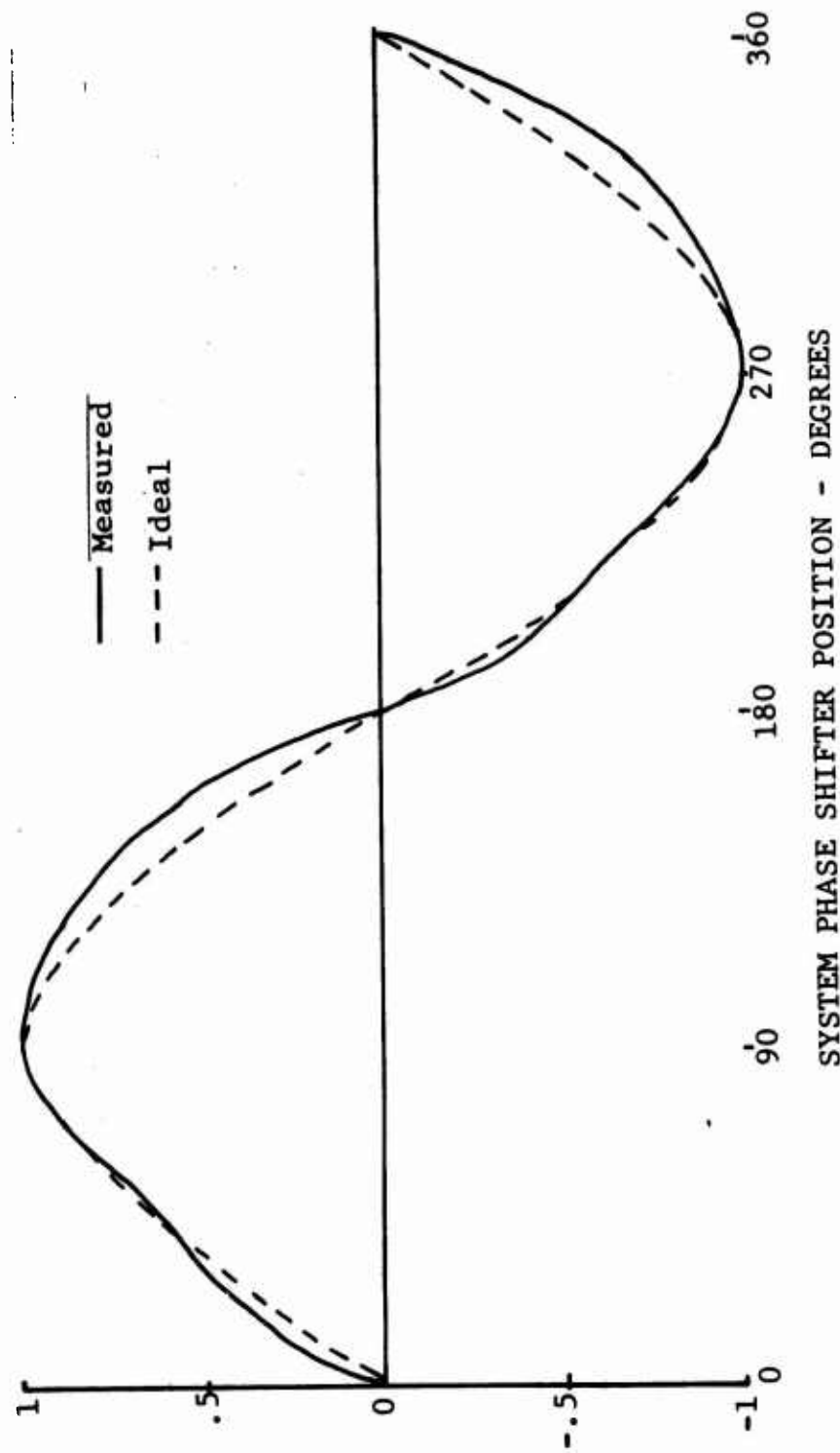
$$\theta_t = \theta_1 + \tan^{-1} \left[\left(\sigma_{TQ} / \sigma_{TI} \right)^{\frac{1}{2}} \right] - \tan^{-1} \left[\left(\sigma_{RQ} / \sigma_{RI} \right)^{\frac{1}{2}} \right]$$

where σ can be defined in record units or in terms of the millivolt levels recorded on magnetic tape. It should be noted that the θ_1 includes the θ_i required to correlate data obtained at different polarizations. Example computations are tabulated in the Figure 2-15 by using the most significant target signals. Figure 2-16 contains typical data illustrating the deviation of system response from the ideal circular function.

2.3.4 Measurements Data Recording and Processing

Short-pulse measurements are obtained by use of procedures identical to those used in obtaining basic calibration data. In this case, the target is placed in the physical location previously occupied by the calibration sphere.

Target data is calibrated by comparing measured data with the data from the reference scatterer. The variables commonly



SYSTEM PHASER SHIFTER POSITION - DEGREES

Fig. 2-16 COMPARISON OF SYSTEM PHASE RESPONSE
WITH A CIRCULAR FUNCTION

associated with data acquisition are target aspect angle, measurement system attenuation or sensitivity level, target configuration, and polarization. These variables are fixed at some known point during the recording of a frame of data. In a typical measurement series, the system attenuator is fixed and the aspect angle is changed while measurements are made at a selected polarization. Thus, a series of data frames is obtained wherein each frame corresponds to a different aspect angle. An angular increment no smaller than 1.0 degree is commonly selected in order to limit the time required for a measurement series.

An attenuation level of zero dB is commonly used on the first series of runs covering the aspect angles of interest. The same aspect region or a portion thereof is then remeasured by using additional system attenuation levels in 20-dB steps until all signal levels of interest may be observed. This process provides a simple means of obtaining, in effect, a wide dynamic range although the single pass dynamic range of the measurement system is about 26 dB. After target data has been obtained by use of the appropriate attenuation levels, the polarization is changed and the sequence of angular coverage and attenuation levels repeated. After measurements have been completed for all polarizations of interest, the initial position of the target is changed, or

a new target configuration is measured by repeating all of the steps described above.

Processing of target data is accomplished by use of a computer program in conjunction with the IBM 360 computer. The primary functions of the program are to edit, calibrate, merge, and reformat the target data in order to produce an output magnetic tape which contains the processed data in card image form. These functions are illustrated in Figure 2-17.

Editing the original magnetic tapes requires the necessary program logic to (1) bypass bad data, (2) compensate for any missing data (if possible), (3) retrieve data from two or more tapes for proper sequencing, and (4) align aspect angles for data taken at two or more attenuation levels for a given set of target parameters. Because of the potential impact of editing on the overall data processing, the following background is provided for better understanding this procedure.

As previously discussed, target data is serially written onto magnetic tape in fixed length records according to the format shown in Figure 2-12. This format provides a means of inserting fixed and variable indicators within the first 20 characters and last 30 characters of each data record so as to uniquely define the measurement parameters associated

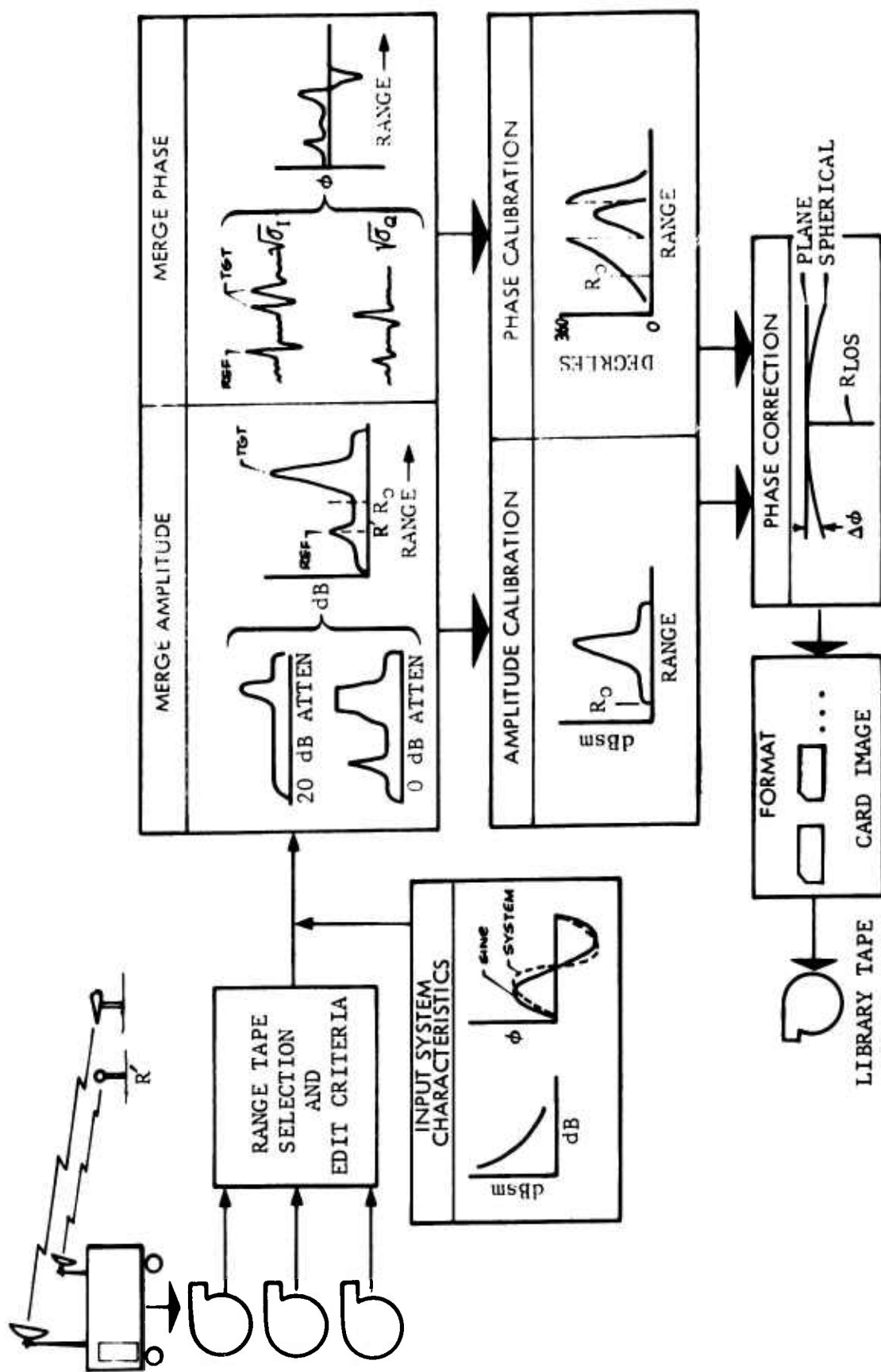


Fig. 2-17 SHORT-PULSE LIBRARY TAPE PROCESSING SEQUENCE

with the data. Of particular interest during editing is the run number (4th character), polarization code (7th character), the ±9999 code (22nd through 25th character), and the system attenuation level (1824th through 1826th character).

At the beginning of a measurement series, the run number is set to zero, and the proper values inserted for the polarization code and attenuation level. If no problems are encountered during the measurement run, these indicators remain unchanged. However, in the event of any occurrence which would invalidate the data being taken, the run number is set to a value of 1, and the measurements retaken. If the editing program senses an increase in the magnitude of the run number, it discards the previous data and replaces it with the new data that is then associated with the higher run number. Values of 2, 3, etc., are used for any subsequent errors encountered while recording data for otherwise fixed measurement parameters. After successfully completing a measurement run (typically a full rotation of the target for a given attenuation level, roll angle, pitch angle, and polarization), the run number is reset to zero and the next series of measurements then taken. The recorded attenuation level is used to properly associate target data obtained at otherwise fixed parameters.

The total number of digital samples taken over the range sampling span of the target far exceeds the capacity of one fixed-length record. Consequently, several records must be serially transmitted and later combined to reconstruct the target signature over the range sampling span. To facilitate this, the algebraic sign of the 9999 code is programmed by the recording system so that the first and last record of a range sweep are easily sensed. The presently adopted data acquisition procedure is such that 30% of the first record and 40% of the last record of a range sweep are used to record the system noise level. Over this portion of the respective records, the -9999 is encoded with the digital samples. Over the remainder of these records, and for all between, the algebraic sign of the 9999 code is positive (see Figure 2-18).

Experience has shown that occasionally the recorder will lose synchronization with the basic system timing, and the last record of a range sweep will be lost. Although the lost data represents less than 1% of that obtained for a typical measurement series, it must be detected so that the following range sweeps are properly reconstructed. The editing program is used to sense the first -9999's encountered in a range sweep, and combine the following records until it senses the change from + to - within a record. If the last

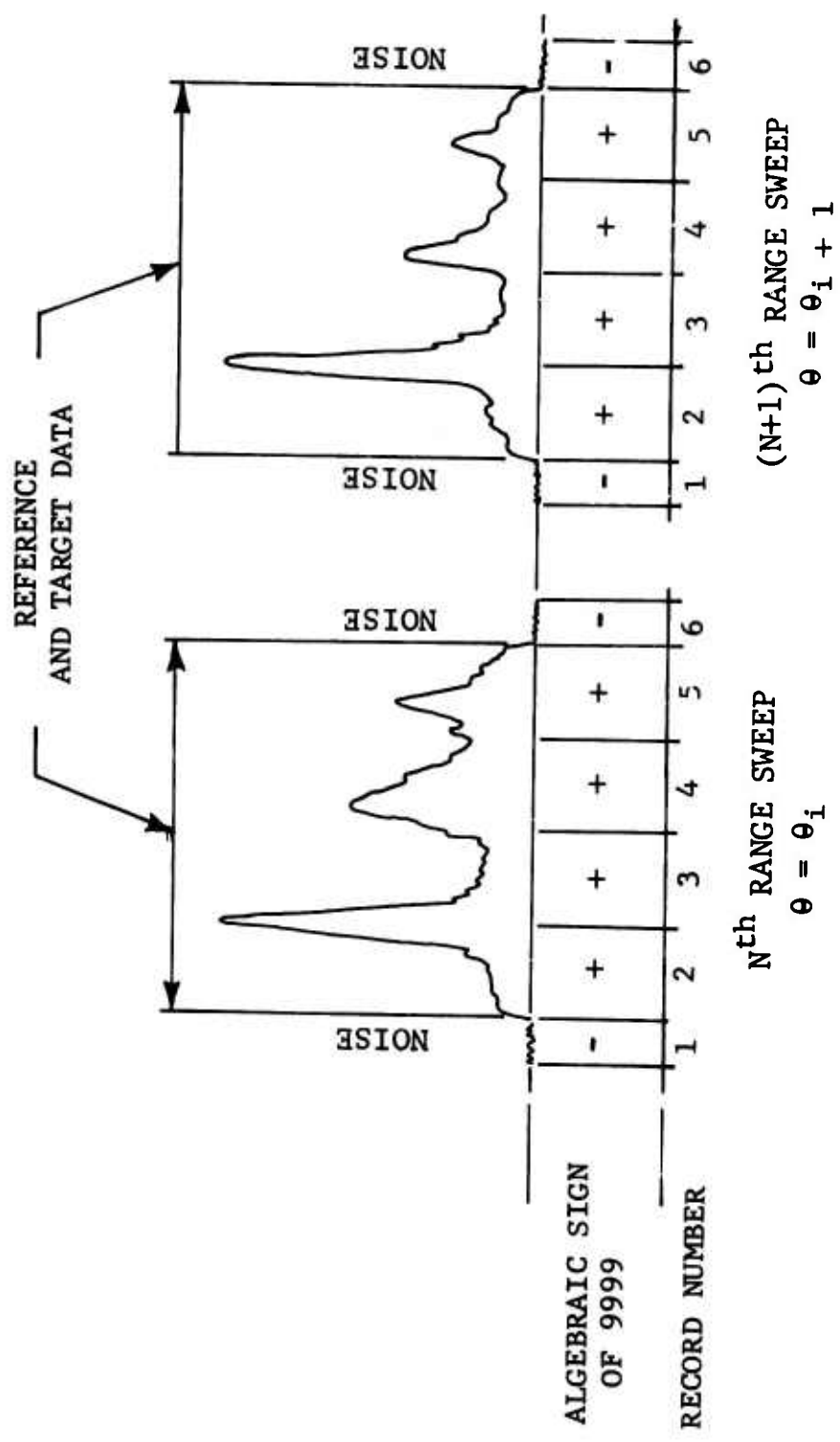


Fig. 2-18 SHORT-PULSE DATA FRAMES

record is missing, a dummy record is inserted so that all range sweeps consist of a fixed number of records.

With the single exception of inserting records for those found missing, no alteration is made to the input data during editing. There presently exists no way of distinguishing between actual target responses and spurious responses generated internal to the radar system.

The editing portion of the program is by far the most complex of any of the program functions since the output of this routine is considered to be error-free by the other routines. Although this greatly facilitates calibration, data merging, etc., it requires that all error conditions be satisfied prior to leaving the editing routine since no further checks are to be made.

Calibration of the target data, both in amplitude and phase, presently utilizes the system response characteristics as library input data which is compiled into the computer program. The program could be used to generate the calibration curves and correction factors since the calibration procedure is also recorded on magnetic tape, however, no apparent advantage would be gained from this action.

The reference scatterer, which appears in each range sweep, is used in conjunction with the input library data to calibrate the target response in each recorded frame. To

accomplish this, the digital data is scanned in order to locate the peak amplitude of the reference. This signal level is used to reconstruct the amplitude response curve, in dBsm, from which each digital sample of the target response is then calibrated. At the range where the peak reference signal is located, the phase, ϕ_R^i , of the reference scatterer is then computed, and corrections are made as necessary to compensate for any nonlinearity in the system phase response.

A phase correction term for the i^{th} polarization, relative to VV, is computed as $\psi_i = (\phi_R^V - \phi_R^i) - \phi_i$ and applied to the target phase response. The value of ϕ_i was established during the system phase calibration procedure. To avoid necessary computations, the attenuation levels associated with otherwise fixed measurement parameters are merged during this calibration process. When a saturated sample is encountered, the control logic is used to search successively higher measurement attenuation levels until an unsaturated sample is found.

Depending upon the size of the target, and the range at which measurements are taken, a final correction to the target phase may or may not be necessary. This correction involves compensating for errors introduced by phase front curvature over the volume of the target. Normally the target dimensions and range geometry are such that this correction is not required.

As illustrated in Figure 2-17 the final step in processing involves reformatting the target data into record image form, and producing a library tape for future analysis.

2.4 Results and Conclusions

All of the long-pulse measurement results obtained during the experimental investigation are described in Volume II of this report. Selected data are also presented in Volume III for comparison with the scattering data obtained by use of analytical expressions. Section 4 of this volume also contains a set of cross section and phase plots of seven vehicle models.

Inspection of these data reveals that the high quality of both amplitude and phase measurements has been maintained during this program. In the case of generic surfaces, the values of measured cross section at specular points have been compared to the values computed by use of the physical optics approximation, and excellent agreement has been revealed.

These measurement data have been utilized in a variety of tasks during this investigation and will surely find extensive use in other investigations. The methods used in obtaining absolute phase measurements have been validated by the results of these measurements as being generally applicable to a variety of phase center studies. Phase investigations of interest include those related to target glint and those

related to the location and motion of the phase centers of antennas such as large reflectors, phased arrays, and monopulse configurations in the presence of other reflecting structure.

A detailed description of the overall measurements capabilities of the Radar Range at the Fort Worth division is contained in Reference 5.

SECTION 3

ANALYTICAL INVESTIGATION

3.1 General

The objective set for the analytical investigation was to develop analytical expressions which would be accurate descriptions of electromagnetic scattering from conducting bodies that contained the following basic generic surfaces and their derivable shapes: finite, right-circular cylinders, frustums, cones, and hemispheres. The derivation of the analytical expressions was performed by Cornell Aeronautical Laboratory (CAL) under subcontract to the Fort Worth Division of General Dynamics. The results obtained by using these expressions were then evaluated by comparing quantitative theoretical predictions with scattering matrix measurements which were performed at the Fort Worth Division. The derivation of the analytical expressions and the results of the quantitative comparison are reported in detail in Volume III of this technical report (Reference 2).

Reference 2 contains a general discussion of the advantages and limitations of a number of analytical techniques which have been utilized by various investigators. These techniques include the exact methods, (1) the separation of variables and (2) the integral-equation formulation, as well

as approximate formulas which are useful in restricted ranges of the parameters that characterize the particular problem of interest. Geometrical Optics and Physical Optics are two approximate theories which may be applied when the targets exhibit minimum dimensions that are at least several wavelengths in extent. The limitations of these two approximate methods are shown to place severe restrictions on their use in the general case in which nonspecular aspects are considered.

The approximate technique, based on the geometric theory of diffraction (GDT), appears to be the technique most universally applicable to the high-frequency case of interest in this investigation. This theory was developed by J. B. Keller at New York University and is largely dependent upon an extension of Fermat's principle in which consideration is given to diffracted rays, as well as reflected (geometrical optics) rays. Although this technique is not based on a rigorous mathematical foundation, the requirement for polarization dependence is retained, and that for reciprocity in bistatic situations is satisfied.

The use of GDT is based upon the hypothesis that scattering from a target (for large ka) occurs only from discontinuities in the surface of the target. Scattering from

these discontinuities (called scattering centers) is approximated by modifying the GDT results for scattering from an infinite wedge or edge. This modification takes the form of a multiplicative divergence factor which accounts for edge curvature and the finite extent of the discontinuity. The polarization-dependent cross section and phase are computed by use of the phasor addition of the scattering computed for each surface discontinuity illuminated by the radar.

At specular points the use of GDT fails to give a finite result; hence, the technique has been modified to include the use of the physical optics approximation for computing the cross section at speculars.

In the analysis of the scattering from a cone, some short-pulse data obtained by use of a sphere-tipped cone were utilized in an attempt to determine if secondary scattering phenomena could be observed. Although secondary scattering was observed at isolated aspect angles, no systematic returns were observed in sufficient detail to be correlated with the geometry of the object.

3.2 Results

Formulas developed on the basis of the modified theory were used to compute the scattering from a selected set of the vehicles upon which scattering matrix measurements were available. Table 3-1 contains a description of these vehicles and the parameters of the radar system used in obtaining the measurements data which are presented in detail in Reference 2.

The results showed a remarkable agreement between the theoretical predicted values of cross section and phase and the measured values. Figure 3-1 contains plots of the computed and measured cross section obtained by use of the frustum-cylinder, Model F5CY5, at a bistatic angle of 10.25 degrees and vertical polarization. Figure 3-2 contains the corresponding plots of measured and computed phase.

Figures 3-3 and 3-4 contain the corresponding results obtained by use of horizontal polarization. The agreement obtained in the case of vertical polarization has been generally observed to be not quite as good as in the case of horizontal polarization, especially in the intermediate aspects and near wells. However, it is known that measurements are most sensitive in these regions when vertical polarization is used.

TABLE 3-1 MEASUREMENT AND COMPUTATION PARAMETERS

MODEL DESIGNATION	FREQUENCY (GHz)	BISTATIC ANGLE (DEGREES)
CY3	5.975	0
CY5	6.0	0
	5.885	10.25
	6.050	30.
CY6	6.0	0
	5.885	10.25
	6.050	30.
C1	6.0	0
C2	6.0	0
C4	5.975	0
F3	6.0	0
F4	6.0	0
	5.885	10.25
	6.050	30.
F5	6.0	0
	5.885	10.25
	6.050	30.
F4CY3	5.975	0
CY4F4	5.885	10.25
	6.050	30.
C2CY3	5.975	0
C4CY5	6.0	0
H3CY3	5.975	0

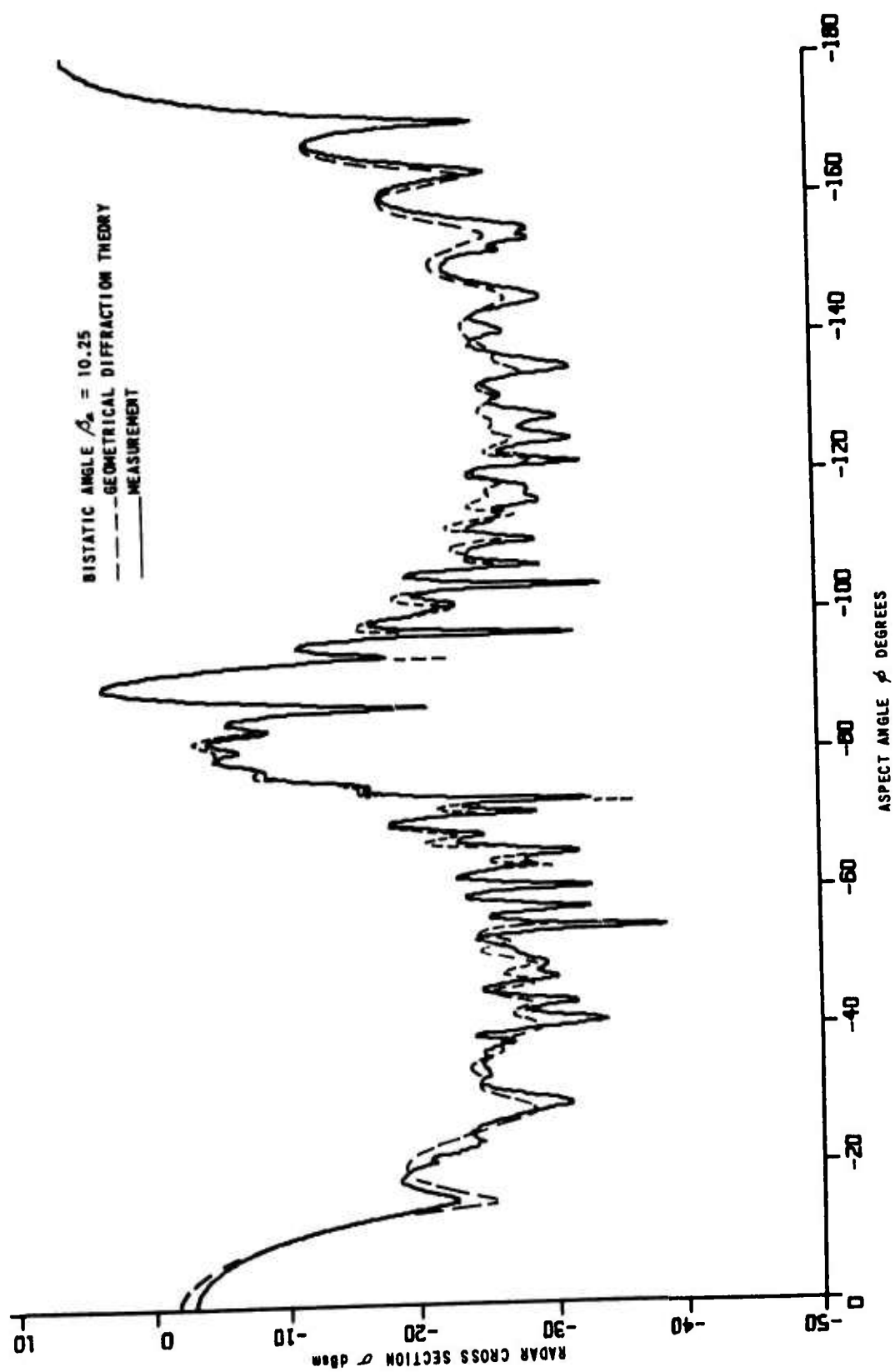


Fig. 3-1 RADAR CROSS SECTION FOR MODEL F5CY5 - VV POLARIZATION

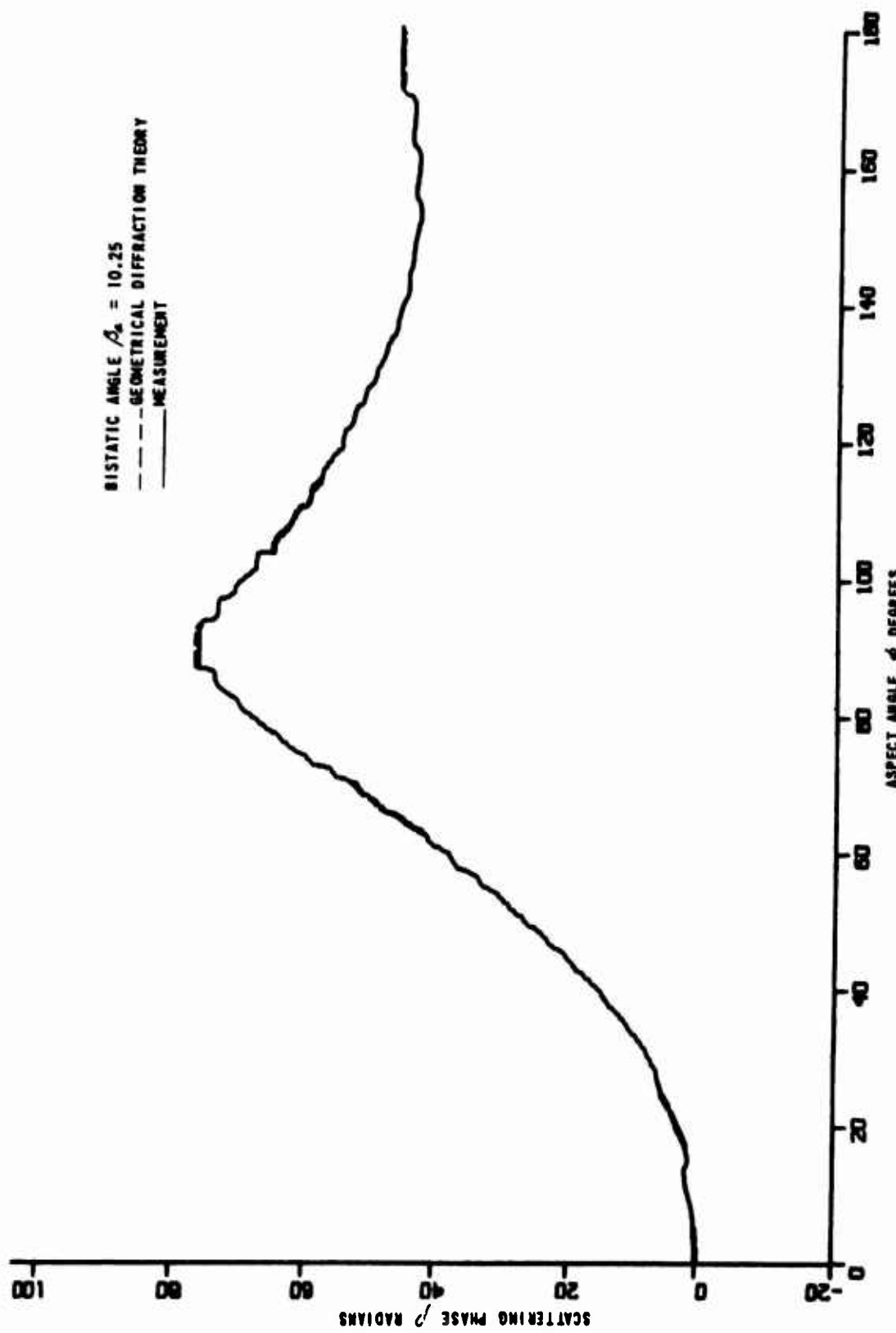


Fig. 3-2 SCATTERING PHASE FOR MODEL F5CY5 - VV POLARIZATION

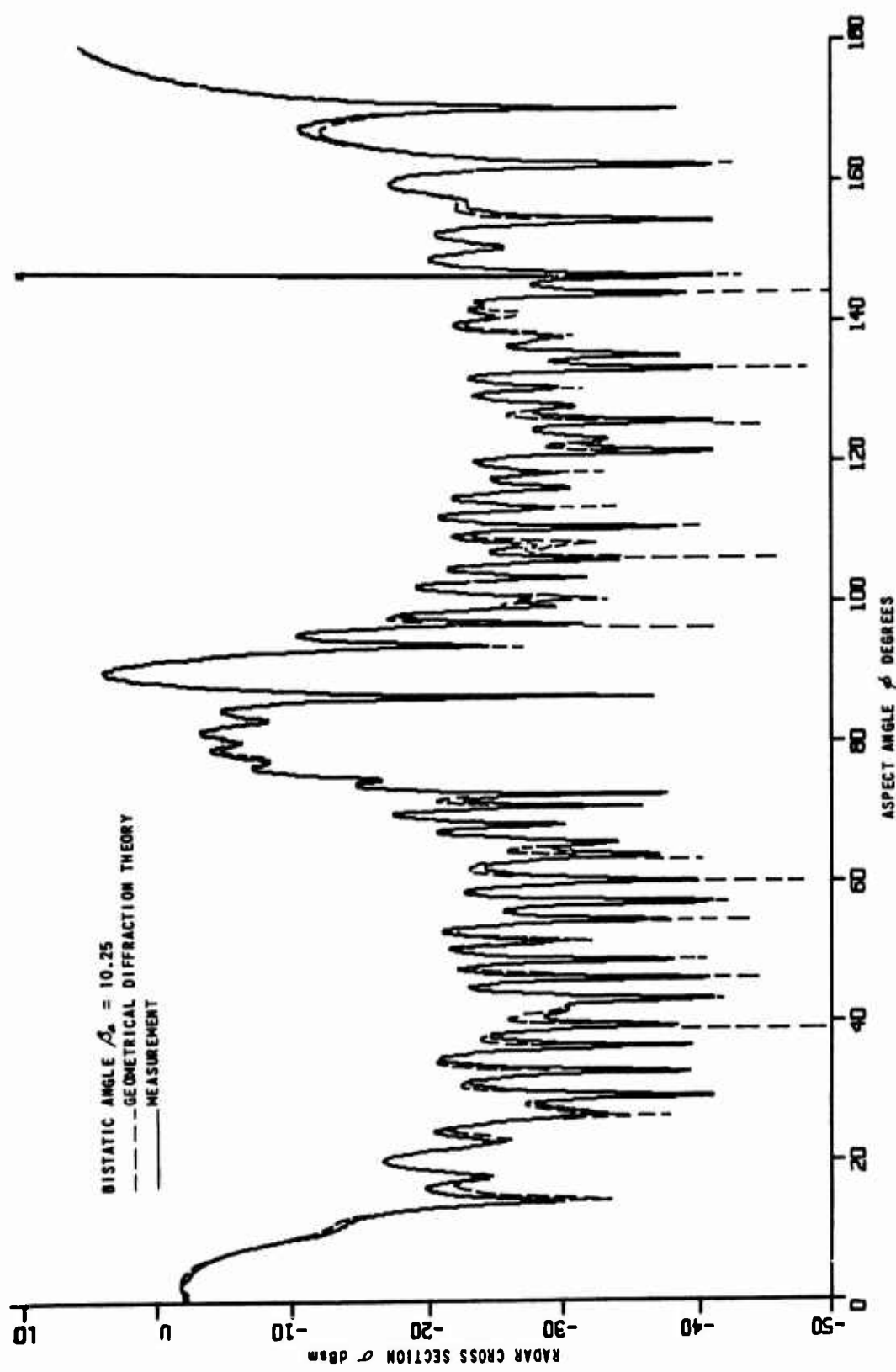


Fig. 3-3 RADAR CROSS SECTION FOR MODEL F5CY5 - HH POLARIZATION

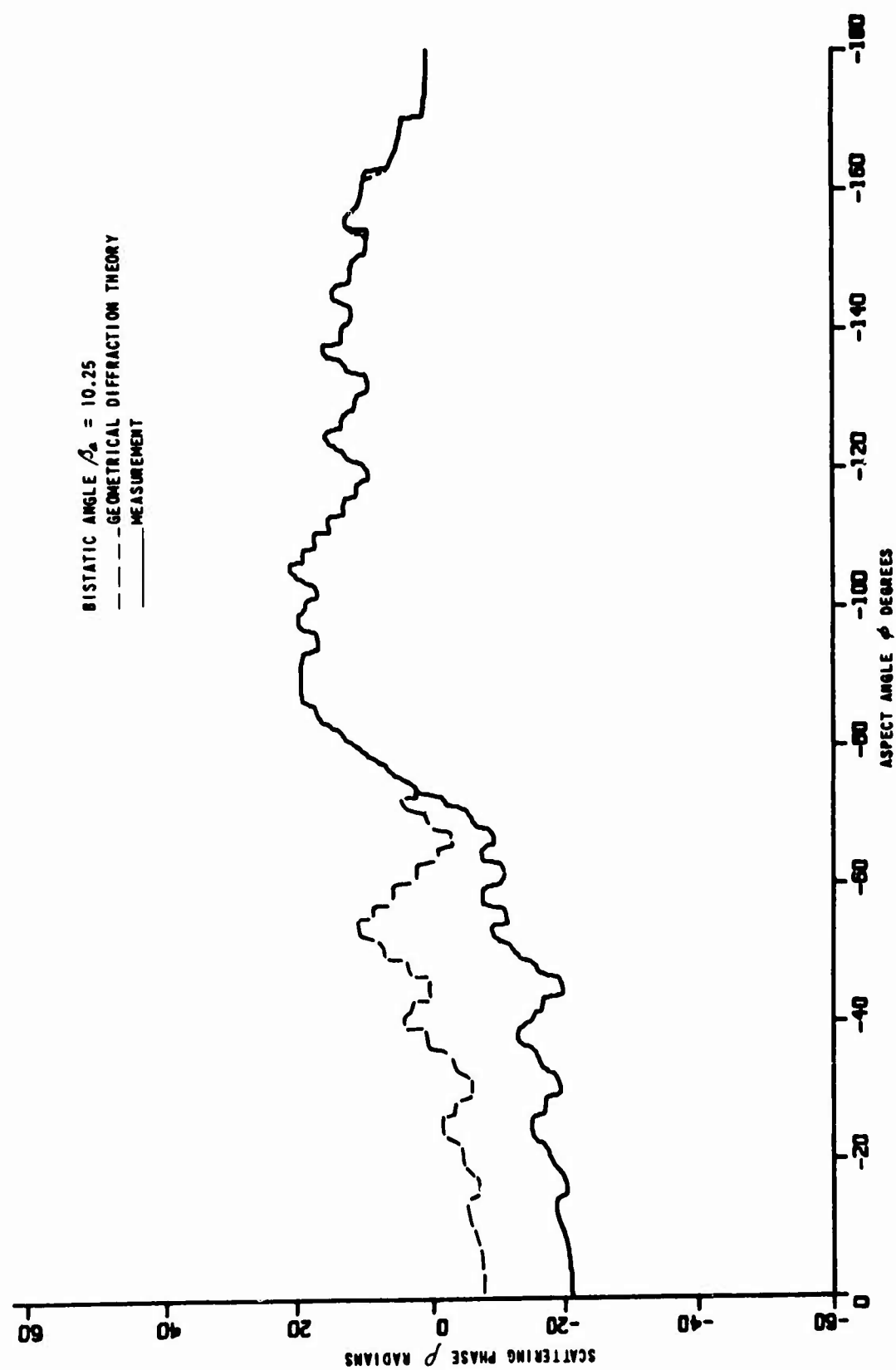


Fig. 3-4 SCATTERING PHASE FOR MODEL F5CY5 - HH POLARIZATION

The deviation between measured and computed phase is thought to be a result of the modulo 2π recording techniques used for both measurements and computations. The results shown in Figures 3-1 through 3-4 are typical of those obtained for all the shapes investigated in this program with the exception of cones and cone-cylinders. The results obtained from investigation of these two surfaces indicated that the use of GDT, in its present form, is severely limited to the aspect interval $\alpha \leq \theta \leq \pi/2 - \alpha$, where α is the half-angle of the cone. An attempt to empirically upgrade theory in this aspect region was unsuccessful, as was the search for any systematic secondary scattering mechanisms via analysis of short-pulse data.

3.3 Conclusions

Coordination between CAL and the Fort Worth Division has led to the definition of measurement models and parameter variations necessary to conduct scattering formula investigations on a variety of vehicle shapes. The basis analyses involved the application of modified geometrical diffraction theory to predict scattering by cylinders, frustums, cones, hemispheres, and derivable shapes. Extensions of theory performed under this contact involved modifications of basic analyses for application at and near those aspects which give rise to specular scattering, and at and near nose-on aspects for a cone.

Resultant formulations were programmed for use on the IBM 360 digital computer for the following shapes: cylinder, frustum, cone, frustum-cylinder, cylinder-flare, cone-cylinder, and hemisphere-cylinder. Theory was evaluated by comparing predicted and experimental values of principal polarization radar cross sections and cumulative scattering phases. Both monostatic and bistatic situations were investigated.

Results obtained under this contract attest to the validity of geometrical diffraction theory for predicting the bistatic scattering matrix of cylinders, frustums, frustum-cylinders and cylinder-flares. Very good agreement with measurement data is generally observed when the minimum target dimension is at least several wavelengths in extent. Further modification of geometrical diffraction theory is required to generate an equivalent capability for the analysis of a cone and a cone-cylinder.

Reference 2 contains an outline of proposed additional analytical effort within the context of geometrical diffraction theory. Furthermore, the very rapid phase changes occurring in plots of predicted and measured values of horizontal polarization phase need to be followed more closely to resolve ambiguities.

Computer time is not a limitation when calculations are based upon geometrical diffraction theory; the complete scattering matrix of each target was predicted at 1801 aspect angles in less than two minutes on an IBM 360/65.

SECTION 4

SUPERPOSITION INVESTIGATION

4.1 General

The objective set for the investigation reported in this section was to establish and evaluate techniques by which SM measurements of sets of generic surfaces can be combined to produce the SM of a composite vehicle formed by the physical interconnection of the set of surfaces. This effort was limited to the use of long-pulse radar signatures. Most scattering vehicles of practical interest can be described or defined in terms of a number of basic generic-type surfaces, such as flat plates, cylinders, spheres, cones, etc. This is especially true in the case of typical aerospace vehicles which tend to be basically roll symmetric and whose shape can generally be reduced to a number of generic surfaces of revolution, e.g., cones, frusta, cylinders, paraboloids of revolution, etc. A technique by which the SM of a vehicle can be accurately determined from SM measurements on a set of simple targets would be highly desirable in terms of time saving and cost effectiveness.

This desirability can be illustrated in a number of ways. For example, once SM measurements were obtained for

a set of generic surfaces, these data would always be available for use in various combinations in order to simulate whatever composite vehicle might be desired. Use of these data would eliminate the necessity of building a model of the composite vehicle and subsequently obtaining the SM by use of a radar range. The only expense, once the generic surfaces had been measured, would be the computer time necessary for producing the desired SM data. The time saving might possibly be even more meaningful since a quick look at the SM of a composite body might be easily obtained within a very short turn-around time in comparison to a term of weeks which is generally required to fabricate a model and obtain the use of an adequate radar scattering range facility.

Also, while a desired target vehicle might be considerably more complex than the composite which can be formed from available measurements, it may be that a good approximation can be obtained by synthesizing the desired vehicle geometry to some degree by use of generic shapes. The investigation discussed in Section V was directed to defining the relationship between SM measurements obtained by use of targets which represent various degrees of physical synthesis to other targets.

The basic approach undertaken in order to accomplish this investigation involves the use of the principle of linear superposition. When this principle is applied to electromagnetic field quantities, it can be stated as follows. The scattered field produced at a point in space is the vector summation of the fields produced by each component of the scattering body considered separately, if it is assumed that there is no coupling between the component body scattering sources. An equivalent statement would be that, in the absence of coupling effects, the total field scattered from a target would be identical to the field obtained by the linear superposition of the fields produced by a set of generic surfaces which represent the target.

It is a well known fact that surface discontinuities constitute significant sources of scattering, and it is obvious that a surface discontinuity will be created whenever a composite body is "broken" to form a pair of component bodies. For example, Figure 4-1 contains an illustration of the manner in which a cone-cylinder might be divided into a cone and a cylinder. When the targets are considered separately, the discontinuity at the interface of the cone and the cylinder is obviously quite different from that presented at the interface of the composite body. A major portion of this investigation is concerned with a

determination of the effects of "coupling" in the sense that coupling describes the relationship between interfacing surfaces.

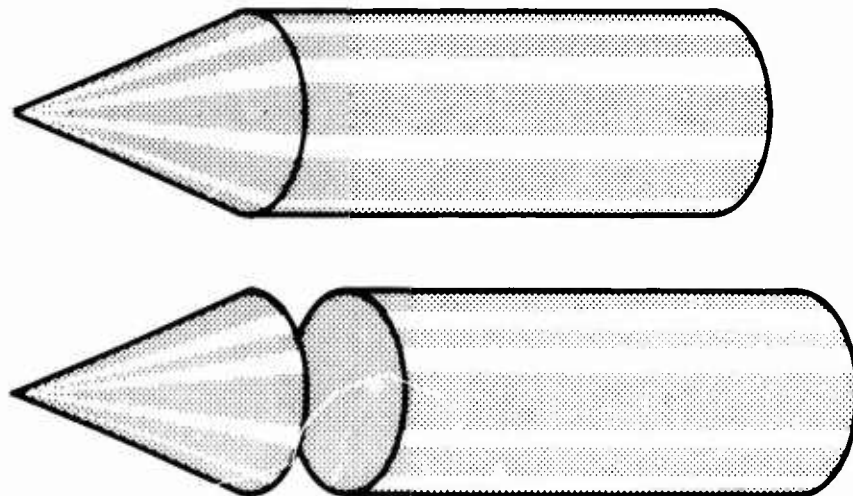


Fig. 4-1 SURFACE DISCONTINUITY BETWEEN CONE AND CYLINDER

4.2 Technical Approach

The general formulation of linear superposition is contained in Equation 4-1 where the computed field at the radar receiver is given by the vector summation of the individual fields produced by the N component surfaces which will be geometrically identical to the composite body when they are positioned correctly in relation to a reference coordinate system. A plane wave illumination is assumed, and the $e^{j\omega t}$ time variation and the amplitude variation with range are suppressed.

$$\bar{E}_S(N) = \bar{E}_S(n_1, n_2, \dots, n_N) = \sum_{i=1}^N \bar{E}(n_i) \quad (4-1)$$

Each parameter, n_i , refers to the nomenclature describing the i^{th} component surface. The subscript S indicates that the field quantity is obtained by linear superposition (coupling effects are not considered). It should be noted that Equation 4-1 holds only for one frequency, polarization, and aspect orientation. The field produced when the composite body is measured is given by $\bar{E}(N)$. Thus, at each aspect angle, the difference $\bar{E}(N) - \bar{E}_S(N)$ is the error produced by ignoring the effects of coupling.

Equation 4-1 can be expressed in terms of cross section and phase by assuming a unit incident field so that $e^{j\phi} = \bar{E}$, i.e.,

$$\sqrt{\sigma_S(N)} e^{j\phi_S(N)} = \sum_{i=1}^N \sqrt{\sigma(n_i)} e^{j\phi(n_i)} \quad (4-2)$$

The amplitude and phase terms on the left-hand side of Equation 4-2 can conveniently be expressed by

$$\sqrt{\sigma_S(N)} = \sqrt{\left\{ \sum_{i=1}^N \sqrt{\sigma(n_i)} \cos\phi(n_i) \right\}^2 + \left\{ \sum_{i=1}^N \sqrt{\sigma(n_i)} \sin\phi(n_i) \right\}^2} \quad (4-3)$$

and

$$\phi_s(N) = \tan^{-1} \left\{ \frac{\sum_{i=1}^N \sqrt{\sigma(n_i)} \sin\theta(n_i)}{\sum_{i=1}^n \sqrt{\sigma(n_i)} \cos\theta(n_i)} \right\} \quad (4-4)$$

The expression for cross section in Equation 4-3 provides a convenient means for examining the errors which arise as a result of errors in the alignment or location of the component surfaces which are being superimposed. Consider, for example, the superposition of two identical point scatters, each exhibiting a cross section of σ_0 square meters. The geometrical relationship between these two scatterers is illustrated in Figure 4-2.

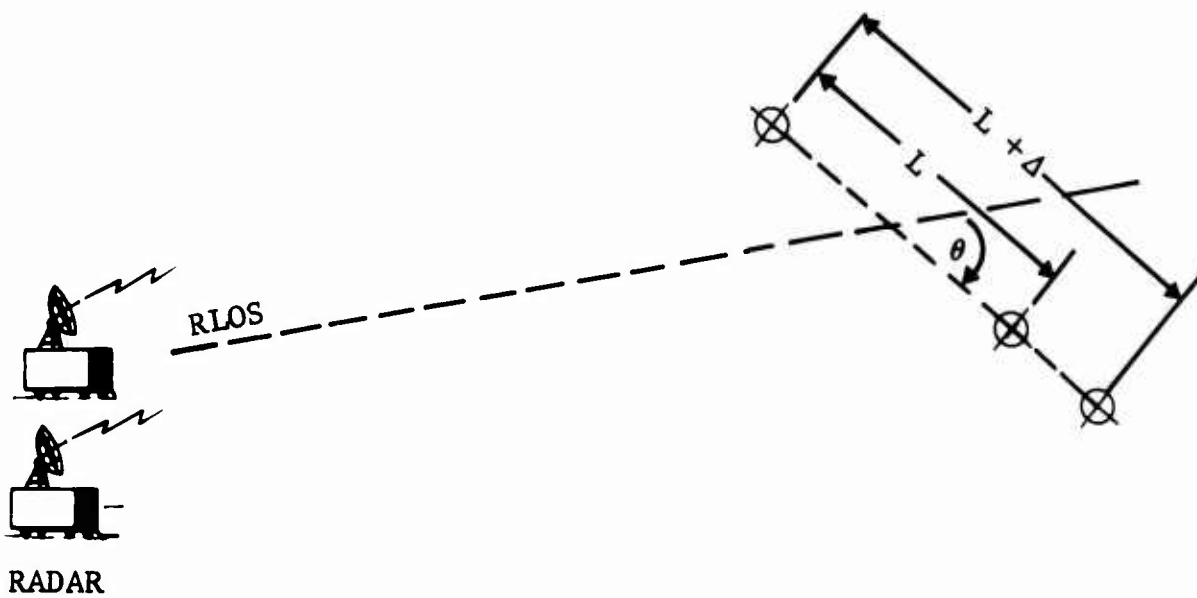


Fig. 4-2 GEOMETRICAL MODEL FOR ALIGNMENT ERROR ANALYSIS

The cross section of the composite structure is given by

$$\sqrt{\sigma} = \sqrt{\sigma_0} [e^{j\phi_1} + e^{j\phi_2}] \quad (4-5)$$

where ϕ_1 and ϕ_2 represent the measured phase of the two scatterers relative to a common geometrical reference point in space (it is assumed that the phase term resulting from the range between the radar and the reference point has been removed). Equation 4-5 can also be written as

$$\sqrt{\sigma} = \sqrt{\sigma_0} [1 + e^{j(\phi_2 - \phi_1)}] \quad (4-6)$$

From Figure 4-2, the difference $\phi_2 - \phi_1$ is seen to be equal to $2kL \cos\theta$ where $L \cos\theta$ represents the projection of the separation on to the RLOS. $2k$ is twice the wave number; the 2 is required to account for the two way scattering path. Expansion of Equation 4-6 gives

$$\sqrt{\sigma} = \sqrt{2 \sigma_0} \sqrt{1 + \cos(2kL \cos \theta)} \quad (4-7)$$

or

$$\sqrt{\sigma} = 2\sqrt{\sigma_0} \cos(kL \cos \theta) \quad (4-8)$$

where the principal value of $kL \cos \theta$ is used. Thus, when the two scatterers reinforce each other ($kL \cos \theta = 2n\pi$) the composite cross section $\sigma = 4 \sigma_0$, and a 6-dB increase in cross section is obtained. Whenever $kL \cos \theta = (2n + 1)\pi$, the scatterers interact destructively, and $\sigma = 0$.

An error in measured phase or, equivalently, an error in the positioning of the two scatterers can be simulated by adding an error term to L . The computed cross section,

obtained when an error, Δ , is added to L is given by

$$\sqrt{\sigma(\Delta)} = 2\sqrt{\sigma_0} \cos [k \cos \theta(L + \Delta)]$$

The error in cross section resulting from this error in position may be expressed as

$$\xi_{\sigma} = \sigma - \sigma(\Delta) = 4\sigma_0 \left[\cos^2(kL \cos \theta) - \cos^2(k(L + \Delta) \cos \theta) \right] \quad (4-9)$$

Observation of Equation 4-9 indicates that the maximum error occurs when $\theta = 0$ degree, i.e., when the position error is colinear with the RLOS. When $\theta = 0$ degrees, Equation 4-9 can be expanded to give

$$\xi_{\sigma} = 4\sigma_0 \left[\cos^2 kL (1 - \cos^2 k) + 2\cos kL \cos k\Delta \sin kL \sin k\Delta - \sin^2 kL \sin^2 k\Delta \right] \quad (4-10)$$

The base distance L can be chosen so that $kL = 2n\pi$ when $n = 1, 2, \dots$ without loss of generality. The error can then be expressed as

$$\xi_{\sigma} = 4\sigma_0 \cos^2 kL \sin k\Delta$$

or

$$\xi_{\sigma} = \sigma \sin^2 k\Delta \quad (4-11)$$

Relative to the correct value of cross section, σ , this error is $20 \log (\sin k\Delta)$ dB above σ square meters, where $0 \leq \Delta \leq \pi/4$. Thus, when $\Delta = 0$, no error is produced; when $\Delta = \pi/4$, the error is as large as the desired cross section. Figure 4-3 contains a plot of the error in dB versus Δ/λ for the case described in Equation 4-11.

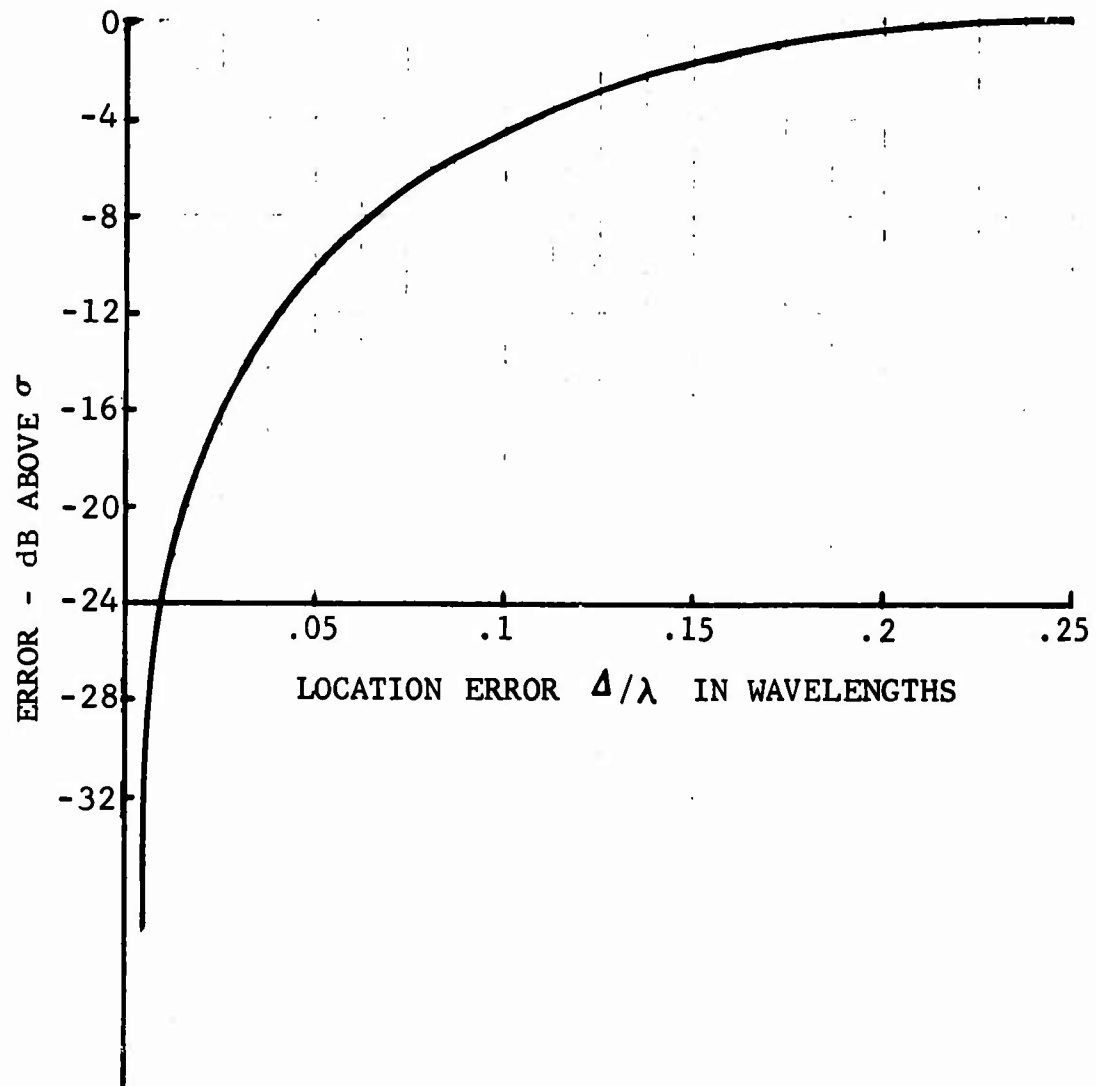
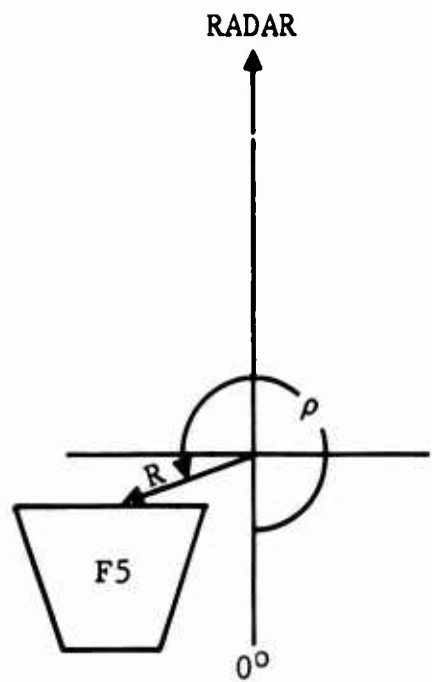


Fig. 4-3 AMPLITUDE ERROR RESULTING FROM LOCATION ERROR

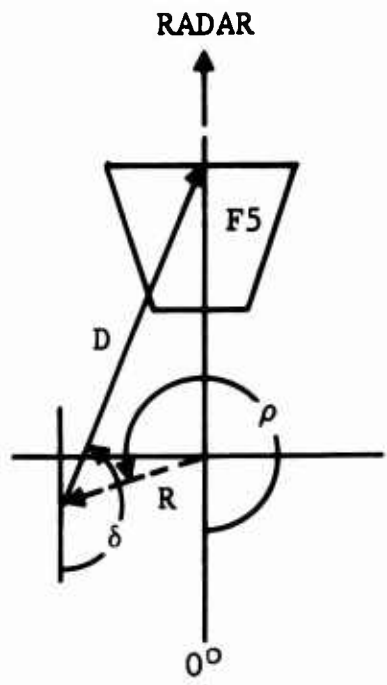
The significant result shown in Figure 4-3 is that a position error of only one-twentieth of a wavelength produces an error less than 10 dB below the error-free value of cross section. One-twentieth of a wave length at C-band corresponds to only one-tenth of an inch or equivalently, to a change in measured phase of 36 degrees.

Equation 4-2 is an expression of the method in which the composite cross section is computed by using superposition. In order to actually implement this expression by using a digital computer, a number of considerations had to be taken into account. In the first place, the measured phase term associated with each aspect angle measurement was an absolute measurement (modulo 2π) of the position of the apparent phase center of the target with respect to the phase reference position in space. The measured phase data of each target to be "superimposed" must be modified so that it corresponds to the phase data which would be measured if the target were actually occupying the location into which it is being superimposed. Figure 4-4 contains an illustration of the general method used to "translate" a target to a new position by modifying its measured phase data.

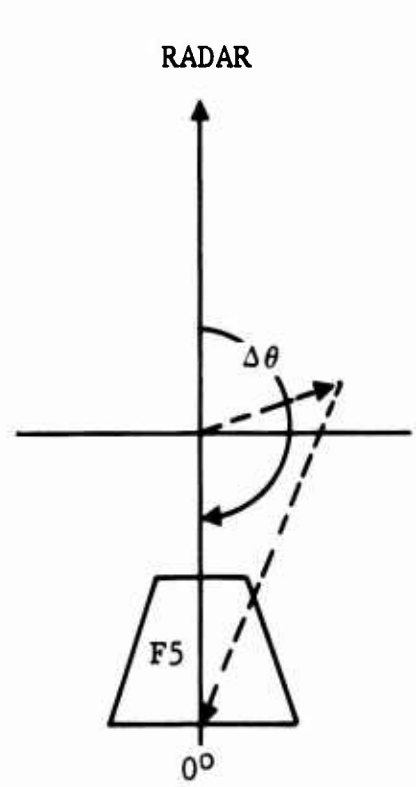
The position of the target is shown in Figure 4-4a relative to the center of rotation of the turn-table, when it was measured separately; in this case, the target was a



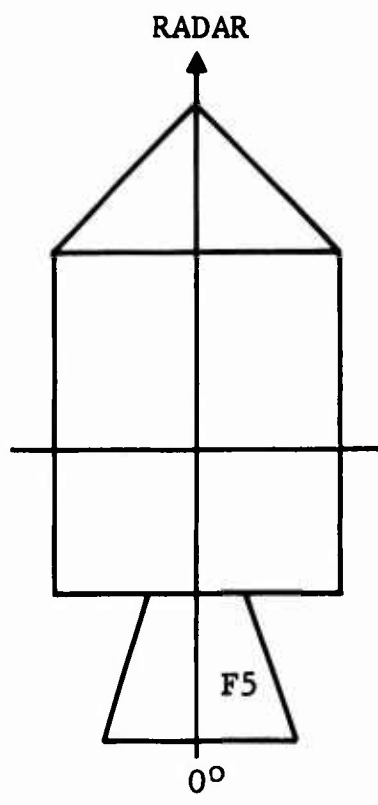
(a) POSITION DURING MEASUREMENT



(b) INTERMEDIATE POSITION



(c) FINAL POSITION



(d) COMPOSITE VEHICLE

Fig. 4-4 EXAMPLE OF TARGET TRANSLATION USING SUPERPOSITION PARAMETERS

frusta. The position vector defined by R and ρ indicates the position of the target reference with respect to the center of rotation.

In order to physically translate the frustum into the desired position for superposition with the cylinder and cone shown in Figure 4-4d, a two step process would be necessary:

1. Shifting of the target reference point so that it is the correct distance from the center of rotation.
2. Rotation of the target, about the center of rotation, until the target axis is located correctly in terms of the composite vehicle reference axis.

In the example shown in Figure 4-4, the vector (D, δ) provides the necessary translation corresponding to Item 1.

A rotation of 180 degrees then brings the frustum to the desired position.

In superposition, this translation is simulated by operating on the measured phase data. Let $\phi(\theta)$ be the measured phase where $-180.0 \leq \theta \leq 179.9$ degrees. The computed value of phase $\phi_c(\theta)$ is given by

$$\phi_c(\theta) = \phi(\theta) + 2kD \cos(\delta - \theta) \quad (4-12)$$

The term $D \cos(\delta - \theta)$ represents the projection of D onto the RLOS. The final position of the frustum is achieved by adding 180 degrees to each value of θ in order to simulate rotation of the target about the center of rotation.

One additional consideration is necessary in order to superimpose vehicle measurements in a reasonable manner. As stated previously, there are some aspect angle regions in which the superposition of target measurements would not be meaningful. This case occurs over angular regions where one or more component surfaces exhibit a surface which is obviously not observed in the case of the composite vehicle. The cone-cylinder example discussed in relationship to Figure 4-1 exemplifies this case, especially near the nose-on region.

This case can be handled by simply ignoring scattering from surfaces over angular regions in which they would be "shadowed" by other portions of the composite vehicle. Thus, each case of superposition consists of defining the location of each component target and defining the shadow regions over which each component target will be ignored.

4.3 Superposition Example (Model F5CY5)

A particular example is presented in the following paragraphs in order to thoroughly explain the method of obtaining and using the various parameters associated with superposition. The target used in this example consists of a frustum (F5) and a cylinder (CY5). Both F5 and CY5 were measured separately and the composite frustum-cylinder (F5CY5) was also measured by using the same radar parameters

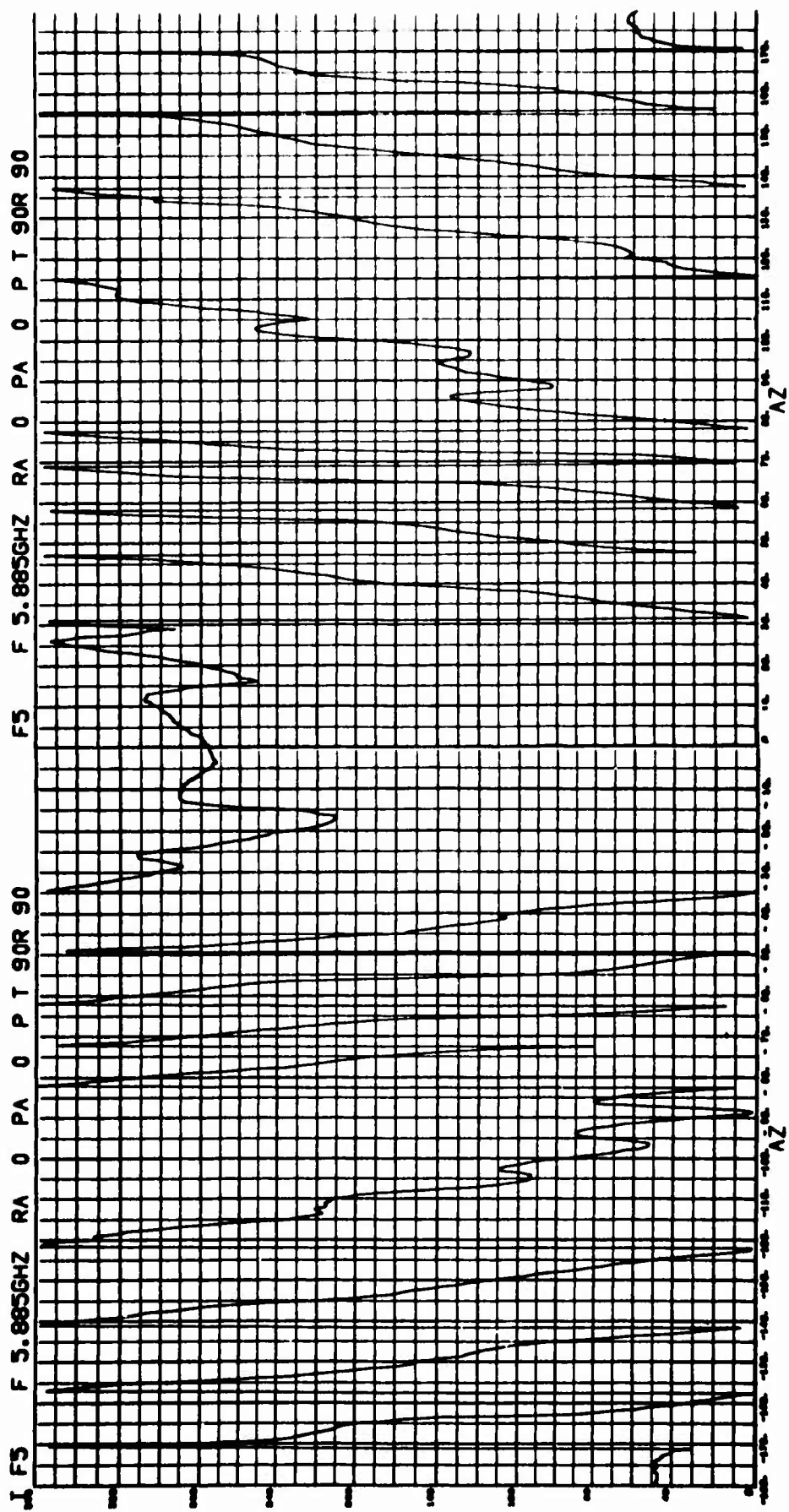


Fig. 4-5 PHASE SIGNATURE FOR MODEL F5 - VV POLARIZATION

for comparison. In this analysis, measurements were obtained at a frequency of 5.885 GHz, a bistatic angle of 10.25 degrees, and vertical polarization of both the transmitting and the receiving antennas.

Figure 4-5 contains an analog plot of the library phase data for F5. The reference point on F5 is located in accordance with the definition presented in Figure 2-3. However, analysis of these phase data indicates that the reference point did not coincide with the center of rotation. If the modulo 360 degrees effect in measured phase is removed by manual analysis of these data, the cumulative phase change is obtained. This data is plotted in Figure 4-6.

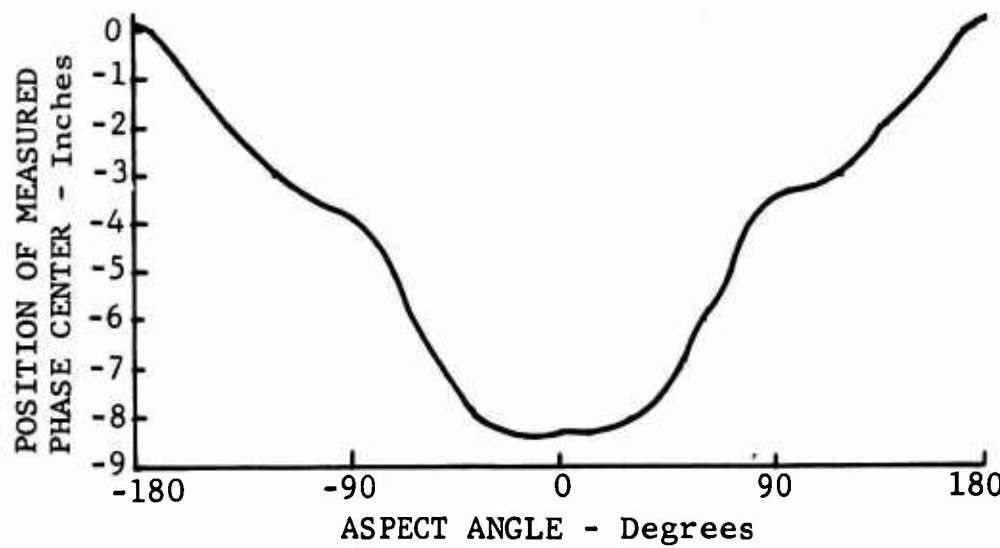


Fig. 4-6 CUMULATIVE PHASE FOR MODEL F5 - VV POLARIZATION

The total change in phase between the -180-degree and the 0-degree aspect determined in this manner is observed to be

$$\psi = 8 \times 360 + 47 + 84 = 3011 \text{ degrees}$$

By allowing for the two way path, the physical phase length between the flat faces of Frustum F5 is computed from

$$\psi_p = 2kL \times 180/\pi \text{ and is}$$

$$\psi_p = (2) (360) (7.421) (5.885)/(11.811) = 2655 \text{ degrees}$$

This physical phase length is computed under the assumption that the phase center of the frustum at its end-on views is coincident with the flat end. This assumption is apparently well-founded in the case of targets in the physical optics region ($ka > 10$). This conclusion can be verified on the basis of measured data on frusta and cylinders in Reference 1.

The difference between the measured and the physical two-way phase is indicative of a position error along the axis of the frustum. In this particular case, since a bistatic radar is being utilized, measured bistatic phase must be transformed so that it has meaning in terms of the position of the target along the RLOS (defined as the bisector of the bistatic angle). The relationship between bistatic phase, ψ_B , and monostatic phase, ψ_M , is shown in Figure 4-7.

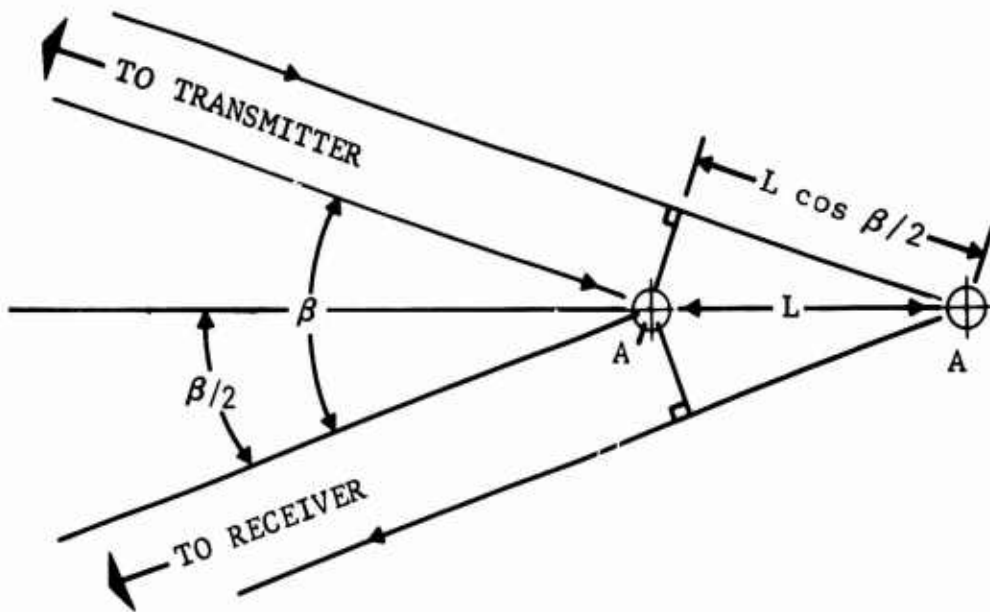


Fig. 4-7 BISTATIC - MONOSTATIC RELATIONSHIP

This relationship may be observed by noting the change in measured phase which would be observed if a point scatterer were moved from position A to position A'. A monostatic radar located on the RLOS would detect a change in phase of

$$\psi_M = 2kL$$

$$\psi_B = 2kL \cos \beta/2$$

where β is the bistatic angle. This difference results from the fact that measured phase is determined by the projection of physical displacement onto the actual radar path. Thus, the physical location along the RLOS of the target phase center, measured by use of a bistatic radar, is

$$R \cos \theta = \frac{\psi_B(\theta)}{2k \cos \beta/2}$$

or

$$\psi_m(\theta) = \frac{\psi_B(\theta)}{\cos \beta/2}$$

where $\psi_m(\theta)$ is the equivalent monostatic phase.

In general, the measured phase is actually the sum of the theoretically perfect phase and the errors contributed by uncertainty of target location and imperfection of system operation. The relationship of these four elements can be expressed as

$$\psi_m(\theta) = \psi_o(\theta) - 2k \cos \beta/2 R \cos(\rho - \theta) - \psi_c$$

where

$\psi_o(\theta)$ is the theoretically perfect bistatic phase

$\psi_m(\theta)$ is the measured bistatic phase

ψ_c is a phase bias introduced during calibration

R, ρ are the polar coordinates of the phase center
with respect to the geometric reference position.

The relationship between ρ , R , and θ are shown in Figure 4-8
for the case of a point scatterer.

Thus, the true phase can be expressed in terms of the measured phase and the phase bias as

$$\psi_o(\theta) = \psi_m(\theta) + 2k \cos \beta/2 R \cos(\rho - \theta) + \psi_c \quad (4-13)$$

The three unknowns (R , ρ , and ψ_c) in Equation 4-13 can be determined if at least three values of θ can be found at which $\psi_o(\theta)$ (the location of the error-free phase center)

can be determined.

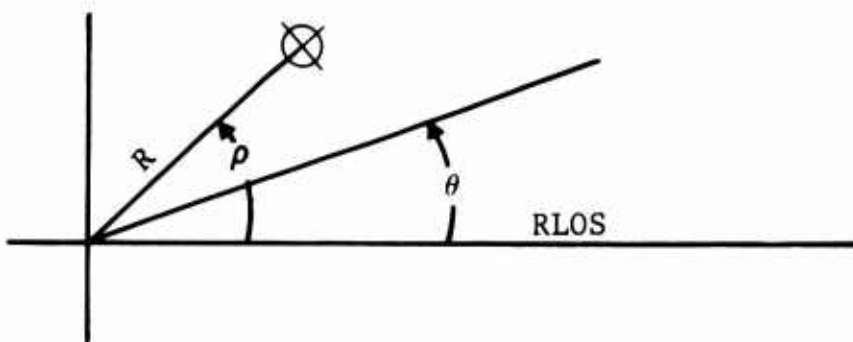


Fig. 4-8 PHASE CENTER COORDINATE SYSTEM

If a target contains large flat-plate surfaces, such as the end-on aspects of cylinders and frustums, the phase center can be identified on these flat plates. Two equations can be formulated on the basis of this identification:

$$\psi_o(\theta) = \psi_m(\theta) + 2k \cos \beta/2 R \cos \rho + \psi_c \quad (4-14)$$

$$\psi_o(180) = \psi_m(180) - 2k \cos \beta/2 R \cos \rho + \psi_c \quad (4-15)$$

Also, in the case of a body of revolution, although the exact position of the phase center may not be known (as a result of body curvature in one dimension) the location of the phase center is known to be the same when the body is viewed from opposite sides. Thus, the difference between $\psi_o(-90)$ and $\psi_o(90)$ must be zero. A third equation can be formulated on the basis of this knowledge:

$$\psi_o(-90) - \psi_o(90) = 0 = \psi_m(-90) - \psi_m(90) - 4k \cos \beta/2 R \sin \rho \quad (4-16)$$

These three equations, 4-14, 4-15, and 4-16 are sufficient for determining ψ_c , R , and ρ for the case of any truncated cone (frustum or cylinder).

In the case of the frustum F5, the following values are desired for $\psi_o(\theta)$.

$$\psi_o(180) = 0$$

$$\psi_o(0) = -2kL\cos\beta/2$$

$$\psi_o(-90) - \psi_o(90) = 0$$

The data in Figure 4-9a illustrate the location of F5 which would produce these values in the absence of location and bias errors

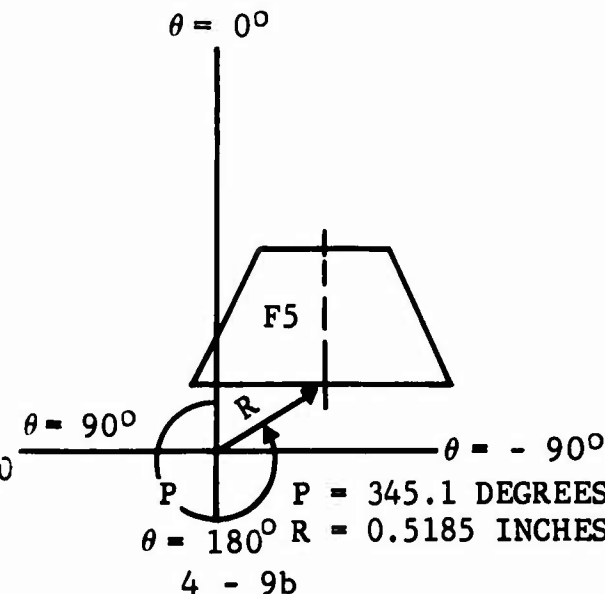
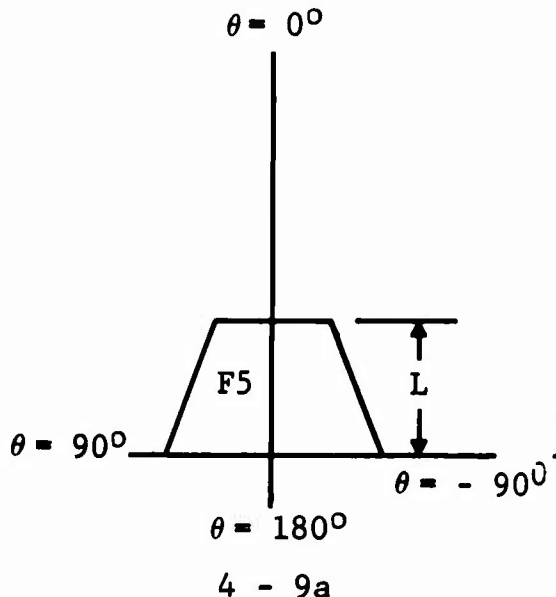


Fig. 4-9 POSITION ERRORS FOR MODEL F5

The following values can be obtained for the parameters β , f , and L for this frustum by reference to Table 2-1.

$$\beta = 10.25 \text{ degrees}$$

$$L = 7.421 \text{ inches}$$

$$f = 5.885 \text{ GHz}$$

Substitution of these values and the value of $\psi_0(0)$ for $\theta = \pm 90, 0, \text{ and } 180$ degrees into Equations 4-14, 4-15, and 4-16 results in

$$0 = \psi_m(180) - 2\frac{(360)}{\lambda} \cos(5.125) R \cos \rho + \psi_c \quad (4-17)$$

$$-2\frac{(360)}{\lambda} \cos(5.125)(7.421) = \psi_m(0) + 2\frac{(360)}{\lambda} \cos(5.125) R \cos \rho + \psi_c \quad (4-18)$$

$$0 = \psi_m(-90) - \psi_m(90) - 4\frac{(360)}{\lambda} \sin(5.125) R \sin \rho \quad (4-19)$$

Subtraction of Equation 4-18 from Equation 4-17 results in the equation

$$2\frac{(360)}{\lambda} \cos(5.125)(7.421) = \psi_m(180) - \psi_m(0) - 4\frac{(360)}{\lambda} \cos(5.125) R \cos \rho \quad (4-20)$$

which can be solved simultaneously with Equation 4-19 to obtain R and ρ .

In order to solve Equations 4-19 and 4-20, the values of

$$[\psi_m(180) - \psi_m(0)] \text{ and } [\psi_m(-90) - \psi_m(90)]$$

must be determined from analysis of the measured phase patterns. This pattern is illustrated in Figure 4-10a with the pertinent features slightly exaggerated. From this pattern, it will be noted that the measured phase center is furthest away from the radar when $\theta = 180$ and

closest to the radar when $\theta = 0^\circ$. A difference

$$\psi_m(180) - \psi_m(0) = 47 + 8(360) + 84 = 3011$$

degrees is obtained by noting the total change in phase between 180 and 0 degrees. The change in phase between $\theta = -90$ and $\theta = 90$ degrees is observed to be -90 degrees, the minus sign indicating that the phase center is closer to the radar at $\theta = -90$ degrees than at $\theta = 90$ degrees. Substitution of these differences into Equations 4-19 and 4-20 gives

$$R = 0.5185 \text{ inches}$$

and

$$\rho = 345.1 \text{ degrees}$$

The actual position of F5 is illustrated in Figure 4-9b.

The data in Figure 4-10b show the phase which would be obtained if the radius arm error were removed by adding a phase term given by

$$2k \cos \beta/2 R \cos (\rho - 180 - \theta)$$

to the values of the measured phase. Since $\cos(\rho - 180 - \theta) = -\cos(\rho - \theta)$, it is evident that this factor could be used to effectively correct the position error. The phase plot resulting from the addition of this factor to $\psi_m(\theta)$ is shown in Figure 4-10b. However, the bias term, ψ_c , is still evident. Substitution of the values for R and ρ into

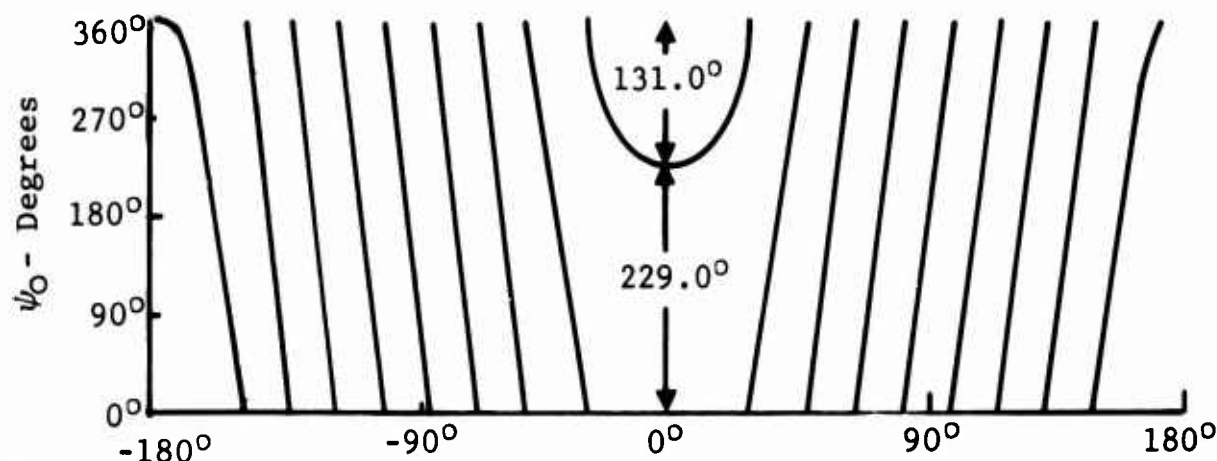


Fig. 4-10c PHASE WITH RADIUS ARM AND PHASE BIAS CORRECTION FOR MODEL F5

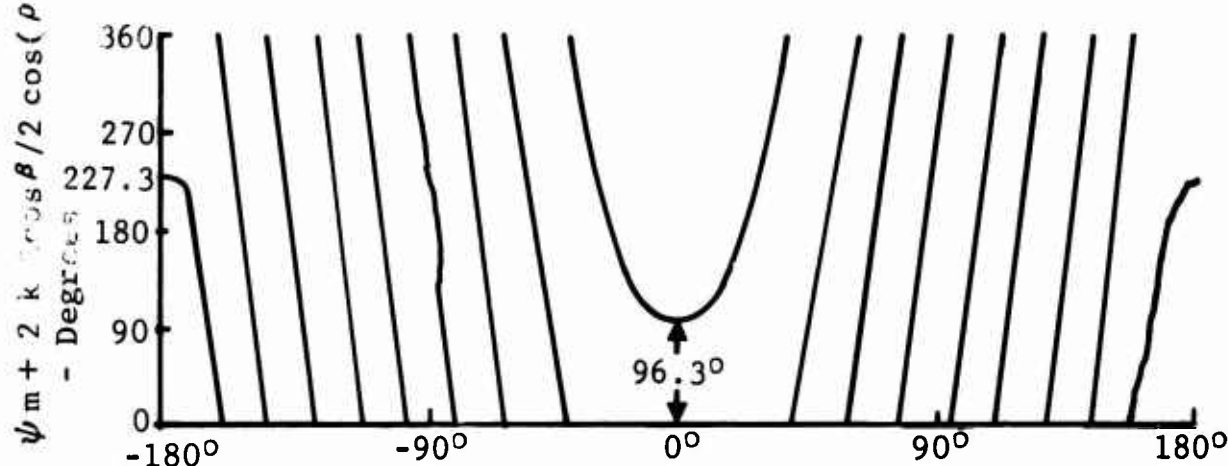


Fig. 4-10b PHASE WITH RADIUS ARM CORRECTION FOR MODEL F5

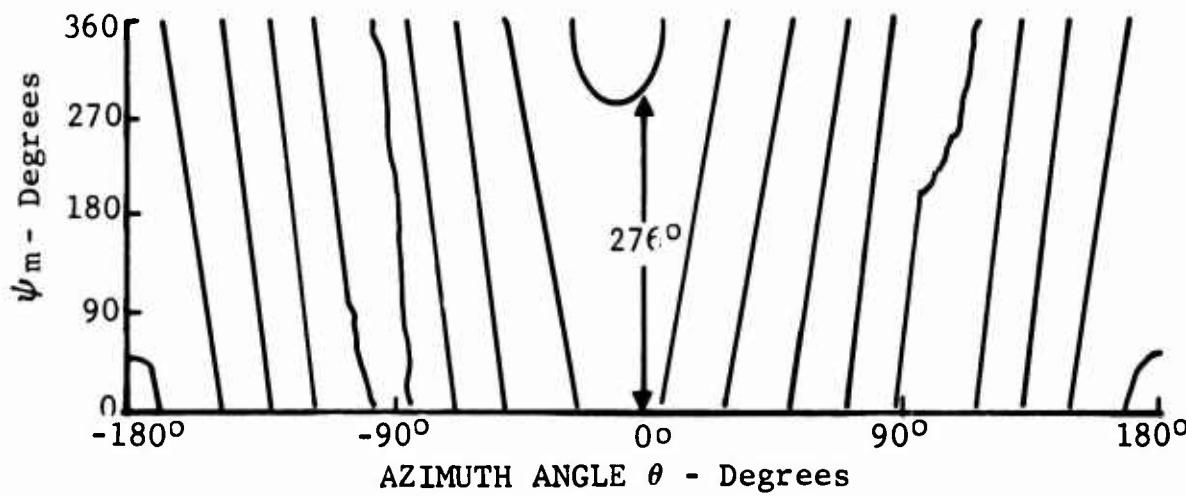


Fig. 4-10a MEASURED PHASE FOR MODEL F5

Equation 4-17 gives

$$\psi_c = 132.7 \text{ degrees.}$$

Addition of ψ_c to all values of

$$\psi_m(\theta) + 2k \cos \beta/2 R \cos (\rho - 180 - \theta)$$

gives the corrected plot shown in Figure 4-10c. Thus,

$\psi(180) = 0$ and $\psi(0) = 229.0$. The desired value for $\psi(0)$ was -2651.5 degrees or -131.5 degrees when this value is converted modulo 360 degrees. -131.5 degrees corresponds to 228.5 degrees in terms of the analog phase plot.

In order to simulate the measurement of a target at a position other than that where measurements are available, the measured phase is transformed by an additive term corresponding to a shift of the target to a new position defined by the polar vector (R', ρ') .

A simulated position shift and a position error correction can be accomplished in one step by determining the vector (D, δ) which is the difference between the error vector (R, ρ) and the desired position vector (R', ρ') . Thus,

$$D \cos \delta = R' \cos \rho' - R \cos \rho \quad (4-21)$$

$$D \sin \delta = R' \sin \rho' - R \sin \rho \quad (4-22)$$

The relationship between the vectors (R, ρ) , (R', ρ') , and (D, δ) is illustrated in Figure 4-11. In the case of simulating model F5CY5, the desired position of the reference point on F5 is given by the vector

(R', ρ') = (8.62, 0.0). Thus,

$$D \cos \delta = 8.62 - .503 = 8.117 \text{ inches}$$

$$D \sin \delta = 0 + .1259 = 0.1259 \text{ inches}$$

therefore,

$$D = 8.118 \text{ inches}$$

$$\delta = 0.89 \text{ degrees.}$$

The values of D , δ , and ψ_c are used as input parameters to transform the measured bistatic phase of Model F5 into the phase which is required for superposition of F5 onto the end of cylinder CY5 with CY5 centered over the center of rotation.

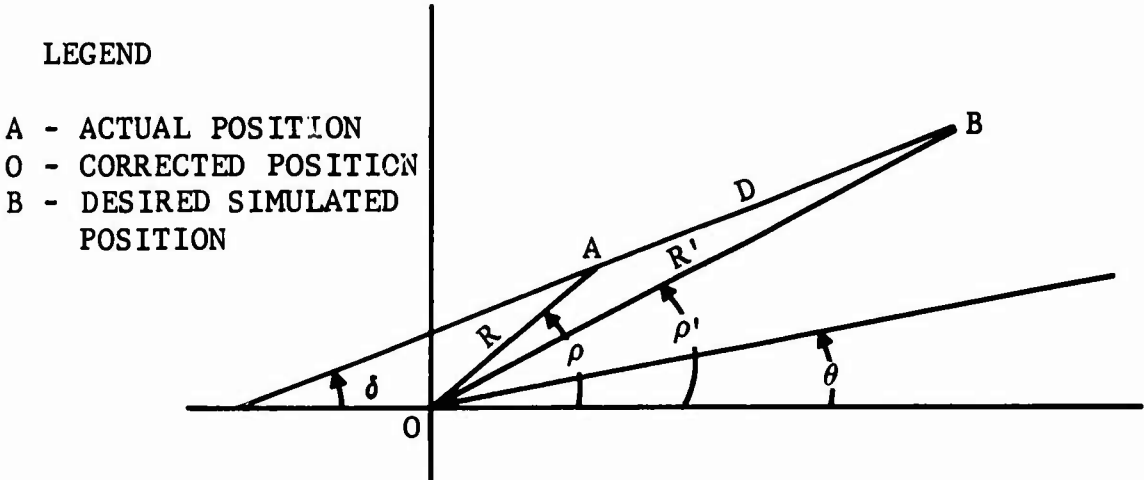


Fig. 4-11 GEOMETRICAL RELATIONSHIP BETWEEN LOCATION VECTORS

Since the centroid has been selected as the reference point on a cylinder, the phase error correction equations for a cylinder are

$$\psi_o(180) - \psi_o(0) = 0 = \psi_m(180) - \psi_m(0) - 4k R \cos \rho \cos \beta/2$$

$$\psi_o(-90) - \psi_o(90) = 0 = \psi_m(-90) - \psi_m(90) - 4k R \sin \rho \cos \beta/2$$

Analysis of the measured phase pattern of CY5 shown in Figure 4-12 gives

$$\psi_m(180) - \psi_m(0) = 8 - 32 = -24 \text{ degrees}$$

and

$$\psi_m(-90) - \psi_m(90) = 95 - 295 = -200 \text{ degrees}$$

Thus,

$$R \cos \rho = \frac{-24}{4k} = -0.0336$$

and

$$R \sin \rho = \frac{-200}{4k} = -0.2798$$

$$R = .2818 \text{ inches}$$

$$\rho = 263.8 \text{ degrees}$$

Substitution of R and ρ into Equation 4-17 gives the bias term

$$\psi_b = 4.0 \text{ degrees}$$

The actual position of CY5 during measurement is shown in Figure 4-13. In order to transform the measured phase of CY5 into position for superposition with F5, it should be noted that the desired position is given by

$$(R', \rho') = (0, 0) \text{ so that}$$

$$D = R = .2818 \text{ inches}$$

$$\delta = \rho - 180 = 83.8 \text{ degrees}$$

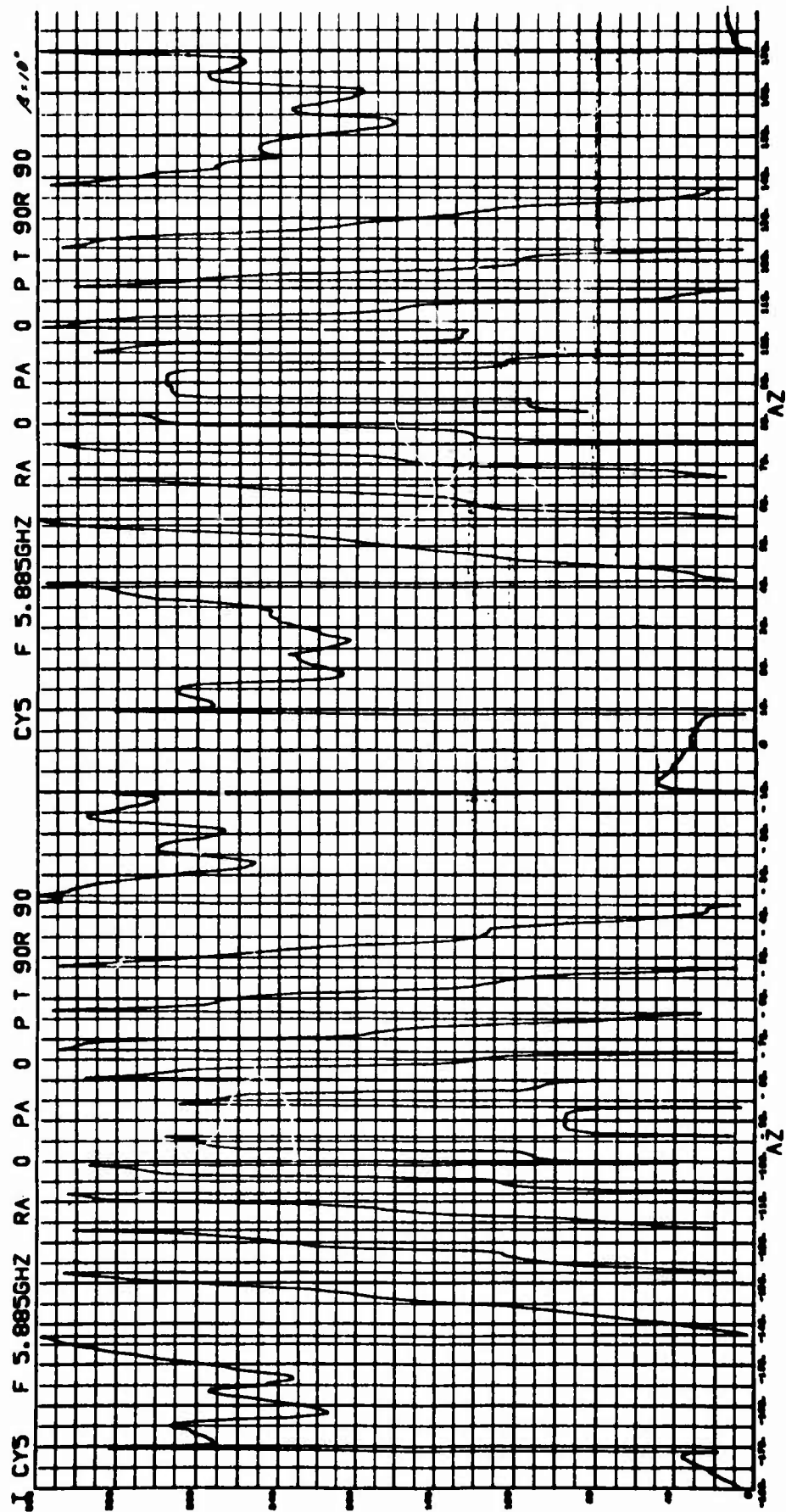


Fig. 4-12 PHASE FOR MODEL CY5 - VV POLARIZATION

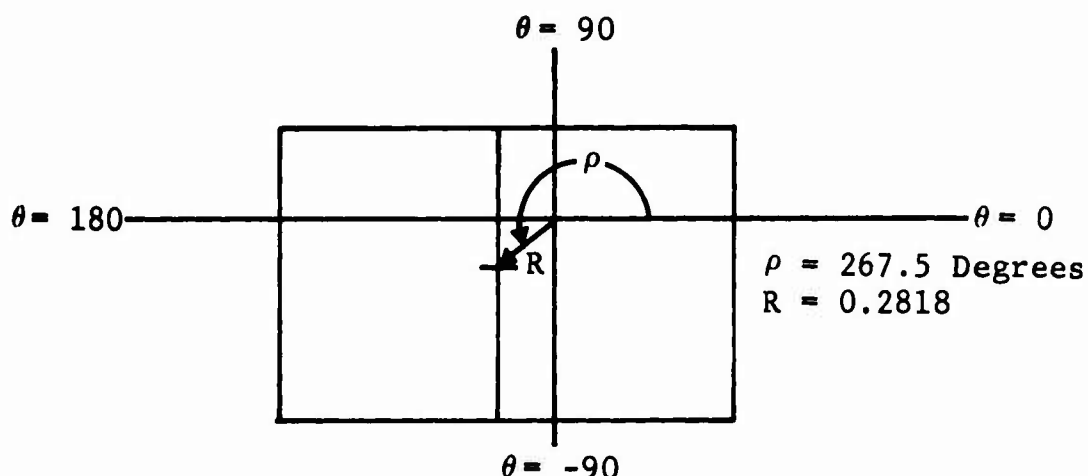


Fig. 4-13 POSITION ERRORS FOR MODEL CY5

In the foregoing discussion, it was assumed that all shifts would be accomplished without changing the direction of the axis of the body. A rotation of the target axis can also be simulated by adding a constant aspect angle to each value of the original aspect angle values. For example, if a value $\Delta\theta$ is subtracted from θ in $\psi(\theta)$ to obtain $\psi(\theta - \Delta\theta)$, the phase plot is simply shifted along the abscissa of Figure 4-12 by $\Delta\theta$ so that the original value of $\psi(\theta)$ would now occur at $\theta = \theta + \Delta\theta$. For example, a value of $\theta = 90$ degrees applied to the phase data of F5 would cause the closest point of approach (originally at $\theta = 0$ degree) to occur when $\theta = 90$ degrees. Figure 4-14 illustrates this example.

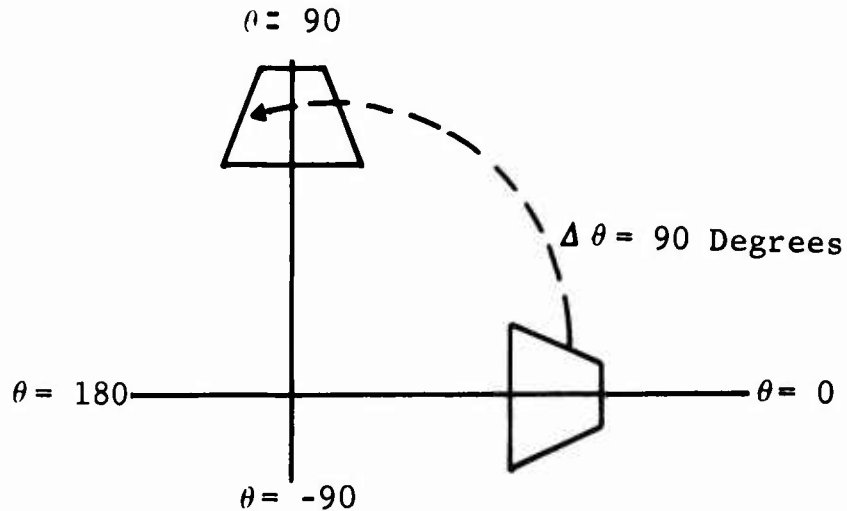


Fig. 4-14 ILLUSTRATION OF VEHICLE ROTATION

A shift of this type provides a means of simulating any position of a target by operations on its measured phase data.

When measured phase data has been transformed by use of D , δ , ψ_c , and $\Delta\theta$ to simulate the correct phase that would be measured with the target in its new position, this new value of phase is inserted into Equation 4-2 to initiate the process of superposition. Equation 4-23 is the same as Equation 4-2 except for the fact that aspect angle is included.

$$\sqrt{\sigma_S(\theta)} e^{j\phi_s(\theta)} = \sum_{i=1}^N \sqrt{\sigma_i(\theta - \Delta\theta_i)} e^{j\phi_i(\theta - \Delta\theta_i)} \quad (4-23)$$

where

$$\emptyset_i(\theta - \Delta\theta_i) = \psi_i(\theta - \Delta\theta_i) + \psi_{ic} + 2k \cos(\beta/2) D_i \cos(\delta_i - (\theta - \Delta\theta_i)) \quad (4-24)$$

The terms used in these equations are defined below:

i = designation of target component

$\sigma_i(\theta)$ = measured cross section for i^{th} target

$\psi_i(\theta)$ = measured phase for i^{th} target at aspect θ

$\emptyset_i(\theta - \Delta\theta_i)$ = phase for i^{th} for use in superposition

ψ_{ic} = phase bias error for i^{th} target

k = wave number

β = bistatic angle

D_i = radius arm required to move the reference point
of the i^{th} target to the desired position

δ_i = position angle of D_i

$\Delta\theta_i$ = aspect angle rotation required for i^{th} target

$\emptyset_S(\theta)$ = superposition phase

$\sigma_S(\theta)$ = superposition cross section

One additional consideration is necessary in order to
effectively superimpose target scattering measurements.

The discussion on coupling between discontinuities must also
be considered in terms of the shadowing of one component by
another. For example, the nose-on aspect of the Cylinder
CY5 is completely shadowed by the frustum F5 when the two
vehicles are connected to form F5CY5. Therefore, it would
not be reasonable to superimpose their respective measurements

near the nose-on aspect. Thus, there is a region, i.e., a "shadow" region centered about $\theta = 0$ degree where the measurements for F5 only should be used. Similarly, near $\theta = 180$ degrees, the back face of F5 is shadowed by CY5 so that a shadow region also exists about $\theta = 180$ degrees. Figure 4-15 is an illustration of these shadow regions.

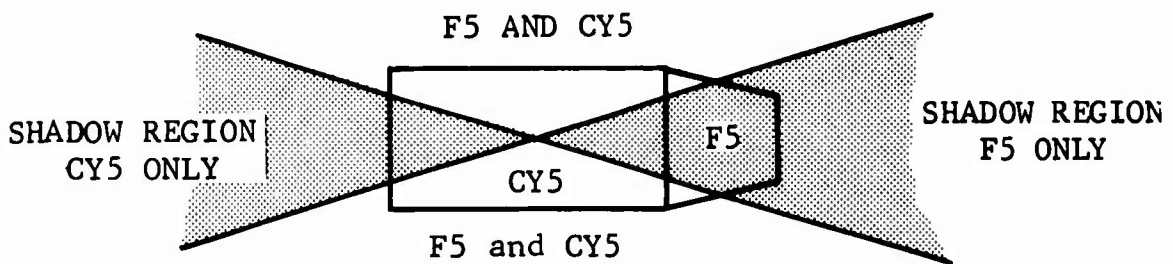


Fig. 4-15 ILLUSTRATION OF SHADOW REGIONS FOR MODEL F5CY5

The use of shadow regions does not eliminate coupling effects; however, it does eliminate the unreasonable errors which would exist if the shadow regions were not used. The primary coupling effect which should be evident in the case of F5 and CY5 is due to the fact that, in the case of superposition, the ring discontinuities at the junction of the targets will be evident only during superposition.

Figure 4-16 contains a flow diagram of the procedures necessary to obtain all parameters which are needed to superimpose a set of targets.

Figure 4-17 contains a logic diagram of the computer program subroutine which is used to superimpose a set of targets.

Figures 4-18 through 4-25 contain analog plots of measured and computed cross section and phase data obtained on Model F5CY5 at a frequency of 5.885 gigahertz and a bistatic angle of 10.25 degrees. Shadow regions of ± 30 degrees on each side of the nose-on and tail-on aspect orientations were utilized. Therefore, the actual process of superposition was utilized over the two aspect regions encompassing 60 degrees on each side of the broadside aspects.

An examination of the cross section patterns in these figures shows a remarkable agreement between the measured and computed values of cross section over a large aspect region. The effects of the ring discontinuities which would be observed at $\theta = 0$ degree and $\theta = 180$ degrees are not evident in these figures, as a result of the large value of cross section exhibited by the flat faces of the frustum and cylinder.

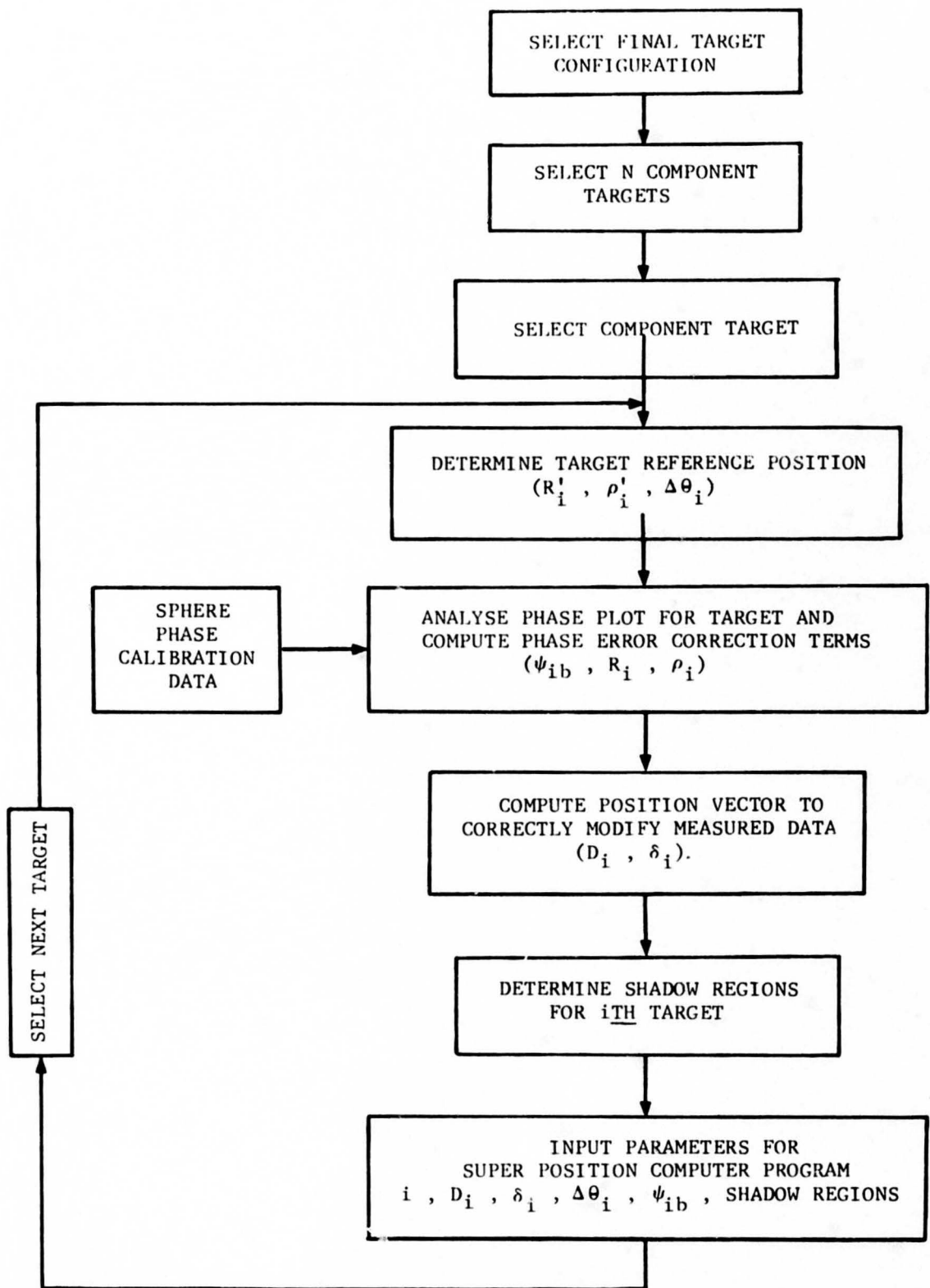


Fig. 4-16 FLOW DIAGRAM OF SUPERPOSITION PROCESS

INPUT PARAMETERS

N - Number of Shapes

I_n - Aspect Shift for n^{th} shape

K_n - Number of Shadow Regions for n^{th} shape

(I_{nk1}, I_{nk2}) - Initial and final aspect angles for k^{th} shadow region and n^{th} shape

D_n - Phase center location radius arm for n^{th} shape

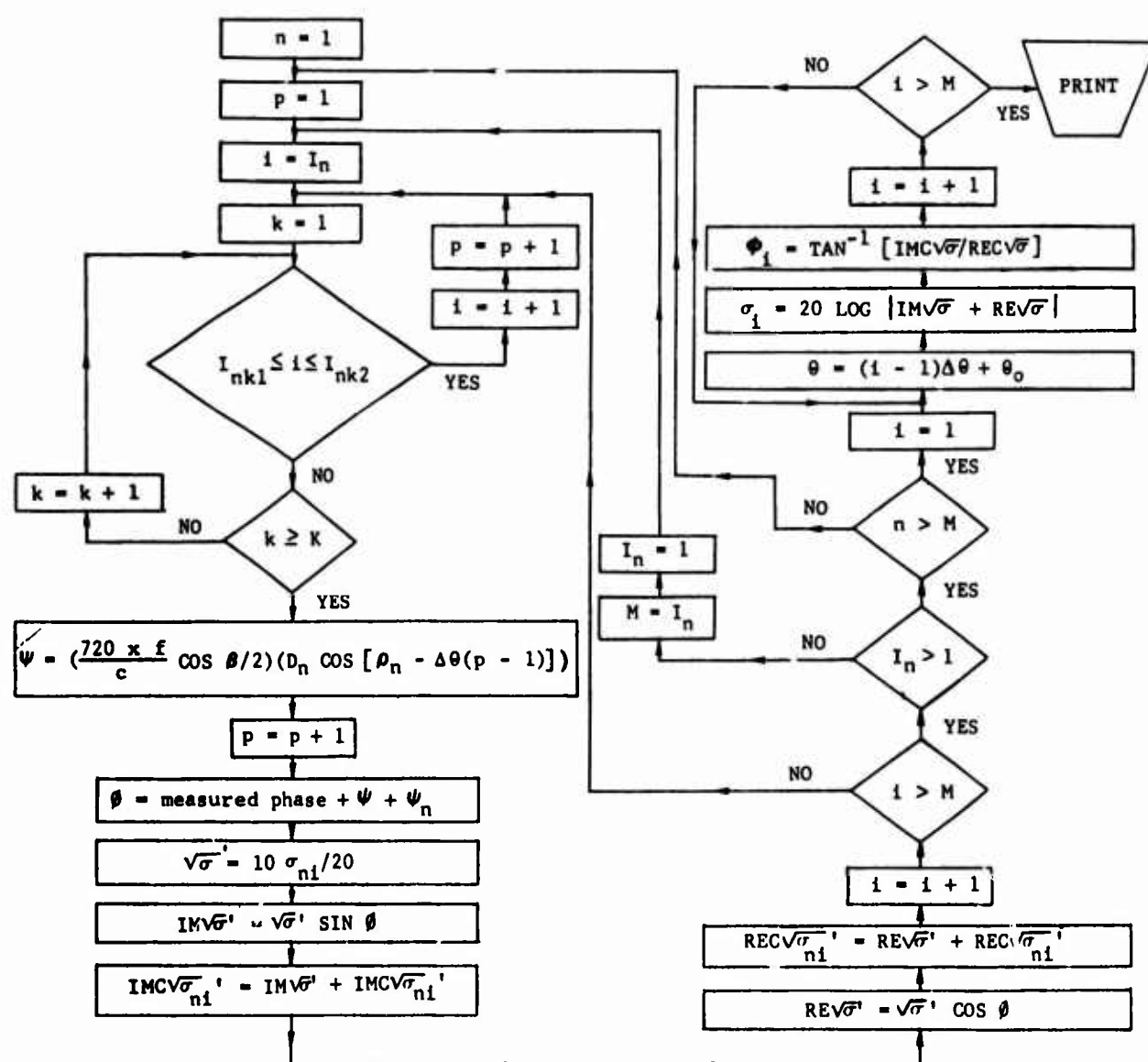
ρ_n - Phase center location position angle for n^{th} shape

M - Number of data points

f - Frequency in GHz

Ψ_n - Phase bias for absolute correction of phase center for n^{th} shape

$\Delta\theta$ - Increment on θ for computation



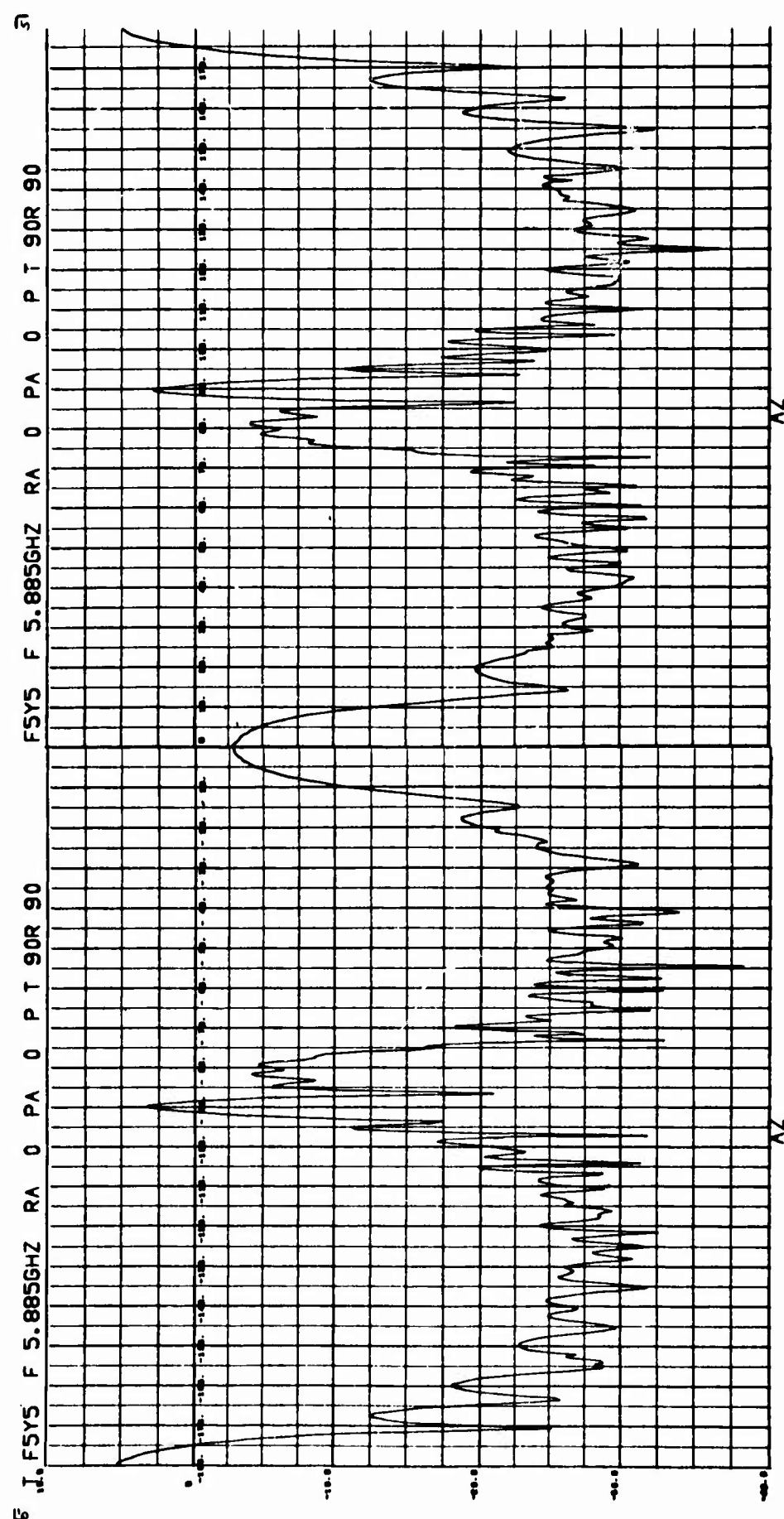


Fig. 4-18 MEASURED CROSS SECTION FOR MODEL F5CY5 - VV POLARIZATION

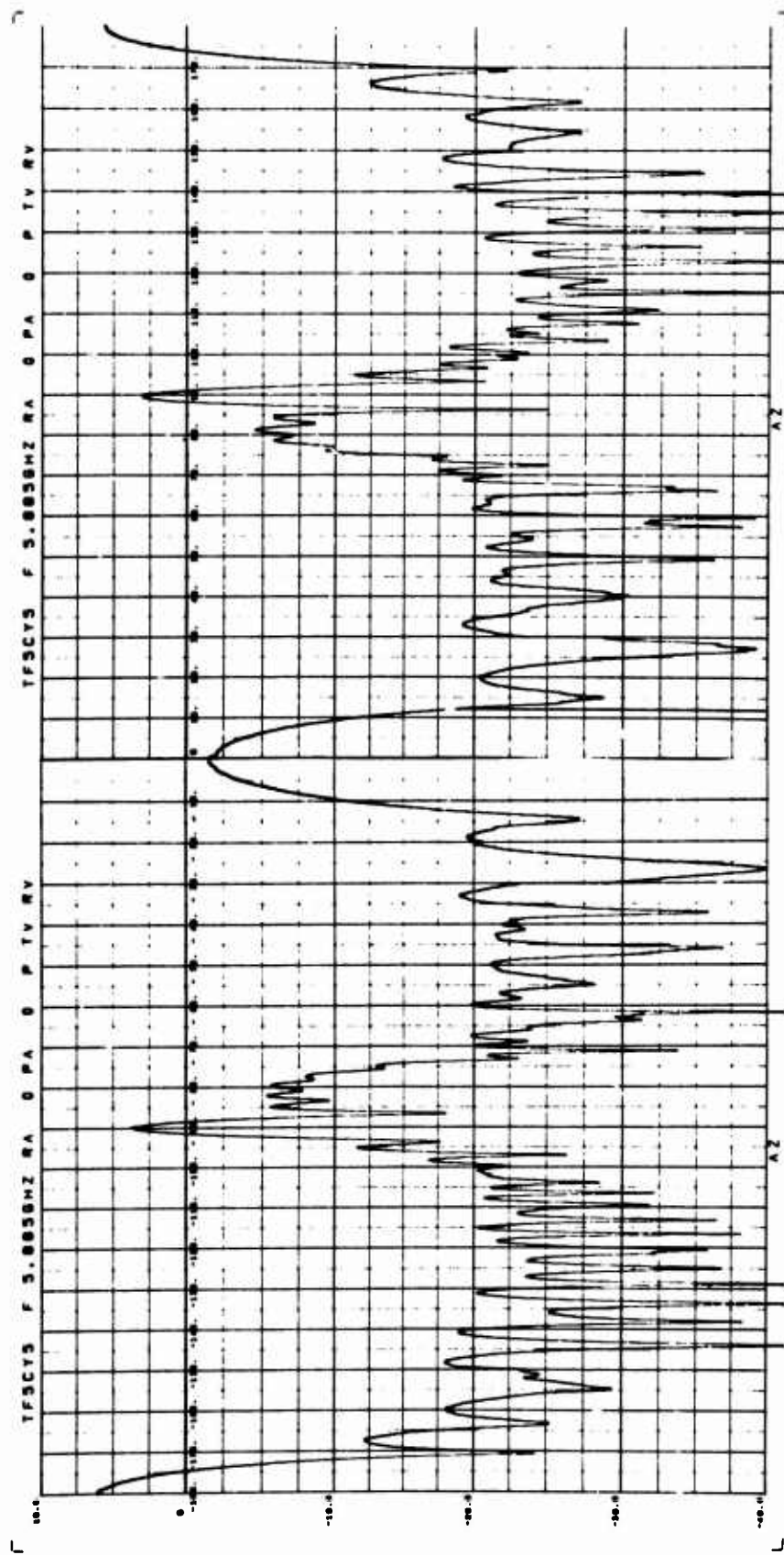


Fig. 4-19 COMPUTED CROSS SECTION FOR MODEL F5CY5 - VV POLARIZATION

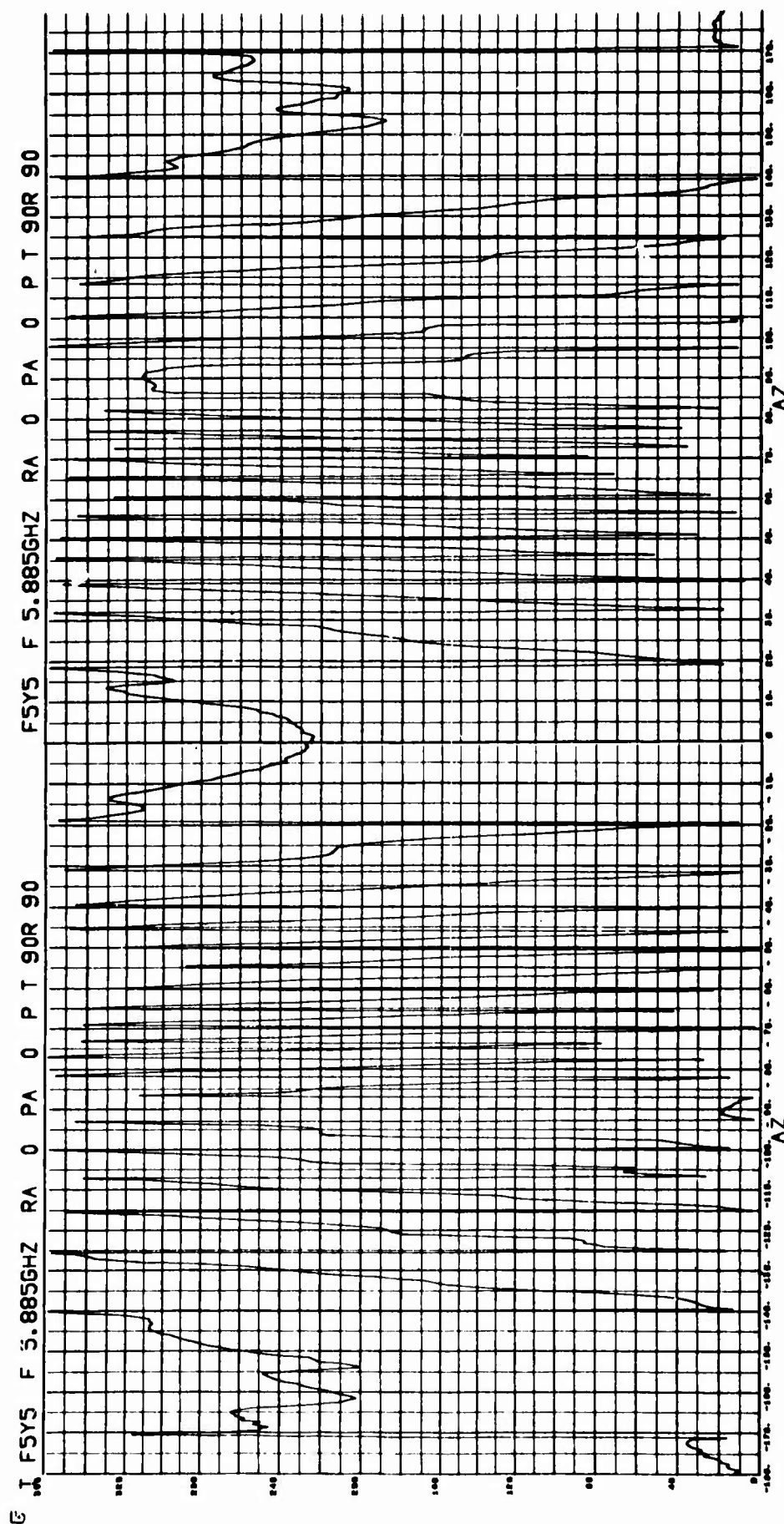


Fig. 4-20 MEASURED PHASE FOR MODEL F5CY5 - VV POLARIZATION

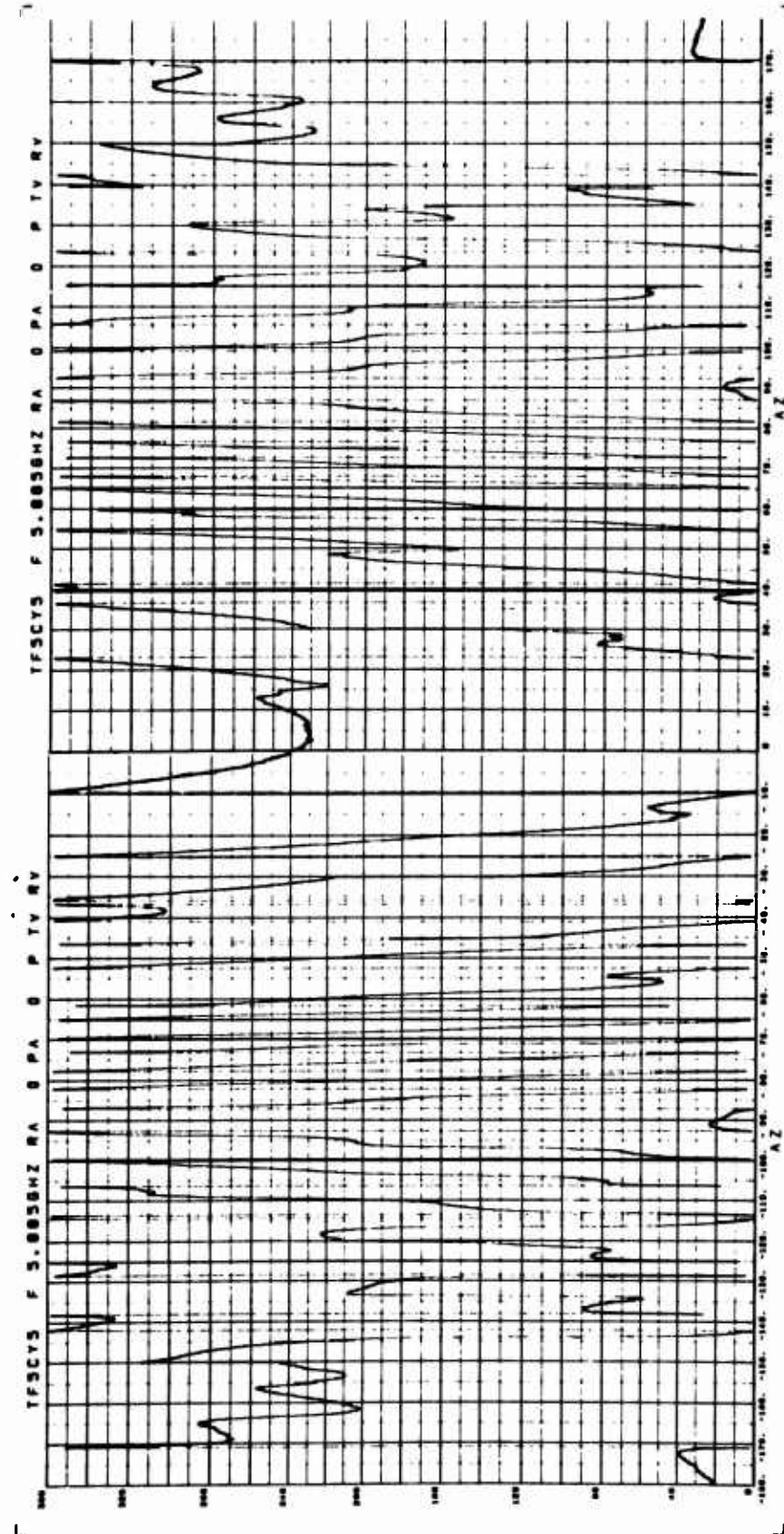
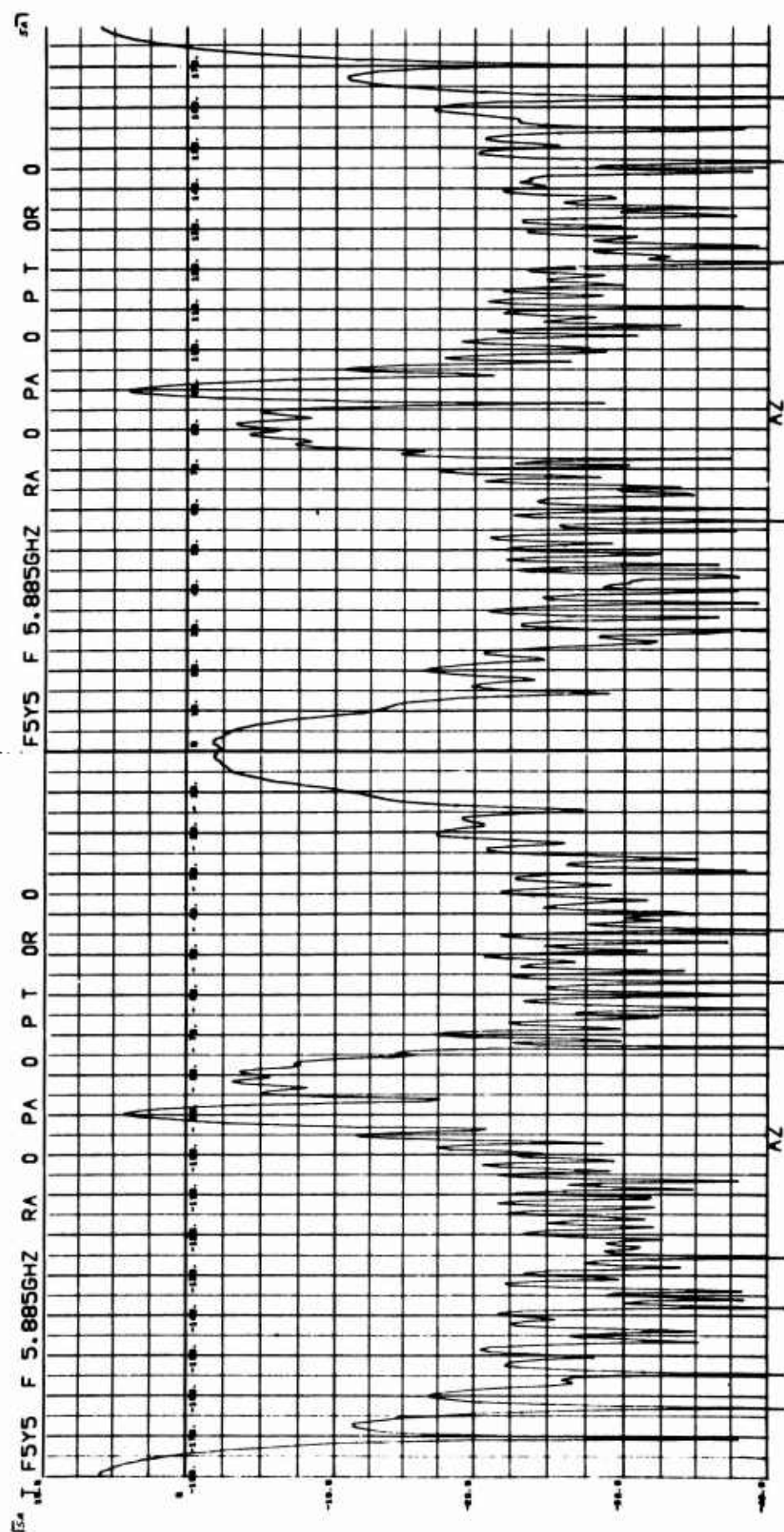


Fig. 4-21 COMPUTED PHASE FOR MODEL F5CY5 - VV POLARIZATION



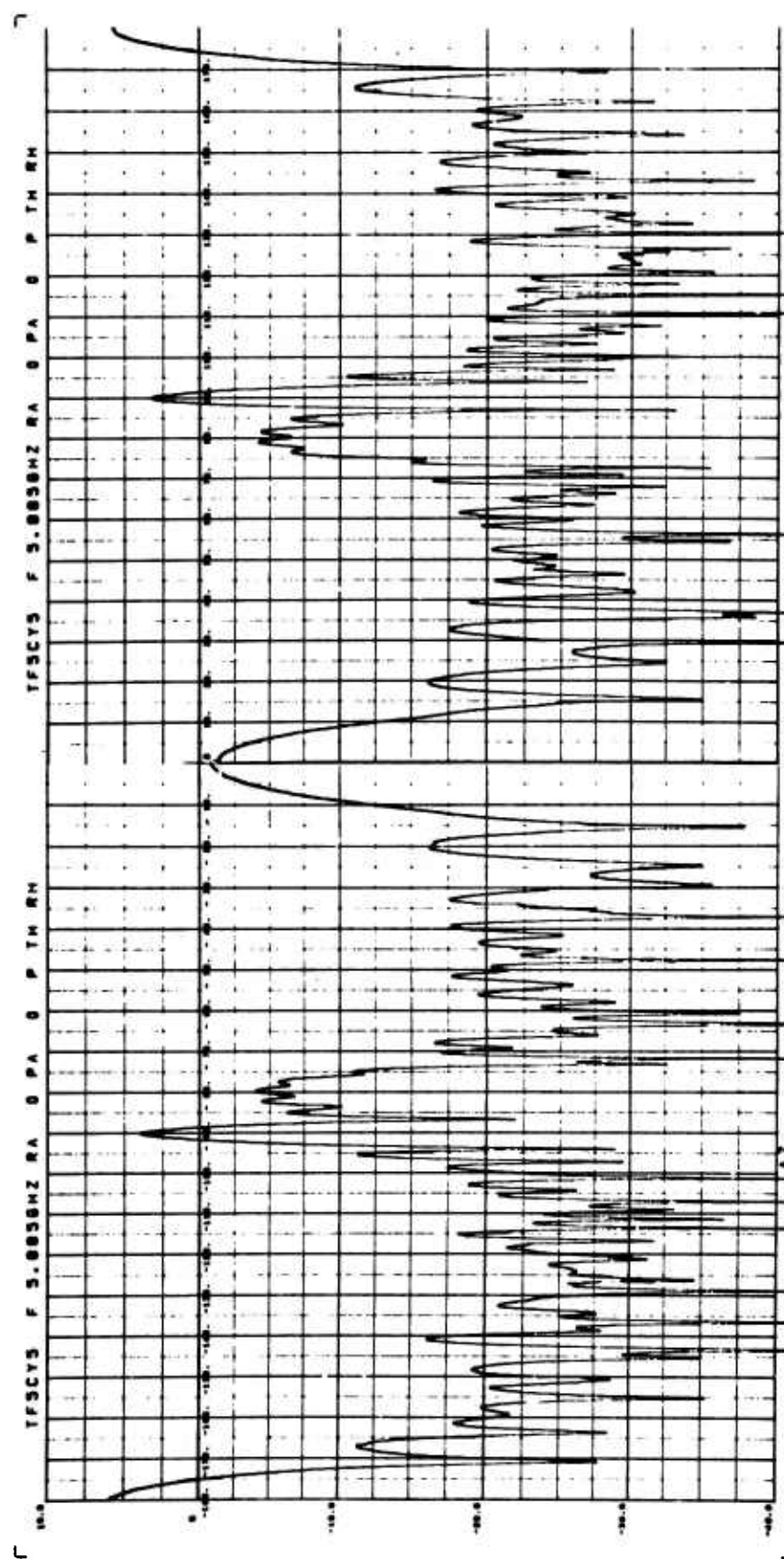


Fig. 4-23 COMPUTED CROSS SECTION FOR MODEL F5CY5 - HH POLARIZATION

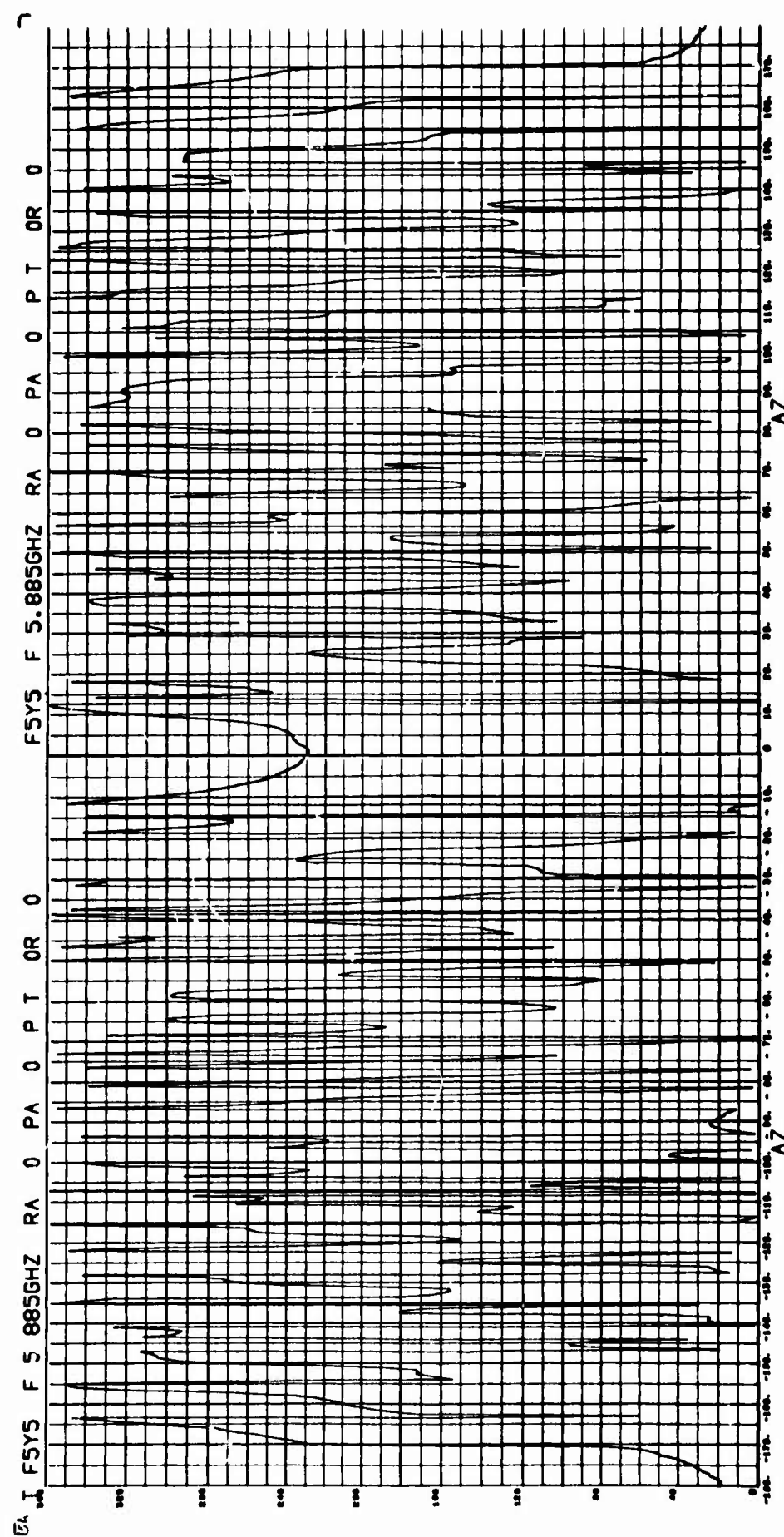


Fig. 4-24 MEASURED PHASE FOR MODEL F5CY5 - HH POLARIZATION

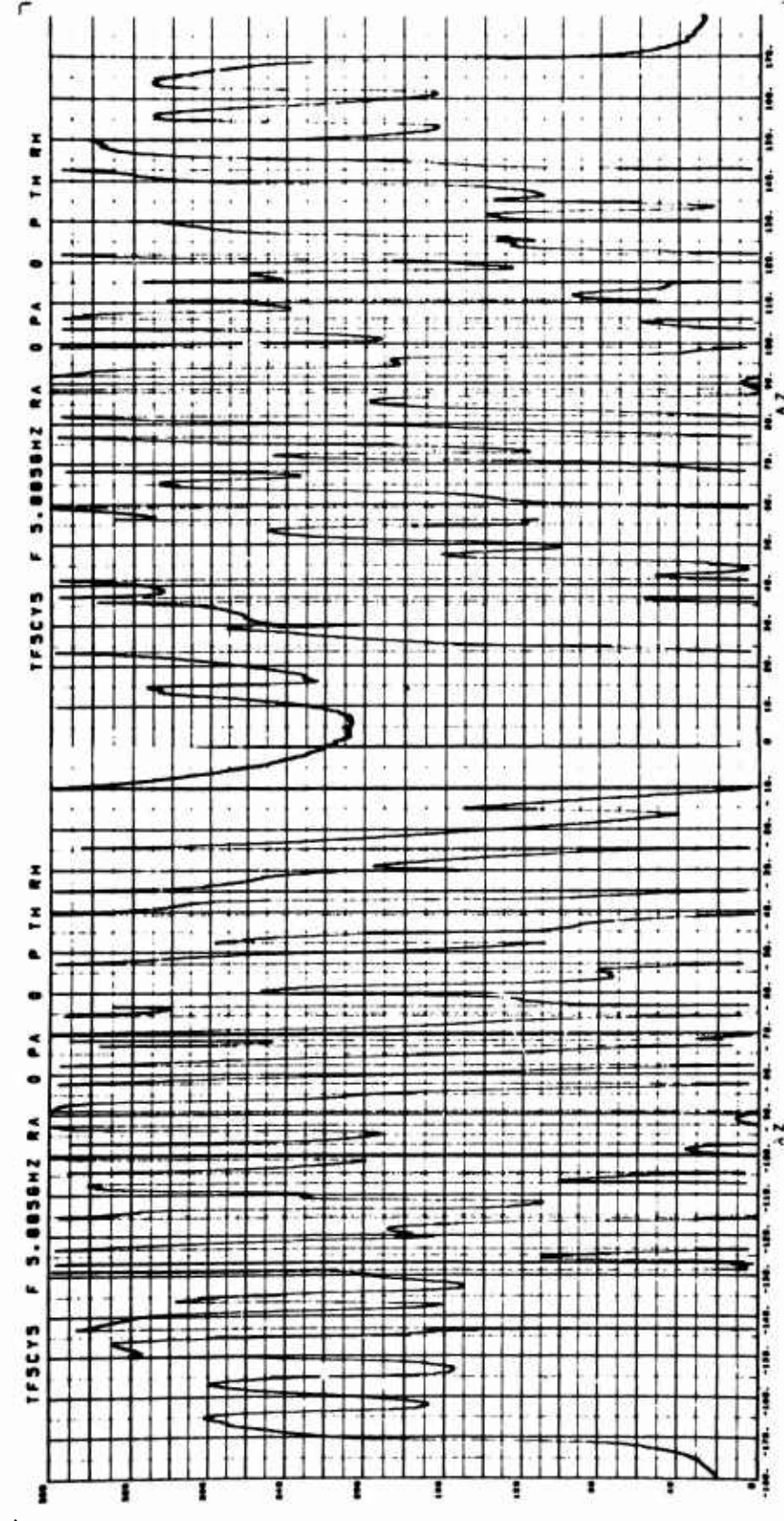
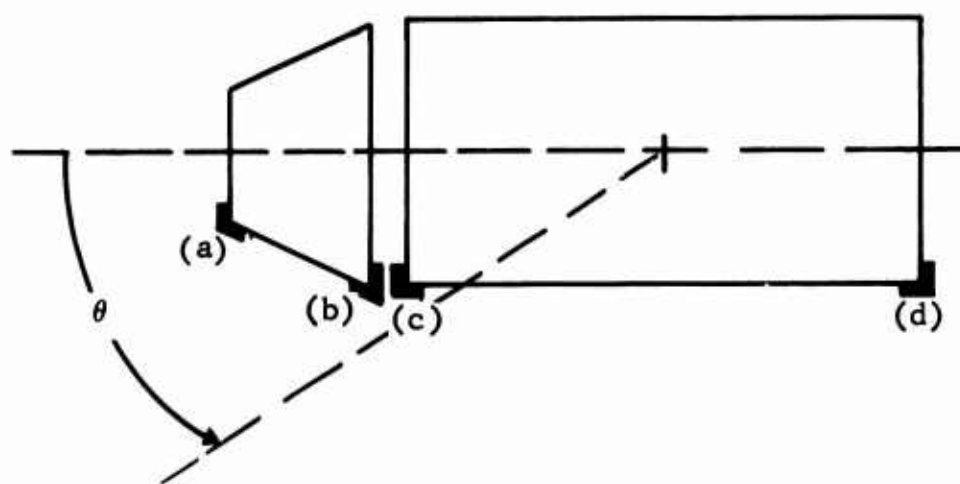


Fig. 4-25 COMPUTED PHASE FOR MODEL F5CY5 - HH POLARIZATION

Near broadside to the cylinder, exceptionally good agreement is observed. Only in the regions between the end-on and broadside aspects are significant errors observed. These errors can be attributed to coupling effects at the interface of F5 and CY5. These effects are illustrated in Figure 4-26.

Even if it could be assumed that scattering centers at (a), (b), (c), and (d) were the only scattering centers illuminated when $\theta \in (0, 180)$ degrees (\in signifies the fact that θ belongs to the interval between 0 and 180 degrees), the following phenomena would contribute to errors.

1. The amplitude of the superimposed scattering centers at (b) and (c) would not be the same as that which would be exhibited by the composite target.
2. The phase center for target F5 and that for CY5 will not in general be the same as that of the composite target. For example, for the case of $0 \leq \theta \leq 90$ degrees, the phase center at vertical polarization is essentially attached to point (a) on F5 in the case of F5 (Figure 4-26) and also for F5CY5. On the other hand, the phase center for the interval $0 \leq \theta \leq 90$, in the case of CY5 is usually at (c). The interaction of these two



**Fig. 4-26 ILLUSTRATION OF COUPLING AT THE
INTERFACE OF TWO VEHICLES**

phase centers during superposition should cause a greater deviation in phase than would be measured; it would also introduce errors away from specular regions. In addition, it would be expected that the superimposed data would exhibit deeper nulls than would be measured, at least in the region of greatest phase change. This is indeed observed in measurements of Model F5CY5 at both horizontal and vertical polarization.

The effects of coupling on phase are vividly demonstrated in Figure 4-27 in the case of vertical polarization. These plots show cumulative phase for both measured and computed cases. It will be recalled that the regions defined by $\theta \in (0, 30)$, $(150, 210)$, and $(330, 360)$ were shadow regions; examination of the data in this figure will indicate that the aspect regions of $\theta \in (30, 50)$, $(-30, -50)$, $(120, 150)$ and $(-120, -150)$ exhibit the greatest phase errors. Although the determination of cumulative phase from the phase plots which are originally plotted modulo 360 degrees is very tedious, and the results are sometimes quite ambiguous, the basic symmetry of these patterns in Figure 4-27 is an implication of their accuracy. The discontinuities in computed phase which occur at the junction of the shadow

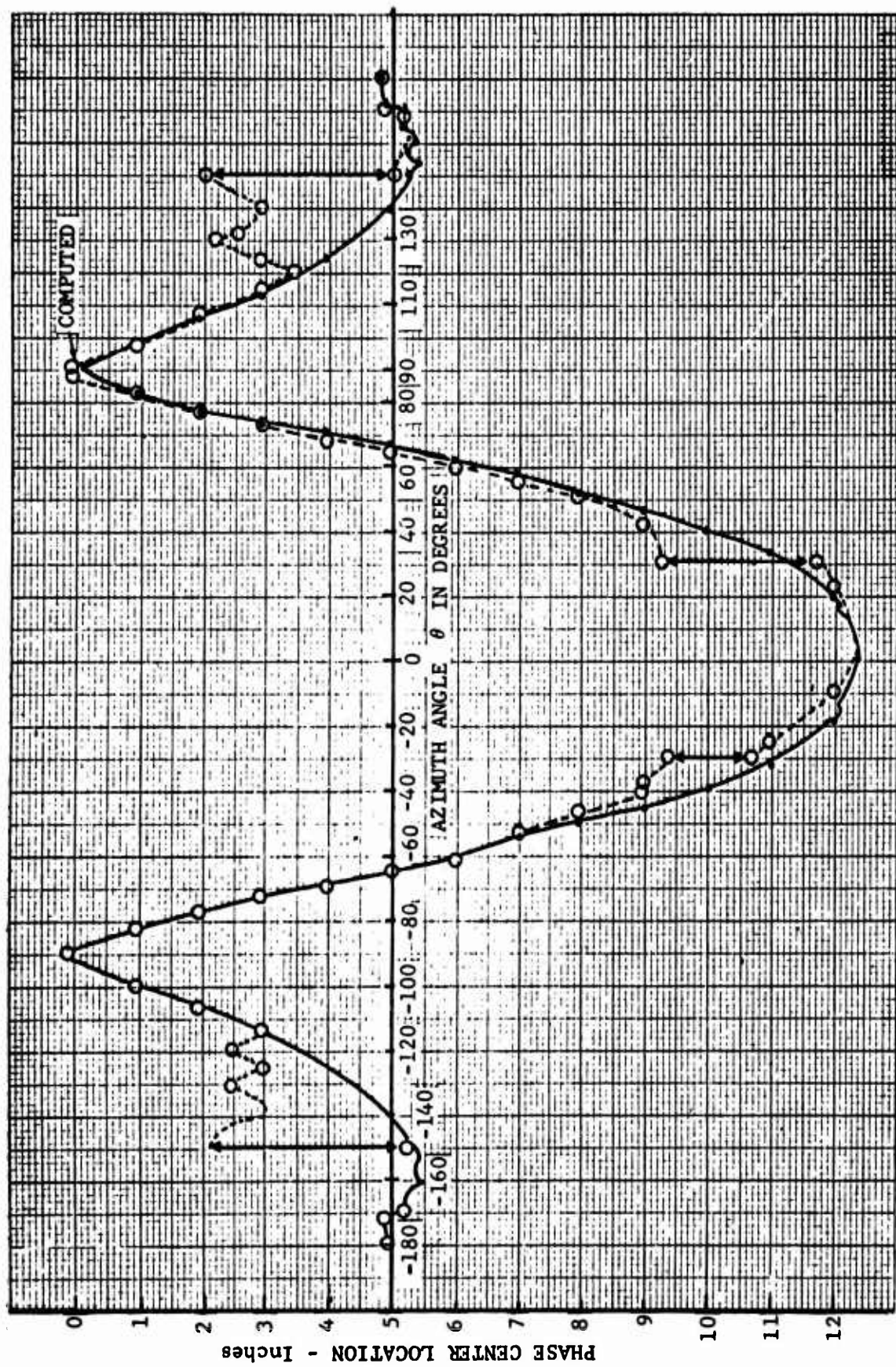


Fig. 4-27 MEASURED AND COMPUTED CUMULATIVE PHASE FOR MODEL F5CY5

regions were determined by assuming that the phase centers of the model and the composite occupy essentially the same position at $\theta = 0, 90, 180$, and 270 degrees.

The data in Figure 4-28 illustrates how the position of the measured and computed phase centers vary with aspect angle by plotting these terms on a polar plot superimposed on an outline scale drawing of the model. This illustration explicitly reveals the aspect regions where coupling effects are most detrimental. These regions are analyzed below:

1. $\theta \in (30, 50)$

In this region, the scattering center at (1) is dominant in the case of F5CY5 and the phase center tends to be located near this point for $\theta \in (0, 90)$. Some interaction between (1) and (3) and possibly (2) is observed in the cross section pattern; however, the small depths of the nulls indicate that this interaction is small. When F5 and CY5 data is superimposed in this region, a large amount of interaction is observed between the scatterer at (1) and those at (2) and (4) on the cylinder. The phase center is observed to be located between (1) and (2) in this region.

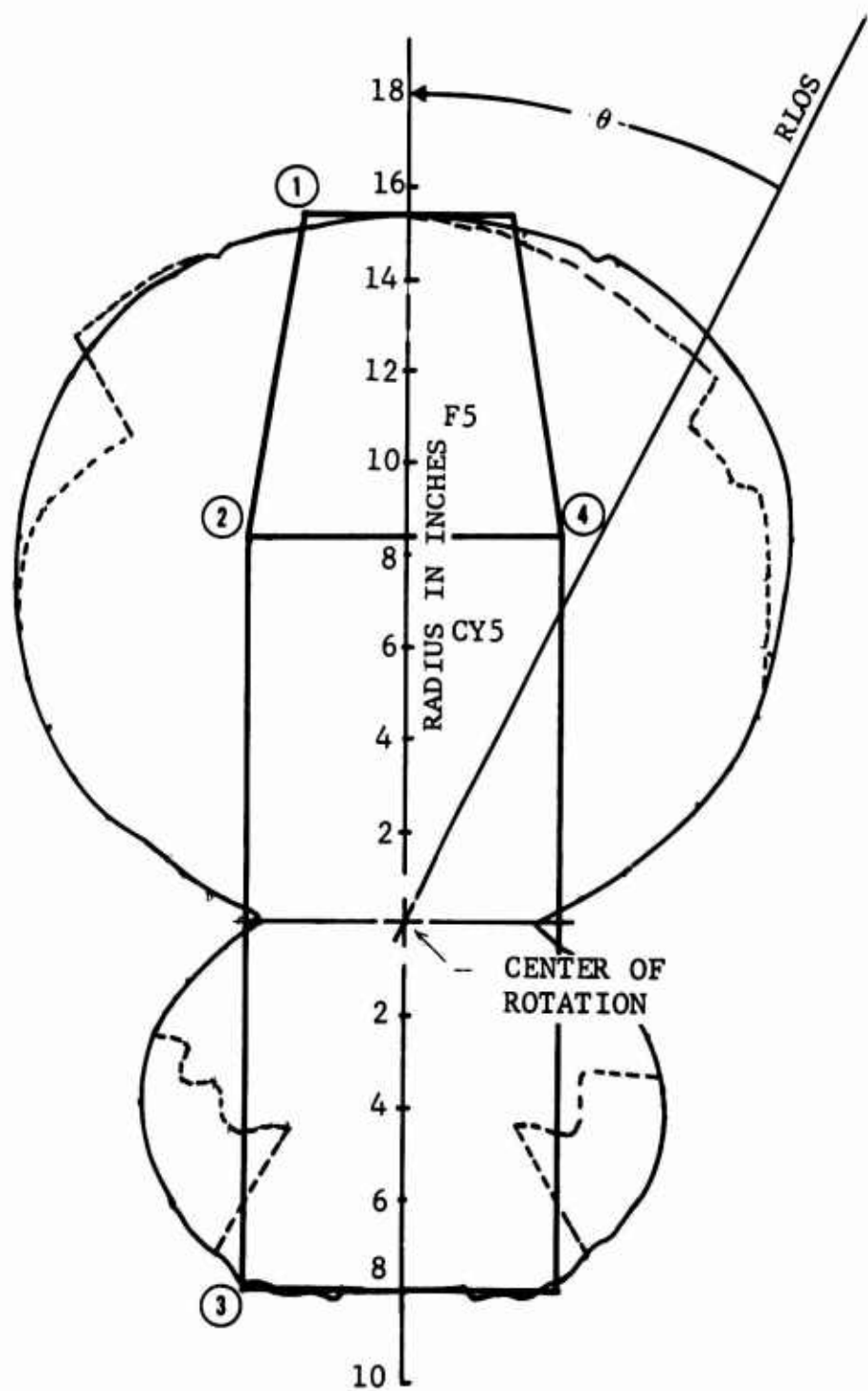


Fig. 4-28 MEASURED AND COMPUTED PHASE CENTER LOCATION FOR MODEL F5CY5 -VV POLARIZATION - POLAR PLOT

However, as the aspect angle is increased, the effect of the scatterer at (4) is diminished, and the phase center tends to approach the same position it occupied on the composite model.

2. $\theta \in (114, 150)$

In this region, the measured phase center tends to be associated with the position of the scatterer at (3). However, when F5 and CY5 are superimposed, the strong scatterers at (2) and (4) on the frustum cause the computed phase center to shift toward the frustum. When $\theta = 115$ degrees, the strength of the scatterer at (4) has diminished to the point where its effects are negligible.

Two important conclusions can be drawn from this analysis. In the first place, a large region exists where the results of superposition provide a quite accurate cross section and phase pattern. This result indicates that the scattering from scatterers which are located on the illuminated side of the target tends to be relatively free of coupling effects. In other words, the composite and the decomposed scattering from the illuminated discontinuity at (2) tends to be fairly similar. On the contrary, if a new scattering center is observed when the target is decomposed, severe errors may be observed in both cross section and phase.

This case is evident in the regions where the scatterer at (4) is illuminated when $\theta \in (0, 90)$. This scatterer would have no effect when F5CY5 was measured over this aspect region.

The results obtained in this investigation by using the remaining targets of interest are presented and discussed in Subsection 4.4

4.4 Superposition Results and Interpretation of Results

In addition to F5CY5, the superposition process was performed by using composite formulations of six other vehicles. These vehicles are described in Table 4-1. The specific values of the radar parameters and the position parameters describing the component surfaces related to the results presented herein are presented in separate tables in the following paragraphs.

The six vehicles which were processed to produce data for this analysis exhibit all of the features which need to be investigated in order to determine the range of applicability of superposition. These vehicles will be considered in the order of the difficulties encountered in interpreting the superposition results.

4.4.1 Model AC4

Table 4-2 contains the values of the pertinent superposition parameters associated with model AC4. This model

TABLE 4-1
SUPERPOSITION TARGETS

Composite Target Identification	Number of Component Surfaces
Frustum-Cylinder Model-F5CY5	2
Smooth Aerospace Model-A2	4
Smooth Aerospace Model-A3	3
Complex Aerospace Model-AC1	4
Complex Aerospace Model-AC4	4
Scientific Satellite Model-X1	4
Scientific Satellite Model-X2	6

Table 4-2 MODEL AC-4 SUPERPOSITION PARAMETERS

COMPOSITE MODEL	FREQUENCY GHZ	BISTATIC ANGLE DEGREES
AC-4	5.975	0.

GENERIC SURFACE	FREQ GHZ	POSITION ERROR				SUPERPOSITION PARAMETERS				SHADOW REGIONS			
		R INCHES	ρ DEGREES	D INCHES	δ DEGREES	$\Delta\theta$ DEGREES	ψ_c	θ_{11}	θ_{12}	θ_{21}	θ_{22}	θ_{31}	θ_{32}
								θ_{11}	θ_{12}	θ_{21}	θ_{22}	θ_{31}	θ_{32}
F2CY5F3	5.975	0.012	180.	0.0	0.0	0.	-32.	0.1	40.	140.	220.	320.	360.
F1	5.975	0.365	183.4	24.43	180.	0.	19.	150.	210.				
P1F4CY3	5.975	0.134	180.	15.95	0.	0.	85.	0.1	40.	320.	360.		
CY2	5.975	0.0	0.0	16.15	180.	0.	-82.	0.1	40.	140.	220.	320.	360.

has been designated as a complex aerospace model as a result of its use in another study; however, it may also be considered to be a smooth aerospace vehicle since it is a body of revolution.

Figures 4-29 through 4-39 contain plots of measured and computed cross section and phase for the VV and HH polarization conditions of Model AC4. Excellent agreement is obtained in the case of VV except in the regions near ± 135 degrees where the computed cross section is lower and more varied than the measured cross section. This region of rather slowly varying cross section in the measured case is a result of scattering from the region near the interface of F1 and CY2. This result will be further discussed below.

A comparison of measured and computed phase is extremely difficult in the case of such models as AC4 which are very long with respect to wavelength (approximately 26 wavelengths one way). Figure 4-33 contains a plot of cumulative phase of Model AC4 although the exact behavior of measured phase in the aspect intervals (50, 70) and (-50, -70) degrees cannot be determined. The position of the measured phase center in space is plotted in Figure 4-34 in polar coordinates, superimposed on a scale drawing of the target model. It is immediately evident

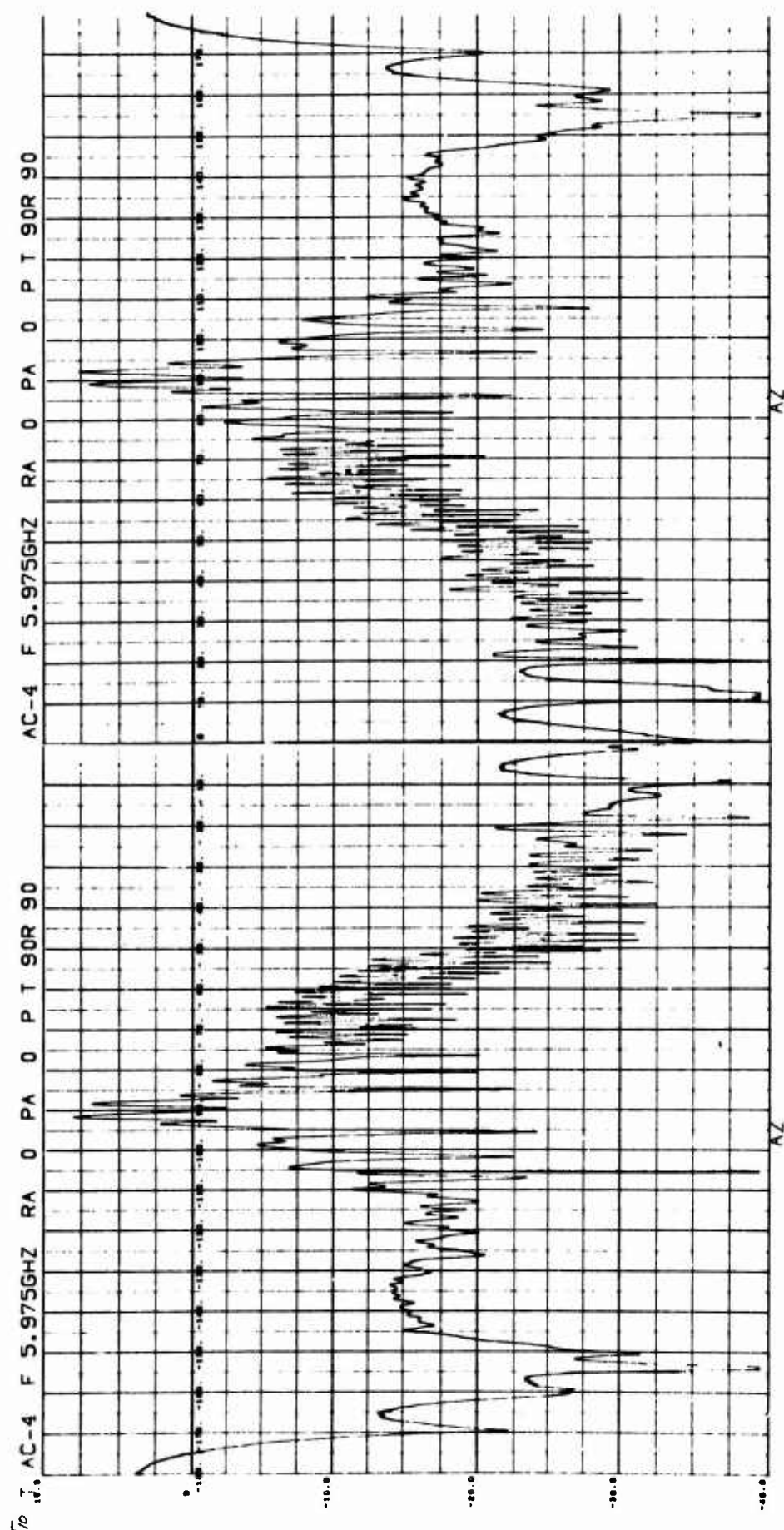


Fig. 4-29 MEASURED CROSS SECTION FOR MODEL AC-4 - VV POLARIZATION

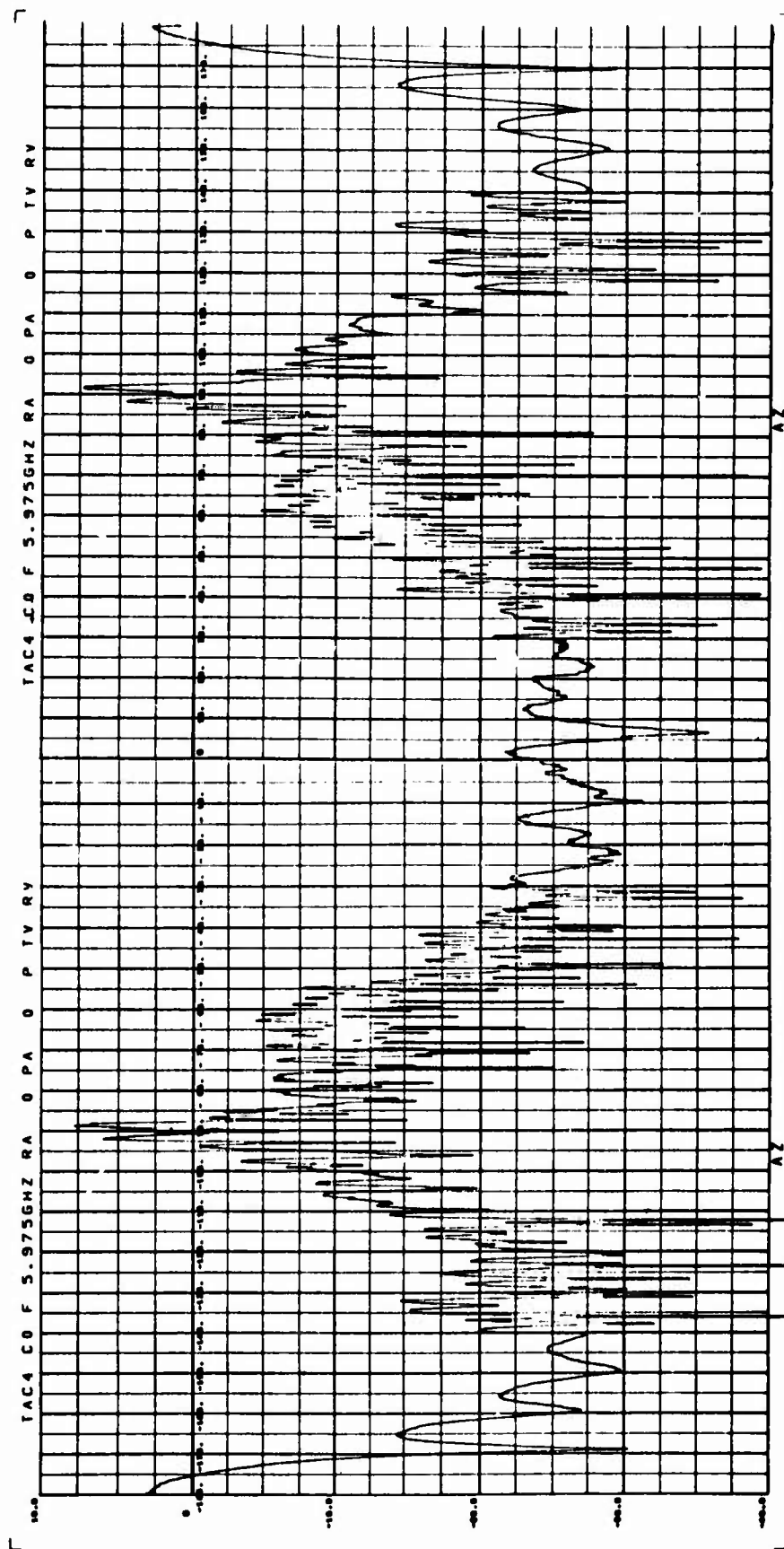


Fig. 4-30 COMPUTED CROSS SECTION FOR MODEL AC-4 - VV POLARIZATION

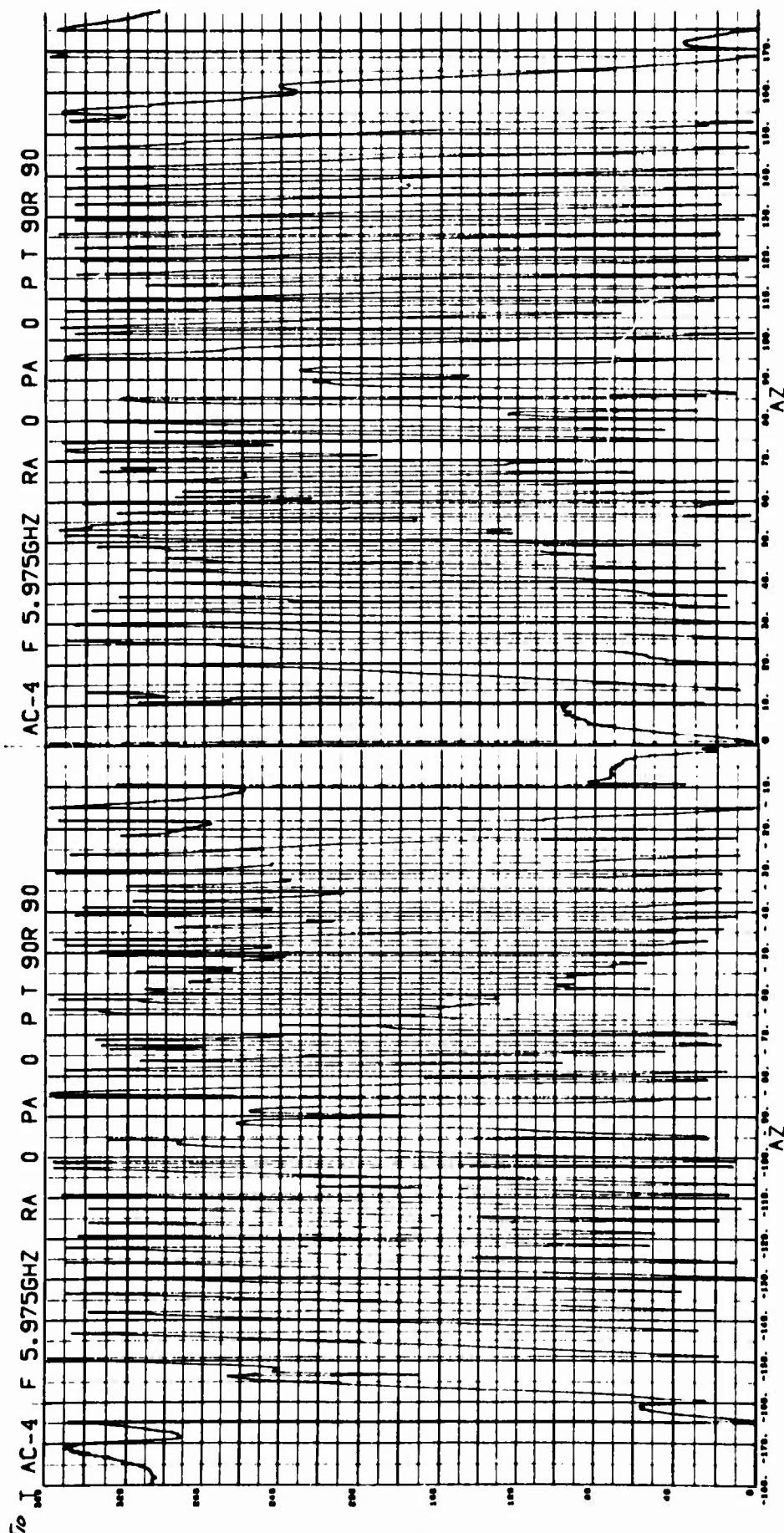


Fig. 4-31 MEASURED PHASE FOR MODEL AC-4 - VV POLARIZATION

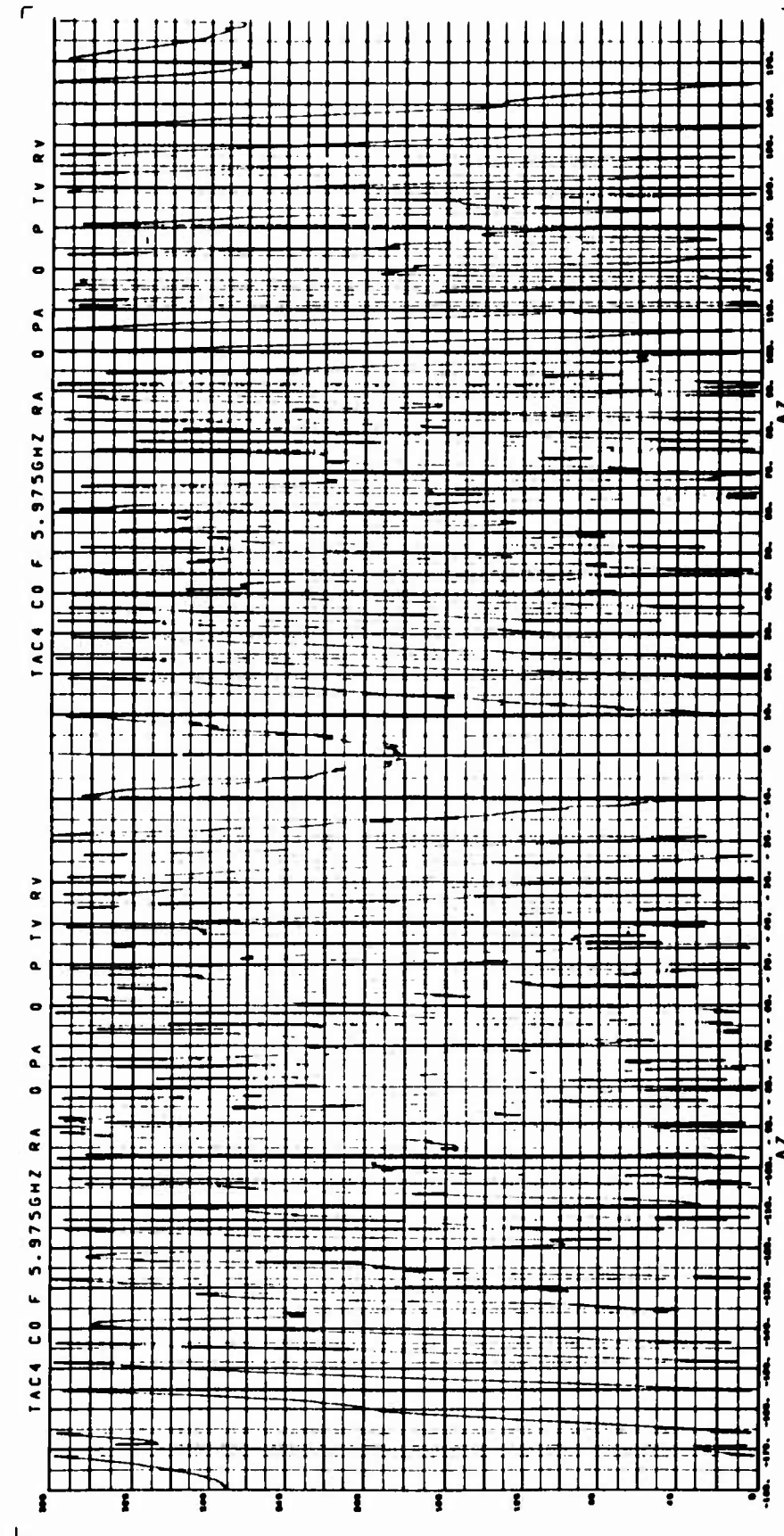


Fig. 4-32 COMPUTED PHASE FOR MODEL AC-4 - WV POLARIZATION

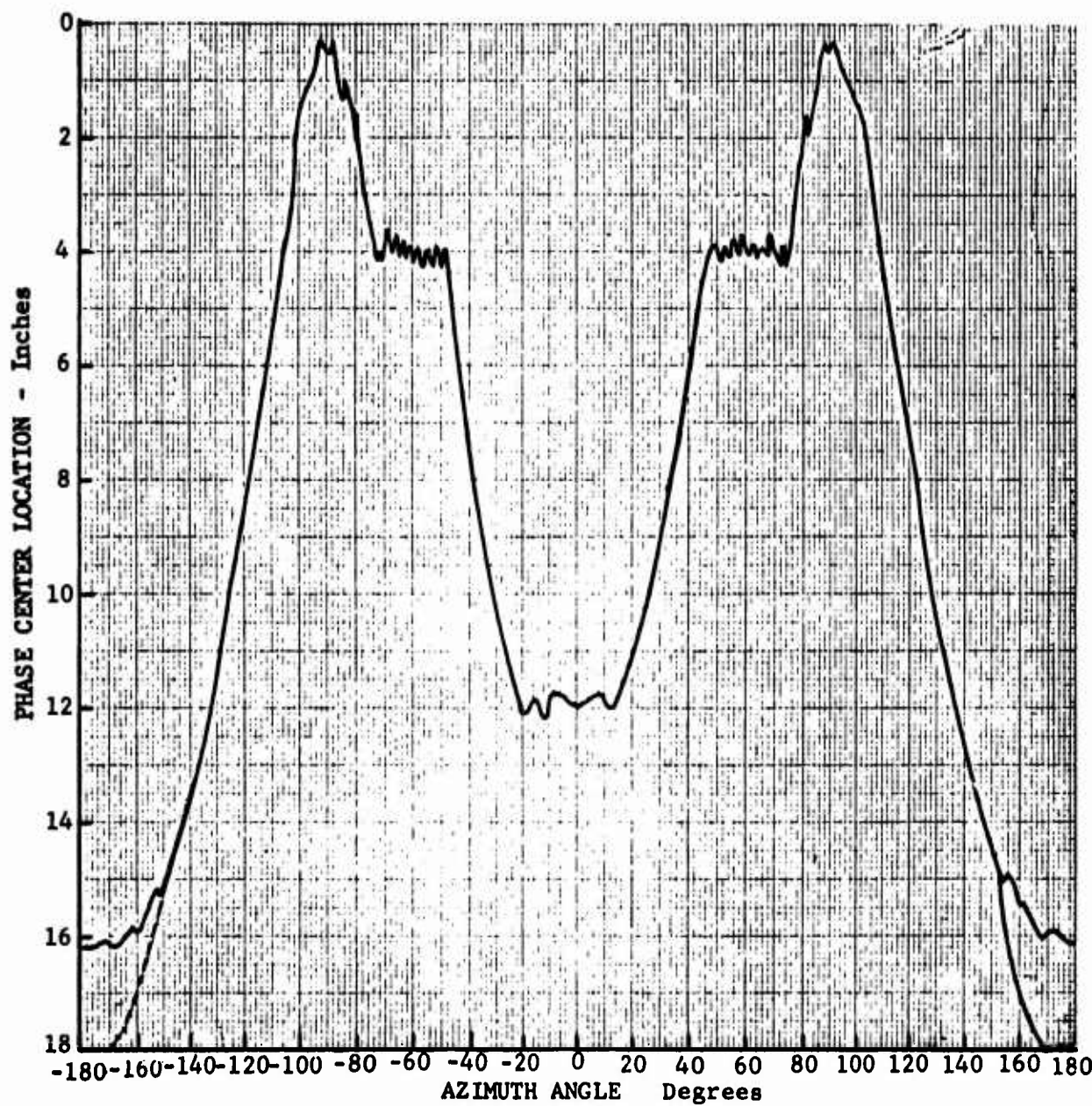


Fig. 4-33 CUMULATIVE PHASE FOR MODEL AC-4 - VV POLARIZATION

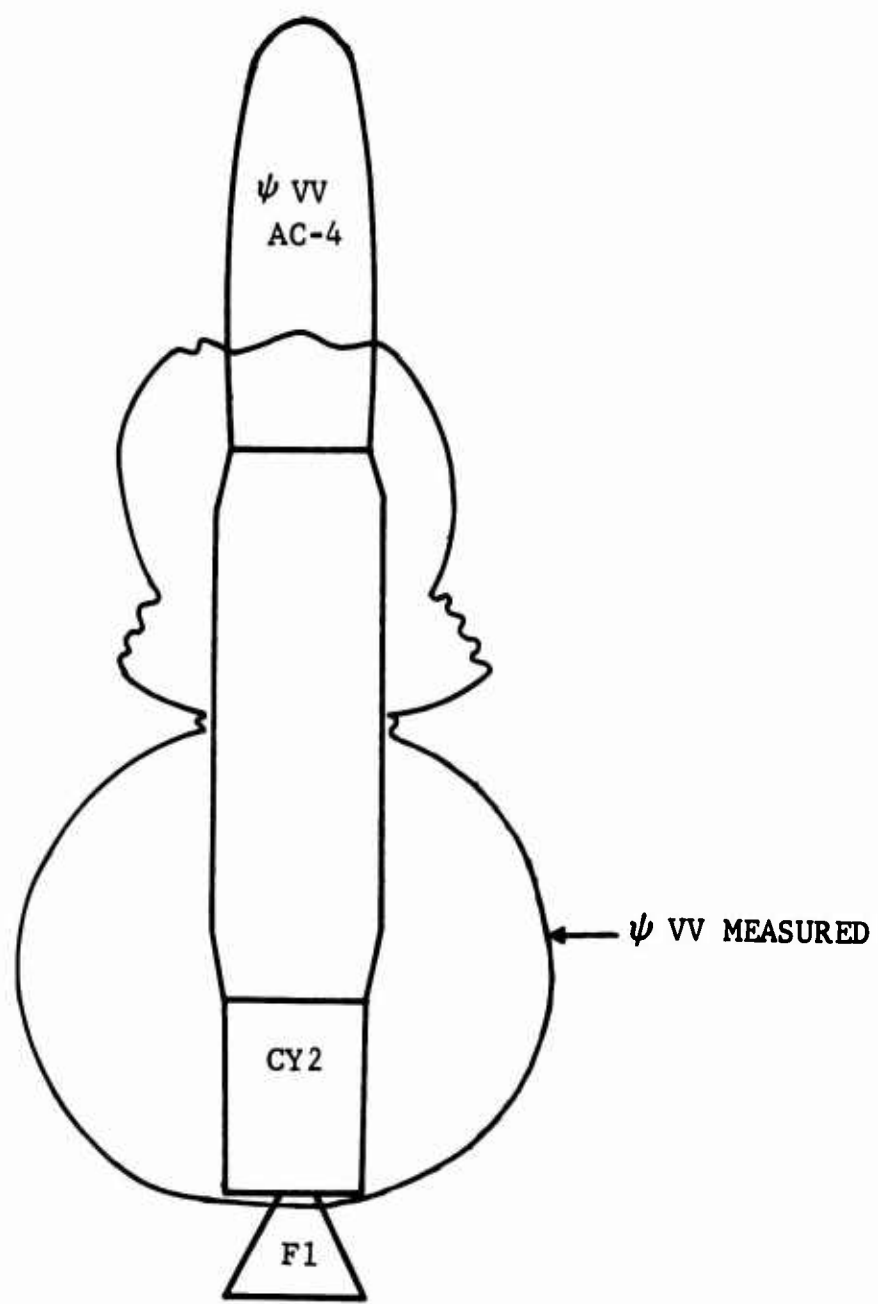


Fig. 4-34 MEASURED POSITION OF PHASE CENTER FOR MODEL AC-4
- VV POLARIZATION - POLAR PLOT

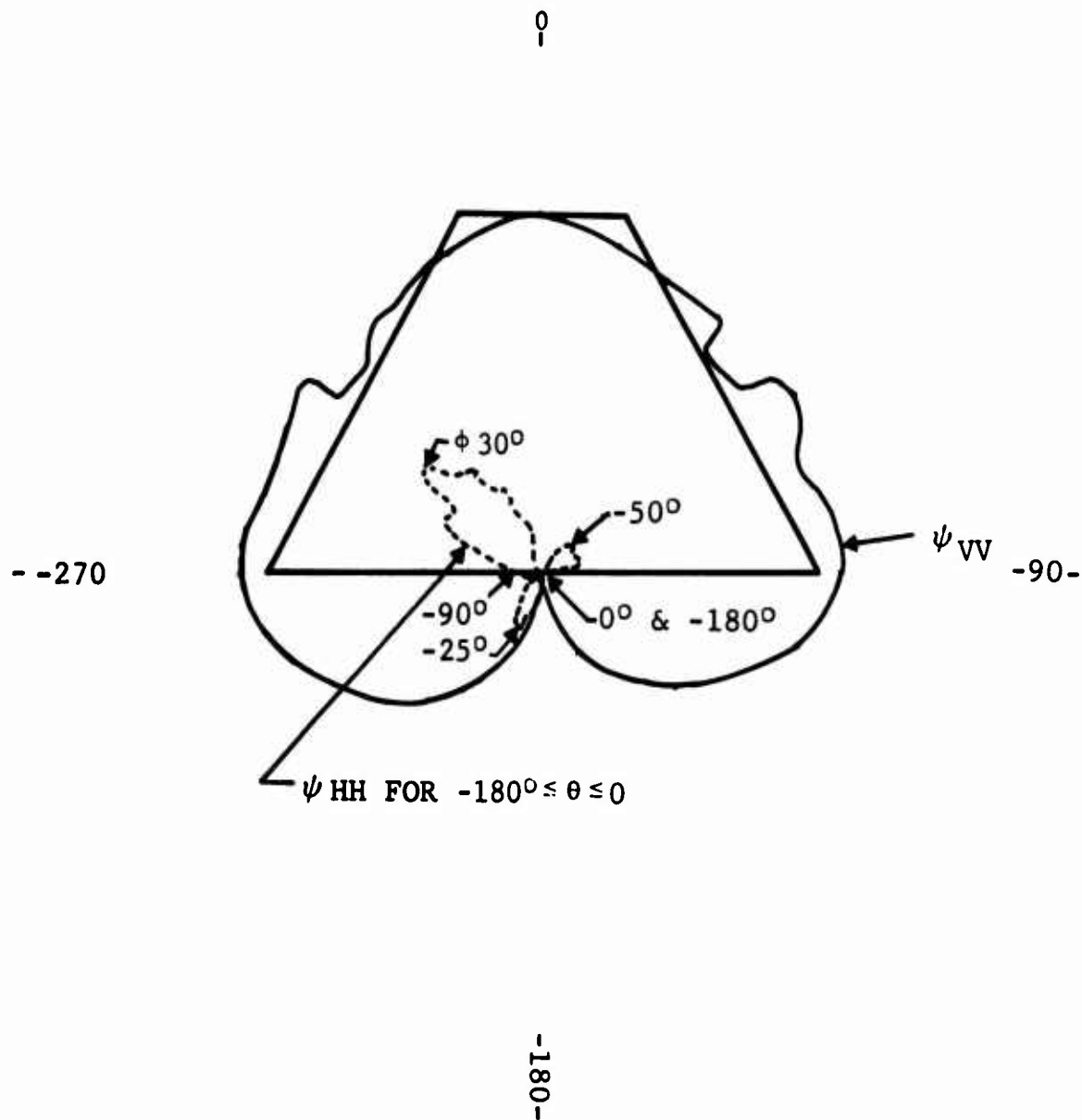
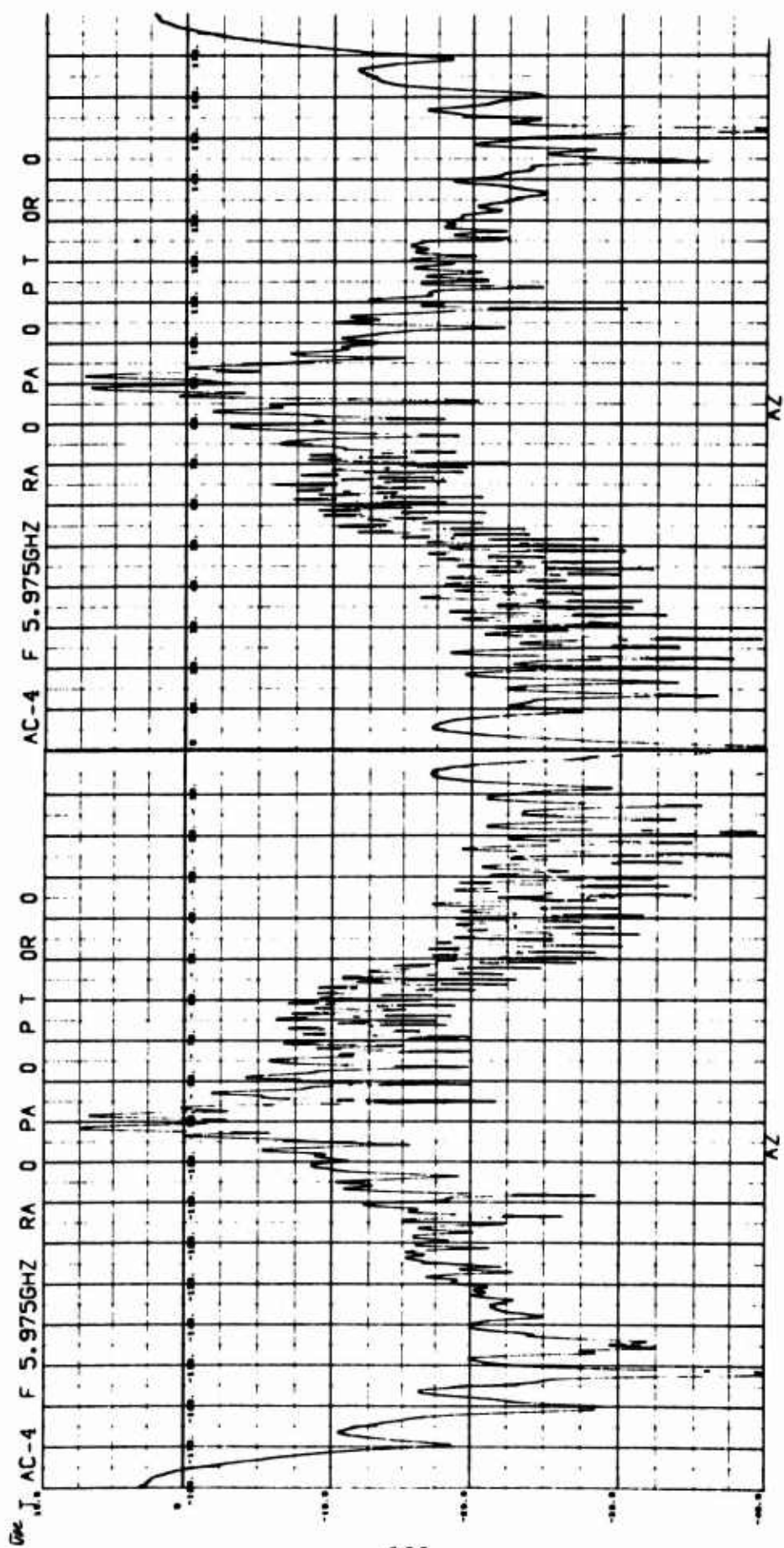


Fig. 4-35 MEASURED POSITION OF PHASE CENTER FOR MODEL F1 - POLAR PLOT



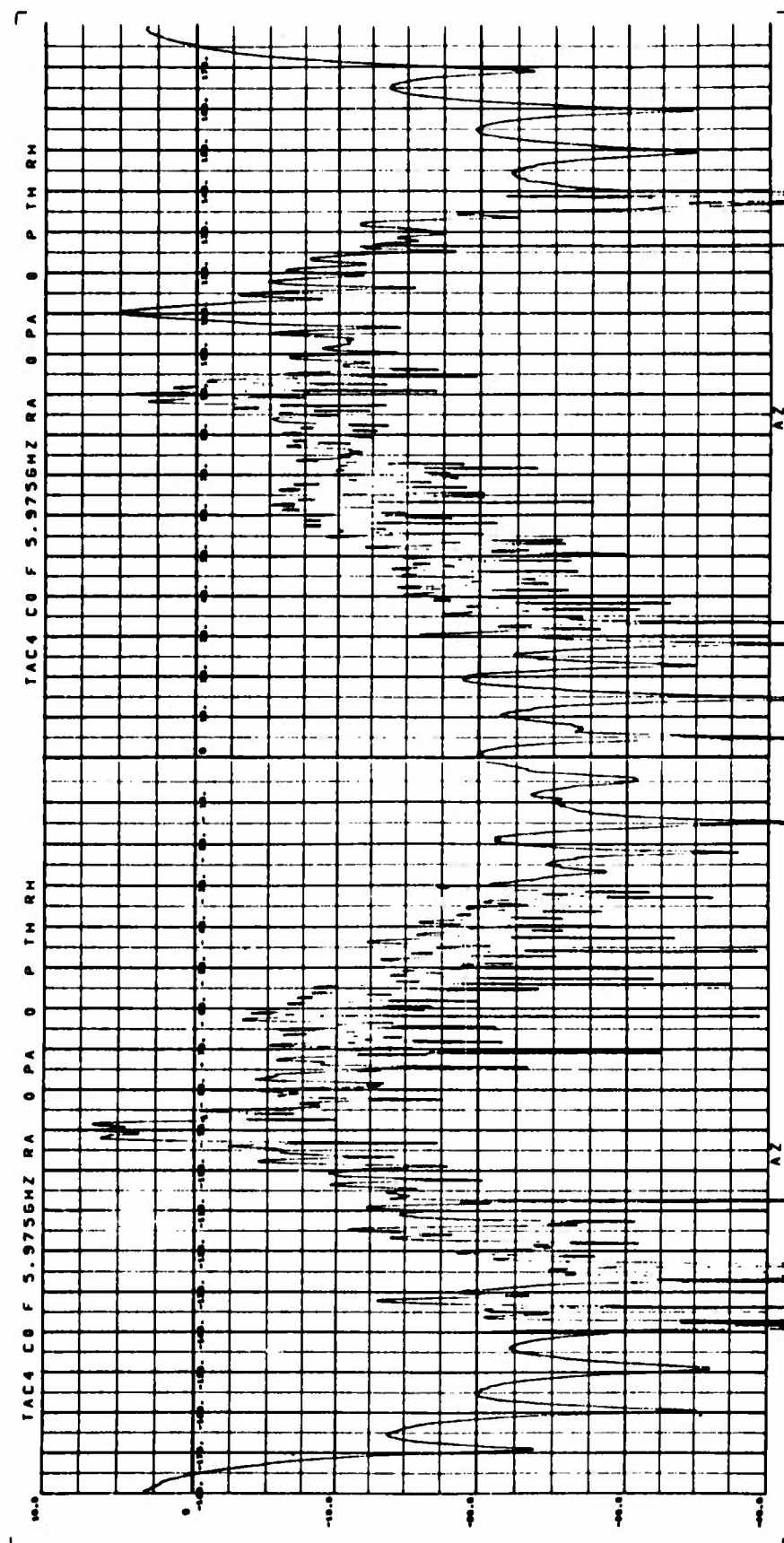


Fig. 4-37 COMPUTED CROSS SECTION FOR MODEL AC-4 - HH POLARIZATION

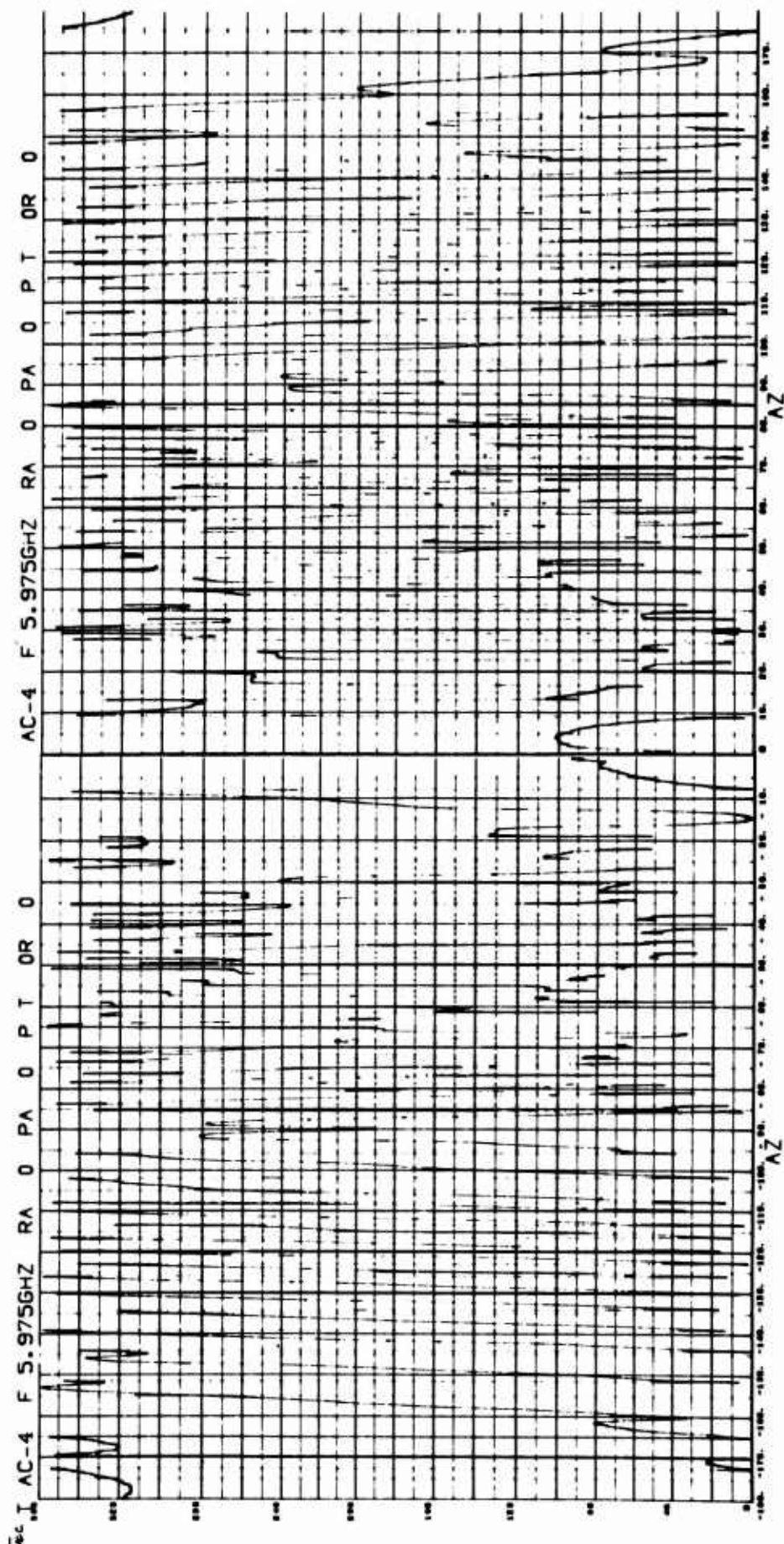


Fig. 4-38 MEASURED PHASE FOR MODEL AC-4 - HH POLARIZATION

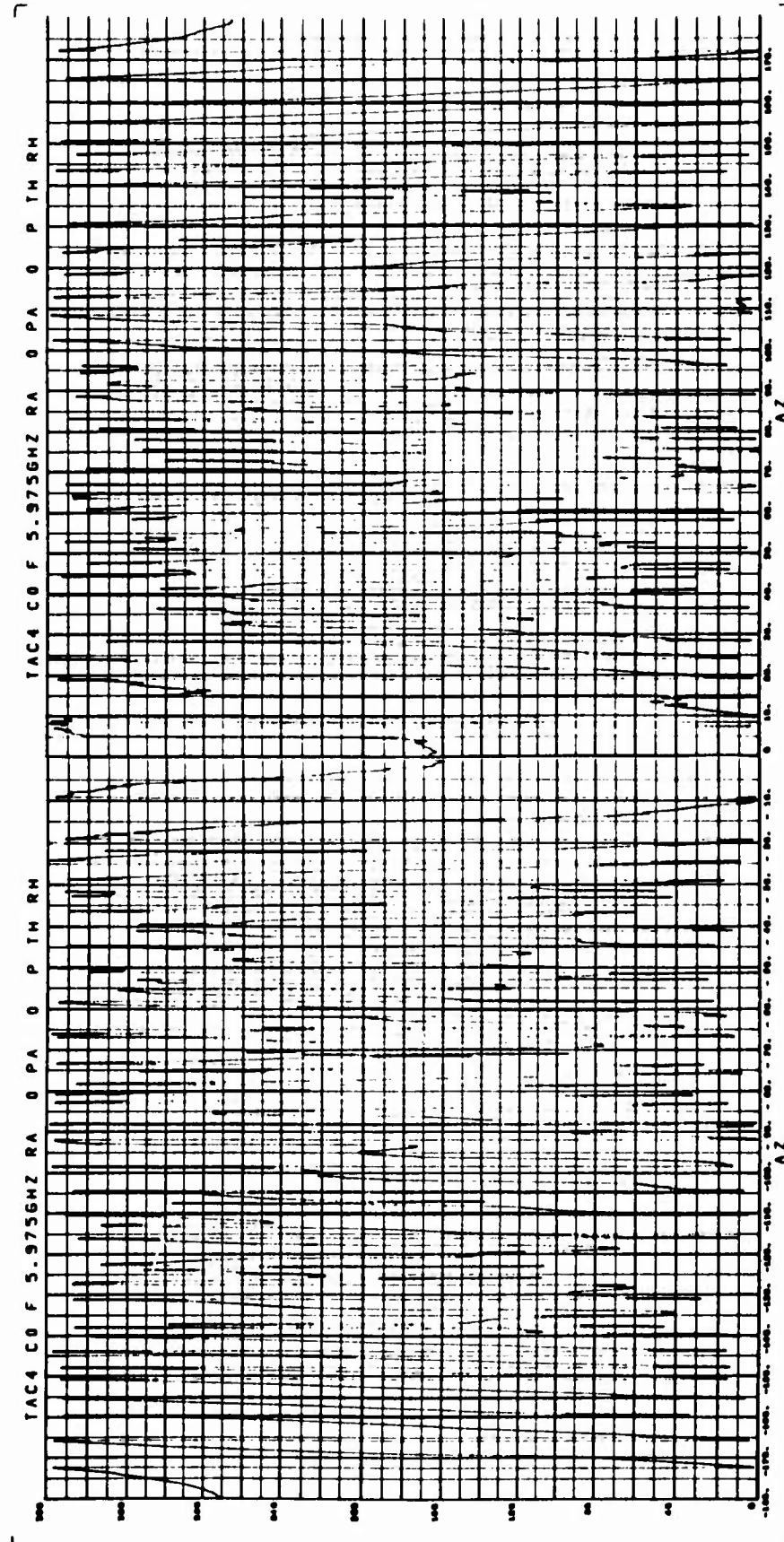


Fig. 4-39 COMPUTED PHASE FOR MODEL AC-4 - HH POLARIZATION

that the total change in position of the phase center is considerably less than the physical dimension of the target. The plot in this figure was positioned so that the phase center locations at the broadside aspects are attached to the side of the main cylinder CY5. When this action is taken, the position of the phase center at $\theta = 180$ degrees is located at the back of CY2 rather than at the back of F1, as might generally be expected. This is an indication of the existence of a significant amount of coupling between the flat ends of F1 and CY2. This is apparently bistatic coupling which results when energy forward scattered from the edge of F1 illuminates the flat end of CY2 which in turn produces backscatter back toward the radar.

The position of the phase center obtained by using ψ_{HH} is generally within the volume of a sphere containing the target on most of the generic models measured during this program. This fact makes it very difficult to track the measured ψ_{HH} phase as a model is rotated. The data in Figure 4-35 demonstrates this phenomenon in the case of ψ_{HH} for Model F1. For clarity, the ψ_{HH} pattern is plotted for only $-180.0 \leq \theta \leq 0.0$ degrees in this figure; however, the pattern is symmetrical with respect to the axis of the frustum. Model F1 was one of the smallest models measured separately in this program. Larger targets

exhibited such rapidly varying phase that ψ_{HH} could not be tracked with a high degree of confidence. GDT was not used to analyze Model F1 during this program since it does not belong to the ka region where GDT is valid. This is primarily a result of the one-wavelength separation between the two scattering centers on the small face of the frustum. Measurements indicate that the phase center at horizontal polarization remains very close to the large ring discontinuity surrounding the large end of the frustum.

A comparison of the HH data contained in Figures 4-36 and 4-37 also indicates a very good agreement between measured and superimposed data except in the region near 110 degrees. The large peak which occurs at 110 degrees in the computed case resulted from a recording error in the measured data for Model F2CY5F3 in the form of a 20-degree shift in aspect angle of all data between +10.0 and +180.0 degrees. Thus, the data in Figure 4-37 is correct for all aspect angles except those included between +40.0 and +140.0 degrees.

The nose-on aspect region also exhibits a fairly large error; a null was observed in measured ψ_{HH} in comparison to a value of -20.0 dBsm for the computed case. Again, this error is attributed to the presence of the large

ring discontinuity at the back of Model P1F4CY3 in the superposition case. This same effect is observed in the VV case; however, the error is not so great.

4.4.2 Model AC1

Model AC1 was identical to AC4 with the exception that aft rack Model AR3 was substituted for Cylinder CY2. Table 4-3 contains the pertinent superposition data used in computing the cross section and phase of this model. Since Model F2CY5F3 was also a part of this model, only the VV case was computed. Figures 4-40 through 4-43 contain measured and computed data for the VV case for Model AC-1.

A comparison of measured and computed values of ψ_{VV} for this target shows a remarkable similarity over a broad range of aspect angles. Serious errors are observed only at the nose-on aspect and in the 20-degree sector between +15.0 and +35.0 degrees. The error at the nose-on aspect is a typical result of the change in scattering which occurs when the characteristics of a ring discontinuity are modified. The physical high value of computed ψ_{VV} in the aspect region between +15. and +35.0 degrees is a result of the rectangular appendage which is attached to the side of Model AR3. The use of a shadow region for Model AR3 extending past 10 degrees to about 35 degrees would have been more appropriate since, near nose-on, the girth of

Table 4-3 MODEL AC-1 SUPERPOSITION PARAMETERS

COMPOSITE MODEL		FREQUENCY GHZ		BISTATIC ANGLE DEGREES	
AC-1		5.975		0.	

GENERIC SURFACE	FREQ GHZ	POSITION R INCHES	POSITION ρ DEGREES	SUPERPOSITION PARAMETERS						SHADOW REGIONS				
				D INCHES	DEGREES	δ	$\Delta\theta$	ψ_c	θ_{11}	θ_{12}	θ_{21}	θ_{22}	θ_{31}	θ_{32}
									DEGREES	DEGREES	DEGREES	DEGREES	DEGREES	DEGREES
F2CY5F3	5.975	0.012	180.	0.	0.	0.	0.	-32.	.1	40.	140.	220.	320.	360.
F1	5.975	0.765	183.4	24.38	180.	0.	0.	19.	150.	210.				
AR3	5.975	0.0	0.0	19.99	180.	0.	-164.	.1	130.	150.	195.	345.	360.	
P1F4CY3	5.975	0.134	180.	15.95	0.	0.	85.	.1	40.	320.	360.			

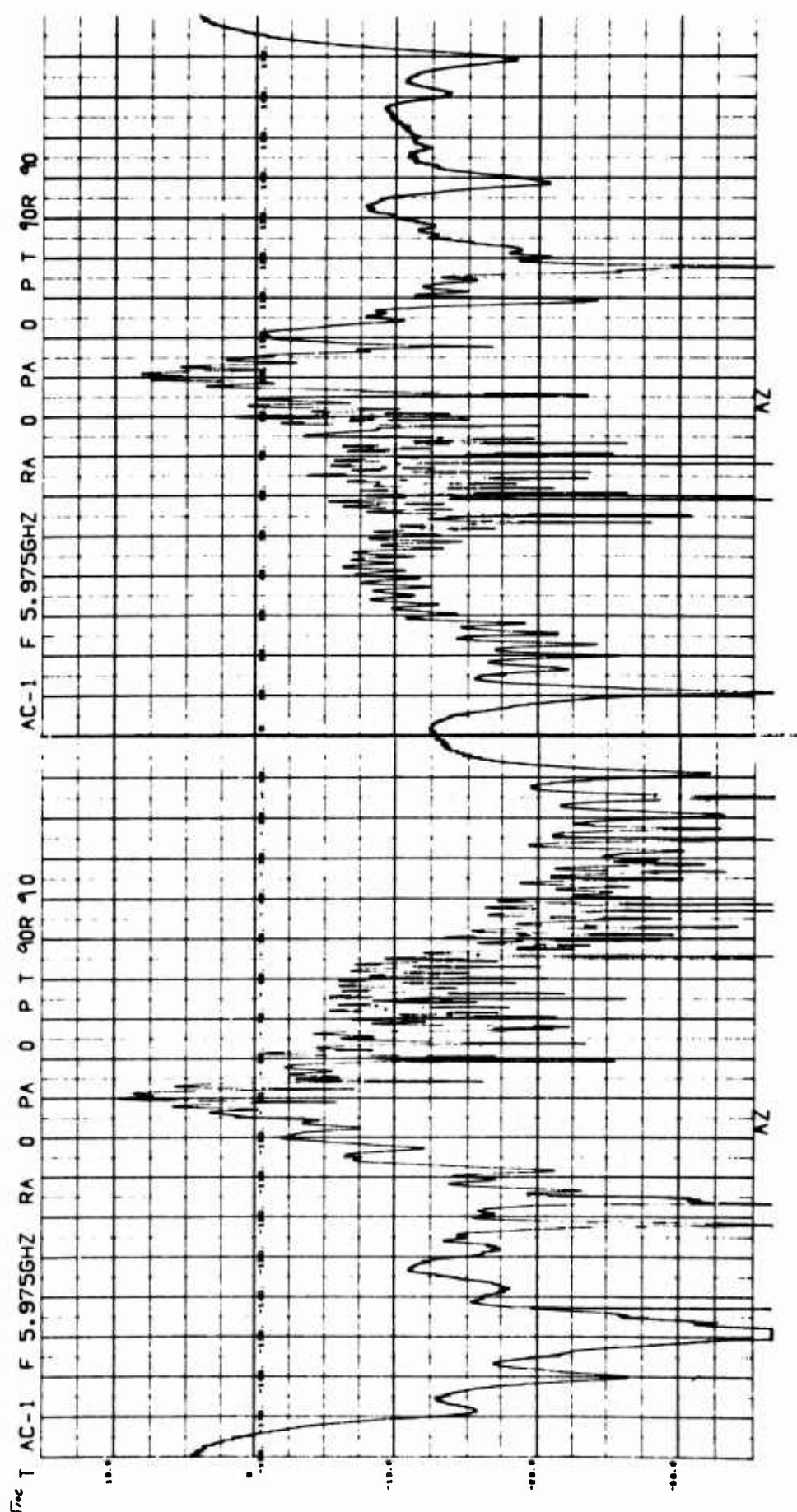


Fig. 4-40 MEASURED CROSS SECTION FOR MODEL AC-1 - VV POLARIZATION

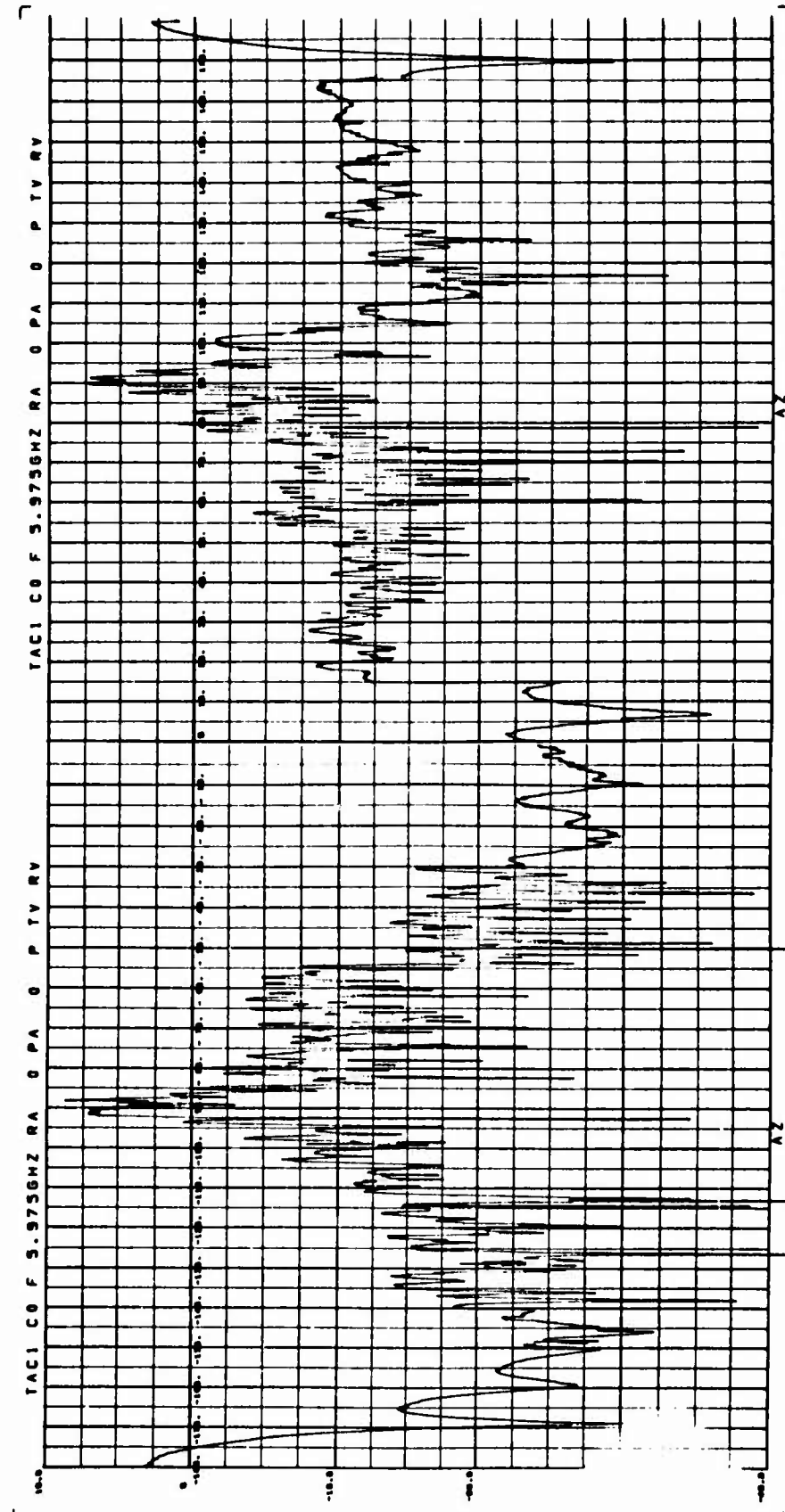


Fig. 4-41 COMPUTED CROSS SECTION FOR MODEL AC-1 - VV POLARIZATION

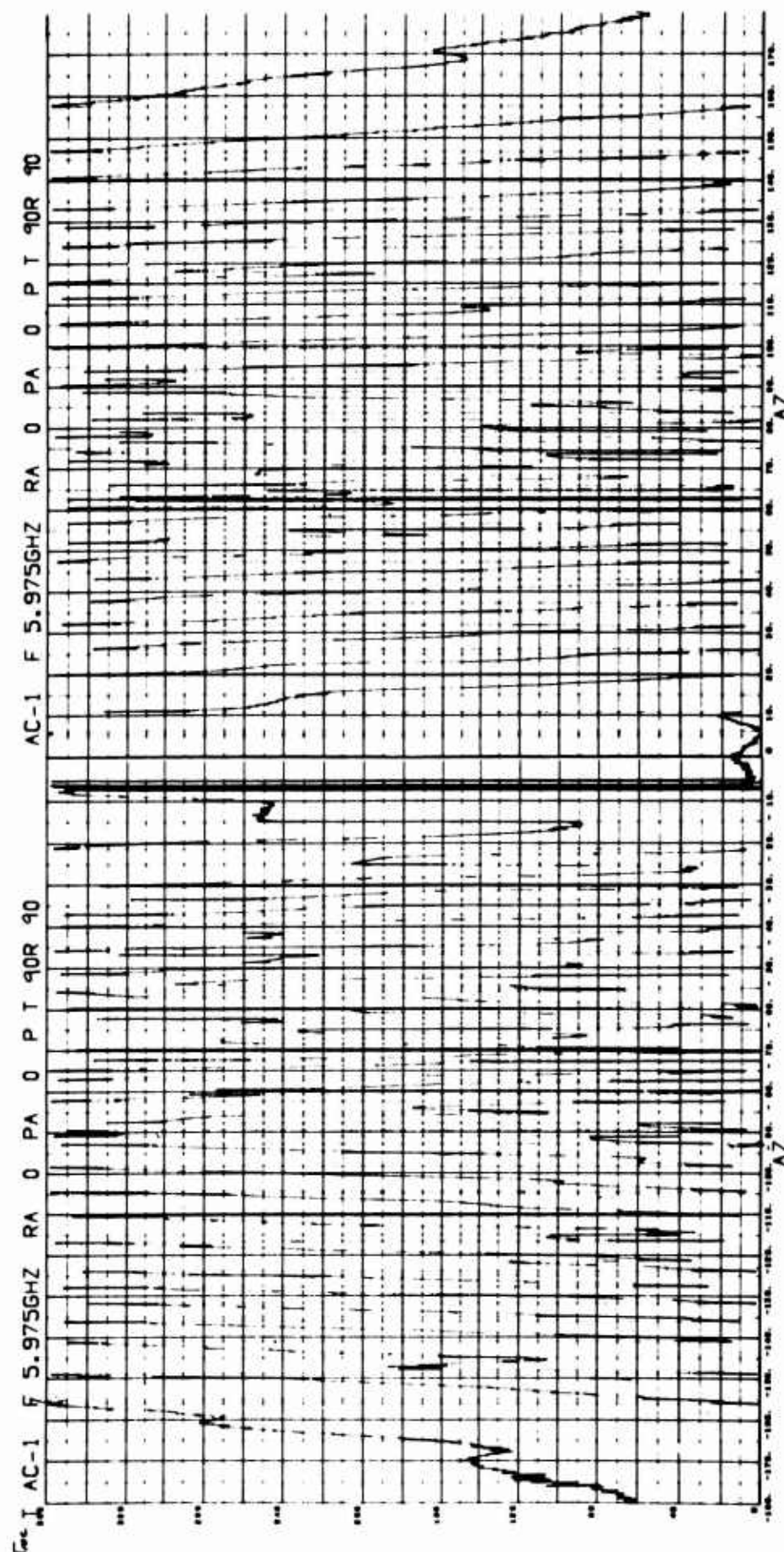


Fig. 4-42 MEASURED PHASE FOR MODEL AC-1 - VV POLARIZATION

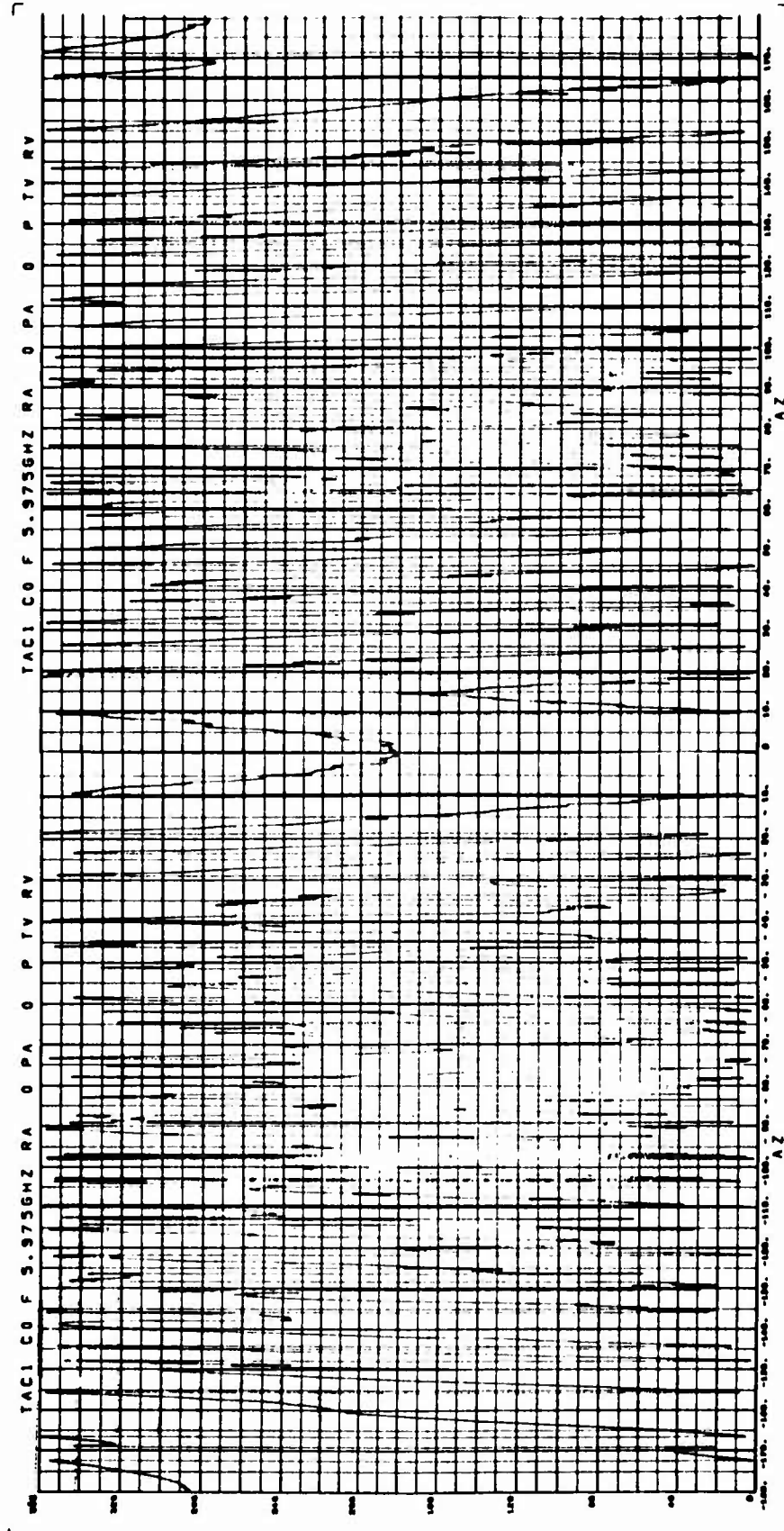


Fig. 4-43 COMPUTED PHASE FOR MODEL AC-1 - VV POLARIZATION

CY5 tends to shadow this appendage, whereas near tail-on, the appendage apparently contributes significantly to within 10 to 12 degrees of tail-on. A polar plot of the position of the target phase center was not successful for this target as can be observed from a visual analysis of the measured phase data in Figure 4-41. However, it is interesting to observe that the phase center tends to move toward the radar when the target is rotated away from the nose-on aspect so that the rectangular appendage is illuminated, whereas it appears to move away or jump when the opposite side is presented. Thus, it appears that the appendage may represent the primary scatterer in the region of positive aspect angles near nose-on.

4.4.3 Model A2

The values of the superposition parameters of Smooth Aerospace Model A2 are contained in Table 4-4. Superposition data on this particular model were obtained by using measured data from four component models. Only vertical polarization was investigated since horizontal polarization data on Model F2CY5F3 was found to contain an uncorrectable azimuth shift. Figures 4-44 to 4-48 contain measured and computed cross section and phase data on this vehicle. A comparison of the measured and computed cross section data contained in Figures 4-44 and 4-45 indicates only two aspect regions

Table 4-4 MODEL A2 SUPERPOSITION PARAMETERS

COMPOSITE MODEL		FREQUENCY GHZ		BISTATIC ANGLE DEGREES	
A2		6.0		0.0	

GENERIC SURFACE	FREQ GHZ	POSITION R INCHES	ρ DEGREES	SUPERPOSITION PARAMETERS				SHADOW REGIONS			
				D INCHES	δ DEGREES	$\Delta\theta$ DEGREES	ψ_c	θ_{11}	θ_{12}	θ_{21}	θ_{22}
F1	5.975	0.365	183.4	16.81	180.	180.	-344.	0.1	30.	330.	360.
F2Y5F3	5.975	0.012	180.	0.0	0.	180.	-40.	0.1	30.	150.	210.
CY1	6.0	0.688	223.9	14.51	181.9	0.	97.	0.1	30.	150.	210.
C1CY3	5.975	0.0	0.0	17.24	0.0	0.	-222.	0.1	30.	330	360.

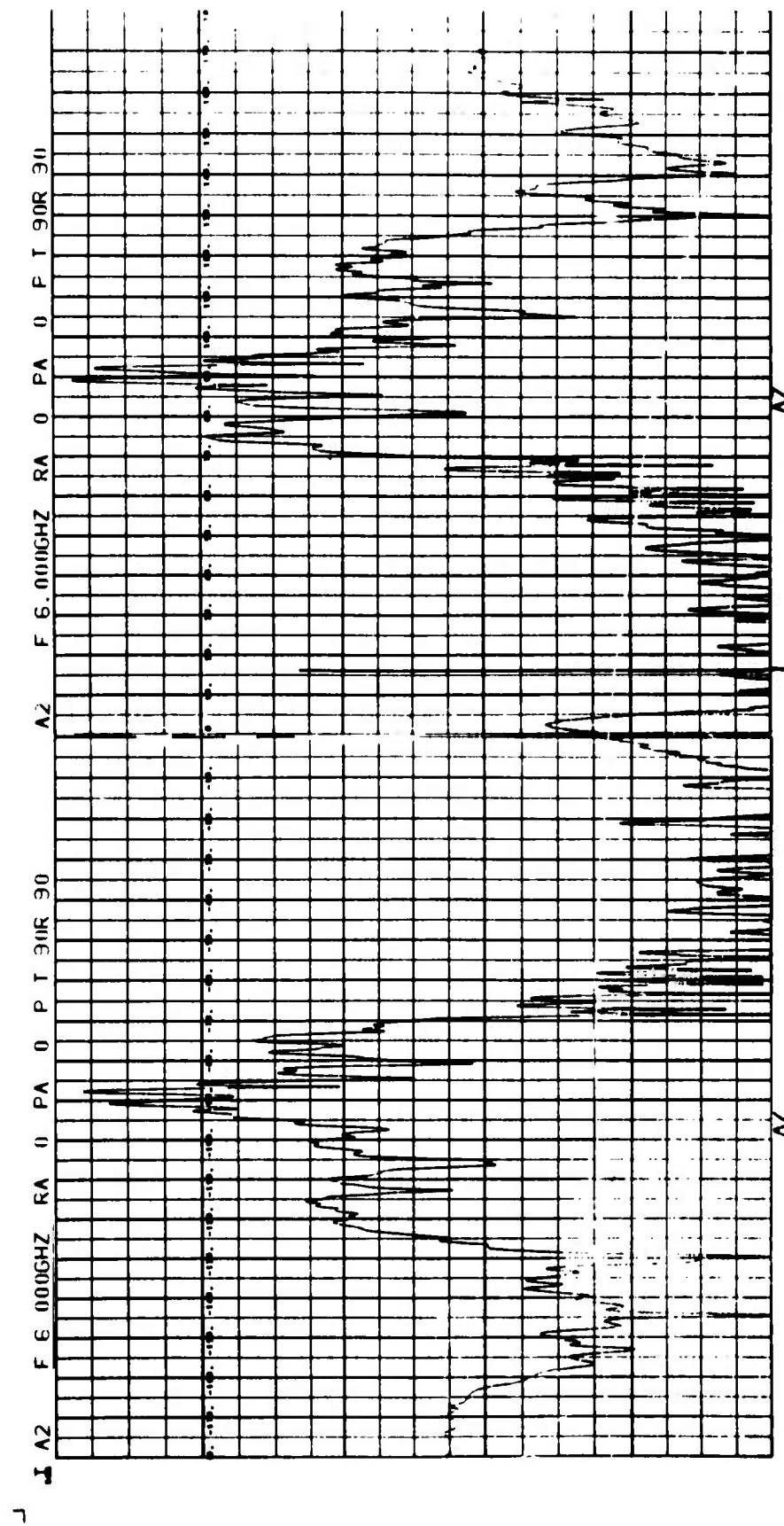


Fig. 4-44 MEASURED CROSS SECTION FOR MODEL A2 - VV POLARIZATION

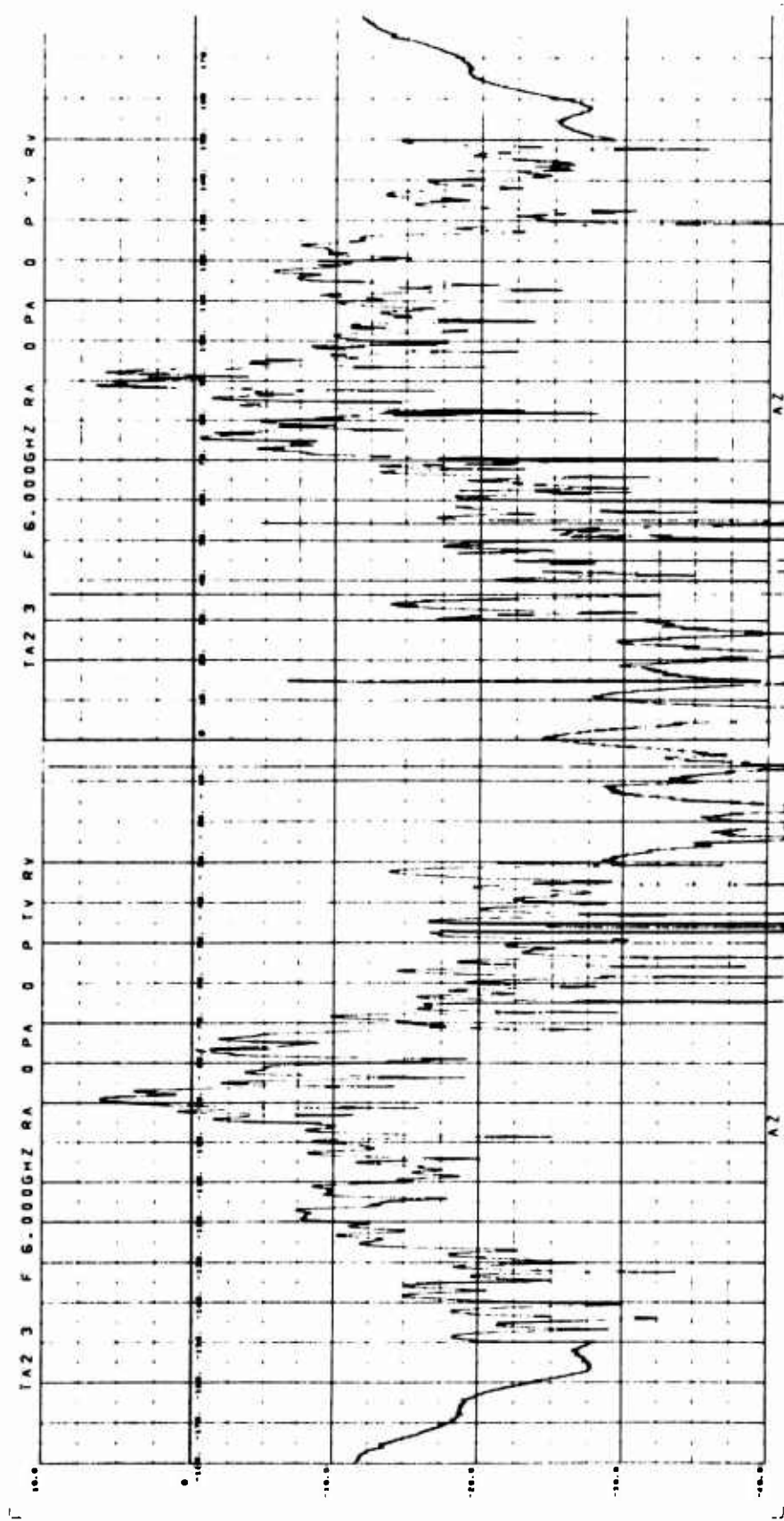


Fig. 4-45 COMPUTED CROSS SECTION FOR MODEL A2 - VV POLARIZATION

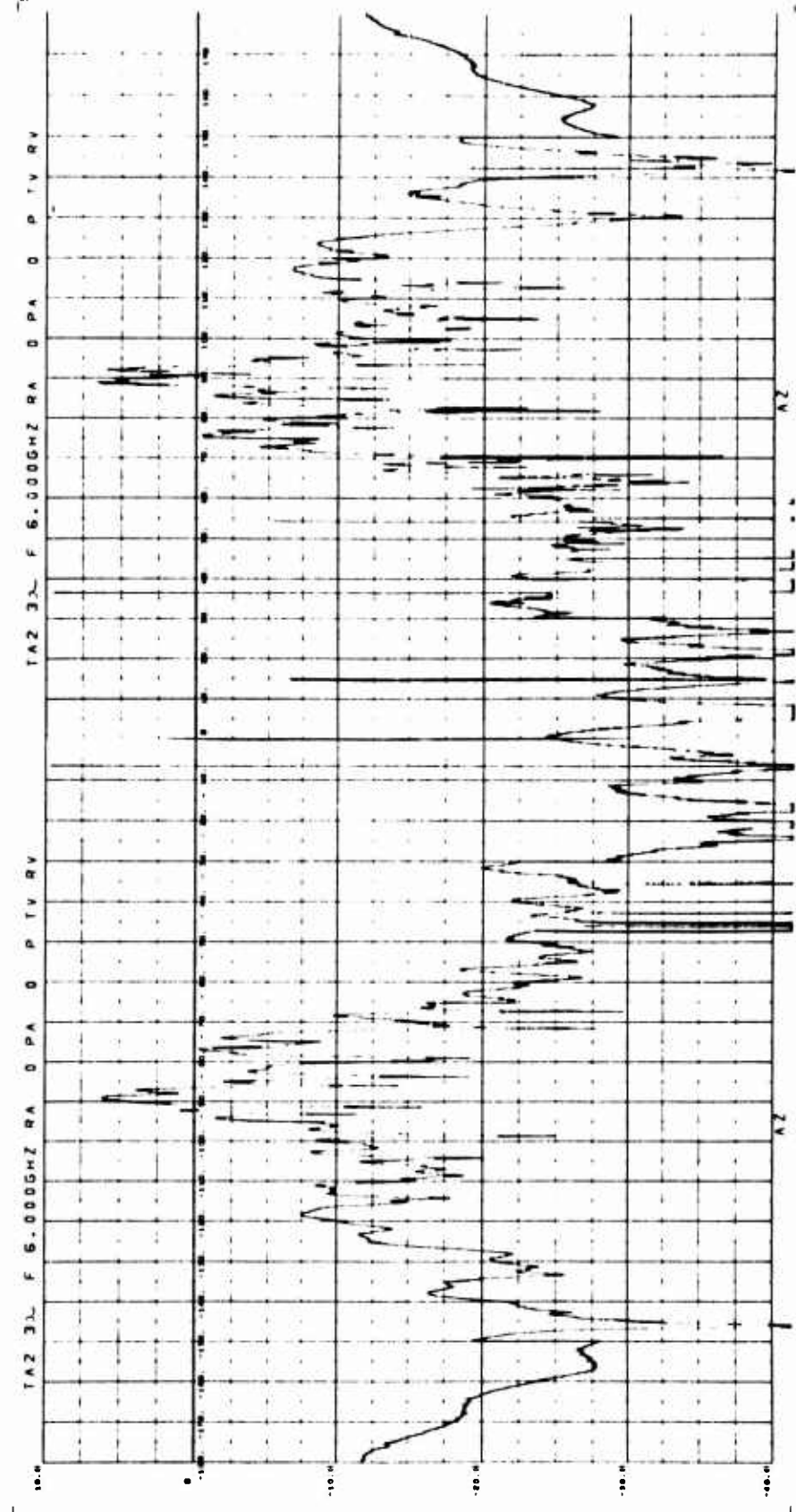
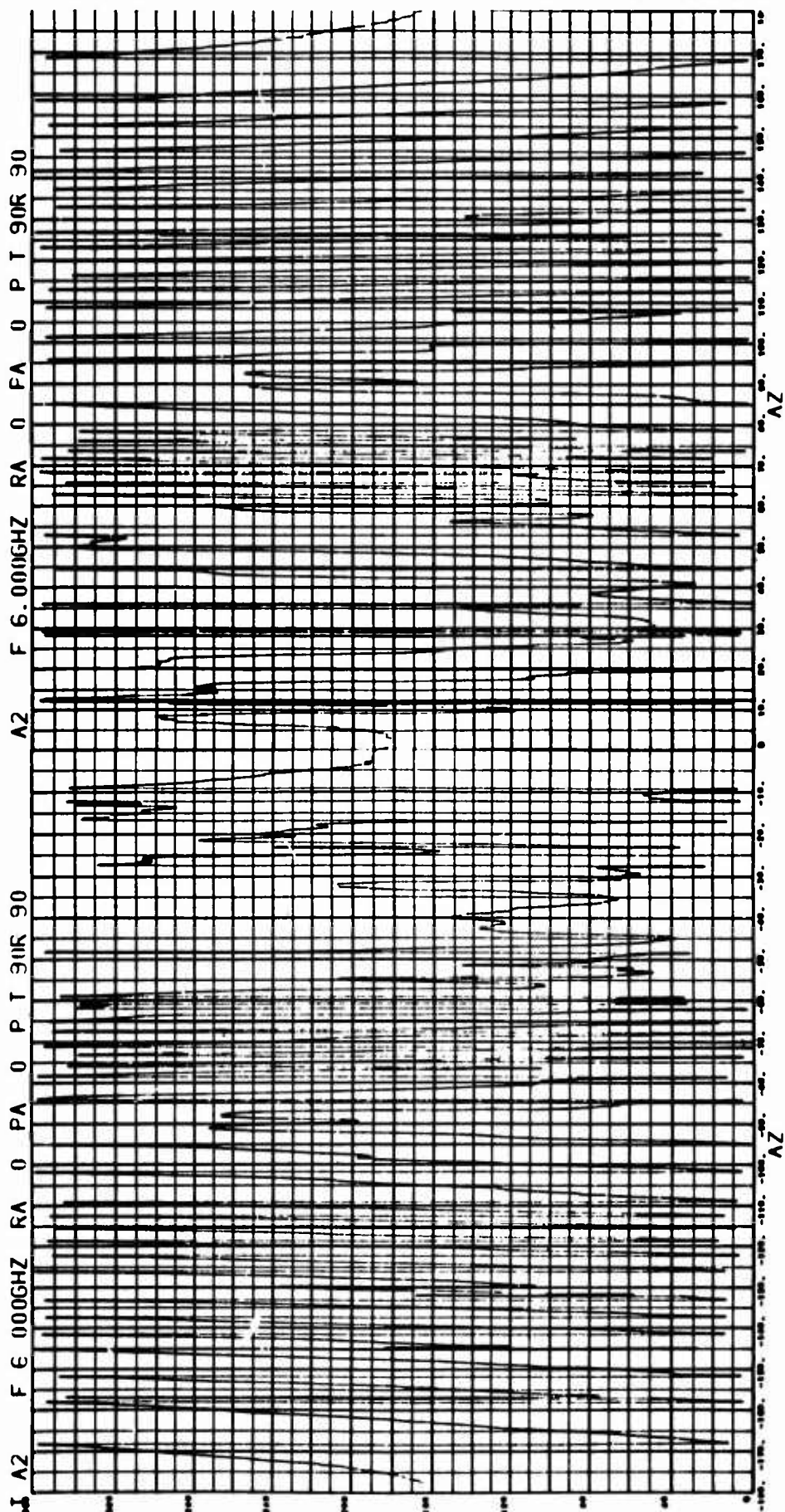


Fig. 4-46 COMPUTED CROSS SECTION FOR MODEL A2-3 - VV POLARIZATION



156

Fig. 4-47 MEASURED PHASE FOR MODEL A2 - VV POLARIZATION

NOT REPRODUCIBLE

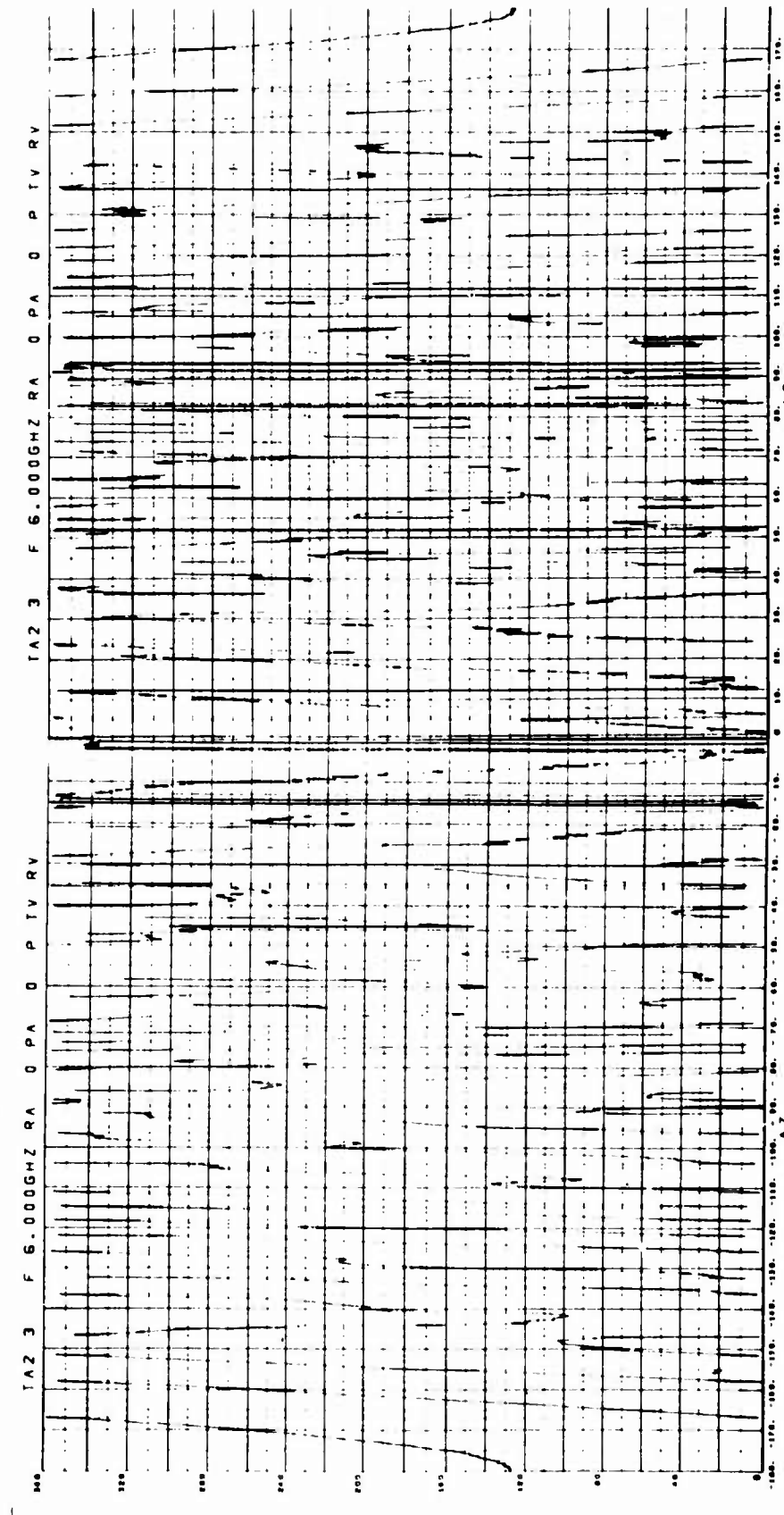


Fig. 4-48 COMPUTED PHASE FOR MODEL A2 - VV POLARIZATION

where measured and computed data is not well correlated. The most serious errors occur in the aspect region just off the nose-on aspect, extending from about 10 degrees to about 65 degrees. Similar errors are exhibited between -10 and -65 degrees as a result of vehicle symmetry. Analyses of the measured cross section values obtained by using each component surface indicate that the large values of computed ψ_{VV} in these regions are a result of the in-phase addition of scattering from all four surfaces rather than that from a single dominant surface. Thus, this error could not be entirely eliminated by simply extending the shadow regions of one of the component surfaces.

A comparison of the measured values of cross section obtained for each of the component surfaces at $\theta = 32.5$ degrees provides the following results:

<u>Model</u>	<u>Cross Section</u> (dBS)
F1	-26.25
F2CY5F3	-22.55
CY1	-23.0
C1CY3	-26.5

The in-phase addition of these four values of σ gives a total cross section of $\sigma = -12.38$ dBsm. The superposition cross section at the peak which occurs at $\theta = 32.5$ degrees in Figure 4-45 is only slightly less than this value, -13.8 dBsm.

At this particular aspect angle, the computed and measured cross section differ by about 25.0 dB. Again, this large error presumably occurs as a result of the fact that (1) superposition data is based on energy which is scattered from scattering surfaces that are not actually illuminated in the composite case and (2) to the changes in coupling at the interface regions of the composite vehicle. In viewing the composite vehicle near the nose-on aspect, a very small contribution would be expected from the discontinuities located at the interface of F2 and CY1 and that of CY1 and F1. However, in the superposition case, these discontinuities would be as significant as any other. In order to better evaluate this particular hypothesis, the superposition parameters contained in Table 4-5 were used. Note that the only changes between the values of these parameters and those contained in Table 4-4 are related to the shadow regions. In this case, Models F1 and CY1 are shadowed through a full 65 degrees on each side of $\theta = 0$ degrees. Also, C1CY3 is shadowed through a full 65 degrees on each side of $\theta = -180$ degrees. These results are contained in Figure 4-46.

Table 4-5 MODEL A2 SUPERPOSITION PARAMETERS

COMPOSITE MODEL	FREQUENCY GHZ	BISTATIC ANGLE DEGREES
A2	6.0	0.0

GENERIC SURFACE	FRQ GHZ	POSITION ERROR R INCHES	SUPERPOSITION PARAMETERS				SHADOW REGIONS			
			DEGREES	D INCHES	DEGREES	ψ_c	θ_{11}	θ_{12}	θ_{21}	θ_{22}
					DEGREES					
F1	5.975	0.365	183.4	16.81	180.	180.	-344.	0.1	65.	295.
F2Y5F3	5.975	0.012	180.	0.0	0.	180.	-40.	0.1	30.	150.
CY1	6.0	0.688	223.9	14.51	181.9	0.	97.	0.1	30.	150.
C1CY3	5.975	0.0	0.0	17.24	0.0	0.	-222.	0.1	65.	295.
									360.	360.
									330.	330.
									245.	245.
									360.	360.
									330.	330.
									250.	250.

The primary differences to be noted in these results are that the error near $\theta = 35$ degrees is reduced by about 5 dB and the fact that the additional shadowing of C1CY3 allowed the nulls near $\theta = \pm 145$ degrees to be observed. The effect of the ring discontinuity of C1CY3 in the nose-on region accounts for the 5dB error which is observed there in both cases.

Measured phase is shown in Figure 4-47 and computed phase for the case described in Table 4-4 is shown in Figure 4-48. The high rates of change of phase with aspect and the jumps which occur at shadow boundaries preclude successful correlation of these data over a wide range of aspect angles. Figure 4-49 shows the relationship between target geometry and the shadow regions used in these computations.

4.4.4 Model A3

Table 4-6 contains the superposition parameters of Model A3, the outline of which is shown in Figure 4-50. This model is a roll-symmetric model, and superposition was accomplished by using three component surfaces. Measured and computed cross section and phase data obtained at both VV and HH polarizations are shown in Figures 4-51 to 4-58.

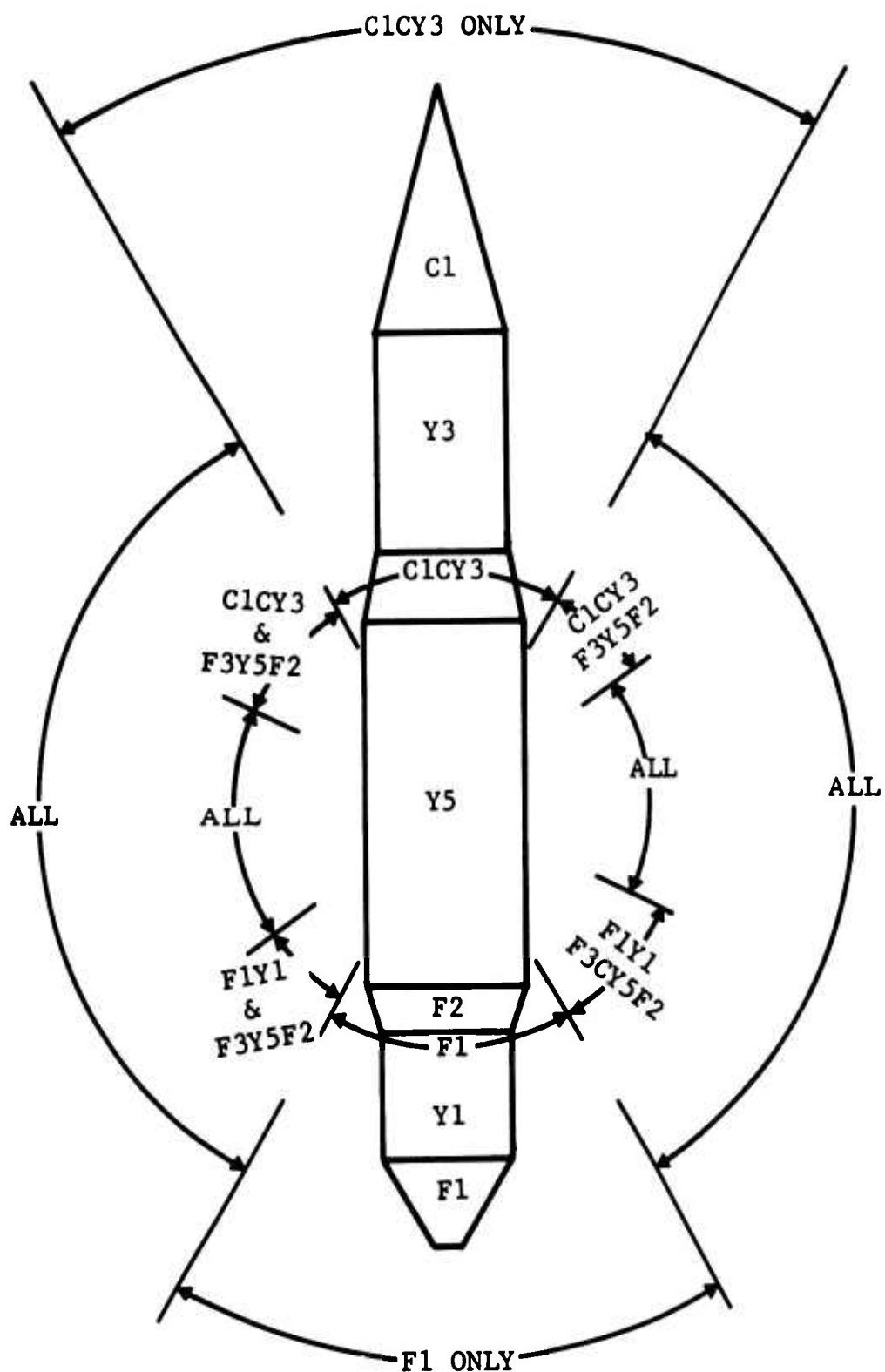


Fig. 4-49 ILLUSTRATION OF SHADOW REGIONS FOR MODEL A2

Table 4-6 MODEL A3 SUPERPOSITION PARAMETERS

COMPOSITE MODEL	FREQUENCY GHZ	BISTATIC ANGLE DEGREES
A3	5.975	0.0

GENERIC SURFACE	FREQ GHZ	POSITION R INCHES	POSITION ρ DEGREES	SUPERPOSITION PARAMETERS				SHADOW REGIONS			
				D INCHES	δ DEGREES	$\Delta\theta$ DEGREES	ψ_c DEGREES	θ_{11}	θ_{12}	θ_{21}	θ_{22}
								DEGREES	DEGREES	DEGREES	DEGREES
H3Y1Y2	5.975	0.963	173.8	20.102	0.0	0.0	6.0	0.1	30.0	330.0	360.0
CY5	6.000	0.678	234.5	0.678	54.5	0.0	223.0	0.1	30.0	330.0	360.0
C3CY3	5.975	0.019	215.8	13.887	180.0	180.0	63.0	0.1	30.0	330.0	360.0

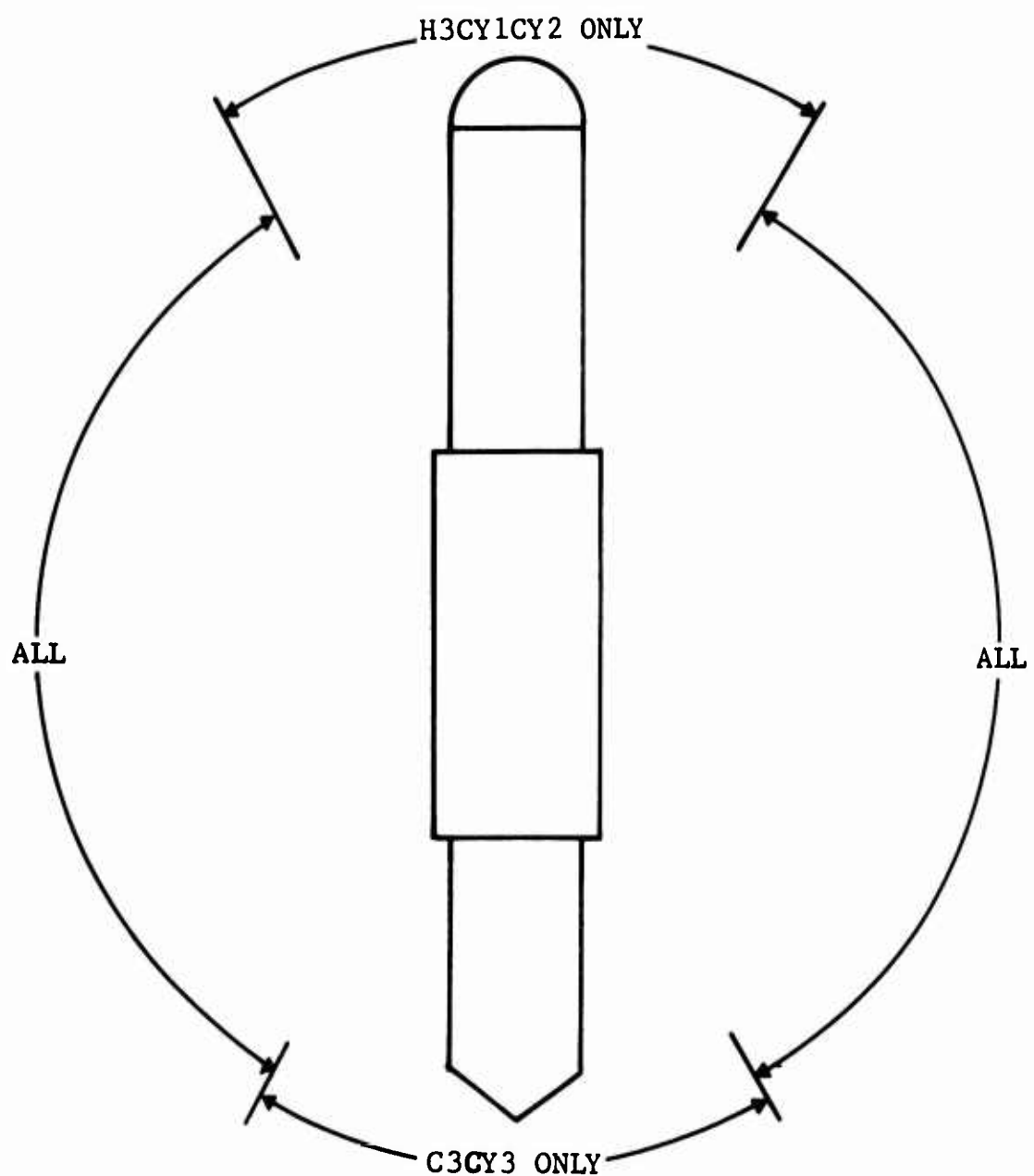


Fig. 4-50 ILLUSTRATION OF SHADOW REGIONS FOR MODEL A3

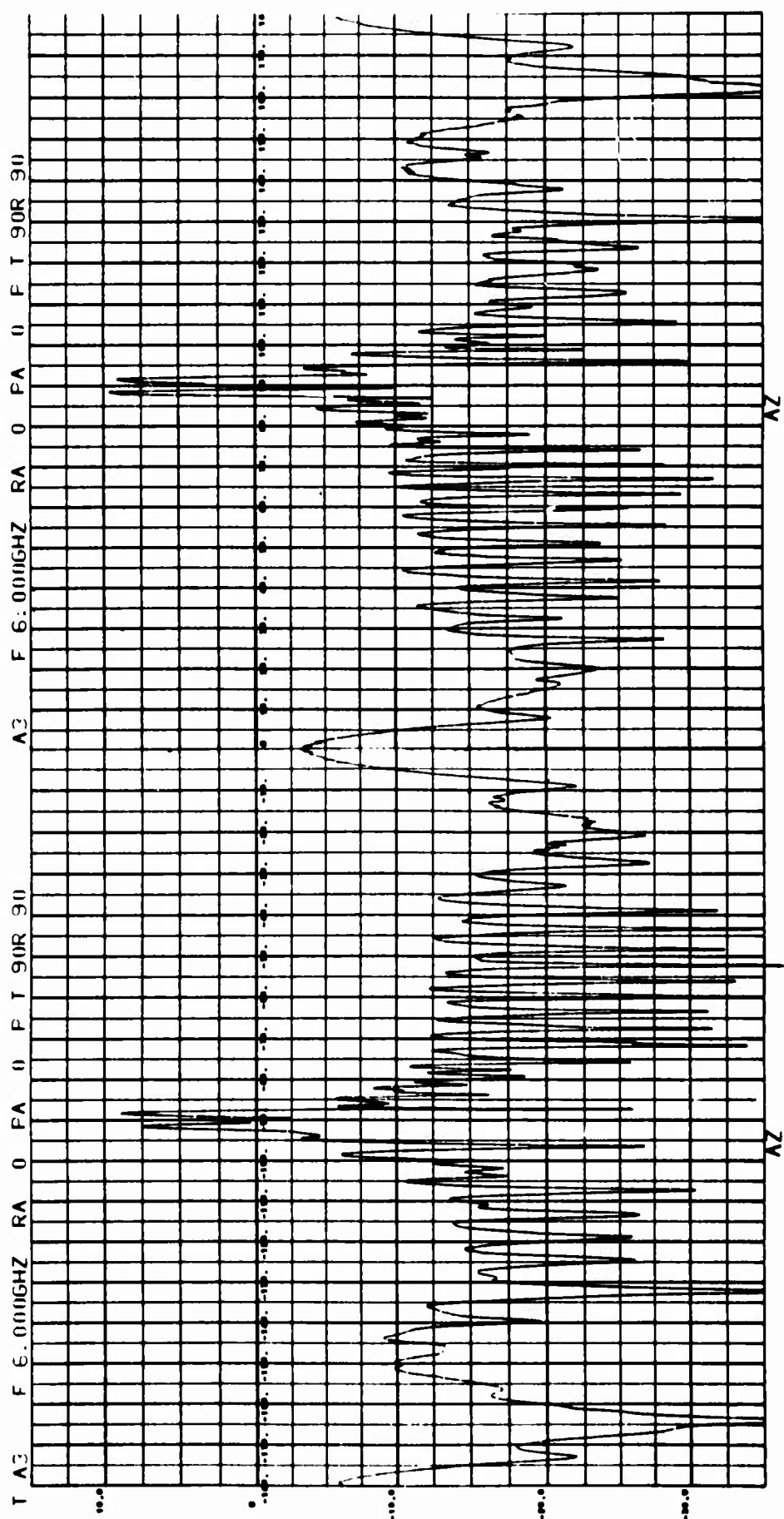


Fig. 4-51 MEASURED CROSS SECTION FOR MODEL A3 - VV POLARIZATION

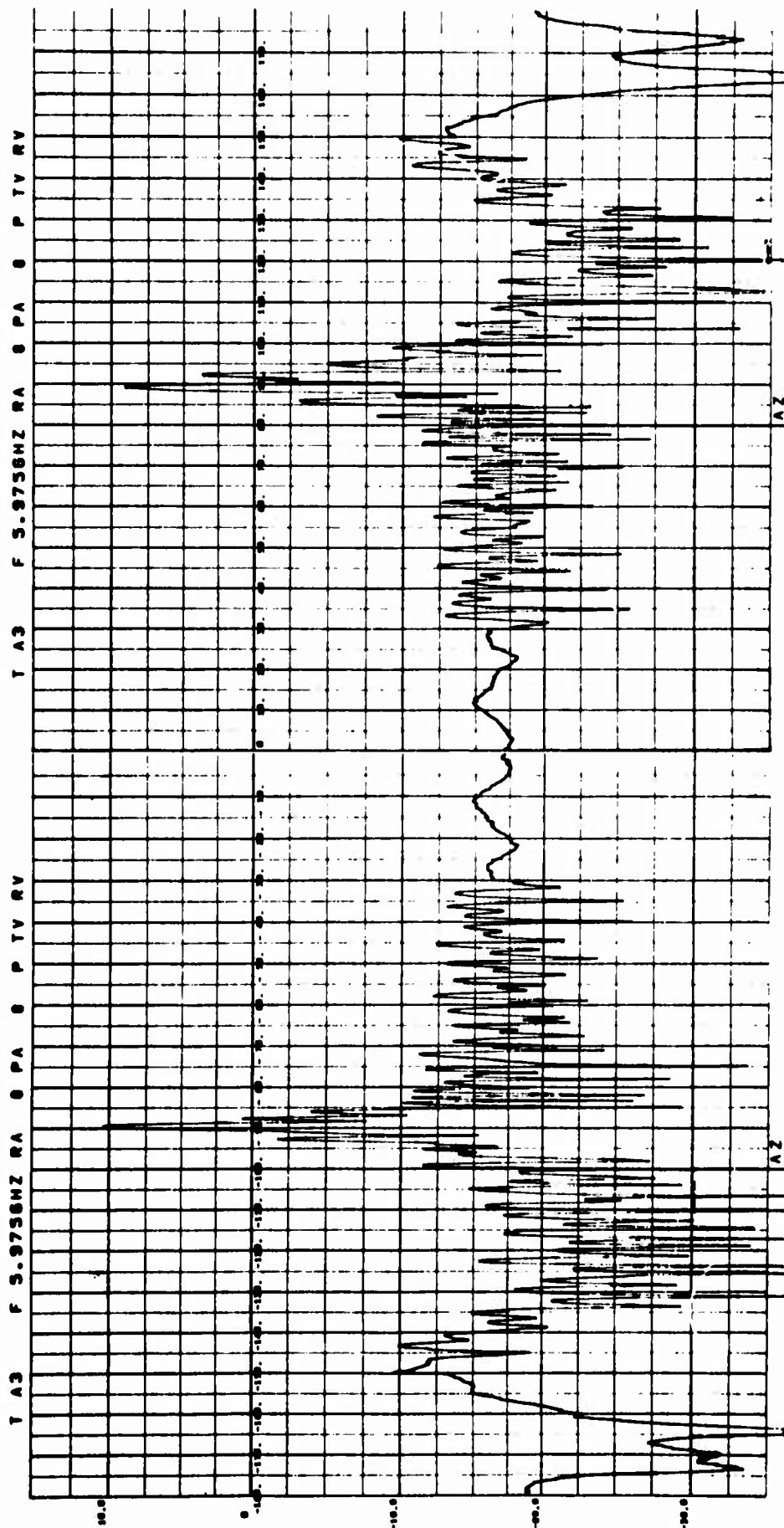


Fig. 4-52 COMPUTED CROSS SECTION FOR MODEL A3 - VV POLARIZATION

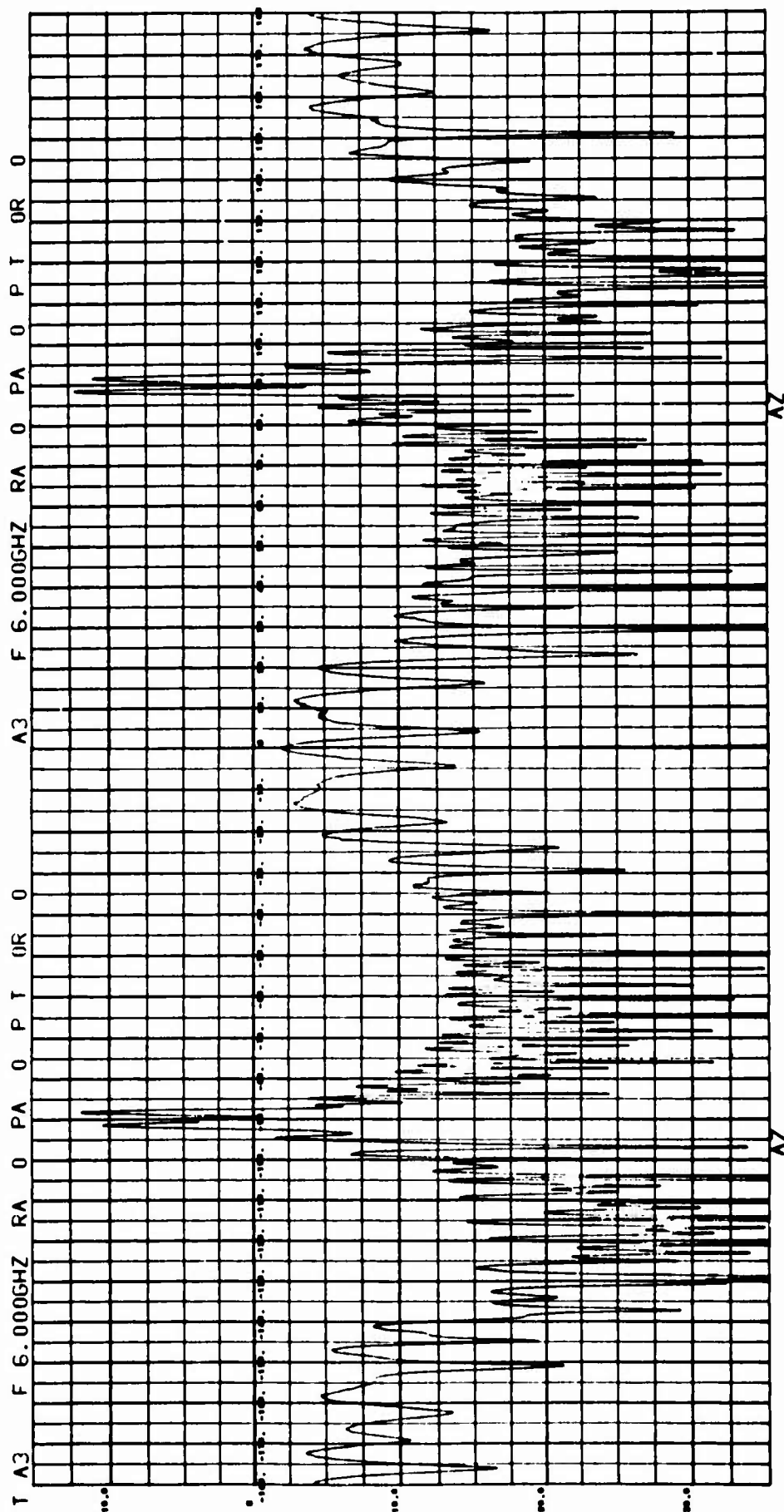


Fig. 4-53 MEASURED CROSS SECTION FOR MODEL A3 - HH POLARIZATION

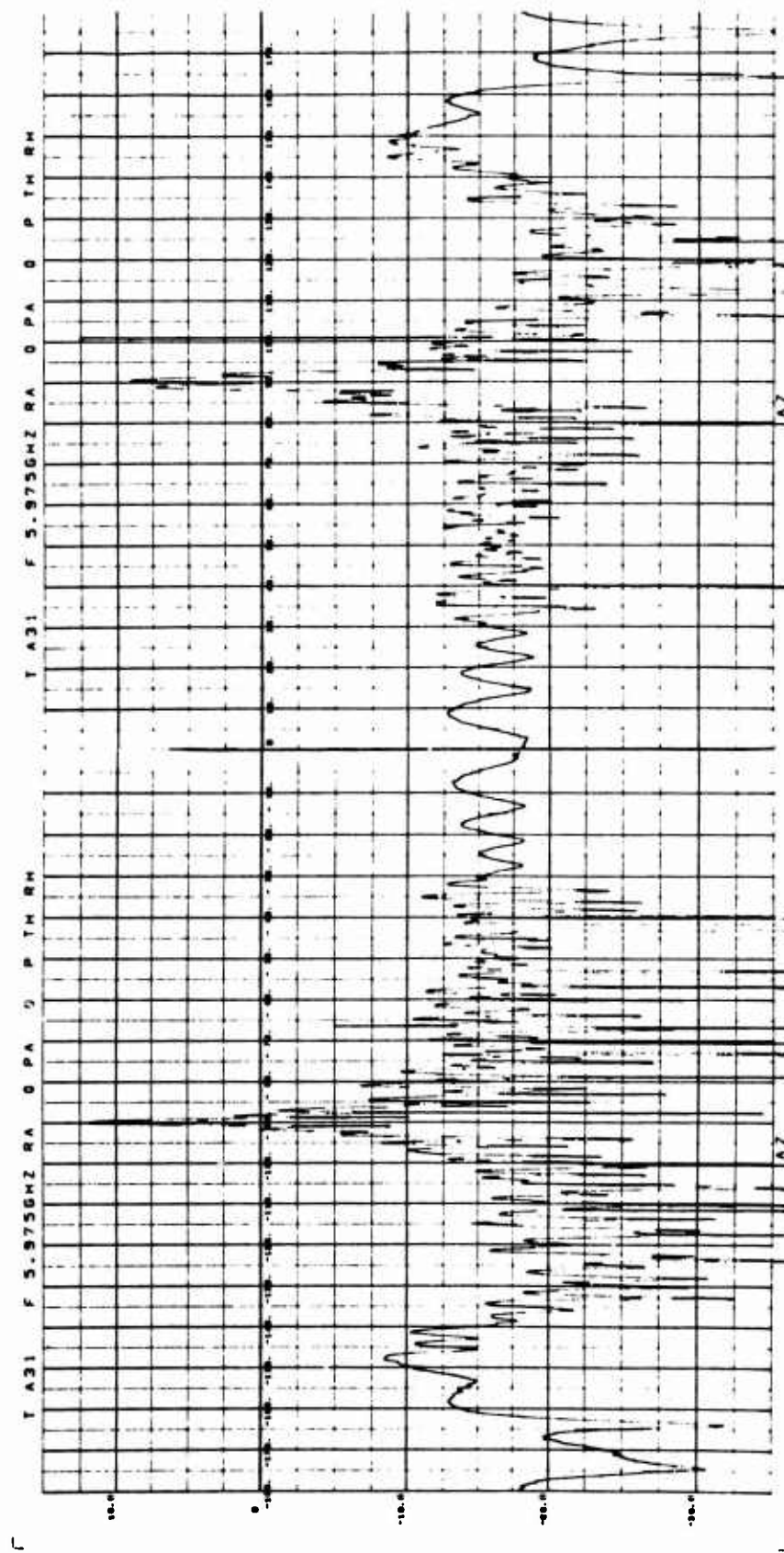
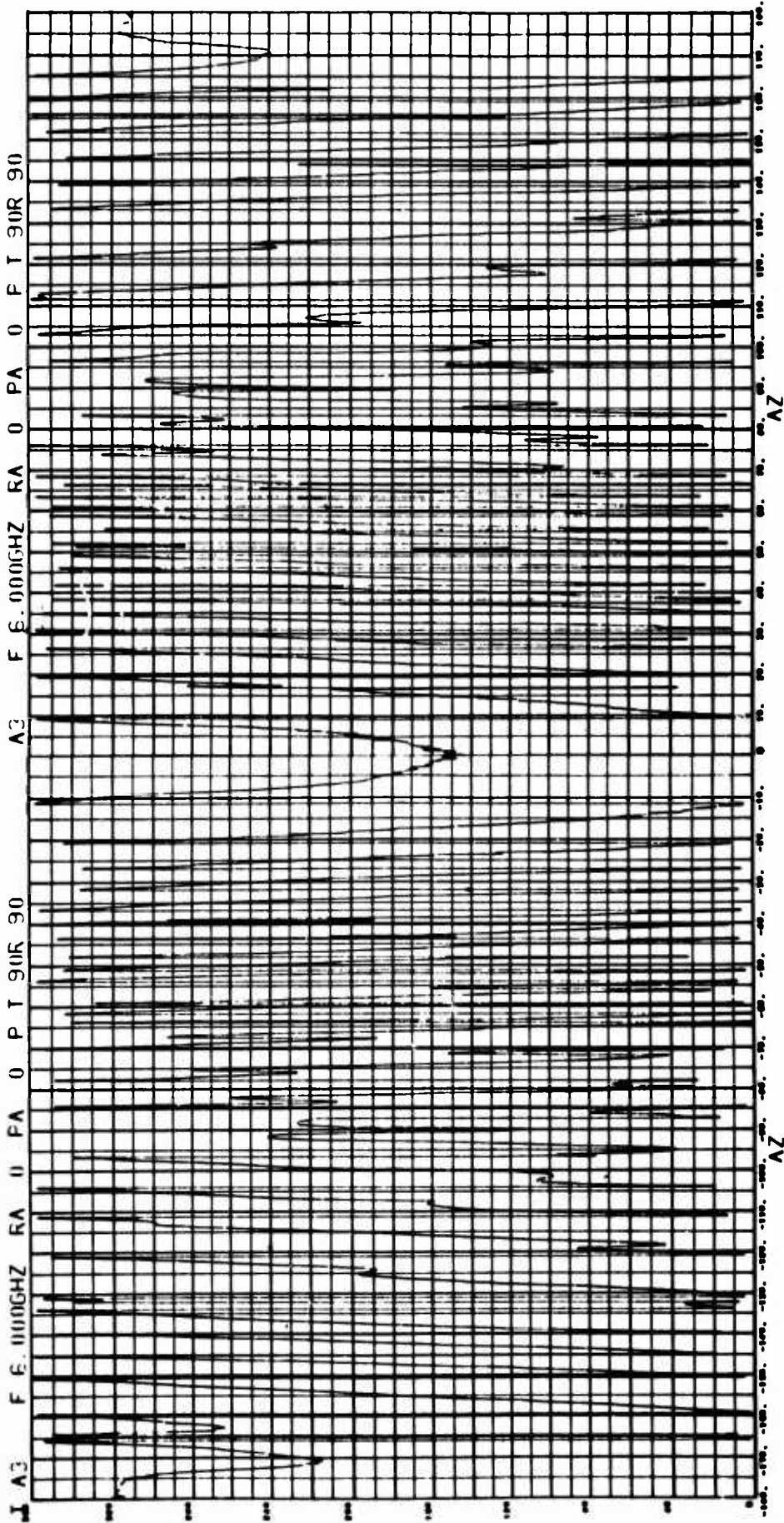


Fig. 4-54 COMPUTED CROSS SECTION FOR MODEL A3 - HH POLARIZATION



169

Fig. 4-55 MEASURED PHASE FOR MODEL A3 - VV POLARIZATION

NOT REPRODUCIBLE

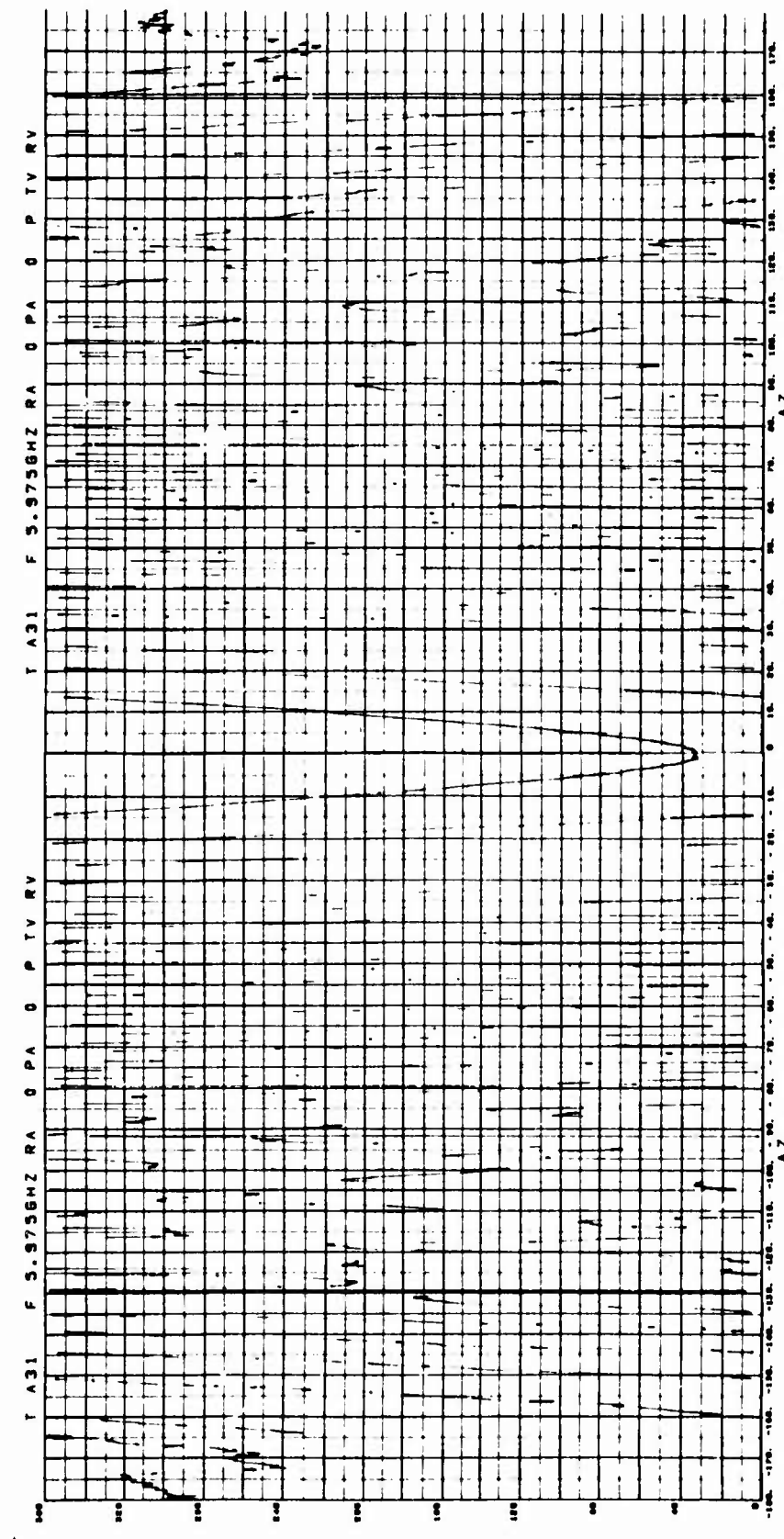


Fig. 4-56 COMPUTED PHASE FOR MODEL A3 - VV POLARIZATION

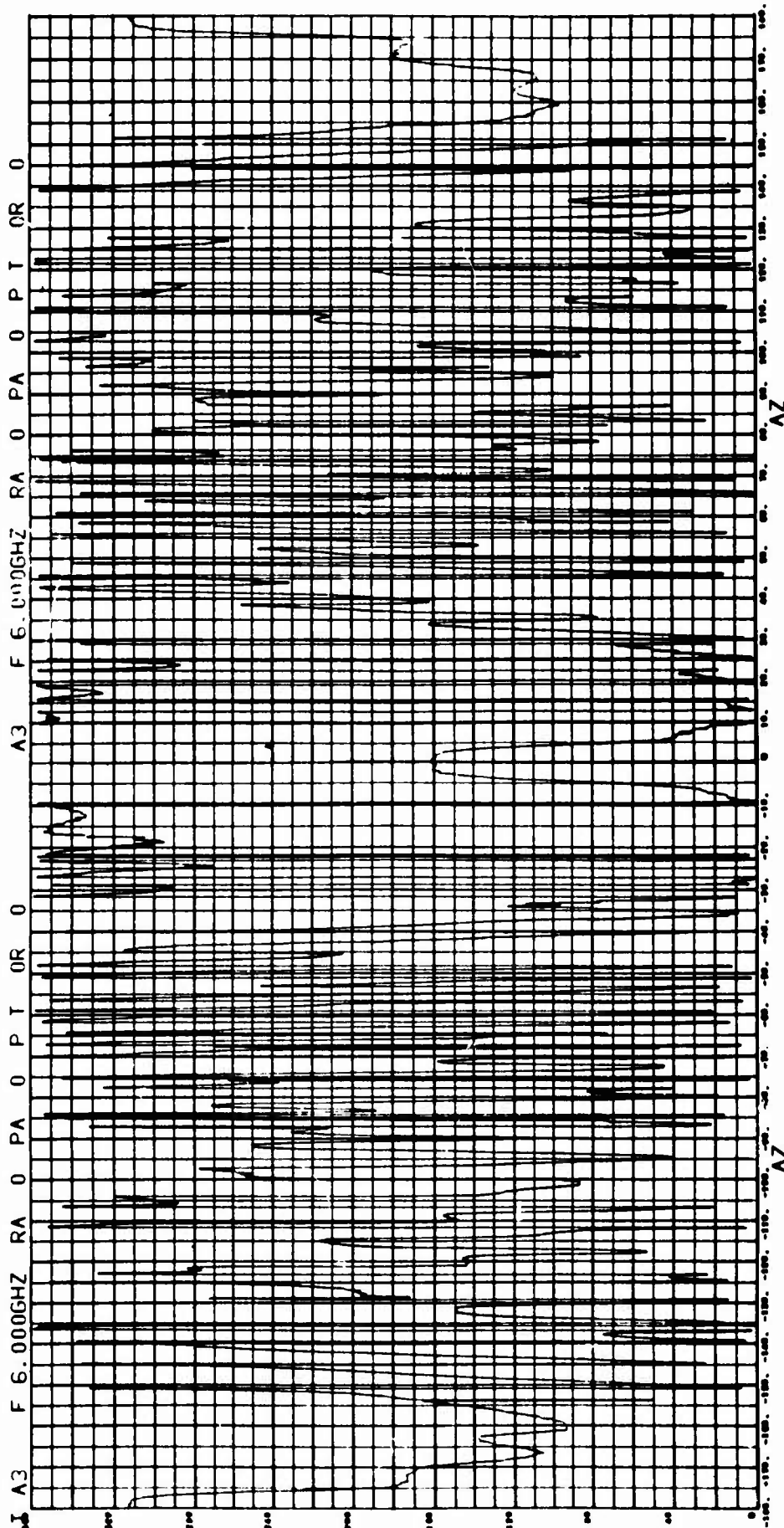


Fig. 4-57 MEASURED PHASE FOR MODEL A3 - HH POLARIZATION

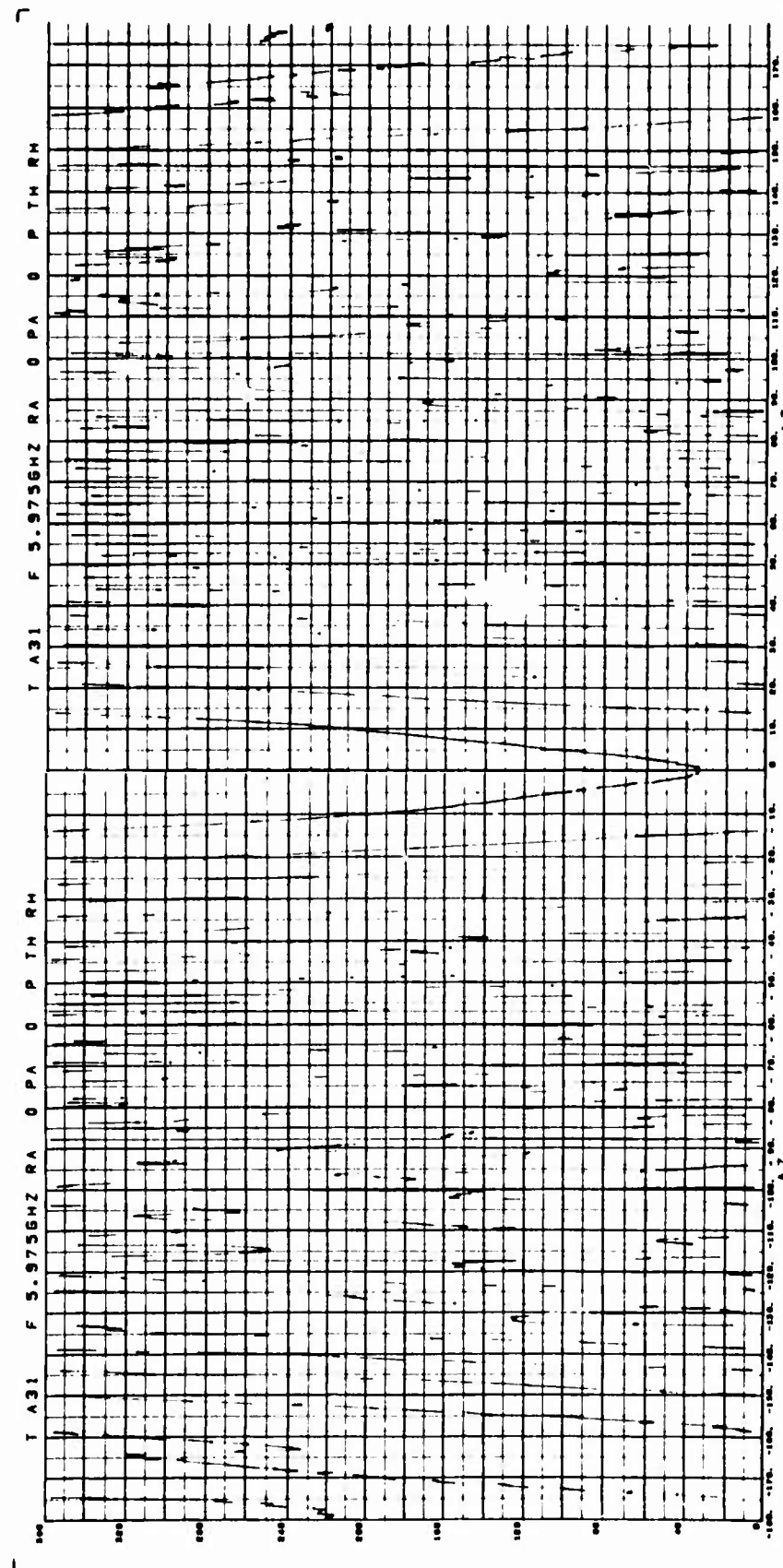


Fig. 4-58 COMPUTED PHASE FOR MODEL A3 - HH POLARIZATION

A comparison of measured and computed data at ψ_{VV} reveals two primary types of error. The most prevalent of these is the amplitude error in the axial aspect regions. Near zero, for example, the large ring discontinuity at the interface of CY2 and CY5 produces a large specular reflection, whereas during superposition this ring cannot be observed without observing the entire end face of CY5. A similar serious error is observed in the region near $\theta = 180$ degrees, and it appears to result from the same type of phenomena. The second type of error occurs in the angular regions where models have been superimposed, and it appears as a decrease in the depths of the nulls of the pattern. This result is actually common to most targets which are superimposed, and it represents the increased number of scattering centers which are observed during superposition relative to the composite case. The same type of errors and approximately the same severity are observed in the case of horizontal polarizations.

Analysis of the phase plots for both polarizations reveals the effects of the use of shadow regions although any attempt to place a physical interpretation on the position of the phase center appears to be of limited value as a result of the discontinuities as well as the high rate of change of phase with respect to aspect.

4.4.5 Model X2

The next superposition vehicle to be considered is Model X2. Model X2 was designed to represent an extremely asymmetrical object which would exhibit a large number of distinct scattering centers. Figure 4-59 contains an illustration of Model X2 in its composite configuration. The center of rotation (the phase reference) was positioned on the center line of connecting rod CR2 at the interface of CR2 and the aft rack AR2. Table 4-7 contains a list of the superposition parameters utilized in this analysis. In the case of this particular configuration, it was subsequently determined that magnetic tape data on Model C3 was not usable; therefore, composite Model C3CY3 was utilized in its place during the superposition process. Figures 4-60 to 4-67 contain plots of measured and computed cross section and phase for Model X2.

A comparison of the computed and measured cross section patterns reveals the fact that the general pattern shapes are quite similar although errors on the order of 2.0 to 2.5 dB are common. In view of the number of scattering centers that contribute in the computed case, these errors are not considered excessive. Also, the configuration of the composite Model X2 is such that significant coupling between scattering centers may be present.

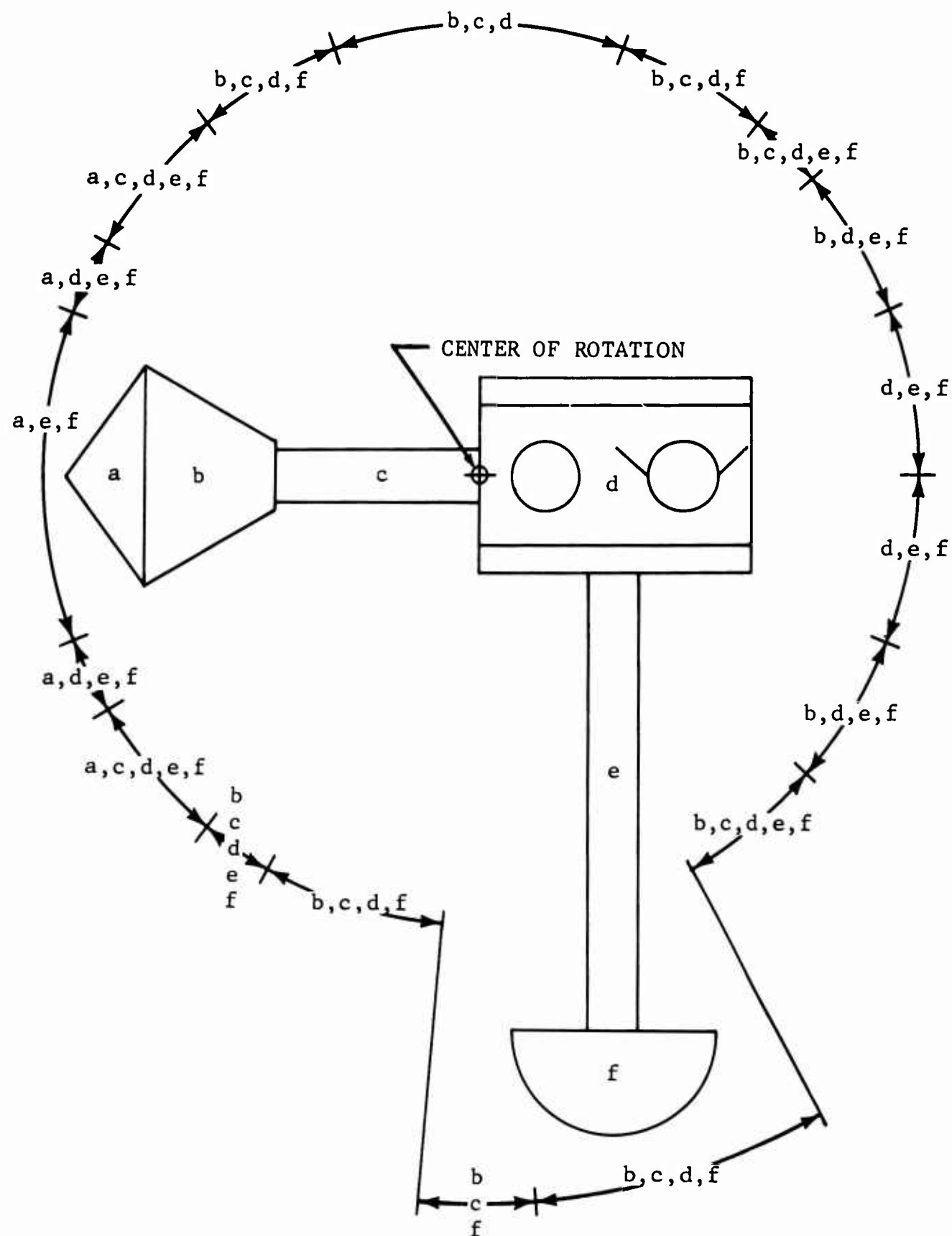


Fig. 4-59 ILLUSTRATION OF SHADOW REGIONS FOR MODEL X2

Table 4-7 MODEL X2 SUPERPOSITION PARAMETERS

COMPOSITE MODEL	FREQUENCY GHZ	BISTATIC ANGLE DEGREES
X2	5.975	0.0

GENERIC SURFACE	FREQ GHZ	POSITION R INCHES	POSITION ERROR ρ DEGREES	SUPERPOSITION PARAMETERS				SHADOW REGIONS			
				D INCHES	δ DEGREES	$\Delta\theta$ DEGREES	ψ_c	θ_{11}	θ_{12}	θ_{21}	θ_{22}
								DEGREES	DEGREES	DEGREES	DEGREES
AR2	5.975	0.0	0.0	8.00	0.0	0.0	-164	160.	200.	265.	275.
C3CY3	5.975	0.019	215.8	4.76	178.8	0.0	63	.1	130.	230.	360.
H3	5.975	0.027	239.6	15.26	285.2	270.0	-36	.1	20.	340.	360.
CR2	5.975	0.077	180.0	9.65	295.0	90.0	-80	.1	40.	150.	210.
CR1	5.975	0.494	0.0	3.00	180.0	0.0	0	.1	40.	150.	210.
F1	5.975	0.365	183.4	10.39	181.2	180.0	19	.1	50.	160.	200.
										320.	360.
										310.	360.

NOT REPRODUCIBLE

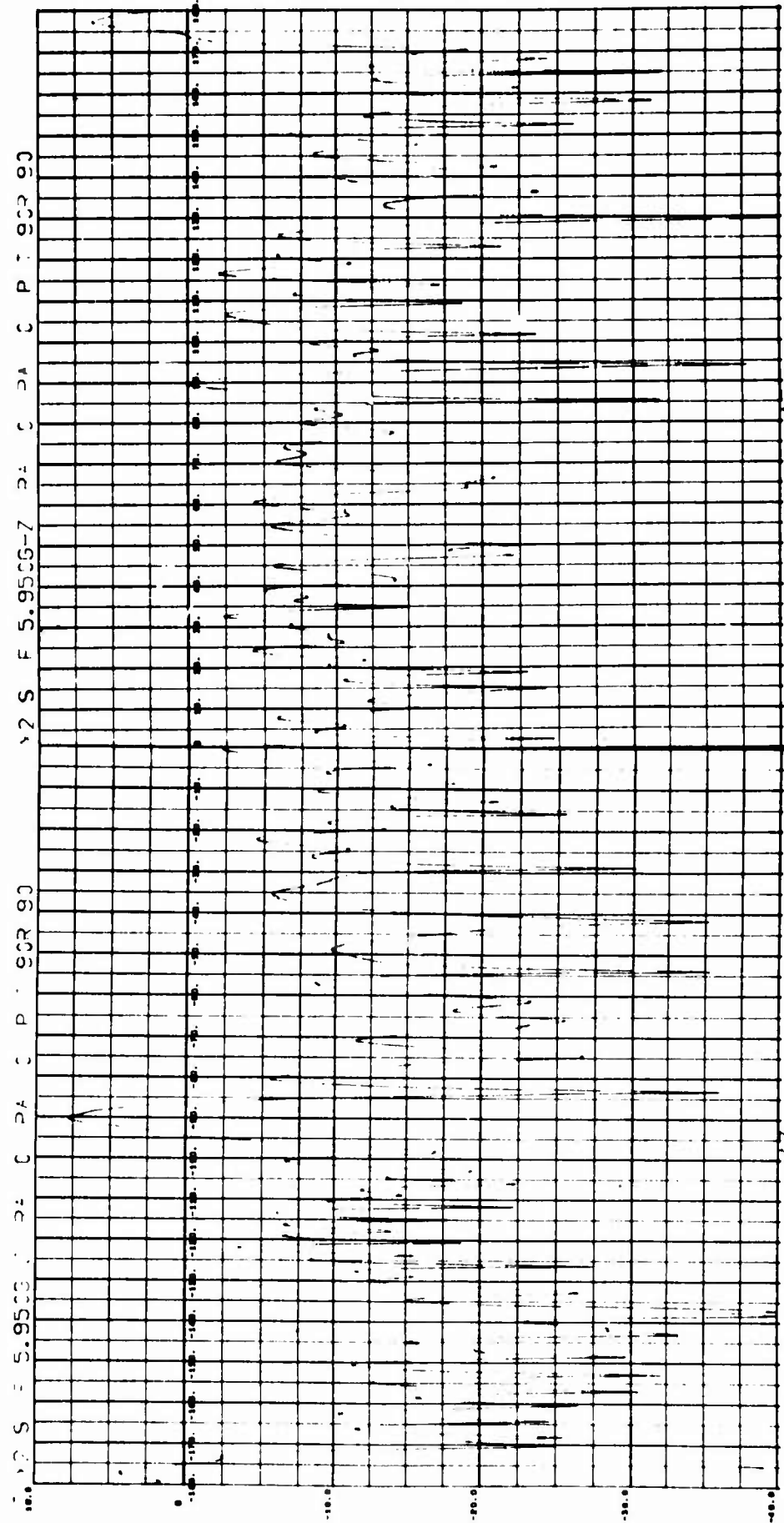


Fig. 4-60 MEASURED CROSS SECTION FOR MODEL X2 - VV POLARIZATION

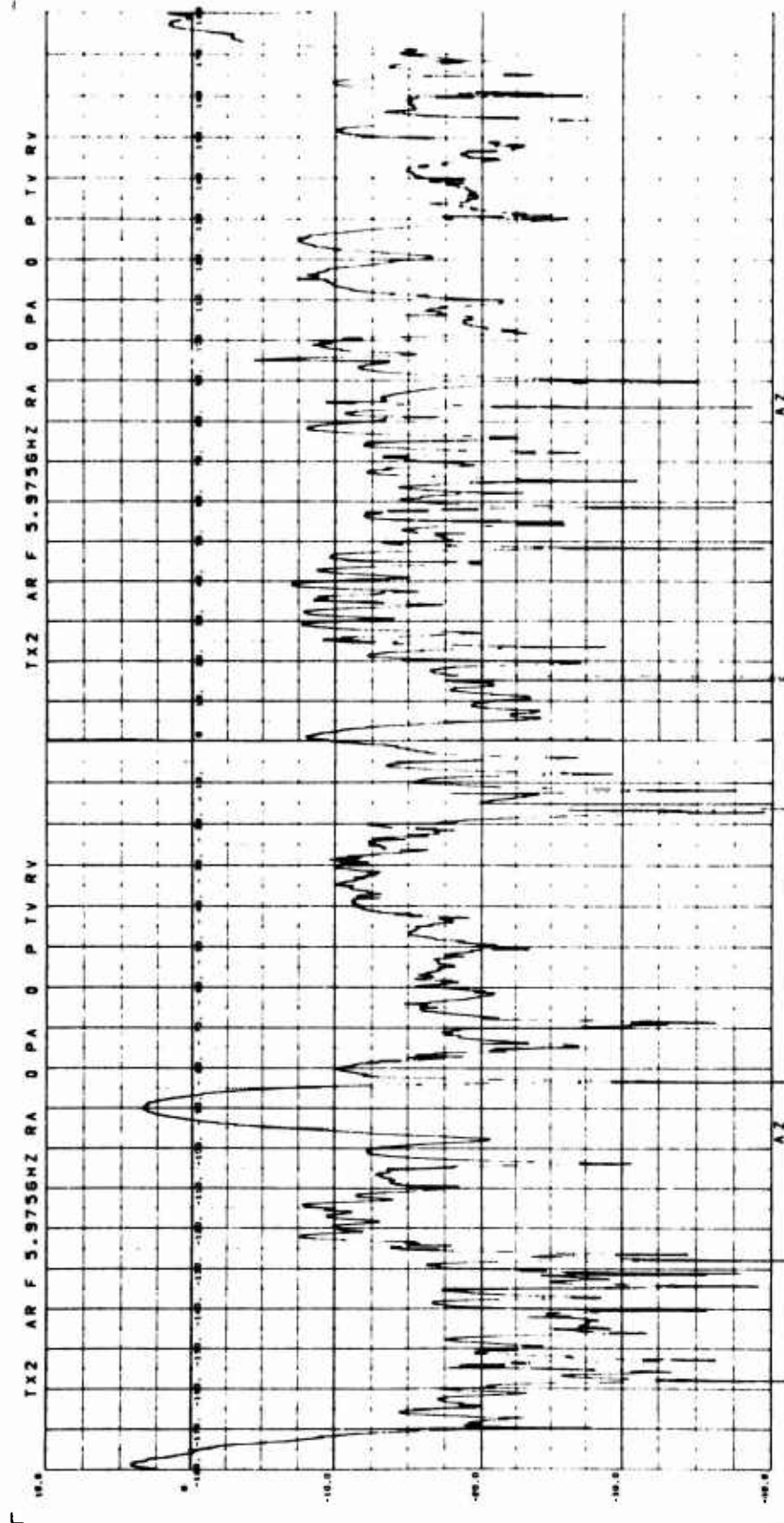


Fig. 4-61 COMPUTED CROSS SECTION FOR MODEL X2 - VV POLARIZATION

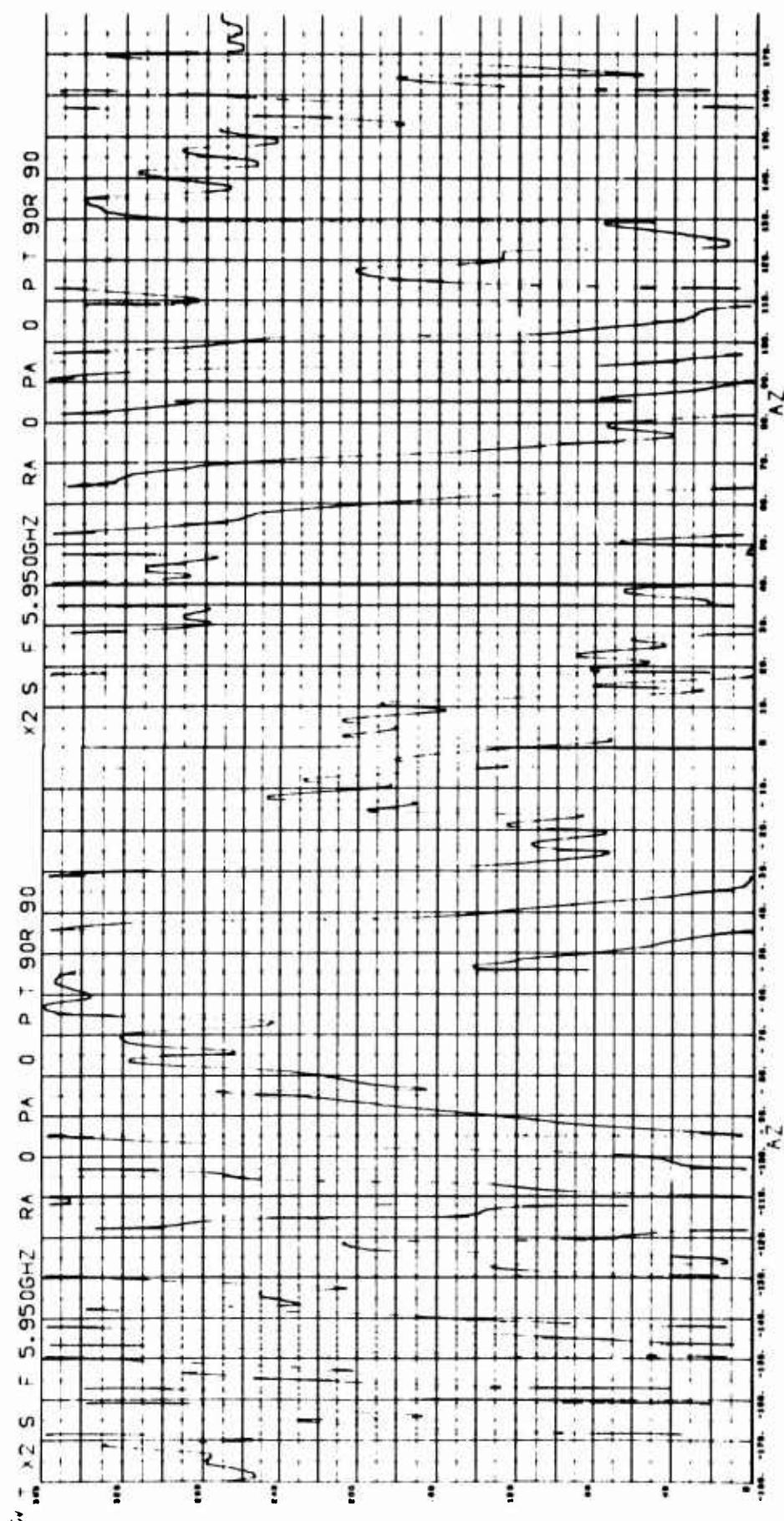


Fig. 4-62 MEASURED PHASE FOR MODEL X2 - VV POLARIZATION

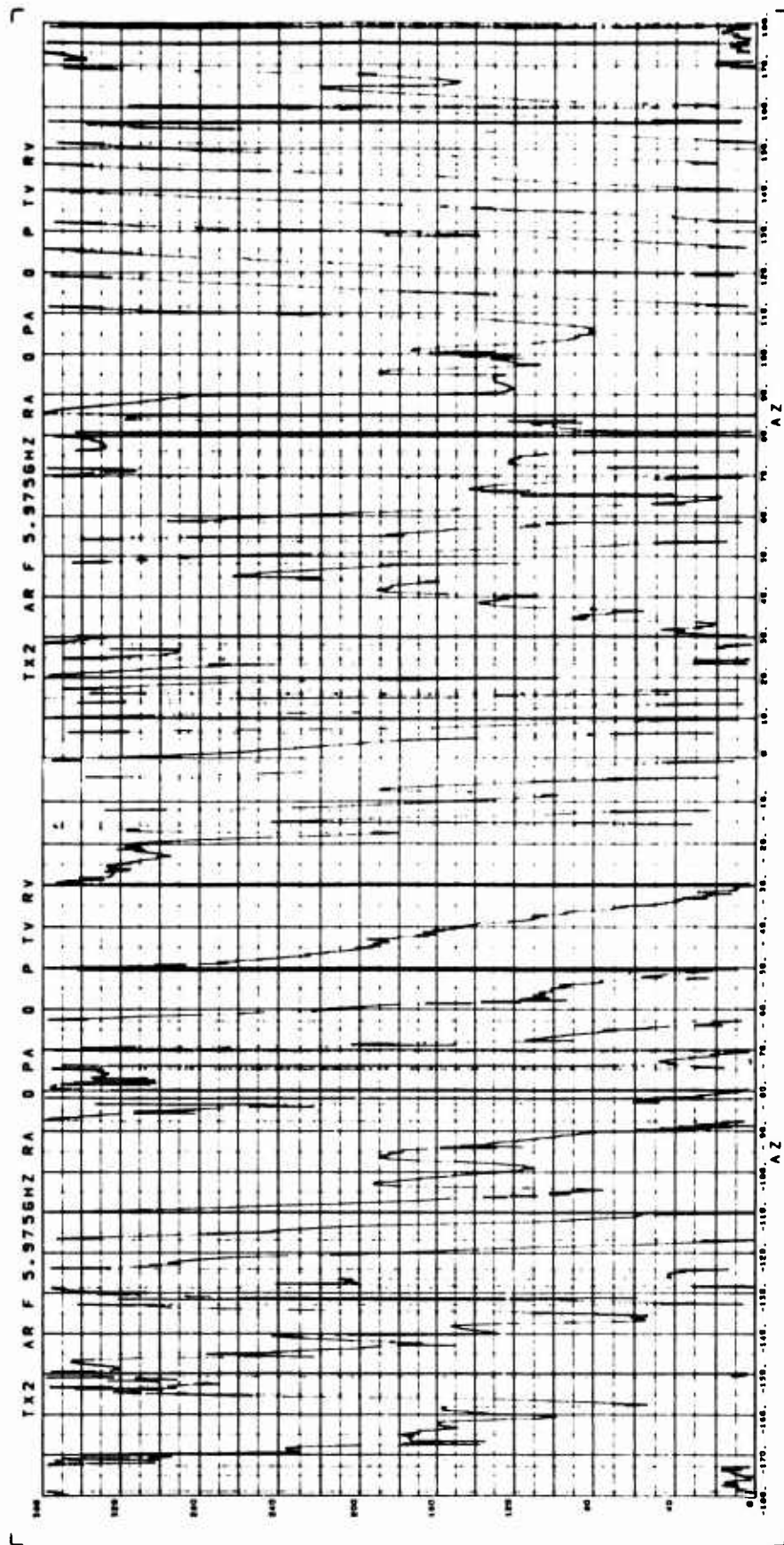


Fig. 4-63 COMPUTED PHASE FOR MODEL X2 - VV POLARIZATION

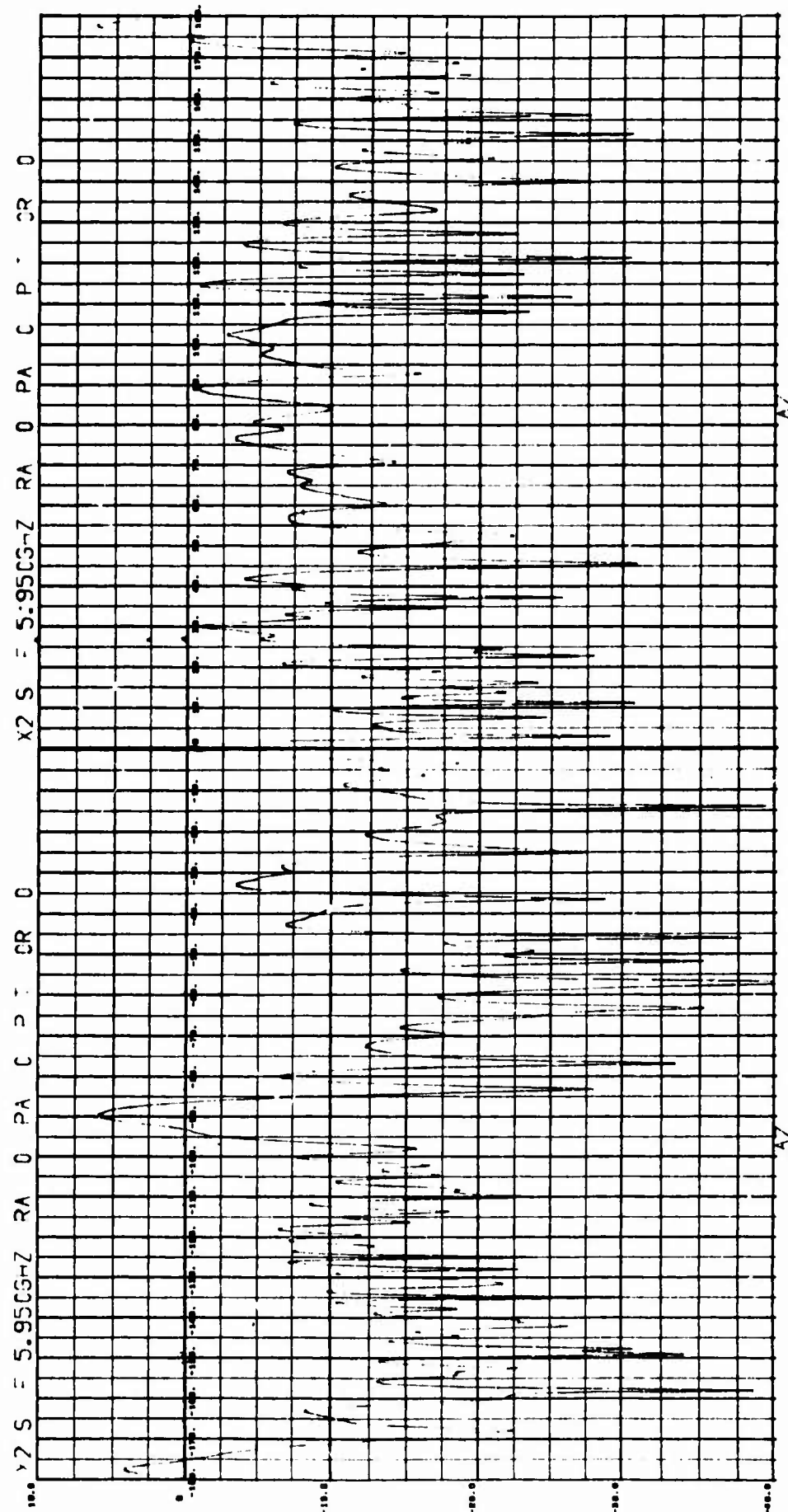


Fig. 4-64 MEASURED CROSS SECTION FOR MODEL X2 - HH POLARIZATION

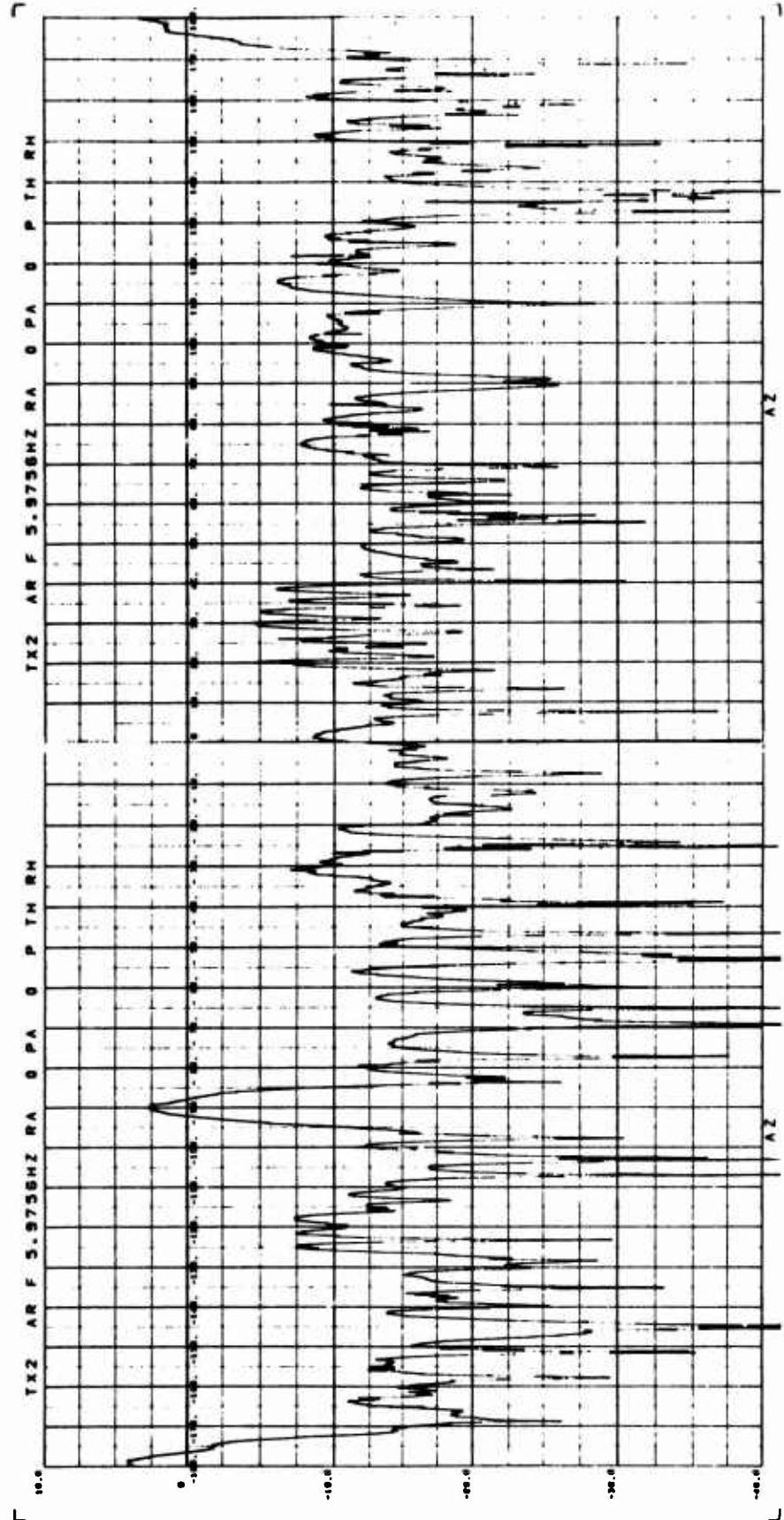


Fig. 4-65 COMPUTED CROSS SECTION FOR MODEL X2 - HH POLARIZATION

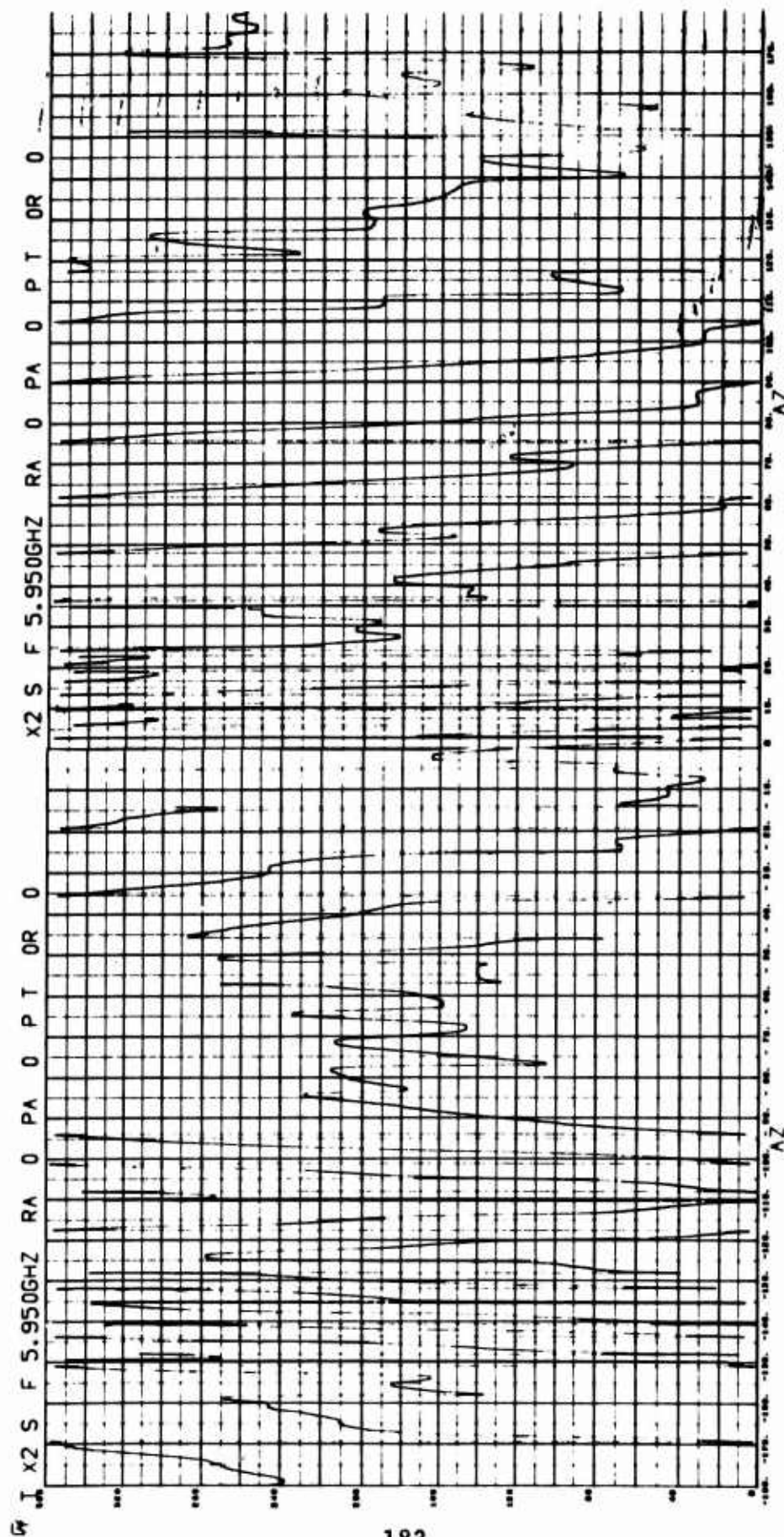


Fig. 4-66 MEASURED PHASE FOR MODEL X2 - LH POLARIZATION

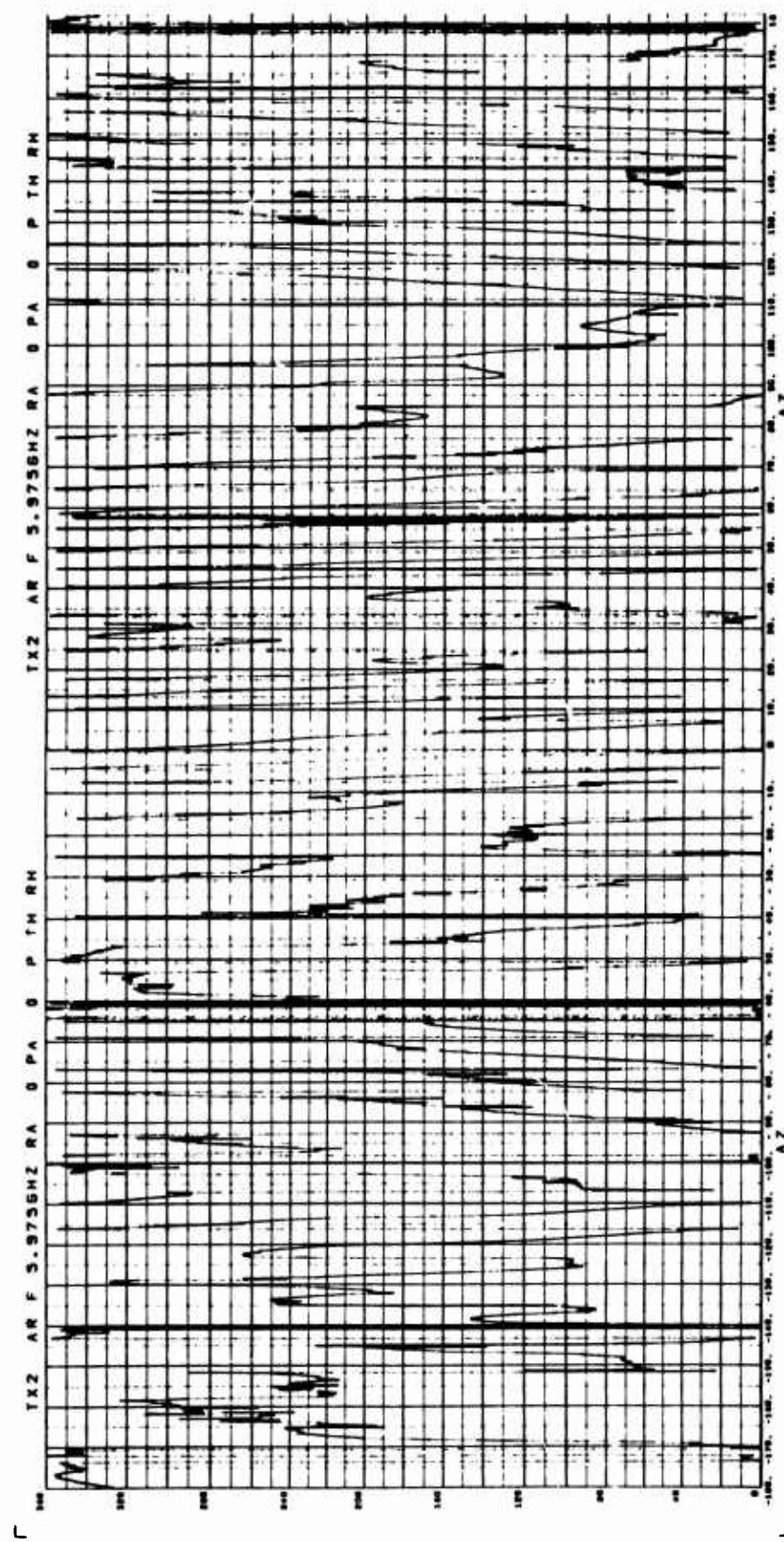


Fig. 4-67 COMPUTED PHASE FOR MODEL X2 - HH POLARIZATION

Computed phase data is observed to exhibit numerous regions where the phase center has jumped from one scattering center to another. Again, in view of the number of scattering centers which contribute in the superposition case, this result is not unexpected. Note that in some aspect regions, five of the six component surfaces are utilized in the superposition process.

It is felt that these results are probably typical of the results to be expected in the case of vehicles which display a large number of dispersed scattering centers and would require the superposition of data from a large number of surfaces.

4.4.6 Model X1

The last superposition model, Model X1, is illustrated in Figure 4-68. Table 4-8 contains the relevant superposition parameters associated with this model. Figures 4-69 to 4-72 contain measured and computed cross section and phase data presented for this model. Analysis of these results reveals that the most serious errors in cross section are contained in the region where Model H2 is assumed to be shadowed by Model H3. The measured cross section pattern indicates that the flat side of Model H2 contributes significantly to the total scattering even when it is optically obscured by Model H3. These results are undoubtedly a

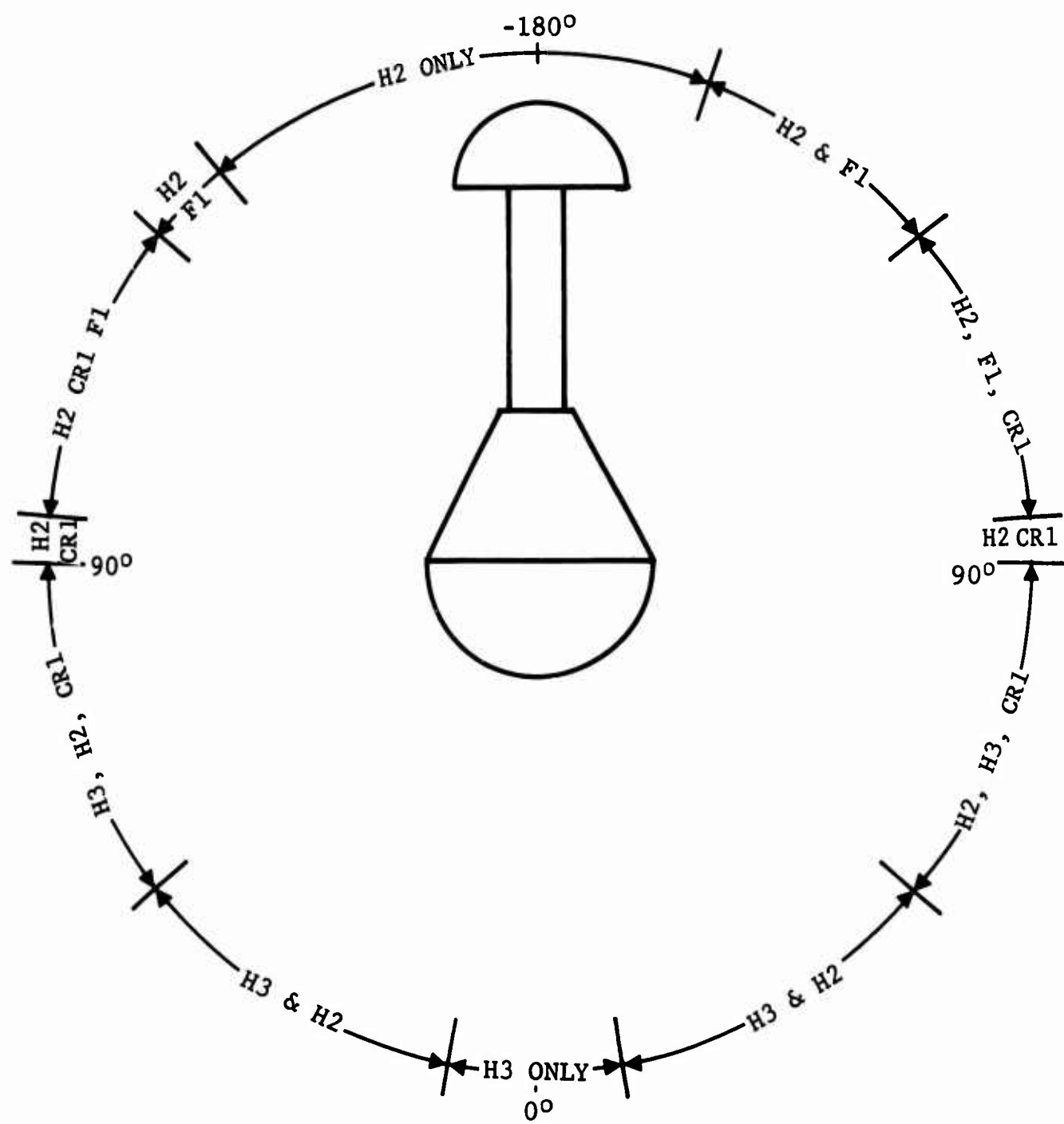
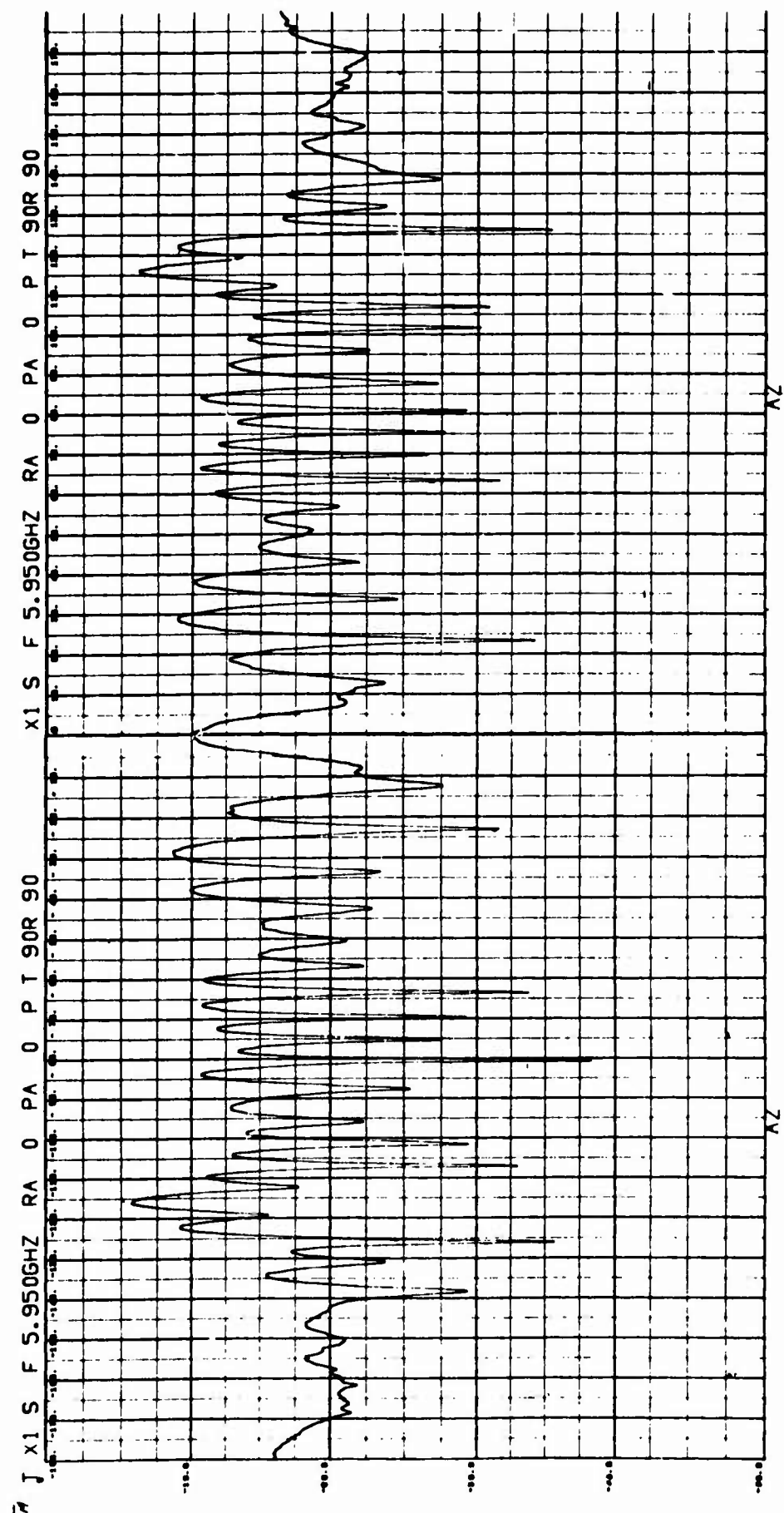


Fig. 4-68 ILLUSTRATION OF SHADOW REGIONS FOR MODEL X1

Table 4-8 MODEL X1 SUPERPOSITION PARAMETERS

COMPOSITE MODEL	FREQUENCY GHZ	BISTATIC ANGLE DEGREES
X1	5.975	0.

GENERIC SURFACE	FREQ GHZ	POSITION ERROR R INCHES	SUPERPOSITION PARAMETERS			SHADOW REGIONS							
			D INCHES	ρ DEGREES	DEGREES	δ	$\Delta\theta$	ψ_c	θ_{11}	θ_{12}	θ_{21}	θ_{22}	θ_{31}
						DEGREES	DEGREES	DEGREES	DEGREES	DEGREES	DEGREES	DEGREES	θ_{32}
F1	5.975	0.365	183.4	.37	3.4	180.	16.	0.1	95.	160.	220.	265.	360.
H2	5.975	0.004	90.	10.03	180.	180.	-22.	0.1	10.	350.	360.		
H3	5.975	0.027	239.6	0.03	59.6	0.	-45.	0.1	90.	270.	360.		
CR1	5.975	0.494	0.0	6.54	180.	0.	-50.	0.1	130.	230.	310.	360.	



188

Fig. 4-69 MEASURED CROSS SECTION FOR MODEL X1 - VV POLARIZATION

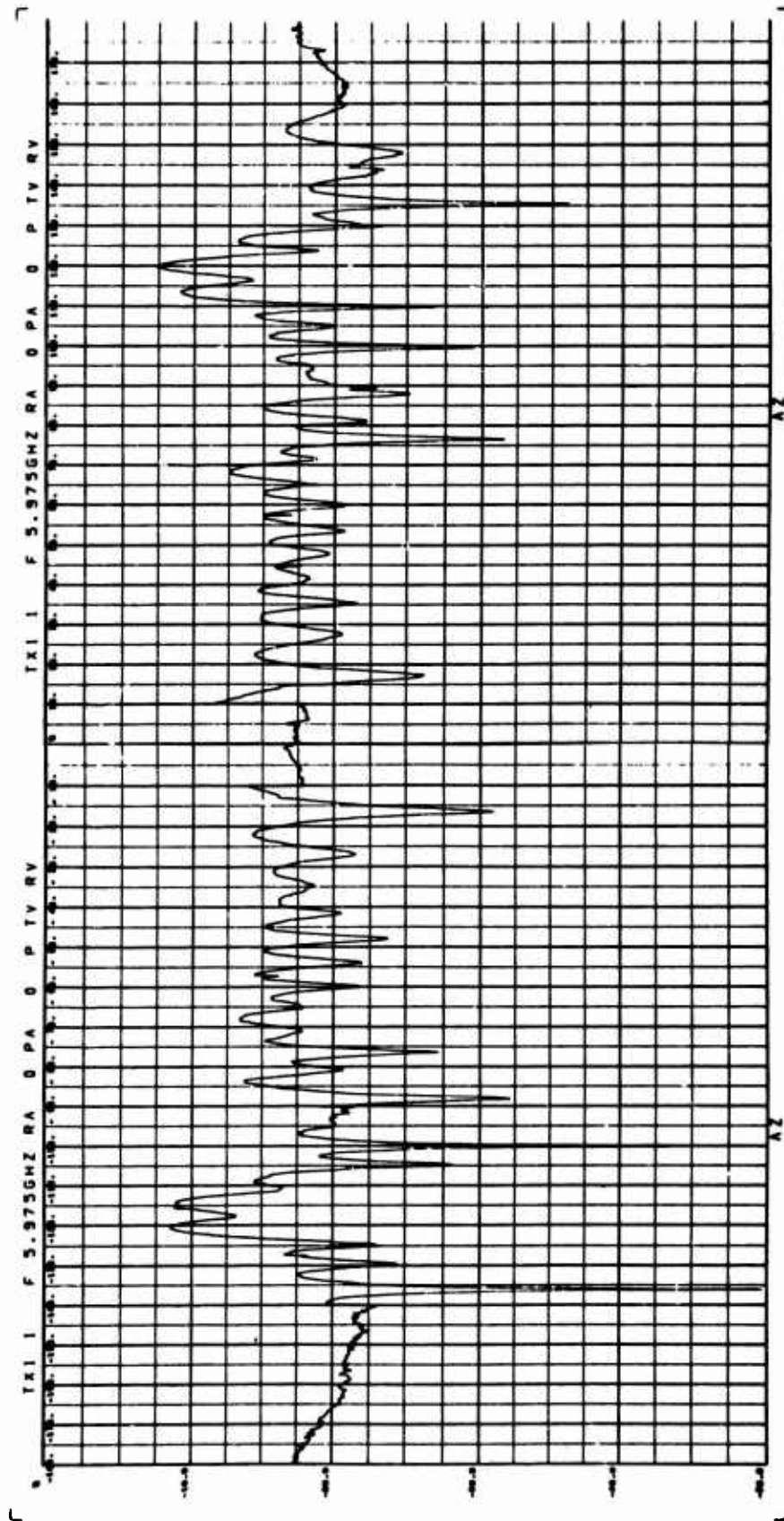
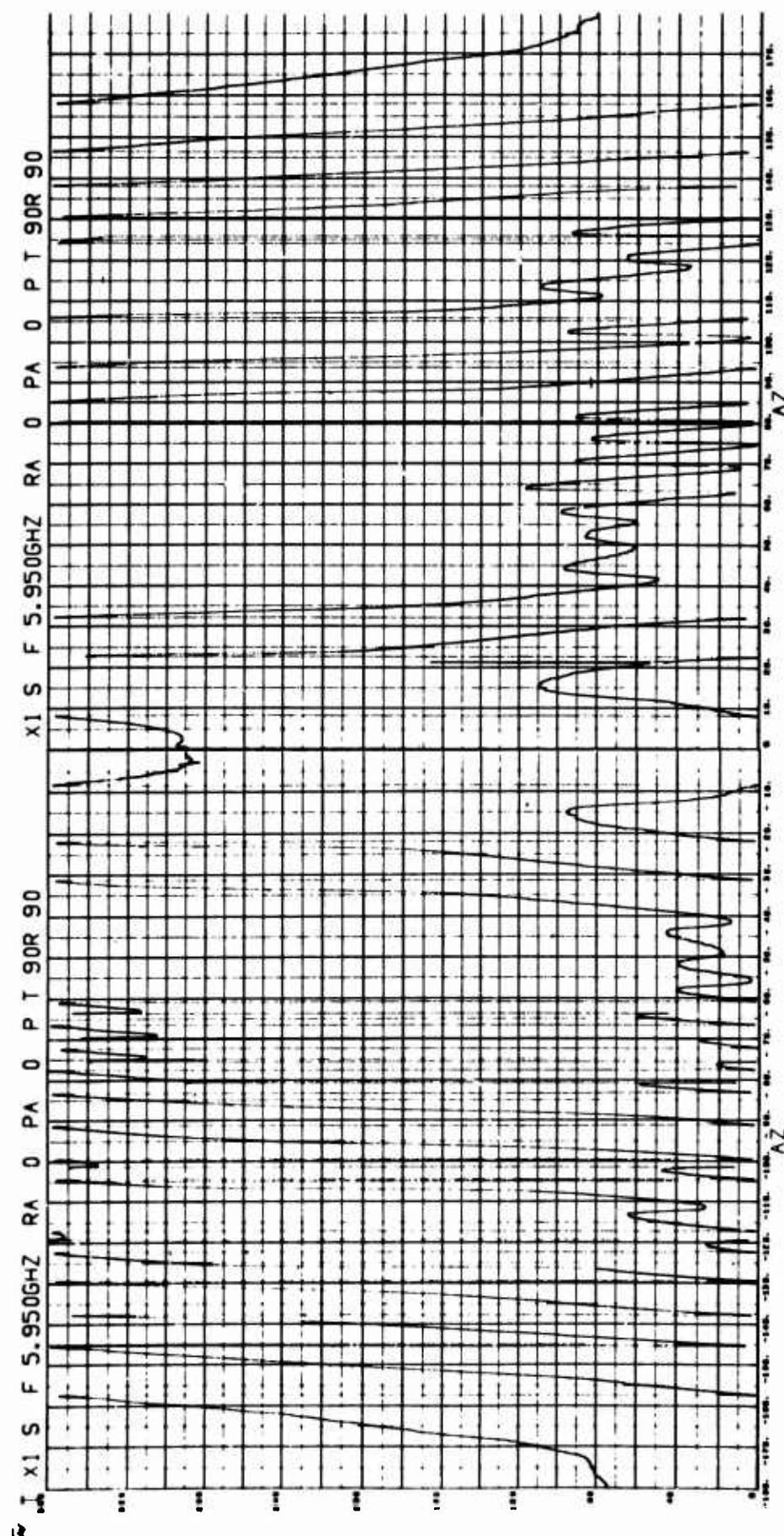


Fig. 4-70 COMPUTED CROSS SECTION FOR MODEL X1 - VV POLARIZATION



190

Fig. 4-71 MEASURED PHASE FOR MODEL X1 - VV POLARIZATION

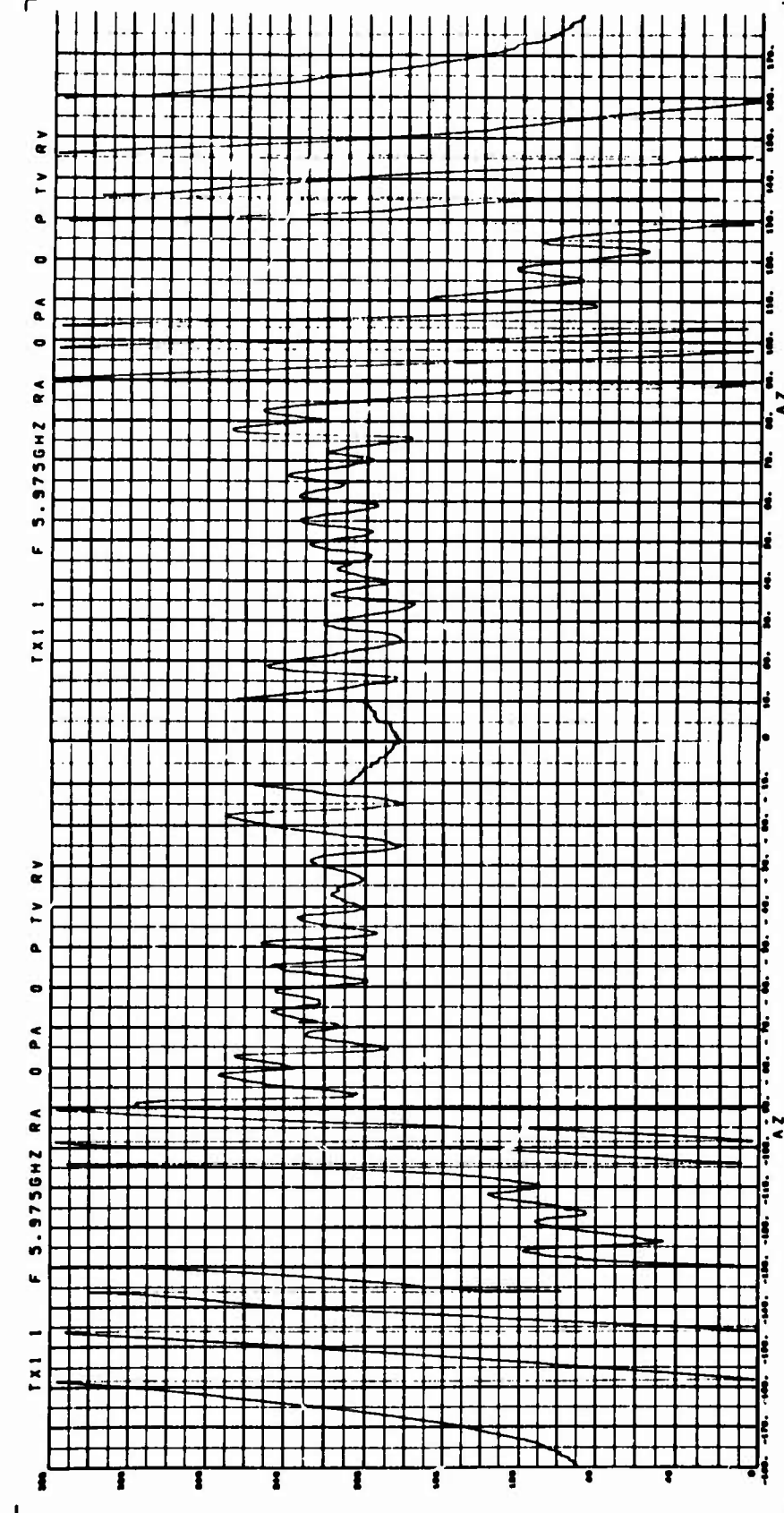


Fig. 4-72 COMPUTED PHASE FOR MODEL X1 - VV POLARIZATION

revelation of a case of significant bistatic scattering between Models H3 and H2. This model would provide an interesting case for evaluation with a short pulse radar. The range resolution of such a system would allow the magnitude of the coupling to be determined experimentally.

4.5 CONCLUSIONS

The data presented in this section are representative of the results obtained, and they exhibit characteristics upon which fairly general conclusions can be based.

The objectives of this investigation were the determination of the range of target characteristics and radar parameters over which the principles of linear superposition can be applied to scattering matrix signatures. A number of these parameters and physical characteristics have been found to be quite significant in terms of the degree of similitude obtained between measured signatures and signatures obtained by use of the superposition technique. These include

1. The number of scattering centers observed
2. Bistatic coupling effects
3. Changes in the number of scattering centers observed as a result of shadowing
4. Changes in surface discontinuities at interfaces of the composite vehicle.

The accuracy of the results obtained by use of the superposition process becomes seriously degraded as the number of significant scattering centers increases. This degradation is primarily a result of radical variations in the position of the target phase center when vehicle measurements are superimposed. This motion corresponds to the interference patterns set up between the phase centers of each of the component vehicle signatures. This effect was well established in analysis of the data presented herein on vehicle F5CY5.

Bistatic coupling was observed in the case of a number of actual measurements, notably in the cases of models AC-4 and X1. In order to accurately synthesize the signature of a target which exhibits bistatic coupling, a model of the bistatic coupling would have to be developed and incorporated into the superposition process. In cases where the position of the target phase center can be accurately determined in space, long-pulse data may be sufficient for determining such a model. However, the observed ambiguities in the position of the phase center, as a function of target rotation of most vehicles of interest in this investigation, precludes the establishment of such a model in the general case. However, the use of high-quality, short-pulse measurements would provide time isolation (range resolution) between

primary and secondary (bistatic) scatterers so that bistatic coupling parameters could be determined.

The selection of shadow boundaries for use in superimposing vehicle signatures should be based upon an analysis of the cross section and phase patterns of the component surfaces. The intent in such a selection is to obtain as smooth a transition as possible between regions where different surfaces are being superimposed. On the basis of the data presented herein, the following criteria pertaining to this selection have been established:

1. Shadow boundaries should be selected so that the significant scattering centers are the same on each side of the boundary.
2. Shadow boundaries should coincide with nulls in the patterns of as many of the component surfaces as possible.
3. In regions where severe bistatic coupling is suspected, less confidence should be placed in the results obtained by use of the superposition process.

The severest errors occurred in the cases where the primary source of scattering from a component surface was a ring discontinuity. This type of discontinuity occurred whenever the aerospace-type vehicles were measured since they, in general, did not exhibit large values of cross

section when they were viewed nose-on. However, the nose-on measurements of their component tips, e.g., cones, hemispheres, and paraboloids, were apparently dominated by scattering from the ring discontinuity at their back edge. In these cases, the decision must be made relative to utilizing (1) the ring discontinuity along, (2) the specular from the surface which interfaces with the ring discontinuity, or (3) to use superposition. None of these methods appears to be adequate as a general solution to this particular problem.

However, since the near nose-on aspect of aerospace type vehicles is of considerable concern to those interested in Ballistic Missile Defense, it may be that further investigations would be fruitful in this area. The number of different nose configurations suitable for re-entry is actually quite small, and it appears that the major scattering sources at these aspects may be located a distance behind the tip and may consist primarily of fins, antennas, and other perturbations.

In aspect regions well removed from the aspects where the vehicle exhibits a large depth along the RLOS, linear superposition may be used with a great deal of confidence since in these regions (1) bistatic coupling is less prevalent, (2) few significant scattering centers are shadowed, and (3) the phase center of the component surfaces are generally well behaved.

The number of vehicle shapes which can be synthesized by use of the 16 generic surfaces measured during this program is innumerable, even for the case of only one frequency. The measurement of these surfaces over a selected spectrum of frequencies would provide a comprehensive bank of data by which "first look" cross section data would be obtained for almost any vehicle of interest in BMD or Space Object Identification (SOI).

SECTION 5

SYNTHESIS INVESTIGATION

5.1 General

The objective set for the investigation described in this section was to determine the feasibility of synthesizing complex radar targets by combining basic generic scattering surfaces. This is in contrast to the effort reported in Section IV which dealt with the computation of signatures for complex radar targets by use of signatures obtained using generic surfaces.

The motivation for the synthesis investigation was the desire to obtain information relative to the sensitivity of radar signatures to vehicle physical detail. Information of this type is of great interest to both the vehicle designer and the radar designer, for one may be interested in designing simple vehicle decoys while the other would like to employ as simple a radar as possible as a means of discriminating between actual target vehicles and decoys.

5.2 Technical Approach

To accomplish this task, generic shapes were combined in varying degrees of physical similitude relative to their actual counter parts of a complex radar target. The scattering matrices of both the synthesized and the actual

vehicle were then measured at a common frequency for a full rotation of the vehicles. An objective comparison of the resulting signature measurements was then undertaken utilizing a number of signature features.

The simplest and most obvious comparison technique is a comparison of the plots of cross section versus azimuth for the actual and the synthesized vehicles. A logical approach to this type of comparison can be achieved by looking first at the envelope of the peak values of cross section and then considering the detailed point-by-point differences in the patterns.

However, it was felt that an automated or computerized comparison would be of greater significance since an operational computerized classification scheme is of definite interest to those involved in SOI and/or BMD. In order to accomplish this comparison, the synthesis investigation was linked very closely with the inverse scattering analysis which is briefly described in Section VI and reported in detail in Reference 3 (Volume IV of this Technical Report). The comparative techniques which were programmed and used to evaluate the results of target synthesis were as follows:

1. Matched Filter Technique
2. Polarization Signature Technique
3. Phase Signature Technique

5.3 Results and Conclusions

Due to the sensitive nature of some of the actual vehicles which were synthesized during this investigation, detailed results of individual comparisons are not included herein. The detailed results of both this and the inverse scatterings analysis are contained in Reference III.

However, there are some quite general results of this investigation which can be reported in this document. For the most part, the targets which were measured during this investigation, both actual and synthesis targets, exhibited approximately the same overall length, i.e., they were in the same kL range. The primary physical differences were obtained by use of different types of generic surfaces which produced considerably different discontinuities at the interface of such surfaces. Figure 5-1 illustrates typical surface discontinuities which were produced using synthesis vehicles.

The radar signatures obtained by use of the three degrees of synthesis illustrated in Figure 5-1 were generally very similar except in two aspect regions (1) nose-on, and (2) the aspect region corresponding to broadside to the cones and frusta. The large errors exhibited near nose-on in the superposition investigation adds credence to the fact that it is very difficult to simulate the long pulse scattering

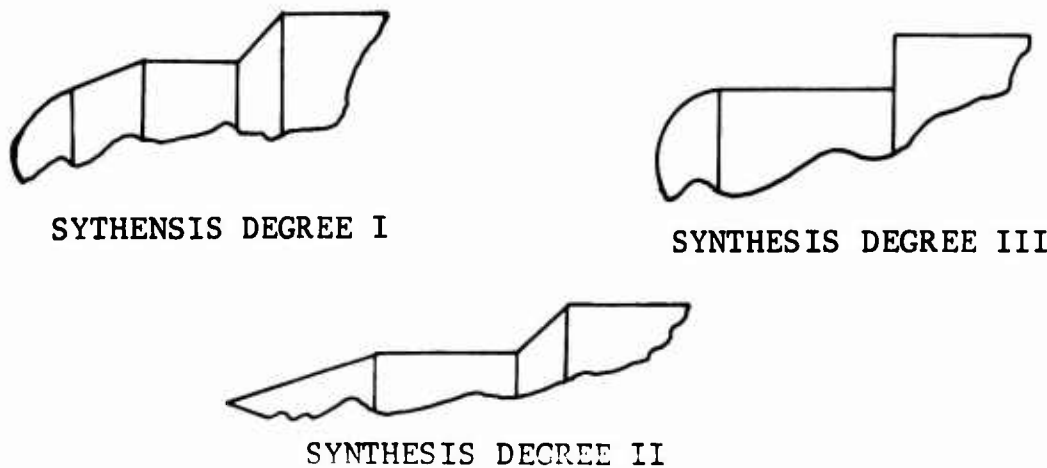


Fig. 5-1 GENERIC SURFACE DISCONTINUITIES EXHIBITED
BY SYNTHESIS VEHICLES

properties of a long narrow object when viewed from the end-on aspect. On the other hand, the similarity between the cross section patterns obtained for the subject vehicles near broadside to the axis of the vehicles indicates a general insensitivity of scattering to changes in the vehicle profile, if the value of kL is not drastically modified.

The results indicate that the scattering properties of an aerospace type vehicle (large length to width ratio) may be easily altered in the angular regions near nose-on for the ka regions corresponding to those used in this investigation.

SECTION 6

INVERSE SCATTERING INVESTIGATION

6.1 General

The objective set for the inverse scattering analysis was to develop, implement and evaluate analytical techniques which can be applied to radar target signatures in order to obtain quantitative measures of the degree of similitude between target signatures. A second objective was to evaluate these results in terms of the degree of similitude between the actual vehicles used to obtain the signatures.

Three distinct analytical techniques were investigated during this investigation. Each of these was based on the use of a different characteristic or set of characteristics of radar signatures. The three techniques are:

1. Matched Filter Technique
2. Polarization Technique
3. Phase Technique.

The salient points of each of these techniques are briefly discussed in the following subsections, however, in view of the potential for the utilization of these techniques in military applications, e.g., SOI and BMD, the bulk of the analysis and results is being published in Volume IV of this

Technical Report. (Reference 3). Target signatures utilized in this investigation included those obtained for use in the Synthesis Investigation described in Section V of this volume.

6.2 Matched Filter Technique

The Matched Filter Technique (MFT) was developed as a true inverse scattering technique. The input data used in conjunction with the MFT consists of measured radar scattering cross section and phase data. The output obtained by use of the MFT consists of a set of numbers which may be directly used to estimate the location of target scattering centers in the coordinate system containing the target vehicle.

6.2.1 Analytical Approach

The total radar cross section of a vehicle may be expressed as the phasor sum of the energy scattered toward the radar receiver from all of the scattering centers on the vehicle. This summation is expressed in Equation 6-1 for the case of N scattering centers.

$$\sqrt{\sigma(\theta)} e^{j\psi(\theta)} = \sum_{m=1}^N \sqrt{\sigma_m(\theta)} e^{j2kL_m \cos(\theta - \theta_m)} \quad (6-1)$$

where

L_m = Radial position of the m^{th} scattering center

θ_m = Azimuth position of the m^{th} scattering center

$$k = 2\pi / \lambda = \text{Wave number}$$

$$\lambda = \text{Wavelength}$$

Multiplication of both sides of Equation 6-1 by the term $e^{-j2kD_i \cos(\theta - \theta_j)}$ and integration of the product over a range of aspect angles from $\theta_0 - \Delta\theta$ to $\theta_0 + \Delta\theta$ gives a function of D_i and θ_j

$$\begin{aligned} \rho(D_i, \theta_j) &= \int_{\theta_0 - \Delta\theta}^{\theta_0 + \Delta\theta} \sqrt{\sigma(\theta)} e^{j[\psi(\theta) - 2kD_i \cos(\theta - \theta_j)]} d\theta \\ &= \int_{\theta_0 - \Delta\theta}^{\theta_0 + \Delta\theta} \sum_{m=1}^N \sqrt{\sigma_m(\theta)} e^{j2k[L_m \cos(\theta - \theta_m) - D_i \cos(\theta - \theta_j)]} d\theta \end{aligned} \quad (6-2)$$

Interchanging the order of integration and summation in Equation 6-2 gives

$$\rho(D_i, \theta_j) = \sum_{m=1}^N \int_{\theta_0 - \Delta\theta}^{\theta_0 + \Delta\theta} \sqrt{\sigma_m(\theta)} e^{j2k[L_m \cos(\theta - \theta_m) - D_i \cos(\theta - \theta_j)]} d\theta \quad (6-3)$$

For given values of $\sqrt{\sigma_m(\theta)}$, the right hand side of Equation 6-3 exhibits a maximum when $D_i = L_m$ and $\theta_j = \theta_m$, i.e., when D_i and θ_j represent the location of the actual scattering centers. Thus, $\rho(D_i, \theta_j)$ in Equation 6-2 can be viewed as a correlation coefficient expressing the correlation between the locations of actual scattering centers (L_m, θ_m) and hypothesized scattering centers (D_i, θ_j) . Equation 6-4

contains the expression showing how the correlation coefficients would be obtained using measured signatures.

$$\rho(D_i, \theta_j) = \int_{\theta_o - \Delta\theta}^{\theta_o + \Delta\theta} \sqrt{\sigma(\theta)} e^{j[\psi(\theta) - 2kD_i \cos(\theta - \theta_j)]} d\theta \quad (6-4)$$

The use of a correlation function or match filter of the form $e^{-j2kD_i \cos(\theta - \theta_j)}$ rather than one containing an amplitude coefficient is based on the following reasoning. In the case of most scattering centers of interest (for example wedges and edges of curved surfaces) GDT shows that the amplitude of the scattered energy varies rather slowly with small changes in aspect. Therefore, it seems logical to assume that changes in total cross section which result from small angular rotations of the target are primarily a result of the change in relative phase between the contributing scattering centers.

Two computer programs were written in order to evaluate the utility of the expression contained in Equation 6-4. The first of these computer programs utilized library data in the form of analytically computed cross section and phase data. The purpose of the analysis using this program was to obtain information concerning the overall resolution which could be realized by use of the MFT. This program is described in the following paragraph.

6.2.2 Application of MFT to Synthesized Signatures

The computer program developed as an aid in the investigation of the sensitivity of the MFT was written in BASIC language for use with the GE 265 time-sharing terminal at the Fort Worth Division. Library data for this program consists of the location and strength (in dBsm) of a set of three discrete point scatters. Each of these scatterers is isotropic, i.e., they scatter equally well in all directions and therefore represent scattering sources of constant strength. Table 6-1 contains a listing of this program designated MFTGE 265. The input and output parameters of this program are defined in Table 6-2. Figure 6-1 shows the geometrical relationship between the input and output parameters.

The total complex scattering pattern which is synthesized by the three discrete scatterers is given by Equation 6-5, which is identical to Equation 6-1 with $N=3$.

$$\sqrt{\sigma(\theta)} e^{j\psi(\theta)} = \sum_{m=1}^3 \sqrt{\sigma_m(\theta_m)} e^{j2kL_m \cos(\theta - \theta_m)} \quad (6-5)$$

The Matched Filter process is based on the computation of a set of correlation functions obtained by correlating a function of the form

$$e^{-j2kD \cos(\theta - \theta_j)}$$

Table 6-1 LISTING OF COMPUTER PROGRAM MFTGE265

```

5 DIMA(30),E(30),G(30)
6 DIM P(36),U(10,36),R(10,36)
15 READ D1,D2,D3,T1,T2,T3,S2,S3
20 READ N1,N2,N3,D0,D4,T4,C2,W1
25 READ C1
26 FOR W2=1 TO W1
27 READ Z(W2)
30 NEXT W
35 PRINT"D1="D1;"D2="D2;"D3="D3
40 PRINT"T1="T1;"T2="T2;"T3="T3;"SR2="S2;"SR3="S3
45 PRINT"N1="N1;"N2="N2;"N3="N3
50 PRINT"LO="D0;"DEL L="D4;"PSIS="T4;"DEL PSIS="C2
55 PRINT"NO. OF WINDOWS="W1
60 PRINT"DEL THETA="C1
65 FOR W2=1 TO W1
70 PRINT"THETA "Z(W2)
75 NEXT W
80 PRINT
85 LET F1=3.14159/180
90 LET D1=12.56636*D1
95 LET D2=12.56636*D2
100 LET D3=12.56636*D3
105 LET C1=F1*C1
110 LET C2=F1*C2
115 LET T1=F1*T1

120 LET T2=F1*T2
125 LET T3=F1*T3
130 LET T4=F1*T4
135 LET R2=10*(S2/20)
140 LET P3=10*(S3/20)
141 FOR I=1 TO N1
142 FOR J=1 TO N2
143 LET U(I,J)=1
144 LET V(I,J)=1
145 NEXT J
146 NEXT I
150 FOR W2=1 TO W1
155 FOR K=1 TO N3
160 LET A(K)=Z(W2)*F1+(K-1)*C1
165 LET E(K)=D1*COS(A(K)+T1)
170 LET F(K)=D2*COS(A(K)+T2)
175 LET G(K)=D3*COS(A(K)+T3)
180 NEXT K
183 FOR J=1 TO N2
185 LET P(J)=T4+(J-1)*C2
187 NEXT J
189 PRINT
190 PRINT"WINDOW" W2

195 FOR I=1 TO N1
200 PRINT"I="I
215 LET L(I)=I2.56636*(D0+(I-1)*D4)
220 FOR J=1 TO N2
225 LET S4=0
227 LET S5=0
230 FOR K=1 TO N3
235 LET F2=L(I)*COS(A(K)+P(J))
240 LET X1=E(K)-F2
245 LET X2=F(K)-F2
250 LET X3=G(K)-F2
255 LET S4=S4+COS(X1)+R2*COS(X2)+R3*COS(X3)
260 LET S5=S5+SIN(X1)+R2*SIN(X2)+R3*SIN(X3)
265 NEXT K
270 LET O=SQR(S4^2+S5^2)
275 PRINT J;O;
280 IF J<>1 THEN 300
285 LET R9=0
290 LET R8=J
295 GO TO 305
300 IF O>=R9 THEN 285
305 LET U(I,J)=U(I,J)*O
306 LET V(I,J)=V(I,J)*O
307 NEXT J
310 PRINT
315 PRINT"BIG="R9;" JBIG="R8
316 IF I<>1 THEN 319
317 LET R7=R9
318 GO TO 320
319 IF R9>=R7 THEN 317
320 NEXT I
321 NEXT W2
322 PRINT
324 LET R6=R7!W1
325 PRINT"BIGGEST="R7
327 PRINT
328 PRINT"PRODUCT OUTPUT NORMALIZED TO BIGGEST!W1="R6
330 PRINT
335 FOR I=1 TO N1
340 PRINT"I="I
345 FOR J=1 TO N2
350 PRINT J;100*U(I,J)/R6;V(I,J)/W1-U(I,J)!(1/W1)
355 NEXT J
360 PRINT
365 NEXT I
370 GO TO 15
1001 DATA 4,4,0,0,180,0,6,-40,5,36,20,2,1,0,10,3,1,20,30,40,
9999 END

```

Table 6-2 INPUT AND OUTPUT PARAMETERS FOR MFTGE 265

<u>Units</u>	<u>Parameter</u>	<u>Description</u>
wavelength	D_1, D_2, D_3	Distance of scatterers 1, 2, and 3 from origin
degrees	τ_1, τ_2, τ_3	Angular position of scatterers 1, 2, and 3
db	SR_2, SR_3	Strength of scatters #2 and #3 relative to scatterer #1
	N_1	Number of delta L's
	N_2	Number of delta ψ 's
	N_3	Number of delta θ 's
wavelength	L_0	Starting value of L
wavelength	ΔL	Increment on L
degrees	ψ_0	Starting value of ψ
degrees	$\Delta\psi$	Increment on ψ
	W	Number of windows to be considered
degrees	$\Delta\theta$	Increment on θ
degrees	$\theta_0(1) \dots \theta_0(W_1)$	Starting values of theta for windows

$\rho(j)$ = correlation coefficient for $\psi(j)$ where $\psi(j) = \psi_0 + (j-1)$
 $L(i)$ = Index signifying results from $L = L + (i-1) \Delta L$

Window 1

$L(1)$

1 $\rho(1) \dots j \rho(j) \dots N_2 \rho(N_2)$

BIG - largest of $\rho(j)$; JBIG j^{th} index for which BIG occurs

.

$L(i)$

1 $\rho(1) \dots j \rho(j) \dots N_2 \rho(N_2)$

BIG - largest of $\rho(j)$; JBIG = j^{th} index for which BIG occurs

.

$L(N_1)$

1 $\rho(1) \dots$

.

.

Similarly for other windows, if any, BIGGEST - Largest value of BIG for all i, j .

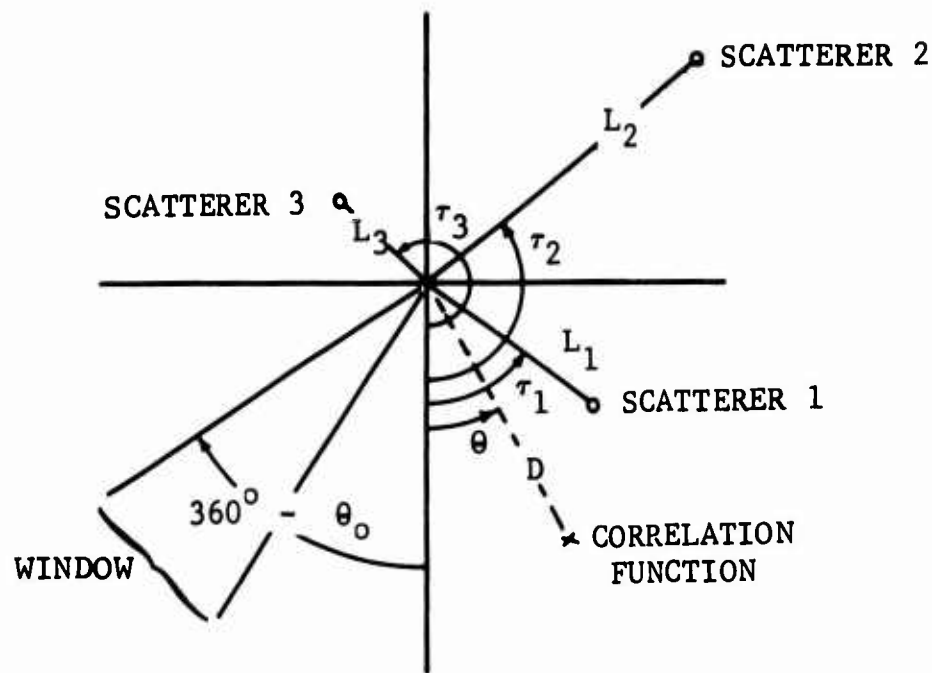


Fig. 6-1 GEOMETRY USED WITH PROGRAM MFTGE 265

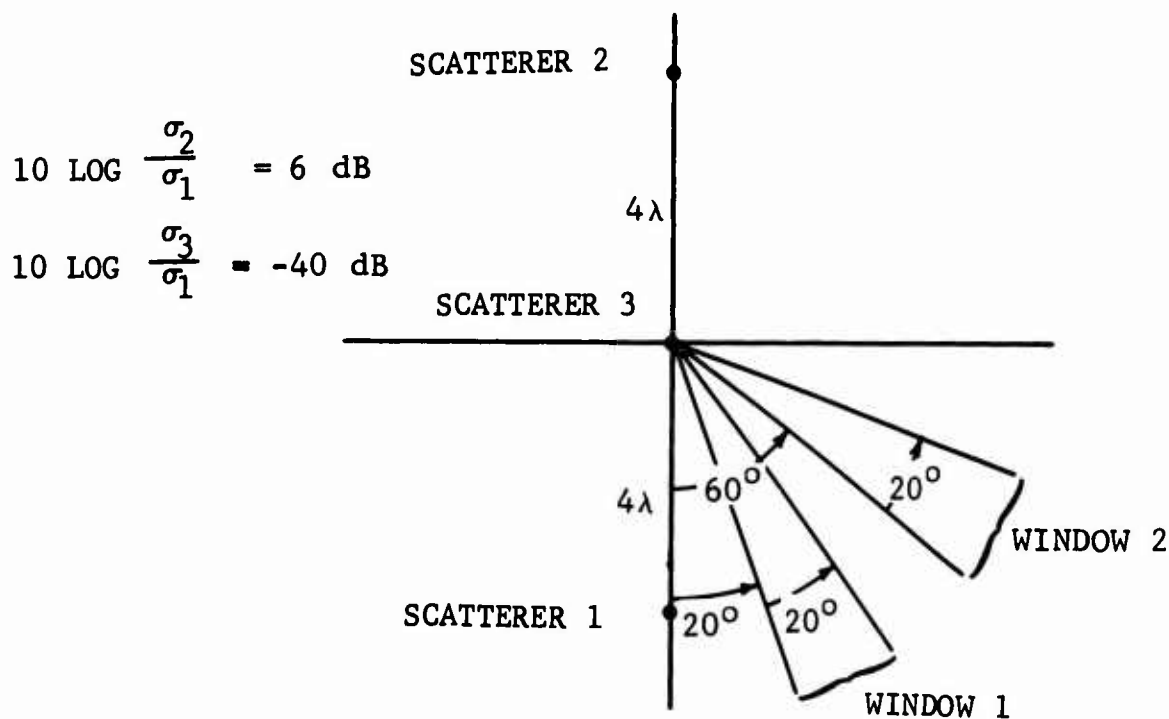


Fig. 6-2 GEOMETRY OF PROBLEM ILLUSTRATED IN FIGURE 6-3

with the pattern expressed in Equation 6-5. This correlation process is expressed in Equation 6-6 which is identical to Equation 6-4 with the measured data replaced by the right hand side of Equation 6-5.

$$\rho(D_i, \theta_j) = \int_{\theta \text{ window}} \sqrt{\sigma(\theta)} e^{j [\psi(\theta) e^{-j2kD_i \cos(\theta - \theta_j)}]} d\theta \quad (6-6)$$

The magnitude of the correlation coefficients, $\rho(D_i, \theta_j)$, as a function of D_i and θ_j provide an indication of the position of the scatterers comprising $\sqrt{\sigma(\theta)} e^{j \psi(\theta)}$ depending upon the size of the theta (θ) window and the sensitivity of the process to the separation and relative strengths of the three scatterers.

The location of the actual scattering centers on a target should be invariant to the size and location of the theta window of observation over a fairly broad region of aspect angle. In other words, the largest correlation coefficient obtained for one window should also indicate the same scatterer location for another window only if there is indeed a scatter located at that point in D, θ space. Figure 6-3a and b show plots of $\rho(D, \theta)$ obtained by plotting ρ versus θ with D as a parameter for the problem geometry shown in Figure 6-2. A 20-degree theta window was used to obtain the data in both Figure 6-3a and b, however the

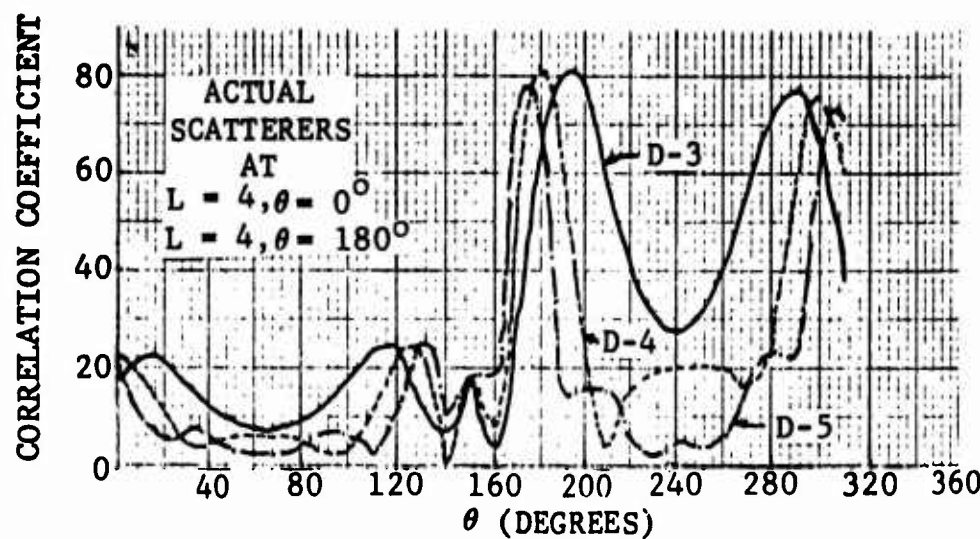


Fig. 6-3a CORRELATION COEFFICIENT FOR WINDOW 1

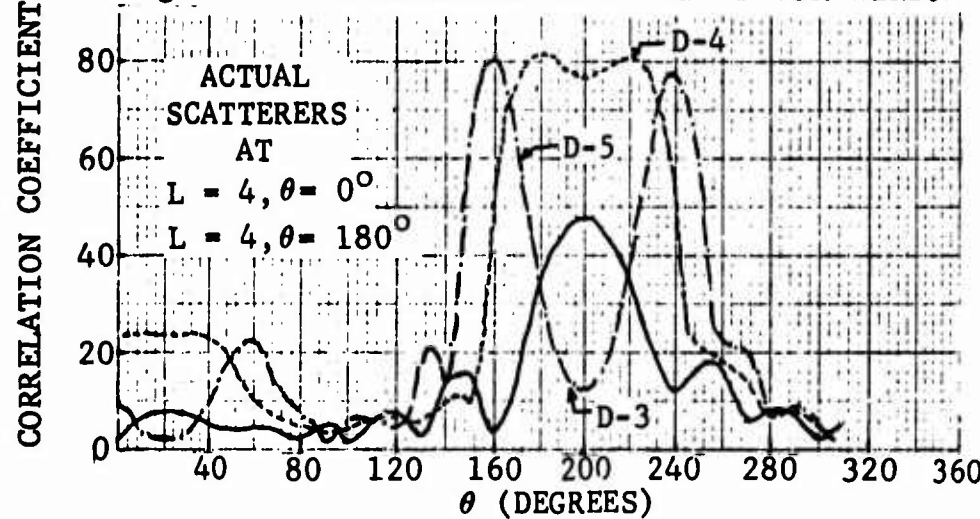


Fig. 6-3b CORRELATION COEFFICIENT FOR WINDOW 2

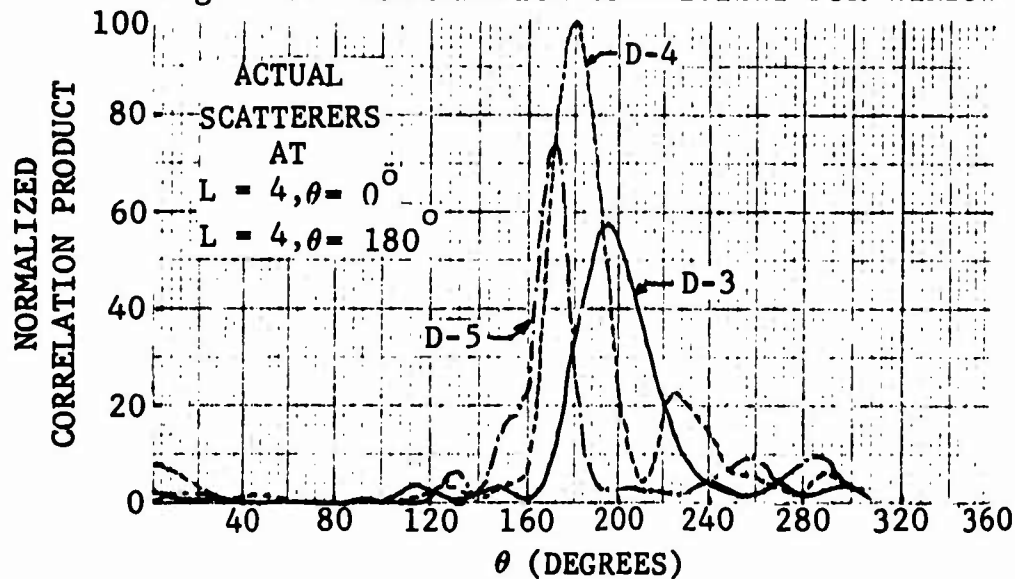


Fig. 6-3c NORMALIZED PRODUCT OF CORRELATION COEFFICIENT FOR WINDOWS 1 AND 2

Fig. 6-3 CORRELATION COEFFICIENTS COMPUTED BY USE OF MFTGE 265

initial value of θ was 20 degrees in the former and 60 degrees in the latter. Thus, windows consisting of the intervals between 20 and 40 degrees and between 60 and 80 degrees are represented. The dominant scatterer located at $L_2 = 4$ and $\tau_2 = 180$ degrees obviously produces the highest value of $\rho(D, \theta)$ when $D = 4$ and $\theta = 180$ degrees. In the case of each plot, however there are other relative maximums the locations of $\rho(D, \theta)$, of which are not invariant to the position of the window. In order to enhance this invariancy, the product of $\rho_1(D, \theta)$ and $\rho_2(D, \theta)$ for windows 1 and 2 was computed and normalized to the largest value of the product and is shown in Figure 6-3c. The invariancy of the location of the dominant scatterer to window position is clearly presented in this figure. In this particular problem, scatterer number 2 was four times as strong as scatterer 1 ($L_1 = 4$ and $\tau_1 = 0$ degree) and scatterer number 3 was negligibly small. Although the presence of a scatterer at $\theta = 0$ degrees is not indicated as conclusively as some of the "ghost" scatterers, the plot in Figure 6-3c indicates that a resolution of ± 1 may be obtained for dominant scatterers using only two windows and synthesized data. The presence of "ghost" scatterers, i.e., the indication that scatterers are located where, in fact, none are present, should be mentioned. In the case of measured data, the

presence of ghosts would not be unreasonable, however in the case of the synthesized data used in this analysis, the assumptions of slowly varying amplitude and discrete location are entirely satisfied. Therefore, other mechanisms must account for the presence of ghosts. This mechanism is associated with the window size utilized in the computation. It can be shown, for example, that the smaller the window size, the easier it is to synthesize a given cross section and phase pattern by use of a variety of scatterer strengths and locations. In other words, the smaller the window, the less unique is the solution of this inverse scattering problem. In the limiting case, an infinite number of scatterers and locations could be used to analytically synthesize the cross section and phase of any target at a single orientation. The use of very wide windows might be justified when using synthesized data, however in the case of measured data a compromise must be attained between the smallest window which provides usable resolution and the largest window which does not violate the assumptions necessary for the MFT to be applied.

6.2.3 Application of MFT to Measured Signatures

In order to examine the utility of the MFT for use with measured signature data, the technique was programmed on the IBM 360 for use with library data on magnetic tape.

This computer program is designated as General Dynamics computer program AG2. A description of these experiments, their results, and conclusion relative to the application of MFT are contained in Reference 3.

6.3 Polarization Technique

The polarization technique of inverse scattering analysis is associated with the polarization properties of the vehicle and their relationship to the symmetry property of the vehicle scattering matrix. This technique is briefly described in this section, however the details of the application of the technique to the synthesis targets described in Section V of this volume are contained in Reference 3.

6.3.1 Analytical Approach

In order to describe the polarization technique it is first noted that the target scattering amplitude can be written in terms of a linear polarization parameter, ρ , and aspect angle, θ , in the form of Equation 6-7.

$$\sqrt{\sigma(\rho, \theta)} = [\sin \rho_r, \cos \rho_r] \begin{bmatrix} \sqrt{\sigma_{VV}(\theta)}, \sqrt{\sigma_{VH}(\theta)} \\ \sqrt{\sigma_{HV}(\theta)}, \sqrt{\sigma_{HH}(\theta)} \end{bmatrix} [\sin \rho_t \\ \cos \rho_t]$$

(6-7)

ρ_r denotes receiver polarization

ρ_t denotes transmitter polarization

Also, the polarization parameter ρ can be interpreted as the angle that the target axis makes with the bases vectors reference used to arrive at the target scattering matrix. (e.g., $\rho_t = \rho_r = 0$ gives $\sigma(\rho, \theta) = \sigma_{HH}(\theta)$ whereas $\rho_t = \rho_r = \pi/4$ gives the cross section which would be measured if the target was rotated 45 degrees counterclockwise about the RLOS as seen from the radar). Therefore, in the case of symmetrical targets, it is easy to demonstrate that if the linear target scattering matrix is obtained by rotating the target in its plane of symmetry then

$\sigma(\pi/4, \theta) = \sigma(-\pi/4, \theta)$ where $\sigma(\pi/4, \theta)$ and $\sigma(-\pi/4, \theta)$ are values computed using the measured scattering matrix and Equation 6-7. However, in the case of a specular scatterer, it is also true that $\sigma(\rho, \theta) = \sigma(\rho + \pi/2, \theta)$ for all ρ . Hence, if a relationship between ρ and θ was generated using the condition denoted in Equation 6-8 then

$$\left\{ \rho : \frac{|\sigma(\rho, \theta) - \sigma(\rho + \pi/2, \theta)|}{|\sigma(\rho, \theta) + \sigma(\rho + \pi/2, \theta)|} < \epsilon \right\} \quad (6-8)$$

for each target measured a graph would be generated such as that illustrated in Figure 6-4. The graph illustrated in Figure 6-4 will be referred to as the target symmetry envelope and as indicated in the figure can be interpreted in

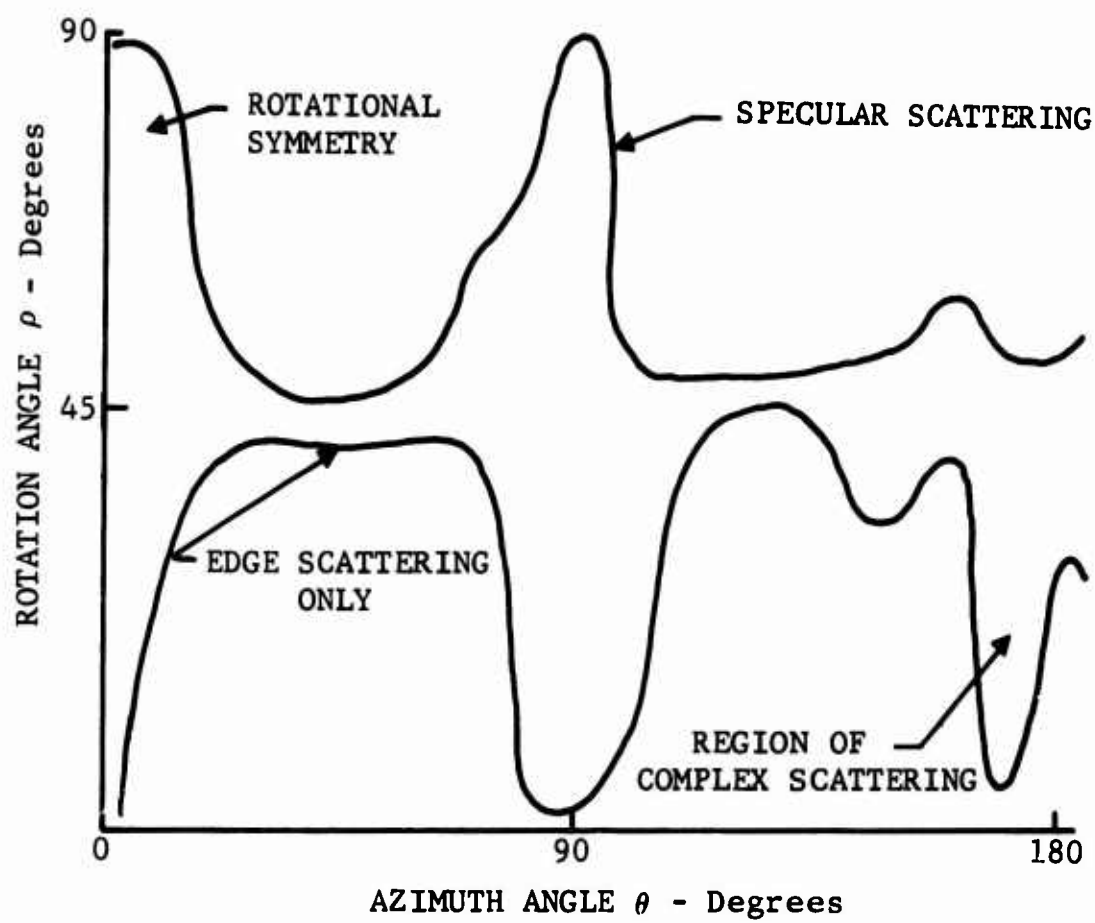


Fig. 6-4 TARGET SYMMETRY ENVELOPE

terms of the apparent geometrical properties of the target. This type of scattering signature representation could be quite useful in the field of SOI to aid in target orientation and identification. In the current application it is used to objectively evaluate the effect on the polarization properties of a target caused by known geometrical perturbations. The results depicted in Figure 6-4 are interpreted in the following manner. The range of polarization angles (or target rotation angles about the RLOS) contained between the upper and lower curves represent the range of angles through which the target could be rotated concurrent with maintaining $\sigma(\rho, \theta) = \sigma(\rho + \pi/2, \theta) \pm$ Threshold Level.

6.3.2 Computation Technique

The basic flow diagram of the computer program (designated General Dynamics computer program AG3) is shown in Figure 6-5. The primary input parameters to this program are the range and the number of target signature points, the linear polarization increments, the aspect interval over which to average, and the threshold level. Input target data is derived from a magnetic tape containing the target scattering matrix in the form of 3600 card image records. Output data from this program consists of the average polarization signature ratios RHOH1 and RHOH2 plotted as a function of the target aspect angle.

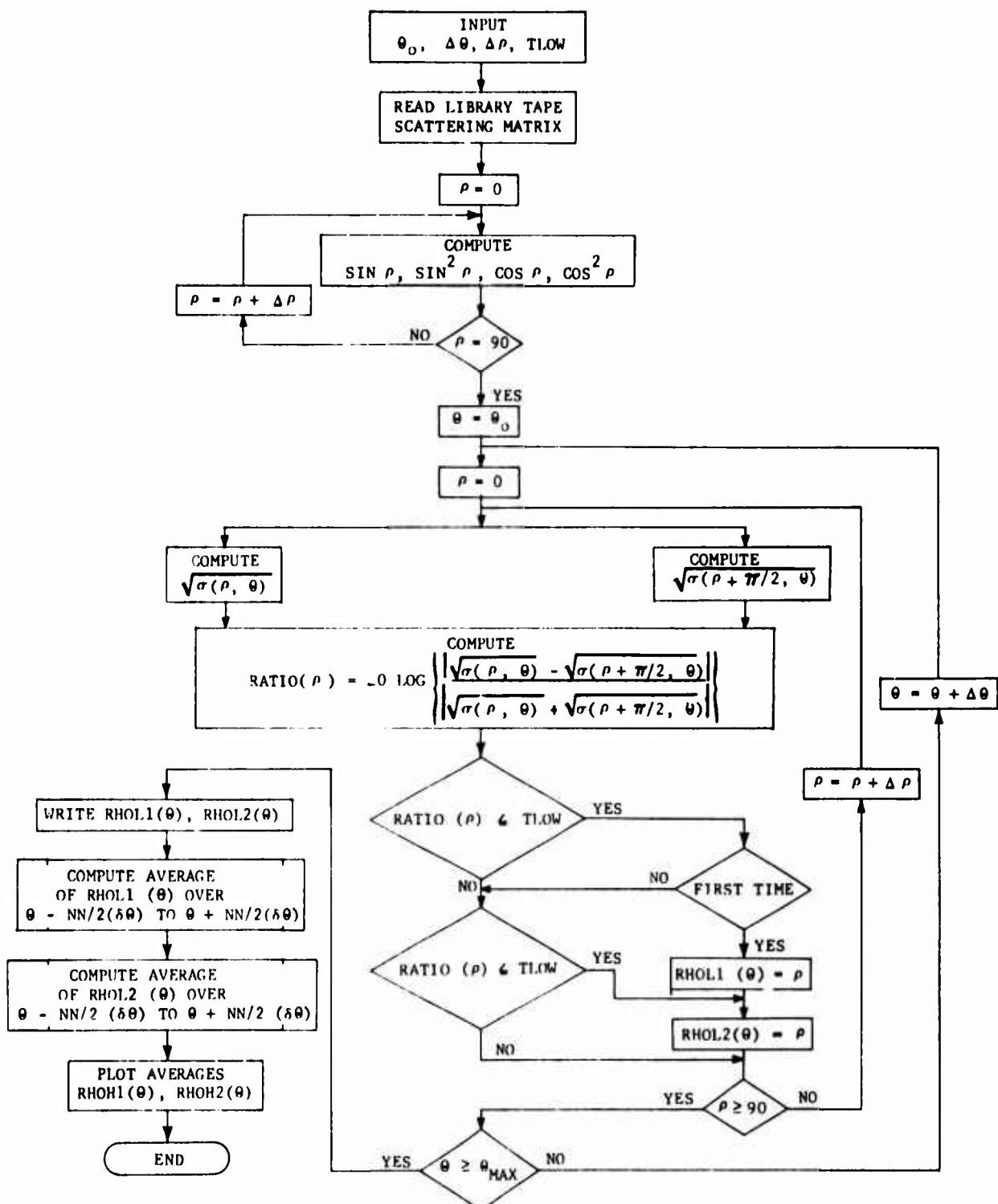


Fig. 6-5 FLOW DIAGRAM OF POLARIZATION PROGRAM - AG3

The threshold level is used to establish the values of the upper and lower limits of ρ at each value of azimuth angle. Thus, the two curves of RHOH1 and RHOH2 in the output represent the first and last values of ρ obtained by use of the threshold level, TLOW = -15 dB.

If, for example, ρ corresponds to the VV polarization then if

$$20 \log \left[\frac{|\sqrt{\sigma_{VV}} - \sqrt{\sigma_{HH}}|}{|\sqrt{\sigma_{VV}} + \sqrt{\sigma_{HH}}|} \right] < -15.0$$

is satisfied, the value of ρ corresponding to 90 degrees would be recorded on the plot at the pertinent aspect angle.

6.4 Phase Signature Technique

The third technique of inverse scattering analysis investigated in this study is based upon the use of the measured phase signatures of the vehicles of interest. Since the phase data obtained in the experimental investigation of this program is referenced to a known space reference, the instantaneous phase center of the synthesized vehicles can be plotted as a function of aspect angle.

6.4.1 Analytical Approach

The purpose of this investigation was to develop a computation technique whereby the absolute location in space of the phase centers of a set of vehicles could be compared.

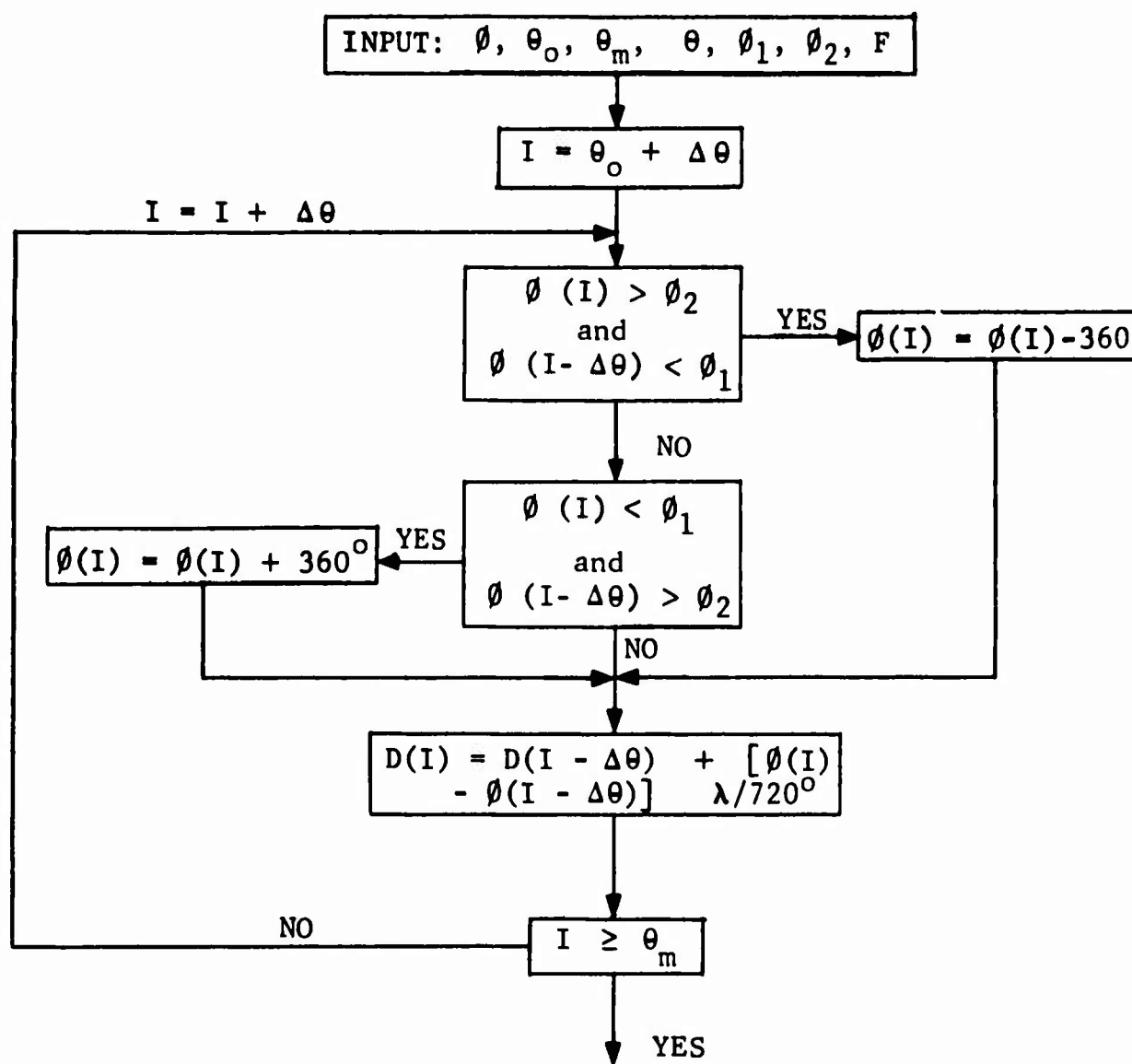
Of primary interest was a comparison of the manner in which the location of the phase centers varied for the synthesis vehicles.

6.4.2 Computation Technique

The phase signature computations routine is a subroutine of the polarization signature program AG3. The basic flow diagram of this routine is contained in Figure 6-6.

6.5 Results and Conclusions

The results obtained by using the inverse scattering techniques described herein to processing measured signatures are contained in Volume IV. Conclusions are reached from analysis of those results relative to the feasibility of each technique.



NEXT PROBLEM

Fig. 6-6 FLOW DIAGRAM OF PHASE SUBROUTINE - AG3

SECTION 7

SHORT-PULSE EQUIVALENCE CLASS TECHNIQUE

7.1 General

The fundamental objective associated with SOI and BMD consists of the identification/classification/designation of targets in sufficient time to make decisions relative to the taking of effective military action to counter any threat to the national security of the United States. The two parameters which virtually control the utility of such a decision-making process are (1) the time required to make a decision and (2) the confidence level which can be associated with a given decision. A classification process which provides decisions in real time is desired; however, its value would be measured by the degree of confidence associated with it. Conversely, the expenditure of many hours or even days in the analysis of signature data to arrive at high-quality decisions would be of little value if only a few minutes were available in which to initiate counter action.

These two parameters, time for decision and confidence in the decision, are obviously in conflict with each other and means of decreasing the former and increasing the latter

are, on the surface, difficult to achieve. A number of items contribute to this difficulty; these include the following:

1. Many scattering parameters must be measured in order to completely describe the scattering properties of most targets.
2. The amount of useful data, i.e., data from which information of value can be extracted, is much less than the total amount generally obtained during a measurement sequence by use of operational radars.

In order to achieve the objectives of SOI and BMD, it appears mandatory that the radar signatures contain a high density of information relative to time. Also, the recording of these signature data must be accomplished in an efficient manner so that available storage capacity is not misused by storing useless information. Finally, processing techniques must be developed to operate on the information which is of greatest significance in making the decision of interest. These three facets of the SOI and BMD problems are illustrated in Figure 7-1.

A number of measurement procedures may be utilized as a means of increasing the amount of information upon which to base identification decisions. These procedures include the use of (1) multiple frequencies, (2) multiple look

angles (multistatic antenna systems), (3) multiple polarizations, and (4) coherent radar systems. A fifth parameter which has been extensively investigated is associated with the change in the scattered return as a function of changes in the aspect of the vehicle. However, if the aspect angle changes very little during the time an object is being observed, this parameter may be of little value. On the other hand, the other parameters listed above may be used to provide information in real time concerning (1) the frequency response of a target, (2) the variation in radar cross section with look angle, (3) the polarization properties of a target, and (4) the location of scattering centers on a target.

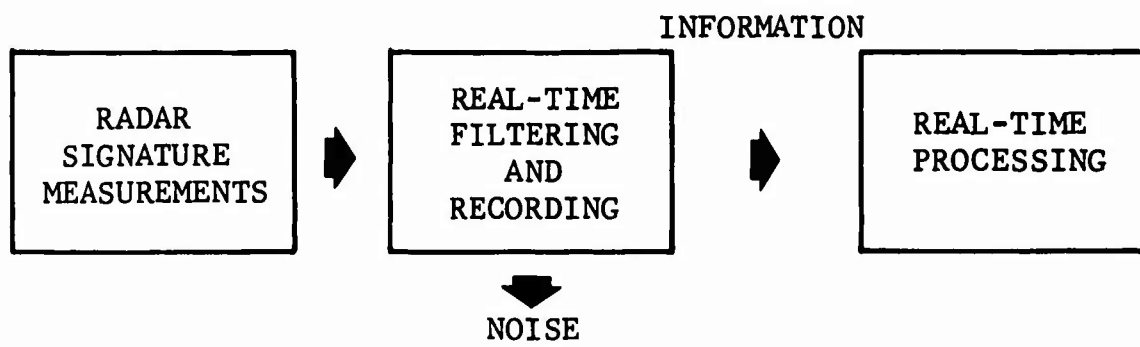


Fig. 7-1 SOI/BMD DATA PROCESSING

A short-pulse radar provides another method of obtaining additional information in real time, i.e., during the period of a single observation of the target. This information is in the form of the target scattering response as a function of depth along the RLOS. This information may provide a direct indication of the location and strength of discrete scattering centers which contribute to the total scattering properties of the target. The variation of the scattering produced by these scattering centers, as a function of polarization, provides additional information of value to real-time decision making. Changes in target aspect will also produce changes in parameters determined by use of short-pulse measurements just as in the case of long-pulse measurements. Consequently, the use of short-pulse signatures may provide the information necessary to make the transition from the non-real-time, manual-pattern analyses which are presently employed to an automated decision-making process that is operated in real time.

The need for automated processes results primarily from the amount of data and the large number of parameters that must be considered and the desire to process data in real time. Manual analyses become severely limited as the number of parameters is increased unless elaborate display techniques are utilized to simplify the visual correlation

of multiple parameters. Also, if multiple targets are to be tracked simultaneously, for example by use of a phased array, the storage of all measured signatures involves a large amount of storage space. This fact again illustrates the need for the real-time filtering and recording of only those signature measurements which contain usable information.

7.2 Technical Approach

The approach to real-time radar signature analysis described herein is based on the use of a generalized technique for (1) reducing the storage required to store pertinent signature information by discarding data of low information content, (2) providing a means of grouping similar signatures for efficient processing, and (3) providing a means of extracting a set of discriminants from these groupings, i.e., discriminants upon which decisions as to the relative and absolute physical characteristics of targets are based. This technique, the Equivalence Class Technique (ECT) is described briefly in Reference 6 and in more detail in Reference 7.

Figure 7-2 is a flow diagram of the four basic processes embodied in the ECT.

The motivation for the use of the ECT is the desire (1) to achieve a logical grouping of signatures which exhibit similar values of one or more significant parameters

and (2) to store, in a highly efficient manner, only those signature parameters which contain information of direct value in automated decision-making processes.

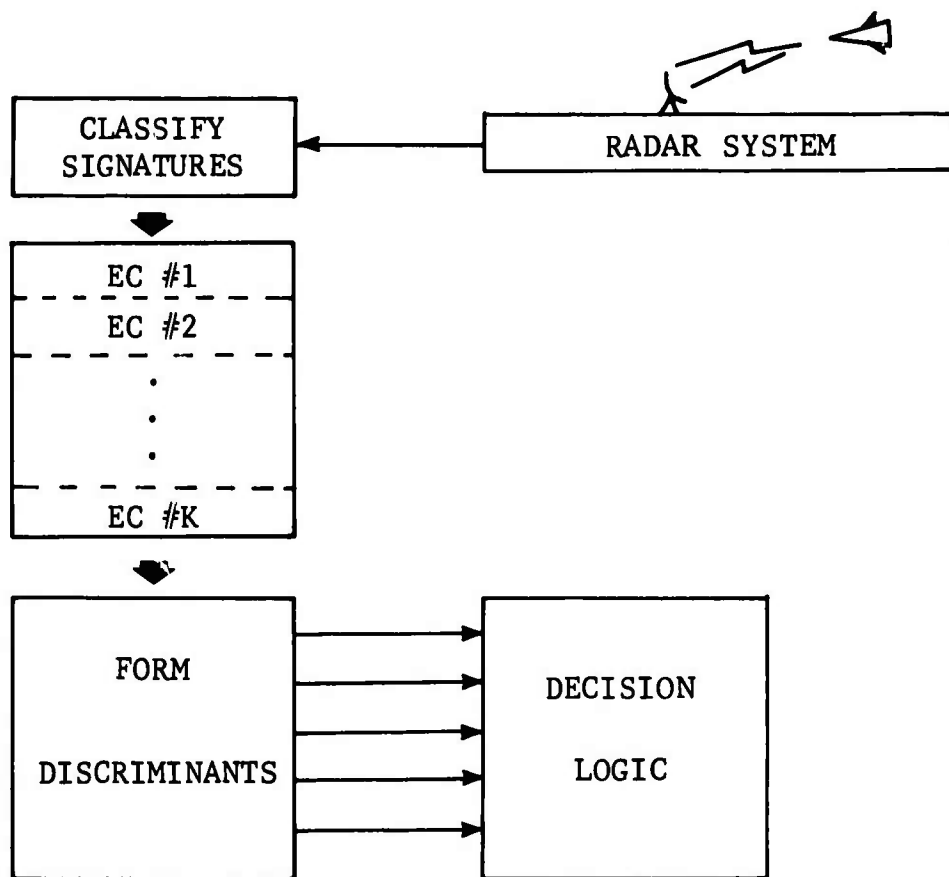


Fig. 7-2 FLOW DIAGRAM OF GENERALIZED ECT

The four steps indicated in Figure 7-2 are common to all ECT's although the particular processes accomplished during each step are determined on the basis of the type of signatures which are being utilized, the manner in which

each equivalence class is established, and the type of decisions of interest.

7.3 Technical Investigation

An ECT based on the use of short-pulse signatures was developed during this investigation. This technique and the resulting computer program will be referred to by use of the acronym SPECT for Short-Pulse Equivalence Class Technique. The details of this investigation are reported in Volume IV of this report (Reference 3), wherein the total inverse scattering investigation is presented.

The following SPECT objectives were established for accomplishment during the scattering principles investigation:

1. Selection of a basis for equivalence classes
2. Definition of a method of forming equivalence classes
3. Determination of the significance of data discarded during the formation of equivalence classes
4. Definition of a set of discriminants for evaluation by use of measured short-pulse signatures
5. Examination of the feasibility of forming discriminants in real time
6. Processing of at least one set of measured data in order to check out the SPECT computer program.

The following additional items are necessary in order to establish the utility of the SPECT concept:

1. Processing of selected data from a set of sample targets to determine an optimum set of discriminants
2. Formation of a set of decision rules based upon the values of the selected discriminants
3. Implementation of decision logic
4. Evaluation of SPECT by use of measured signatures of selected targets
5. Implementation of a real-time version of SPECT
6. Simulation of real-time acquisition of selected signatures.

7.4 Results and Conclusions

7.4.1 Results

A computer program, SPECT, was written and checked out by use of an edited short-pulse tape. The processed data consisted of short-pulse signatures obtained by use of a sphere-capped cylinder which was scheduled for use as an orbiting radar calibration target. The edited tape was produced by processing a set of radar-range tapes by use of a computer program which is described in Volume I.

Figure 7-3 contains an illustration of the processes accomplished by use of this program. A simplified flow diagram of the SPECT computer program is shown in Figure 7-4.

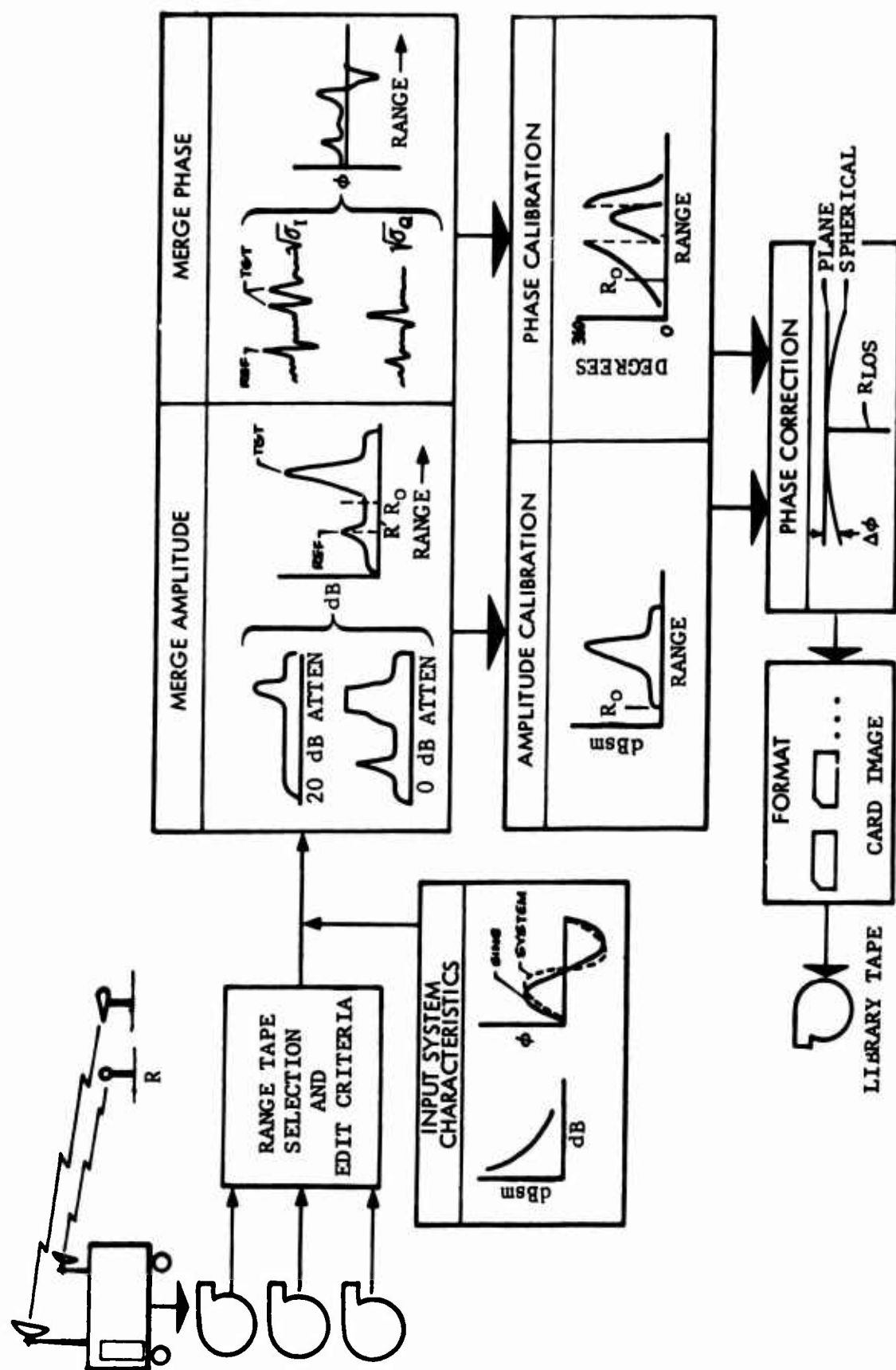


Fig. 7-3 SHORT-PULSE LIBRARY TAPE PROCESSING SEQUENCE

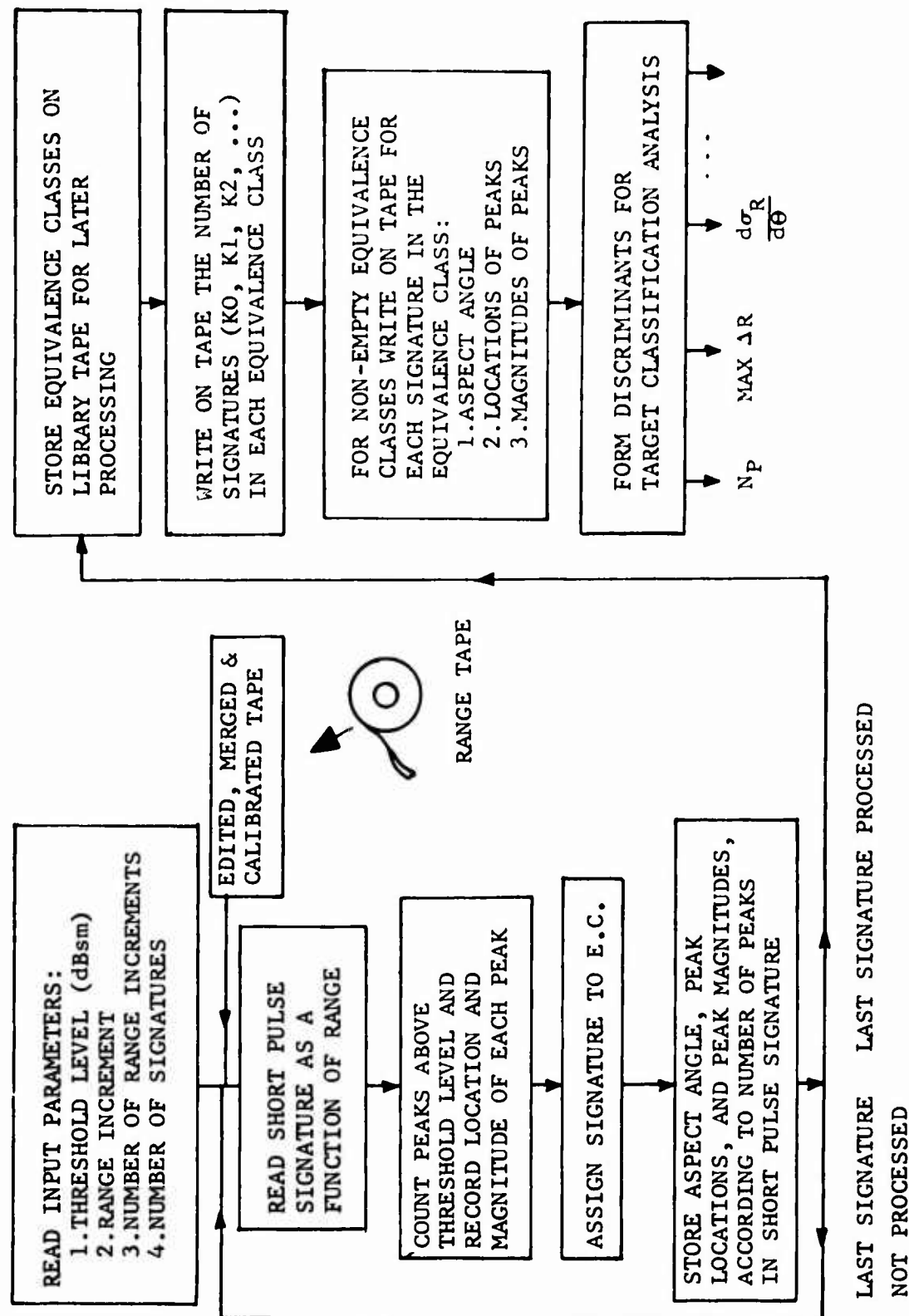


Fig. 7-4 COMPUTER PROGRAM SPECT PROCESSING SEQUENCE

The use of these data was sufficient to check out the operation of the SPECT program up to the point of writing the equivalence classes onto magnetic tape to enable evaluation of the equivalence class formulation.

7.4.2 Conclusions

The present version of the SPECT program may be used to formulate measured short-pulse signatures into a set of equivalence classes from which a set of discriminants can be selected for evaluation. The development of a SPECT program for use in real-time classification will involve the use of hardware which can be used to efficiently filter signature data and record only those data containing information of value in the decision of interest. In order to fully evaluate the SPECT concept, it will be necessary to process selected data on a number of vehicles which exhibit a variety of physical characteristics.

SECTION 8

RECOMMENDATIONS

In the broad spectrum of scattering technology covered during this program, a number of the investigations warrant additional study, notably some of the new techniques of inverse scattering analysis which were introduced during this program. Volume IV contains recommendations on the investigation of additional areas related to these techniques. As an example, the use of the superposition technique appears to have merit in obtaining "quick look" data on the radar cross section of fairly complex radar targets. The feasibility of establishing a bank of signatures for this use would be based upon defining the ranges of the parameters of interest to potential users. These parameters include (1) vehicle physical characteristics, (2) frequencies, and (3) allowable errors. It is recommended that such an investigation be initiated on the basis of establishing the cost and effectiveness of such a bank.

REFERENCES

1. Investigation of Scattering Principles, Volume II,
Scattering Matrix Measurements, General Dynamics Report
FZE-792, Fort Worth: General Dynamics-Fort Worth
(July 1968)
2. Investigation of Scattering Principles, Volume III,
Analytical Investigation, General Dynamics Report
FZE-793, Fort Worth: General Dynamics-Fort Worth
(July 1968)
3. Investigation of Scattering Principles, Volume IV,
Inverse Scattering Analysis, General Dynamics Report
FZE-794, Fort Worth: General Dynamics-Fort Worth
(August 1968) (Document SECRET) (Title Unclassified)
4. An Analysis of the Scattering Matrix Measurements
Capabilities of a Ground Plane Radar Cross-Section
Range, Technical Documentary Report No. RADC-TDR-64-317,
Rome Air Development Center, Rome, New York (June 1964)
AD NO. 605519.
5. Radar Cross Section and Measurement Capabilities,
General Dynamics Report FZE-675, Fort Worth: General
Dynamics-Fort Worth (June 1968)

6. Gruver, G. W., Scattering Matrix Utilization Study,
Technical Report No. RADC-TR-67-392, Rome, New York:
Rome Air Development Center AD NO. 820553.

7. Gruver, G. W., An Application of Equivalence Class
Techniques to Radar Signature Analysis, Unpublished
Ph.D Dissertation (1968)

UNCLASSIFIED

Security Classification

DOCUMENT CONTROL DATA - R & D

(Security classification of title, body of abstract and indexing annotation must be entered when the overall report is classified)

1. ORIGINATING ACTIVITY (Corporate author) General Dynamics, Fort Worth Division P.O. Box 748 Fort Worth, Texas 76101		2a. REPORT SECURITY CLASSIFICATION Unclassified
		2b. GROUP N/A
3. REPORT TITLE Investigation of Scattering Principles, Volume I		
4. DESCRIPTIVE NOTES (Type of report and inclusive dates) Final		
5. AUTHOR(S) (First name, middle initial, last name) Dr. George W. Gruver		
6. REPORT DATE May 1969	7a. TOTAL NO. OF PAGES 253	7b. NO. OF REFS 7
8a. CONTRACT OR GRANT NO F30602-67-C-0074	9a. ORIGINATOR'S REPORT NUMBER(S) FZE-791	
b. PROJECT NO 6512	9b. OTHER REPORT NO(S) (Any other numbers that may be assigned this report) RADC-TR-68-340, Volume I	
c. Task No: 651207		
d.		
10. DISTRIBUTION STATEMENT This document is subject to special export controls and each transmittal to foreign governments, foreign nationals or representatives thereto may be made only with prior approval of RADC (EMASS), Griffiss AFB, New York 13440.		
11. SUPPLEMENTARY NOTES RADC Project Engineer: John C. Cleary AC 315 330 2118	12. SPONSORING MILITARY ACTIVITY Rome Air Development Center (EMASS) Griffiss Air Force Base, New York 13440	
13. ABSTRACT The objective of this effort was to establish and apply the mechanics of radar scattering from complex objects in terms of actual measurement data and the resulting empirically derived mathematical relationships. Volume I contains a summary of each task as well as detailed documentation on the experimental and superposition investigations. Volume II contains radar range measurement data used in the experimental portion of the effort. Volume III contains the results of the analytical investigation, which uses geometric diffraction theory to predict radar cross section and scattering phase. Volume IV contains the potential military applications and results of the inverse scattering investigation.		

DD FORM 1 NOV 68 1473

UNCLASSIFIED
Security Classification

UNCLASSIFIED
Security Classification

14 KEY WORDS	LINK A		LINK B		LINK C	
	ROLE	WT	ROLE	WT	ROLE	WT
Scattering Matrix Measurements Radar Range Radar Target Long Pulse Short Pulse Statistical Analysis Statistical Signature Analysis Equivalence Class						

UNCLASSIFIED
Security Classification